



Feasibility Study of a Hybrid Process for Improving Cold Incremental Sheet Forming of Titanium Alloy

A thesis submitted in fulfilment of the requirements for the
degree of Doctor of Engineering in Advanced Manufacturing:
Forging and Forming

Department of Design, Manufacturing and Engineering
Management, University of Strathclyde

Michael Thomas McPhillimy

Abstract

Titanium is used for high value engineering components where high strength-to-weight ratio and corrosion resistance is a critical requirement. However, the production of complex components made from titanium alloys is limited due to their limited formability at low temperature, which necessitates thermal activation to increase their formability and ductility. High temperature forming is expensive. To justify the use of titanium alloys in industry the benefits gained must be sufficient to justify the high cost. A potential route for increasing the use of titanium alloys in industry is to improve their formability at ambient room temperature. Incremental sheet forming (ISF) is an innovative metal forming technology which uses a computer numerical controlled (CNC) tool to incrementally form sheet parts in place of a dedicated punch and die combination. ISF can increase the forming limits of sheet metal, meaning high temperature forming may no longer be necessary to process titanium alloys. However, sheet thinning and springback during room temperature ISF are two major drawbacks which compromise performance and can result in complete failure of the part. To counter thinning, the introduction of a pre-ISF additive step to thicken the titanium preform in areas of predicted thinning was investigated. This novel hybrid technology has been developed with the aim of improving thickness homogeneity in ISF titanium parts. The main gap in knowledge was the non-availability of data and research on a pre-ISF additive step, and its impact on the geometric accuracy and part quality of titanium sheet parts formed by ISF.

In the present research, laser metal deposition (LMD) was used to locally thicken a commercially pure titanium (CP-Ti) grade 2 sheet. No further surface preparation was performed on the tailored material following LMD. The mechanical behaviour of the tailored material was investigated using room temperature uniaxial testing. In-situ digital image correlation (DIC) measured the strain distribution across the surface of the material throughout. The goal was to examine the impact the additive pre-ISF step had on the room temperature formability of the LMD tailored CP-Ti sheet. The uniaxial

tensile testing found that isotropic mechanical properties were obtained within the sheet plane in contrast to the anisotropic properties of the as received (AR) material and build height appeared to have little influence on strength. The in-situ DIC evaluation analysis showed strain to concentrate between the LMD tracks. Microstructural analysis showed distinct regions through the cross-section of the LMD thickened material with a heat affected zone (HAZ) at the interface between the top LMD layer and the non-transformed substrate material. Grain growth and intragranular misorientation in the LMD deposit was observed. A finite element analysis (FEA) simulation of the uniaxial tensile test was modelled to generate a FE material model for the anisotropic CP-Ti sheet. Building a material model of the tailored sheet and simulating the ISF process was not possible within the project time span, rather it was suggested for future research. ISF with a back support die was performed on a LMD thickened CP-Ti sheet. A GOM Atos metrology technique was used to generate a 3dimensional representation of both a LMD tailored preform and the sheet following ISF, as well as a previously formed AR CP-Ti part to compare. The results showed thickening the sheet in areas of predicted thinning helped achieve greater thickness homogeneity across the sheet following room temperature ISF. However, nucleation and development of cracks in the forming direction followed by catastrophic failure was observed in the 60° angled section of the LMD tailored sheet during ISF, earlier than the AR CP-Ti sheet. Some wrinkling was seen in the preform in response to LMD however fixtures and a post-LMD residual stress relief heat treatment ensured springback was limited. Further exploration of the LMD thickened material with a room temperature Nakajima test showed lower strain limit under the equi-biaxial strain state. Lack of surface preparation was considered as a likely cause of premature failure. This was briefly investigated, and more thorough analysis was recommended. Despite some issues, this technique shows potential for the room temperature forming of titanium parts and further investigations should be performed in the future to explore its capability.

The literature review and experimental investigation contained in this thesis has identified and provided data and research on a pre-ISF additive step, fulfilling the above

identified knowledge gap. Based on the research results, suggestions for further studies have been proposed and the major industrial relevance have been discussed.

Acknowledgements

I wish to express my gratitude to my supervisors; Prof. Paul Blackwell (First supervisor) and Dr. Evgenia Yakushina (Second supervisor) for their guidance and support.

I would like to acknowledge the entire staff of both the Advanced Forming Research Centre (AFRC) and the Department of Design Manufacturing & Engineering Management (DMEM) for their help and expertise. With special mention to Dr. Dorothy Evans, Dr. Giribraskar Sivaswamy, Michael Canavan, Dr. Diego Gonzalez, Prof. Jonathan Corney, Dr. Shanmukha Moturu, Ahmed Elsayed, Kornelia Kondziolka, Ryan O'Neill, Jacqueline Schramm, and Ian McKenzie. I am particularly grateful to Prof. Yi Qin who was instrumental in my decision to enrol in the EngD programme.

I am very thankful of the staff at Pascoe Engineering and Laser Additive Solutions for their collaborations.

A shout out to my fellow PhD and EngD cohort whom I shared this experience with. James, Michail, Beatrice, Angus, Jonny, Matthew, Calum, David, and Peio.

Finally, to my parents and brothers. I couldn't have completed this without your support.

Declaration of authenticity and author's right

“This thesis is the result of the author’s original research. It has been composed by the author and has not been previously submitted for examination which has led to the award of a degree.”

“The copyright of this thesis belongs to the author under the terms of the United Kingdom copyright acts as qualified by the University of Strathclyde regulation 3.50. Due acknowledgement must always be made of the use of any material contained in, or derived from this thesis.”

Signed:

Date:

Proclamation of academic honesty

“I declare that this submission is entirely my own original work. I declare that, except where fully referenced direct quotations have been included, no aspect of this submission has been copied from any other source. I declare that all other works cited in this submission have been appropriately referenced.

I understand that any act of academic dishonesty such as plagiarism or collusion may result in the non-award of my degree.”

Signed:

Date:

Publications

The underlisted publications were undertaken by the candidate in contribution to the application for an Engineering Doctorate degree;

1. McPhillimy, M.; Yakushina, E.; Blackwell, P. (2022) Tailoring Titanium Sheet Metal Using Laser Metal Deposition to Improve Room Temperature Single point incremental forming. *Materials*, 15, 5985. <https://doi.org/10.3390/ma15175985>
2. Yang, S., McPhillimy, M., Supri, T. B. M., & Qin, Y. (2018). Influences of process and material parameters on quality of small-sized thin sheet-metal parts drawn with multipoint tooling. *Procedia Manufacturing*, 15. <https://doi.org/10.1016/j.promfg.2018.07.395>

Table of Contents

Abstract.....	i
Acknowledgements	iv
Declaration of authenticity and author’s right.....	v
Proclamation of academic honesty	vi
Publications	vii
1 Introduction.....	1
1.1 Problem statement.....	2
1.2 Thesis structure	3
1.3 Programme of work flowchart	4
2 Literature Review	6
2.1 Engineering metals.....	6
2.2 Conventional Sheet Forming	15
2.3 Incremental Sheet Forming.....	23
2.4 Hybrid Manufacturing	37
2.5 Additive Manufacturing.....	41
2.6 Gaps and research focus.....	53
3 Experimental Approaches and Analysis Methods.....	54
3.1 Investigation approach for tailoring CP-Ti sheet with LMD.....	54
3.2 Engineering Tooling	54
3.3 Experimental setup and material testing	58
3.4 Results characterisation and analysis.....	75
3.5 Overview of research approach	76
4 Mechanical testing of additively thickened CP-Ti sheet	78

4.1	Chapter overview	78
4.2	Experimental Procedure.....	78
4.3	Results.....	92
4.4	Summary	103
5	Finite element analysis of a uniaxial tensile test	105
5.1	Chapter overview	105
5.2	Experimental approach	106
5.3	Results.....	113
6	Material analysis of additively thickened CP-Ti sheet.....	118
6.1	Chapter overview	118
6.2	Experimental Procedure.....	118
6.3	Results.....	121
6.4	Summary	131
7	ISF of an additively tailored CP titanium preform	132
7.1	Chapter overview	132
7.2	Experimental procedure	132
7.3	Results.....	150
7.4	Summary	165
8	Biaxial testing of additively tailored CP-Ti blanks	167
8.1	Chapter Overview	167
8.2	Experimental procedure	168
8.3	Calculating strain	178
8.4	Results.....	184
8.5	Summary	189

9	Conclusions and future research.....	193
9.1	Major findings.....	193
9.2	Contributions to knowledge.....	194
9.3	Reflections and future work.....	196
	References	198
10	Appendices.....	212
10.1	Product Design Specification for Fixture Design.....	212
10.2	Engineering Drawings, LMD Fixture.....	215
10.3	Engineering Drawings, ISF Fixture.....	219
10.4	Engineering Drawings, LMD/ISF blank material	229
10.5	Engineering Drawings, LMD/ISF preform	230
10.6	Engineering Drawings, Nakajima testing of LMD material	239
10.7	Engineering Drawings, Nakajima testing of as-received material	242
10.8	LMD sub-contractor logbook	244
10.9	MATLAB code, Tensile testing data.....	251
10.10	MATLAB code, Alicona profile	252
10.11	MATLAB code, Alicona roughness.....	253
10.12	MATLAB code, Generating mesh .txt file	256
10.13	MATLAB code, Generating IPF map	259
10.14	MATLAB code, Multiple curve fitting	261
10.15	MATLAB code, Nakajima FLD.....	263
10.16	MATLAB code, Material hardening curve	265
10.17	Material anisotropic function parameters	266

Table of Figures

Figure 1 Programme of work flowchart.	5
Figure 2 Unit cells of α and β phases (Lutjering & Williams, 2007).....	8
Figure 3 Typical CP-Ti microstructures: (a) Equiaxed; (b) Lamellar.....	10
Figure 4 Drawn CP-Ti cups at various temperatures (F. K. Chen & Chiu, 2005).....	12
Figure 5 Principle of operation of the SEM (Ortiz Ortega et al., 2022).....	14
Figure 6 Load extension diagram (Marciniak et al., 2002).....	16
Figure 7 Main deformation modes (Marciniak et al., 2002).	17
Figure 8 The FLC (Den & Carless, 2012).....	18
Figure 9 Forming limits (Soeiro et al., 2015).....	19
Figure 10 Fracture modes: (a) Mode I; (b) Mode II; (c) Mode III (Richard & Kuna, 1990).....	20
Figure 11 ISF process (Park & Kim, 2003).....	23
Figure 12 Application areas of ISF (Lu et al., 2019).	25
Figure 13 Deformation mechanisms in ISF (Sheng & Long, 2019).	27
Figure 14 Forming Limit Curve (FLC) of ISF (Ai & Long, 2019).....	28
Figure 15 Thinning at transitional zone during ISF (Ai & Long, 2019).....	30
Figure 16 Thinning in response to forming angle (N. Kumar et al., 2019).....	31
Figure 17 Typical geometric errors in ISF (Lu et al., 2019).	32
Figure 18 Fracture face of SPIF parts showing oblate-type voids	33
Figure 19 Deformation in DSIF with schematic displaying dimple direction	34
Figure 20 Micro-cracks seen above crack in ISF	34
Figure 21 Ductile crack growth (Anderson, 2005).....	35

Figure 22 Transition point in CP-Ti ISF part (Hussain & Gao, 2007).....	36
Figure 23 Back-drawing in ISF (G. Ambrogio et al., 2009).	37
Figure 24 Residual stress after ISF and LMD (Tebaay et al., 2020).....	39
Figure 25 Powder feed system.	42
Figure 26 Powder bed system.....	43
Figure 27 Hardness profiles (X. Li et al., 2005).....	45
Figure 28 Epitaxial and columnar grain structure in Ti-64 (Mahamood, 2016).	46
Figure 29 Ti deposit (Meacock & Vilar, 2008): (a) Thin wall; (b) Interface.....	49
Figure 30 Serrated colonies in LMD sample of pure Ti (Barro et al., 2021).	50
Figure 31 LMD fixture: (a) Fully assembled; (b) Back-support assembly.....	55
Figure 32 ISF fixture.	57
Figure 33 LMD and ISF fixture fully assembled.	58
Figure 34 GOM ATOS system: (a) Dual-camera setup; (b) During scanning.....	59
Figure 35 LMD processing cell.....	60
Figure 36 Developing LMD machine parameters.	61
Figure 37 Carbolite furnace.....	64
Figure 38 Tensile test specimen geometry.	64
Figure 39 Nakajima FLD specimen geometry for the development of the mini FLC. 65	
Figure 40 Stochastic (speckle) pattern on tensile specimen for DIC.	66
Figure 41 Zwick/Roell Z150 load cell tensile testing machine.....	67
Figure 42 Zwick BUP 1000 machine.	68
Figure 43 DIC setup during uniaxial tensile test.	69
Figure 44 DMU 125 5-axis CNC: (a) Machine exterior; (b) Machine interior.....	70

Figure 45 Material preparation equipment: (a) Precision saw; (b) Mounting press; (c) Grinder and polisher; (d) Electrolytic polisher.....	71
Figure 46 Quanta FEG SEM 250.	74
Figure 47 Microhardness tester.	74
Figure 48 Alicona Infinite Focus microscope.	75
Figure 49 AR CP-Ti material properties: (a) BC map (b) True stress vs strain curves.	79
Figure 50 CP-Ti powder (Cp-Ti ₂ Advanced Powders, n.d.).....	80
Figure 51 ISF formed titanium part.....	81
Figure 52 PAM-STAMP thickness measurement.	82
Figure 53 LMD material locations and areas proposed for AR specimen extraction ..	83
Figure 54 Tensile specimen size and location within LMD pad.	85
Figure 55 LMD machine setup.....	86
Figure 56 Colour map of known residual stress distribution from XRD results.....	87
Figure 57 Post-processing equipment: (a) XRD machine; (b) Furnace.	88
Figure 58 Stress relief annealing process.	89
Figure 59 Blue oxide surface following heat treatment.	90
Figure 60 Example of fracture face for fractography.....	91
Figure 61 Microhardness testing: (a) Machine; (b) Measuring diagonals.	92
Figure 62 Yield stress and ultimate tensile strength.....	93
Figure 63 Elongation (%) at break.	94
Figure 64 Tensile test results in RD: (a) True stress vs strain; (b) Fractured specimens.	95

Figure 65 Tensile test results in 45°: (a) True stress vs strain; (b) Fractured specimens.	95
Figure 66 Tensile test results in TD: (a) True stress vs strain; (b) Fractured specimens.	95
Figure 67 Effective surface strain at 90% extension for RD: (a) AR; (b) 0.3 mm LMD; (c) 0.6 mm LMD; (d) 0.9 mm LMD.....	97
Figure 68 Effective surface strain at 90% extension for 45° (a) AR; (b) 0.3 mm LMD; (c) 0.6 mm LMD; (d) 0.9 mm LMD.....	97
Figure 69 Effective surface strain at 90% extension for TD: (a) AR; (b) 0.3 mm LMD; (c) 0.6 mm LMD; (d) 0.9 mm LMD.....	98
Figure 70 Effective surface strain at 90% extension on opposing sides (a) RD 0.9mm LMD side; (b) RD 0.9 mm substrate side; (c) TD 0.9 mm LMD side; (d) TD 0.9 mm substrate side.....	99
Figure 71 Fractography sample surfaces: (a) AR material; (b) LMD layer.....	100
Figure 72 Fractography analysis: (a) Zone A AR; (b) Zone B AR; (c) Zone C LMD; (d) Zone D LMD.	101
Figure 73 Vickers hardness results: (a) LMD surface; (b) Along gauge.	102
Figure 74 Geometry simplification and final model geometry (units in SI).....	107
Figure 75 Meshed tensile specimen with refined mesh in necking region.	108
Figure 76 Abaqus pre-processing: (a) Part model with sets; (b) Mesh.	109
Figure 77 Barlat 91 yield function results.	111
Figure 78 Fitting to experiment data to generate material hardening curve.	112
Figure 79 Elongation of gauge (ΔL): (a) node displacement; (b) elongation.	114
Figure 80 Simulation result: (a) tensile specimen; (b) force-elongation curve.....	114
Figure 81 Stress v strain comparison: (a) Engineering curve; (b) True curve.	115

Figure 82 Key material zones in material study.....	119
Figure 83 Alicona Infinite Focus microscope.....	120
Figure 84 AR CP-Ti EBSD maps: (a) IPF; (b) BC map.....	121
Figure 85 Surface morphology of 0.3mm LMD sample: (a) 3d representation; (b) Top surface; (c) Surface profile.....	122
Figure 86 Cross section of 0.6mm thickened LMD material.....	124
Figure 87 Cross section of 0.9mm thickened LMD material.....	125
Figure 88 Thermal cycle of LMD and post-print stress relief on tailored material ...	126
Figure 89 AR CP-Ti EBSD maps: (a) IPF; (b) BC.....	127
Figure 90 LMD microstructures: (a) IPF map 0.6 mm; (b) BC map 0.6 mm; (c) IPF map 0.9 mm; (d) BC map 0.9 mm.....	128
Figure 91 EBSD analysis of 0.9 mm LMD sample: (a) x2000 IPF map; (b) misorientation of enclosed HAGB; (c) misorientation of segmented LAGB.....	129
Figure 92 ISF fixture.....	133
Figure 93 Roller ball tool: (a) Tool assembly; (b) Ball bearing within chamber.....	134
Figure 94 CNC 5-axis machine with tool/sheet location.....	134
Figure 95 Design of LMD added thickness: (a) 3dimensional representation of ISF formed part; (b) Informing thickening area using die projection.....	135
Figure 96 Circle tool path pattern (not drawn to scale).....	139
Figure 97 LMD tailored preform for ISF: (a) Post LMD; (b) 3d representation.....	140
Figure 98 ISF setup: (a) LMD/ISF fixture assembly (closed); (b) Assembly in machine; (c) Fixture and tool holder/controller.....	142
Figure 99 Fixture assembly with sheet installed for ISF.....	143
Figure 100 ISF LMD part scanning procedure.....	148
Figure 101 Fractography sample preparation: (a) Section; (b) Mounted sample.....	149

Figure 102 LMD part scans: (a) LMD tailored preform; (b) LMD/ISF part	151
Figure 103 Thinning rate of the AR and LMD sheets during ISF	152
Figure 104 Surface roughness: (a) 20° section; (b) 40° section; (c) 60° section.	153
Figure 105 Surface roughness (Ra) calculations: (a) Sample orientations; (b) Sample 1; (c) Sample 2; (d) Sample 3; (e) Sample 4.	156
Figure 106 Micro-cracks and propagated cracks on surface of sample 4.	156
Figure 107 Analysis of crack formation and shape.	158
Figure 108 Fractography of fracture face on zig-zag crack.	158
Figure 109 Fractography images: (a) Substrate side of LMD sample; (b) Fracture within LMD layer; (c) Grain cleavage on surface of LMD layer.....	161
Figure 110 Microstructure images of 20° section: (a) IPF map; (b) BC map.....	162
Figure 111 Microstructure images of 60° section: (a) IPF map; (b) BC map.....	163
Figure 112 Nakajima test schematic.....	168
Figure 113 FLC schematic (Paul, 2013).....	169
Figure 114 Strain values for ISF of titanium above the FFLC (Gatea et al., 2018)...	170
Figure 115 Nakajima test piece geometry: (a) Dimensions; (b) Correlation between gauge width (X) and strain state.	171
Figure 116 Adapted miniature FLC specimen.	171
Figure 117 Generating LMD tailored sheet for Nakajima test.....	173
Figure 118 Strain determination (J Adamus et al., 2015).	175
Figure 119 Nakajima test setup: (a) BUP machine; (b) Hemispherical punch.	176
Figure 120 Successful Nakajima test sample: (a) Before; (b) After.	177
Figure 121 Section lines perpendicular to the fracture opening.....	177

Figure 122 Forming limit diagrams (FLD's) containing forming limit curves (FLC's): (a) AR CP-Ti blanks; (b) LMD CP-Ti blanks.	179
Figure 123 Cracks propagating at edge of sample resulting in void result.	180
Figure 124 Multiple peaks: (a) Areas of split high strain readings; (b) The resulting strain curve.	180
Figure 125 Interpolating data to solve for multiple peaks: (a) Maximum curve; (b) Interpolation and mirroring of data.	181
Figure 126 Final fitted curve from treated data.	182
Figure 127 Scheme of time-dependent methodology (M B Silva et al., 2015).	182
Figure 128 Time-dependant strain calculation: (a) Fracture; (b) Strain points.	183
Figure 129 FLC curve for the AR CP-Ti material.	186
Figure 130 FLC for the LMD thickened CP-Ti material.	188
Figure 131 Change in angle of roller ball tool during back supported ISF.	190
Figure 132 Pole figures: (a) AR CP-Ti; (b) 0.3 mm LMD; (c) 0.9 mm LMD.	191

Table of Tables

Table 1 Metallic crystal structures (Clemens et al., 2017).....	6
Table 2 Minimum yield stress for each CP-Ti grade (Lutjering & Williams, 2007)...	11
Table 3 LMD parameter development cycle.....	61
Table 4 Material specimen grinding and polishing process for CP-Ti.....	71
Table 5 Chemical composition of CP-Ti50A (TIMET, n.d.).....	79
Table 6 Thickness measurements.....	82
Table 7 Pad location, orientation, and LMD deposit thickness.....	83
Table 8 Deposit layer patterns and directions	84
Table 9 XRD residual stress measurements.....	86
Table 10 Plastic anisotropy coefficient.....	110
Table 11 Uniaxial and biaxial yield stress factor.....	110
Table 12 Material properties extracted from the engineering stress vs strain curves.	116
Table 13 Groove depths of LMD material samples.....	123
Table 14 Final thickness predictions using sine law (in mm).....	136
Table 15 GOM thickness measurements of ISF CP-Ti sheet (in mm).....	136
Table 16 Required LMD thickening calculations.....	137
Table 17 ISF progress documentation.....	144
Table 18 Surface grinding depth to flatten LMD builds.....	164
Table 19 New specimen gauge width and testing strain state.....	172
Table 20 Design of Experiments for Nakajima test.....	172
Table 21 Strain approximation results comparison for sample ID#2.....	183
Table 22 Results of Nakajima test for AR CP-Ti test specimens.....	184

Table 23 Results of Nakajima test for LMD thickened CP-Ti test specimens. 187

Chapter 1

1 Introduction

Titanium is the ninth most abundant element found in the earth's crust and is produced using the Kroll process (Bedinger, 2013). Titanium is largely used in the automotive, energy, chemical and food industries, with approximately 40% of its use in the aerospace and aviation industries thanks to excellent strength to weight properties (Boyer & Briggs, 2005; Stjohn & Nie, 2017). Titanium is typically divided into two groups, commercially pure and titanium-based alloys. Commercially pure titanium (CP-Ti) is near to pure titanium ($\geq 99\%$). CP-Ti is classified into four grades depending on the residual oxygen content. The hexagonal close-packed (HCP) crystal structure of CP-Ti means it exhibits low ductility at room temperature (F. K. Chen & Chiu, 2005). Often thermal activation is required to improve the ductility and formability of CP-Ti resulting in high processing costs associated with tooling and heating. As such, improving low temperature forming of CP-Ti is industrially relevant. CP-Ti was selected as the material of choice for this study due to industrial interest in improving its formability. It was selected over Ti-6Al-4V, the work-horse of titanium alloys, because it has higher ductility at low temperature making it a more realistic choice to form by incremental sheet forming (ISF) at low temperatures. ISF is a process which forms sheet metal by performing localised incremental deformation with a single hemispherical tool controlled by a computer numerical controlled (CNC) machine. The tool follows a pre-programmed toolpath to achieve the desired part geometry. The flexibility of ISF reduces development time for small batch productions which can provide industrial manufacturers a competitive advantage (Kim & Yang, 2000). ISF has been shown to increase a materials formability compared to conventional stamping and pressing processes (Allwood et al., 2007). Therefore, investigating room temperature ISF of CP-Ti will be advantageous for industry as the results may lead to cost reductions and quality improvements for small batch sheet part production using CP-Ti and other

difficult to form sheet materials at low temperatures. However, a major drawback of room temperature ISF is localised sheet thinning and springback which limit the use of ISF in industry (Jagtap & Kumar, 2019). Additive manufacturing (AM) is a popular process currently being adopted across industry due to its ability to fabricate components previously not attainable by traditional manufacturing processes. Laser metal deposition (LMD) is a variant of AM which has been highlighted as a potential route to improve the geometrical accuracy of parts made by ISF at ambient room temperature, specifically by reinforcing the preform sheet with thickened areas in predicted thinning zones. This thesis investigates the above identified novel hybrid LMD/ISF process with the aim of successfully forming a CP-Ti sheet part at room temperature to extend achievable formability and improve final part thickness homogeneity.

1.1 Problem statement

1.1.1 Research aim

This EngD project aimed to determine the effectiveness of tailoring CP-Ti sheet preforms with localised areas of increased thickness using LMD to improve sheet thickness homogeneity following room temperature ISF, and report on the findings.

1.1.2 Research objectives

- Assess the impact of a pre-ISF additive thickening step on the room temperature formability of a CP-Ti sheet. In addition, investigate the effectiveness of pre-ISF LMD to improve part quality and geometric accuracy.
- Determine if thickening CP-Ti sheet with LMD impacts its room temperature mechanical properties.
- Examine and compare the microstructures of as received (AR) and LMD thickened CP-Ti material.
- Investigate the failure behaviour of both AR and LMD thickened CP-Ti sheet following mechanical testing and room temperature ISF.

- Perform finite element analysis (FEA) to generate a material model of the anisotropic CP-Ti sheet, with the greater objective of supporting a FEA simulation of ISF to further investigate the impact of key process parameters on the performance of hybrid ISF.

1.2 Thesis structure

The EngD thesis has been structured as follows:

- An opening abstract which provides a general overview of the research project including a literature study and a brief overview of the experimental techniques.
- Chapter 1: Contains an introductory chapter which provides a general rationale behind the research, aims and objectives.
- Chapter 2: A review of recent and current literature in the areas of ISF, hybrid manufacturing and AM. The literature review helped to define the knowledge gap which informed this research investigation.
- Chapter 3: Contains the experimental method and techniques followed to perform this research. This chapter was written with the aim of providing a guide for future researchers to accurately reproduce this experimental work.
- Chapter 4: Describes the process of developing and realising the AM pre-ISF step on the CP-Ti sheet, followed by an investigation into the room temperature uniaxial tensile properties and surface strain behaviour of both the LMD thickened and AR CP-Ti material.
- Chapter 5: Contains a summary of the FEA simulation used to model the AR material and validate it against the stress vs strain curves generated by room temperature uniaxial tensile testing.
- Chapter 6: Contains an investigation into the microstructural change undergone by the CP-Ti material in response to LMD thickening. The results were compared to those of the AR CP-Ti material.
- Chapter 7: Details the ISF experiment trial to examine the impact of the pre-ISF LMD step on the geometric accuracy of the ISF part. The part produced by the

room temperature hybrid LMD/ISF process was compared to the AR CP-Ti sheet part of comparable geometry formed by ISF.

- Chapter 8: Details an experimental Nakajima BUP test used to examine localised strain evolution on the surface of both the AR and LMD thickened CP-Ti material when formed under strain conditions present in ISF, and the creation of forming limit curves to compare the results.
- Chapter 9: Contains concluding remarks on the major findings of the EngD research, and recommendations for future research in the area.
- Appendices: Details experimental equipment and processes used as well as MATLAB scripts for data analysis and engineering drawings.

1.3 Programme of work flowchart

The main route followed to complete the aim and objectives of this research investigation are outlined in the following programme of work flowchart, Figure 1. Overall, experimental trials and simulations were used to address the knowledge gap identified in the literature review.

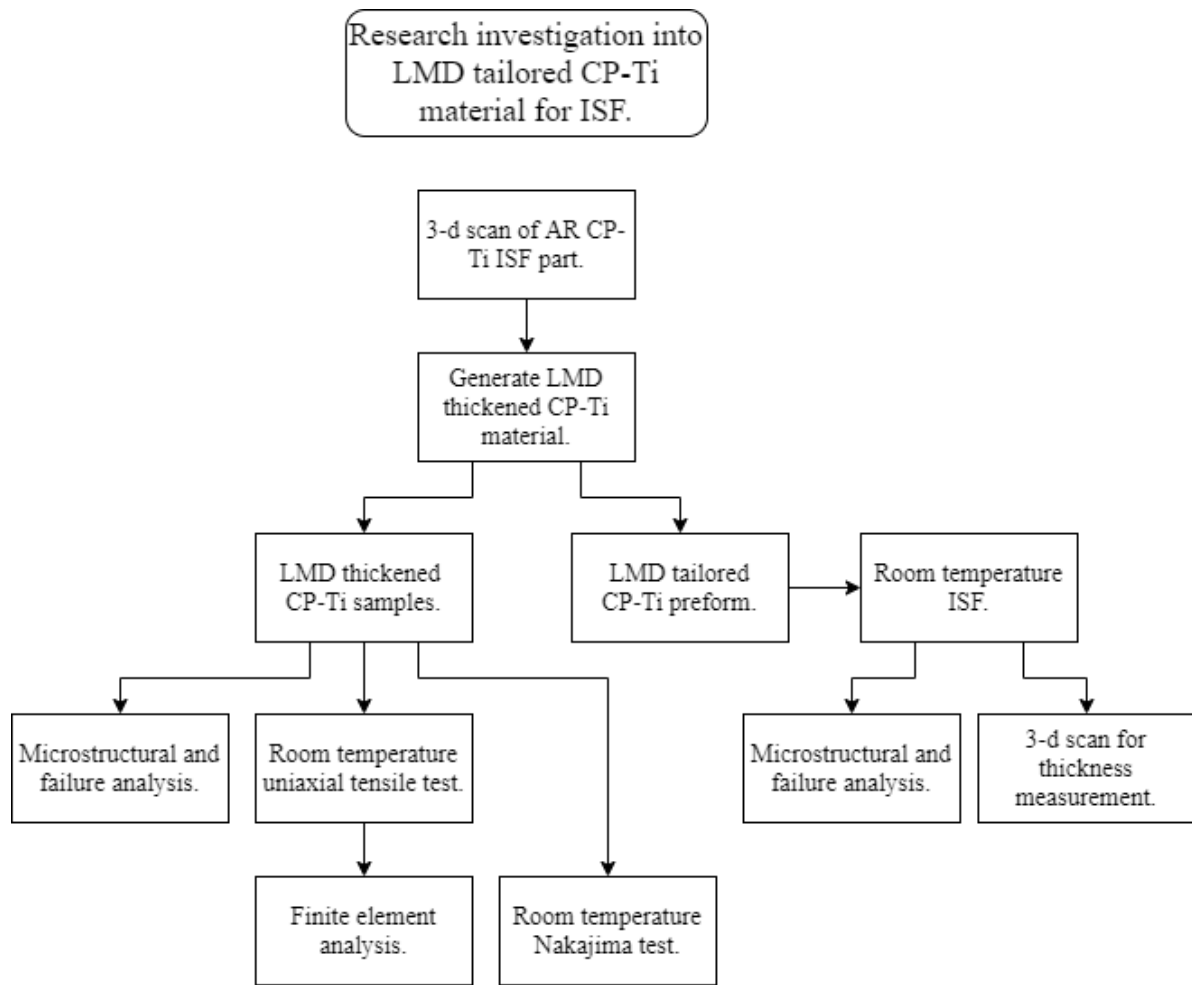


Figure 1 Programme of work flowchart.

Chapter 2

2 Literature Review

2.1 Engineering metals

2.1.1 Metal properties

Engineering metals serve an important purpose in industry, which is to form lightweight structures and withstand loading without breaking or exhibiting excessive deflection. The ability of an engineering metal to achieve this is dependent on its material properties. The material properties of engineering metals are largely dependent on two factors, the geometrical atomic arrangements and the atomic bonding. The structure of engineering metals at the smallest level is defined by the arrangement of atoms relative to each other. This geometric atomic arrangement is the three-dimensional structure known as the crystal structure. The atomic bonding present in engineering metals is primarily metallic bonding (Clemens et al., 2017). There are three common crystal structure, face-centered cubic (FCC), body-centered cubic (BCC) and hexagonal closed-packed (HCP), Table 1.

Table 1 Metallic crystal structures (Clemens et al., 2017).

Crystal structure	Atoms per cell	Slip systems	Coordination no.
FCC	4	12	12
BCC	2	48	12
HCP	6	3	12

At a higher structural level, the atomic arrangements are grouped together to form the microstructure. The microstructure is described by the grains and present phases, with their structure, shape, and size impacting material properties (Clemens et al., 2017).

2.1.2 Titanium

Titanium is an engineering metal with exceptional material properties. The specific material properties key to its success are its high strength to weight ratio and resistance to corrosion. Despite these advantageous properties it is also highly reactive to oxygen and hydrogen which limits its industrial application. However, its high strength and low density make titanium useful for aerospace applications which demand lightweight parts without compromising strength (Adamus, 2006). Despite this, titanium has limited deformation capabilities and high work hardening which makes it difficult to form at low temperatures. The oxide layer of titanium protects its surface from corrosion which makes it popular for use in corrosive environments, such as for medical devices. However, the high reactivity of titanium in oxygen rich environments can cause embrittlement which necessitates the use of inert gas during any elevated actions (forming, additive manufacturing, or a heat treatment by itself) to maintain desirable material properties (Leyens & Peters, 2003). There two main types of crystal structures present in titanium are HCP and BCC, Figure 2. HCP which is also known as the alpha (α) phase. The HCP unit cell consists of the basal plane (0002), one of the three prismatic planes $\{1010\}$, and one of the six pyramidal planes $\{1011\}$ (Leyens & Peters, 2003). The HCP crystal structure has two close-packed atomic planes separated by three atoms in the centre. One atom is centered within the unit cell and various fractional atoms are at the unit cell corners (four one-sixth atoms and four one-twelfth atoms), making up two atoms in total per unit cell. Close-packed refers to the HCP's efficiency in packing spheres and is formed by stacking the (0002) basal planes on one another in an AB AB AB sequence. BCC is also known as the beta (β) phase (Lutjering & Williams, 2007). The BCC unit cell has atoms at each corner of the cube and one at the centre. There are no close-packed planes meaning BCC has no stacking sequence. Pure titanium undergoes an allotropic phase transformation at 883°C. This is the β transus (β_T) temperature. Above β_T the BCC crystal structure exists and below β_T the microstructure will be fully HCP or a mixture of HCP + BCC. The formability of titanium is determined by the crystal structure. HCP is the most difficult to form thanks to its limited slip planes (Leyens & Peters, 2003). Slip planes are typically the planes

with the highest density of atoms and the direction that slip planes correspond to are the smallest lattice translation vectors in the system. A slip system is the product of the number of slip planes and slip directions present in a crystal atomic structure. The number of slip systems determines the number of dislocations which can glide, with more slip planes resulting in greater formability. The HCP phase of titanium has three slip systems, whereas FCC and BCC have a maximum of twelve and forty-eight respectively.

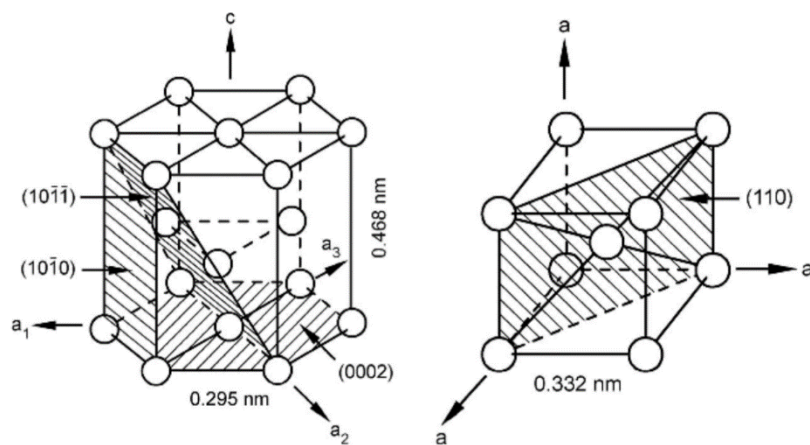


Figure 2 Unit cells of α and β phases (Lutjering & Williams, 2007).

The properties of a material are largely determined by its microstructure. Thermal and mechanical processing lead to changes in a materials microstructure. Cooling from the β phase field results in a lamellar microstructure in titanium, while recrystallisation results in an equiaxed microstructure (Leyens & Peters, 2003). Both the lamellar and equiaxed microstructures can exhibit fine and coarse phase arrangements depending on processing conditions. Microstructure type and phase size further influence the materials mechanical properties. An equiaxed microstructure offers relatively good ductility and strength properties. To exhibit an equiaxed microstructure the material must undergo high levels of mechanical work at ambient temperatures to achieve recrystallization (Leyens & Peters, 2003). Unlike equiaxed microstructures, the lamellar microstructure consists of coarse lamellar plates of α and exhibits moderate strength, fatigue crack growth resistance, and low ductility compared to the equiaxed

microstructure. This is created by cooling past β_T until α nucleates at grain boundaries and grows as lamellae into the prior- β grains. These lamellae are fine or coarse depending on cooling rates, with faster cooling rates creating fine lamellae and slow cooling rates creating coarser lamellae. Titanium is recognised as having poor formability due to its high yield stress and yield stress to ultimate tensile stress (UTS) ratio (J Adamus, 2006). Increased formability is achievable at high forming temperatures however this necessitates specialised tooling and additional set up costs. Springback is a significant drawback when forming sheet titanium as titanium alloys are characterised by large elastic deformation due to low Young's Modulus (YM) meaning sheet titanium can exhibit springback at bending angles up to 30° to the sheet plane reducing geometric accuracy (Adamus, 2016). Gas diffusion is a potential limitation in high temperature environments due to the reactive nature of titanium and can lead to its embrittlement (J Adamus, 2006). Likewise, hot forming titanium creates alpha phase which depends on post-processing for removal (Weiss & Semiatin, 1998).

2.1.3 Commercially pure titanium

Commercially pure titanium (CP-Ti) is a popular titanium alloy for industry applications which require excellent corrosion resistance properties, such as in the production of medical devices or the construction of petrochemical processing equipment (Lutjering & Williams, 2007). Chemical and marine industries also utilise CP-Ti for its useful material properties (Yamanaka et al., 2019b). CP-Ti has good durability and often low life costs as compared to cheaper alloys such as stainless steel. The Erichson cupping test has shown CP-Ti grade 2 to have good drawability compared to other titanium alloys with properties similar to that of deep drawn steel, as well as the lowest value of springback for the titanium alloys (Adamus, 2016). CP-Ti is an alpha (α) titanium alloy and exhibits anisotropic mechanical properties (Leyens & Peters, 2003). Rolled sheet CP-Ti is highly anisotropic (Wang & Huang, 2003). This means for CP-Ti both the yield stress (YS) and YM vary in the longitudinal and transverse directions (Lutjering & Williams, 2007). Fewer easy glide systems at room temperature also result in greater crystal anisotropy with potential for texture strengthening (Wang

& Huang, 2003). CP-Ti also exhibits excellent creep behaviour due to the limited ability for atoms to diffuse and crystals to deform in hexagonal lattices. It also has a lower density than beta (β) alloys making its strength to weight ratio a great advantage for high performance applications. The high density of β alloys is a result of alloying with heavier elements such as Mo or V (Leyens & Peters, 2003). CP-Ti also exhibits excellent weldability making it particularly suitable for AM. CP-Ti is an α titanium alloy and exhibits a hexagonal allotropic form at low temperatures. The typical microstructures of CP-Ti are equiaxed and lamellar, Figure 3. The microstructure is typically determined by processing conditions, compositional difference and cooling rates (Yadav & Saxena, 2019). A fully lamellar structure has higher fracture toughness and high crack resistance while the fully equiaxed structure has high cycle fatigue resistance (Yadav & Saxena, 2019).

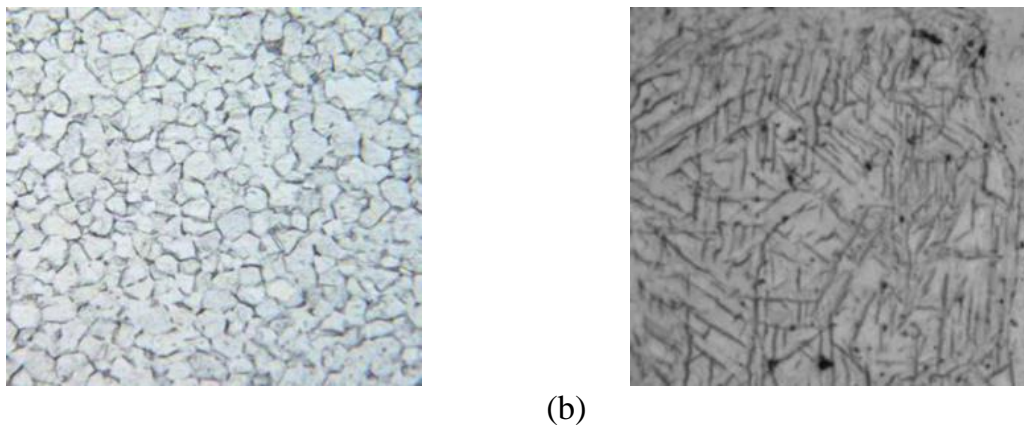


Figure 3 Typical CP-Ti microstructures: (a) Equiaxed; (b) Lamellar.

Alloying titanium changes the transformation temperature (Stjohn & Nie, 2017). There are four grades of CP-Ti which are differentiated by the percentage volume of substitutional alloying elements (e.g. Al or Sn) or interstitial elements (e.g. O, C or N) (Lutjering & Williams, 2007), Table 2. CP-Ti grade 1 offers relatively high room temperature formability and is often used for deep drawing applications but has the lowest strength level of all the grades, often being used for applications which require excellent resistance to corrosion. CP-Ti grade 2 has tensile strength levels between 390 and 540 MPa and is the most used grade of all CP-Ti grades in industry. CP-Ti grade 3

has higher strength compared to grade 1 and good formability so can be used for components with reduced wall thicknesses. CP-Ti grade 4 has the highest of all commercially pure grades with a strength of 740 MPa, however forming complex parts with this grade requires temperatures up to 300°C.

Table 2 Minimum yield stress for each CP-Ti grade (Lutjering & Williams, 2007).

CP-Ti grade	O (max. %)	Fe (max. %)	$\sigma_{0.2}$ (MPa)
1	0.18	0.20	170
2	0.25	0.30	275
3	0.35	0.30	380
4	0.40	0.50	480

The HCP crystal structure of CP-Ti can result in significant anisotropic behaviour in response to deformation. The YM of CP-Ti varies, from 145 GPa in response to loads acting vertically to the basal plane compared to 100 GPa to loads acting parallel to the basal plane (F. K. Chen & Chiu, 2005). Typically, cold rolling results in a split basal texture for CP-Ti which contributes to its anisotropy (Chun et al., 2005). Anisotropy is generally a limitation for sheet material however it can allow for stiffness variations to be designed into a sheet part. The limited ductility of CP-Ti is the result of additional deformation on secondary slip systems and mechanical twinning (Leyens & Peters, 2003). HCP metals such as CP-Ti also differ from cubic metals in that limited slip systems result in twinning being the dominant deformation mode (Wang & Huang, 2003). However, heat activation can improve the ductility and formability of CP-Ti with a proportionate decrease in YS and increase in elongation when CP-Ti sheet is heated to 100°C and even further at 200°C during deep drawing (F. K. Chen & Chiu, 2005), Figure 4.

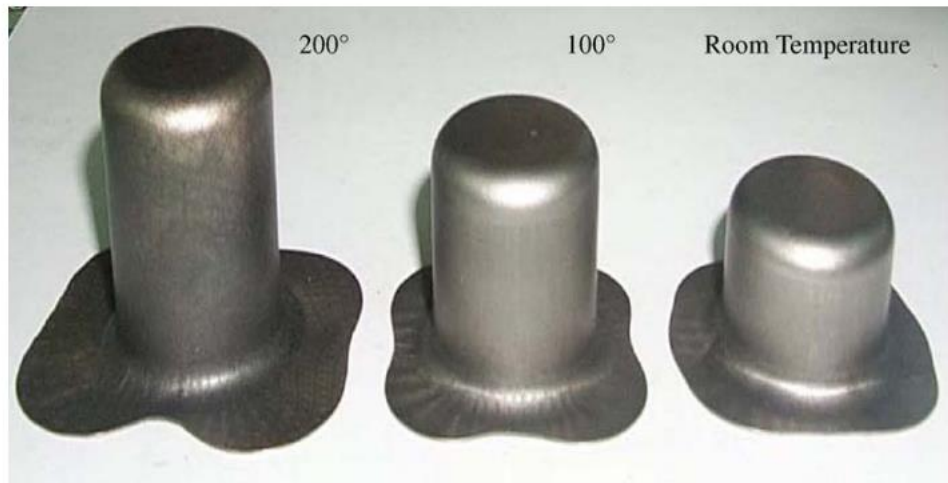


Figure 4 Drawn CP-Ti cups at various temperatures (F. K. Chen & Chiu, 2005).

CP-Ti consists of equiaxed α grains, developed when annealing cold-worked alloys above the recrystallization temperature. The recrystallisation temperature of CP-Ti is between 646°C and 669°C (Gammon et al., 2004). Equiaxed α grains have small grain sizes when worked and annealed in the α phase field as grain growth is inhibited due to low temperatures and the presence of impurities which pin grain boundaries (Stjohn & Nie, 2017). Elongated α grains exhibit in longitudinal sections of alloys which have undergone unidirectional cold working and have a preferred orientation in the direction of the cold work. YS and flow stress can also vary depending on directionality, with lower values in the RD and higher values in the TD. This increases almost linearly with increasing angle away from the RD.

2.1.4 Material characterisation

To build a clear picture of an engineering metals mechanical performance capability it must be characterised. There are a variety of material characterisation methods available to investigate a materials mechanical and microstructural properties.

- The tensile test is used to describe the mechanical properties of a material when it is subjected to uniaxial tension. This is performed by pulling a tensile specimen at a constant rate until yield stress and measuring the level of deformation, typically with an extensometer. The immediate result of this test is a load-

elongation curve which is used to generate a stress vs strain curve. The engineering stress, σ , is described by:

$$\sigma = \frac{F}{A_o}, \quad \text{Equation 1}$$

where F is the force and A_o is the original (zero stress) cross-sectional area. The engineering strain, ε , is defined as

$$\varepsilon = \frac{l - l_o}{l_o} = \frac{\Delta l}{l_o}, \quad \text{Equation 2}$$

where l is the specimen gauge length at a given load and l_o is the original (zero-stress) gauge length.

- The hardness test is a test method used to measure both the macro and microhardness of a material (Struers, n.d.). It is performed using a microhardness tester. The Vickers method is a type of hardness test used for small and/or thin parts. Vickers hardness is calculated by optically measuring the diagonals of the impression left by a diamond indenter. These measurements are then converted to the HV value mathematically. For performing microhardness testing the material surface needs to be polished to ensure the diamond indentation is measurable by the software. The indentation time is typically 10-15 s and the sample thickness should be a minimum of 10 times thicker than the indentation depth. To avoid measurement inaccuracies, it is suggested to ensure a minimum of three diagonal widths between each indentation and a minimum diagonal width of 20 μm . These test requirements are explained further in ISO 6507 “Metallic Materials – Vickers Hardness Test” which ensures repeatable and accurate results.
- Optical microscopy is used to generate magnified images of material surfaces which gather a significant amount of information and can be used to tell a story about the materials processing history. With optical microscopy the morphology of a surface is examined using an eyepiece fitted with a camera for imaging

(Ortiz Ortega et al., 2022). This can take images with a resolution limited to a submicron scale using wavelength of 400-700 nm. Optical microscopy is fast and relatively simple to perform. It is low costing and highly functional. Characteristics such as shape and size of grains can be examined at magnifications near to 1000x (Ortiz Ortega et al., 2022).

- Another form of microscopy is electron microscopy. Greater magnifications are achievable by electron microscopy which is performed using a scanning electron microscope (SEM) (Ortiz Ortega et al., 2022), Figure 5. An SEM contains an electron column, specimen chamber, and computer control system (Ortiz Ortega et al., 2022). The electron column is maintained under vacuum conditions during operation and an image is produced by colliding a beam of electrons with a material sample. The electron beam is generated by an electron gun inside the column. The electron beam impacts the sample at a force subject to the accelerating voltage which typically varies between 2 and 30 kV. Secondary electrons are released from the surface in response to the electron beam impact which are collected by a secondary detector and an image is produced.

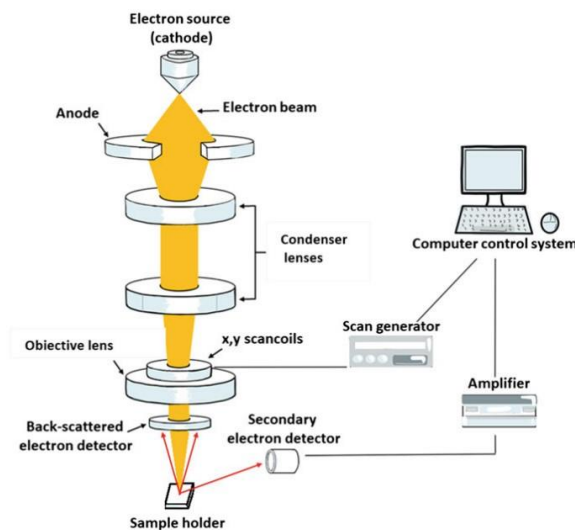


Figure 5 Principle of operation of the SEM (Ortiz Ortega et al., 2022).

2.2 Conventional Sheet Forming

2.2.1 Sheet Forming Methods

There are various techniques used to form sheet metal parts, each with unique properties which offer distinct advantages. Sheet metal parts typically exhibit with relatively high stiffness and strength with respect to their geometry. Provided are some of the key forming mechanisms.

- Bending is the simplest forming mechanism as plastic deformation only appears in the bend region.
- Stretching is the lengthening of a sheet by applied pressure, tensile stress, and material locking.
- Stamping or draw die forming are metal forming operations which use stretching to manufacture sheet parts. A typical stamping assembly includes a punch, draw ring and blank holder, and is often used to manufacture car body panels.
- Deep drawing is like stamping, however deeper parts are formed by allowing more material to be drawn inward to form high angle sides. Most of the deformation in deep drawing is in the flange, which is subject to compressive stresses. However, small stretching can also occur when the sheet is in contact with the draw punch.
- Coining and ironing are when through thickness compression is the principal deformation force which result in a reduced wall thickness in sheet metal parts.

Forming can be performed at cold or hot temperatures depending on material or part complexity. Hot forming involves the bending, stretching, and flattening of metal at high temperatures (typically above 600°C), and can result in better strength and corrosion resistance in parts. However, production cost is approximately 20-40% higher than cold forming. As such, there is a cost incentive to improve the capabilities of cold forming.

2.2.2 Sheet Forming Deformation

Elasticity and plasticity describe the change in shape of a material in response to an applied stress. Elastic deformation is when a material deforms under a load and returns to its original shape when the load is removed. Plastic deformation is when the material does not return to its original shape after the load is removed. A load versus extension diagram graphically displays the relationship between the load applied to a test piece, and the elastic and plastic properties of a material, Figure 6. This diagram is the typical output of the tensile test. There are several key values given by this diagram which describe a materials response to an applied stress. P_y is the moment a material stops forming elastically and begins to plastically deform in response to the applied stress. This is followed by uniform deformation when the cross-sectional area of the test piece decreases, and the length increases during uniform deformation. Strain-hardening occurs during the uniform deformation stage which is when the strength of a material increases in response to plastic deformation. Strain hardening is determined by the materials UTS which defines the moment a material can no longer uniformly deform in response to the stress. Beyond the UTS the deformation becomes non-uniform, and a diffuse neck appears followed by material failure. This is the typical elastic-plastic response of sheet metal to an applied load. A load vs extension diagram is useful for visualizing the elastic/plastic behaviour of a material.

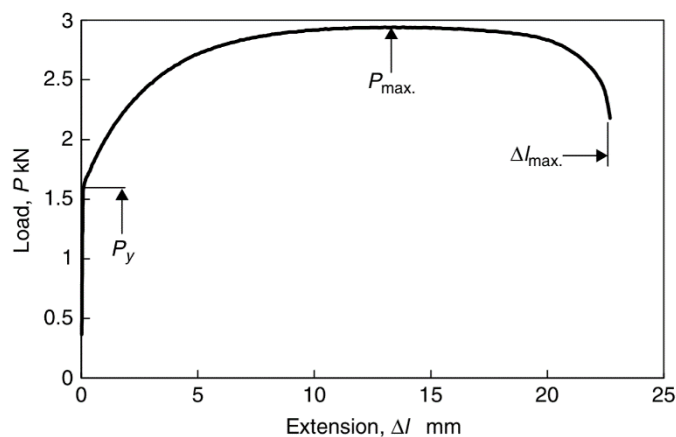


Figure 6 Load extension diagram (Marciniak et al., 2002).

The principal modes of deformation in uniform sheet forming can be defined by shape changes in circles which have been etched on the surface of a sheet metal sample (Marciniak et al., 2002). This is a useful method used to analyse the forming capability of a sheet metal and is typically associated with the Nakajima test. The Nakajima test is a stretch-forming based test used to analyse the stretching of a material at different stress conditions. From the Nakajima test a forming limit curve (FLC) is made which determines the limits to which a material can be stretched. Depending on the geometry of the material specimen for testing, the material can be stretched under various strain paths which mimic real-world stretching conditions for many sheet applications. All possible strain paths exist between OA and OE in the following schematic, Figure 7. The most common deformation modes present during sheet metal forming are equal biaxial tension, plain strain, uniaxial tension, pure shear and uniaxial compression (Marciniak et al., 2002). Equal biaxial tension can result in rapid thickness reduction and work hardening. Plain strain is when a sheet only extends in one direction which can see splitting occur. Uniaxial tension is when a sheet is deformed when a free edge is stretched, meaning stretching and contraction occur in opposite directions. Pure shear sees membrane stresses and strains as equal and opposite, so the sheet deforms with no thickness change and work hardening occurs. Finally, uniaxial compression is commonly seen at the sheet edge during drawing and results in sheet thickening which corresponds to strain path OE.

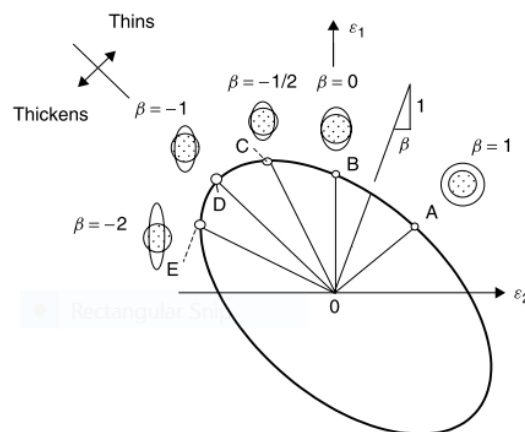


Figure 7 Main deformation modes (Marciniak et al., 2002).

The amount of deformation which a sheet metal part can undergo is limited by its eventual failure. The moment of failure depends on the deformation mode present and the sheet materials properties. It is a forming limit diagram (FLD) which contains the FLC (Den & Carless, 2012), Figure 8.

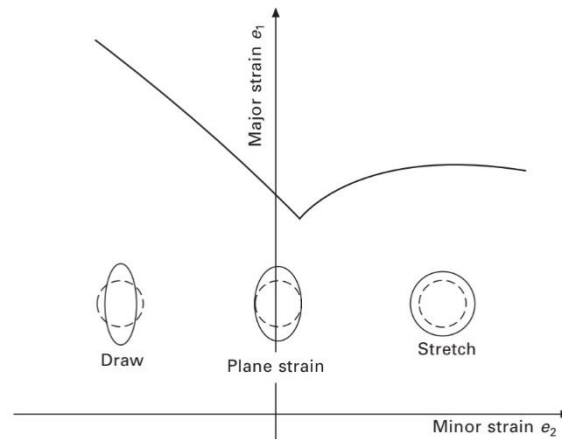


Figure 8 The FLC (Den & Carless, 2012).

The FLC describes a materials formability which is useful in determining the extent a material is capable of being transformed before failing. The FLC is only valid when the forming mechanism(s) satisfy the following restrictions:

1. A straight strain path.
2. Absense of bending.
3. Absense of through-thickness shear.
4. A condition of plane stress.

In the FLC, the major strain is always positive unlike the minor strain which can be both positive and negative (Den & Carless, 2012). The FLC can determine strain paths of different deformation modes including biaxial tension, equal tension, and compression. It is an essential tool for understanding material failure limits and deformation modes. Material formability can be increased significantly if any of the restrictions which validate the FLC are violated (Emmens & van den Boogaard, 2009). This will include when a complex strain path is used, bending is incorporated, through-thickness shear occurs, or a contact stress is applied. The most common failures which occur during the

forming of sheet metal are necking, wrinkling and fracture. Failure occurs when the maximum and minimum strain values exceed the fracture forming limits. There are three different types of failure in the principal strain space (Soeiro et al., 2015), see Figure 9. The first is wrinkling which occurs when the in-plane stresses are compressive. The second is necking which is a result of localised thinning. Finally, strain loading conditions can result in cracks which grow until catastrophic failure of the sheet which is known as fracture.

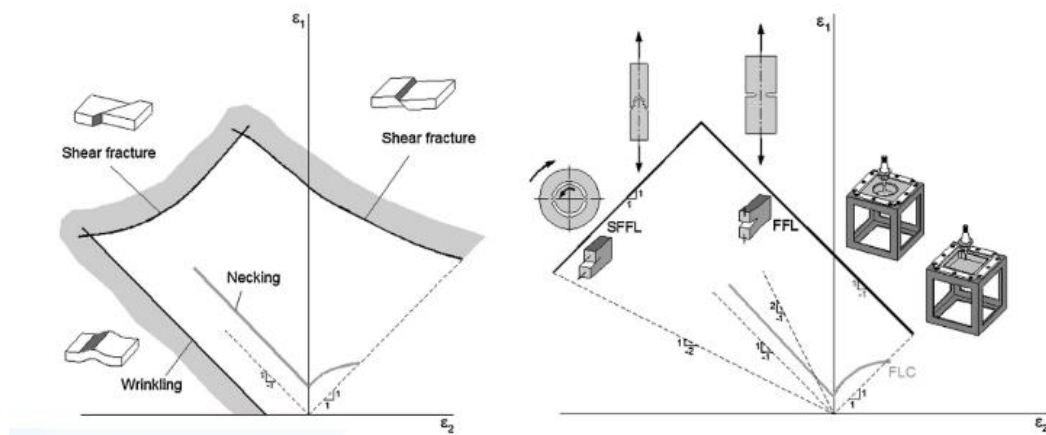


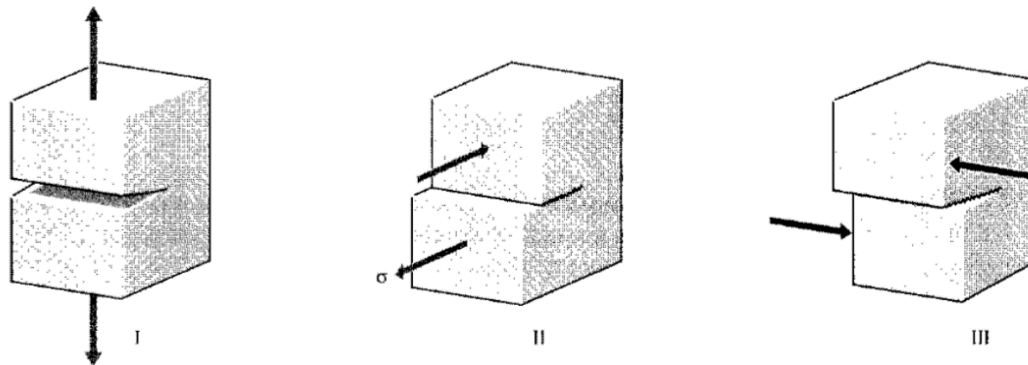
Figure 9 Forming limits (Soeiro et al., 2015).

There are three fracture modes which result from imposed stresses from the following loading conditions (Richard & Kuna, 1990), Figure 10:

- Mode I (tensile stress)
- Mode II (in-plane shear vertical to the crack front)
- Mode III (anti-plane shear parallel to the crack front).

Mode I is a normal-opening mode and modes II and III are shear sliding modes (Roylance, 2001b). Fracture mechanics can be used to determine load direction and the resulting crack propagation. When an existing crack in the material exists prior to forming, despite stresses acting on the material being lower than would normally cause yield or failure, it is possible for cracks to propagate (Roylance, 2001a). Early onset failure is often a result of pre-existing cracks in the material. Plastic flow and failure in

sheet metal forming is a result of the competition between fracture modes II and III (Isik et al., 2014).



(a)

(b)

(c)

Figure 10 Fracture modes: (a) Mode I; (b) Mode II; (c) Mode III (Richard & Kuna, 1990).

Two major deformation mechanisms in sheet metal forming are slip and twinning. Slip is the dominant mode of deformation and is responsible for the rotation of crystals. Slip results in a translation of a crystal parallel to a crystallographic plane. The slip direction can sometimes align with the direction of the applied stress causing the orientation of the crystal to change in response to the deformation direction. However, it is generally shear stresses that generate slip at 45° to the primary stress axis. In slip, the sheared lattice is identical to the original lattice as each atom makes the exact same movement taking the overall lattice forward by integral number of lattice vectors (Cottrell, 1967). A slip band is made up by the steps produced during slip on the crystal surface. Unlike slip, deformation twinning is when a crystallographic volume transforms into an orientation with a mirror symmetry relative to the original crystal. Or in other words, oriented in a twin relationship to it. This results in a discrete orientation change compared to the gradual orientation change during slip. The vectors describing a twinning displacement are not basic lattice vectors due to the mirror image (Cottrell, 1967). The twinning region is relatively thick at $10^3 - 10^5$ atomic layers, unlike during shear which is only a few crystal layers thick. Abrupt changes in crystal orientation are possible in deformation twinning (Suwas & Ray, 2014). During slip not all the material

will make the transition simultaneously from the un-slipped state to minimise the amount of material in a high energy configuration. So, the slipped region of a material grows at the expense of an interstitial region with a narrow interface to minimize the amount of material in the high-energy transitional state. The interstitial region is referred to as a dislocation. Slip, twinning, and transformation dislocations exist depending on how the new crystal structure is being formed (Cottrell, 1967). A material consists of many grains. When a material is subjected to load a grain deforms in a unique way as it is constrained by neighbouring grains. This effect can make a material microstructure very complex. The grains can also undergo changes in orientation in response to deformation which can add complexity to the microstructure. Microstructure is important as it can be used as a basis to understand the processing history of a material. Room temperature deformation is the processing of material at ambient temperature (typically between 15-24°C). The percentage of cold work, CW , is given by

$$\% CW = \frac{A_O - A_F}{A_O} \times 100 \quad \text{Equation 3}$$

where A_O is the original cross-sectional area and A_F is the final cross-sectional area after cold work. An increase in cold work increases the hardness and strength of a metal alloy. This is recognised as strain hardening.

2.2.3 Sheet Forming Limitations

There are several key limitations to sheet metal forming which can reduce final part quality. These limitations are exaggerated when forming a material with low ductility. These are as follows:

- Springback is the elastic recovery of sheet metal following the release of forming loads after the sheet forming operation is complete. During springback a sheet metal part partially returns to its original geometry. Springback reduces geometric accuracy and can introduce part variability which may disrupt subsequent forming operations and assembly. The severity of springback is

largely dependent on the magnitude of the bending moment distribution which is a function of the internal stress distribution in the sheet metal part (Firat et al., 2008). Other contributing factors are the YM and YS of the material, material thickness, and bend angle (Den & Carless, 2012). Springback deformation is considered unavoidable during sheet metal forming as it is a result of unbalanced stress developed across the surface and through the thickness of a sheet when the stamping die is removed (Firat et al., 2008). This is especially true when forming parts from lightweight materials such as high-strength steel, aluminium, and titanium. Additional clamping and heat treatments can reduce springback.

- Anisotropy is the change in a sheet's mechanical properties with respect to direction. Anisotropy is primarily a result of the rolling operations used during the production process (Den & Carless, 2012). Crystallographic structure can cause anisotropic properties resulting in orientation dependent mechanical characteristics as shown by Rauch (1998) and First et al. (2008).
- Wrinkling is a form of buckling which occurs when a sheet experiences compressive stress during forming. Wrinkling can be controlled by increasing blank holder force, however this may result in reduced material flow and potential part failure (Den & Carless, 2012). Blank design is another method of reducing wrinkling.
- Earing, like wrinkling, is the result of non-uniform deformation caused by sheet anisotropy. It results in wavy edges of the sheet largely thanks to the anisotropic properties of the metal. Earing is costly as it necessitates post-processing to remove excess material.
- Sheet thinning occurs when an external load causes a decrease in the cross-sectional area of a sheet in response to an increase in length. Thinning continues until the point when the strain-hardening effect is balanced by the rate of decrease in the cross-sectional area and the load reaches a maximum value. This typically occurs at a materials UTS. Beyond the UTS is when necking begins.
- Necking is when strain is localised to a small region in the sheet and is the result of non-uniform deformation across the cross section and leads to a diffuse neck

(Marciniak et al., 2002). Necking is typically the first step before eventual fracture as the non-uniform extension will continue within the neck until the sheet metal fails (Den & Carless, 2012).

- Work hardening is the strengthening of a material in response to plastic deformation and can inhibit further sheet deformation. Work hardening is created by dislocation to dislocation strain field interactions, which means dislocation motion is hindered by the presence of other dislocations. More plastic deformation, a high density of dislocations, and more pronounced resistance to dislocation motion occur as a result (Clemens et al., 2017).

2.3 Incremental Sheet Forming

2.3.1 ISF Process Description

Incremental Sheet Forming (ISF) is a flexible sheet forming process in which sheet metal is clamped along its edge and deformed by localised strain from a specially designed tool (Park & Kim, 2003), Figure 11.

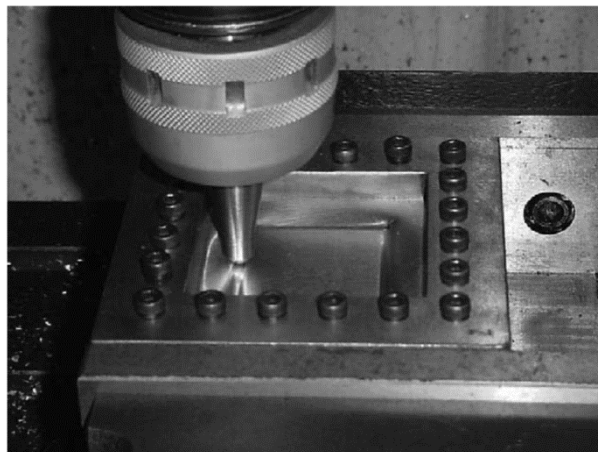


Figure 11 ISF process (Park & Kim, 2003).

The most common technique of incrementally forming sheet metal is with a solid hemispherical indenter (Jackson & Allwood, 2008). The indenter is typically held within a tool which follows a pre-programmed path and is controlled by a computer numerical controlled (CNC) machine. The tool is moved in a series of passes across the

sheet surface until the desired shape is formed of the sheet blank material. ISF can be performed die-less, with a partial die, or with an opposing tool. The partial die and tool are used to provide the sheet with back support during deformation. The main property of ISF which is always the same is the forming mechanism. A significant advantage which the ISF forming mechanism provides over traditional forming techniques is the increased forming limits of the material (Allwood et al., 2007). This makes it possible for ISF to fabricate sheet components from typically difficult to form materials. The flexible nature of the ISF tooling configuration provides greater flexibility compared to more conventional forming methods as it takes away the need for expensive matched tooling sets. This makes ISF better suited for low batch or custom manufacturing productions where high design flexibility is required. It is because of these advantages that there is now academic and industrial interest in ISF.

2.3.2 ISF Applications

In traditional sheet forming applications there are typically large investment costs associated with manufacturing dies and punches. This is economical for large scale manufacturing. However, for low scale productions such as prototyping this is not economically viable. The flexibility, low tooling costs, short lead times, and improved formability make ISF desirable for low scale productions (Lu et al., 2019), Figure 12. ISF becomes economically and technologically beneficial as a manufacturing process for batch sizes lower than 100. Prototyping, spare part production, and fabrication of aircraft components fit into this scale of production. However, car production scales are almost always larger than 100 so use of ISF in the automotive industry, except for prototyping, is not economically justifiable unless applying it within the premium niche vehicle sector. Also, the cost of ISF can be justified for some biomedical applications where 1-offs are needed. An drawback of ISF is its poor geometric accuracy which limits its use in the aircraft and automotive industries (Lu et al., 2019). Optimising ISF is essential to ensure industry benefit from the advantages ISF can provide.

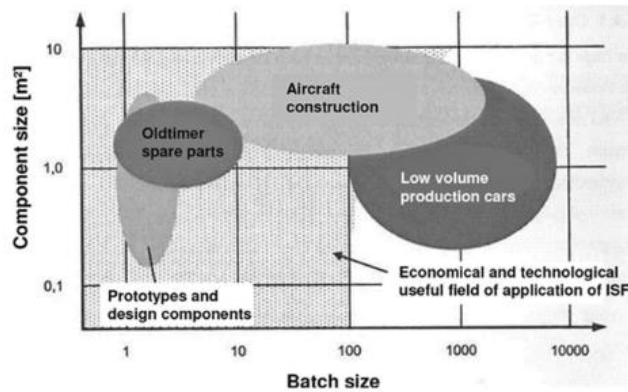


Figure 12 Application areas of ISF (Lu et al., 2019).

2.3.3 Single point incremental forming

Various forms of ISF have been the subject of several research studies looking to benefit from their advantageous properties. One such variant of ISF is Single Point Incremental Forming (SPIF). SPIF utilises a single tool which is controlled by a CNC machine. The tool movement follows a pre-programmed toolpath. The forming area of the sheet blank is typically left unsupported. This flexibility is not possible through traditional forming techniques such as deep drawing or stamping which necessitate a permanent die and punch system to achieve the desired sheet form. The flexibility of SPIF allows rapid design changes to be made by adjusting the tool path program, removing the need for designing and fabricating new tooling which is a lengthy and costly process. Two point incremental forming (TPIF) is largely the same as SPIF except the sheet is supported by a die, partial die, or even an opposing tool. A second tool provides back pressure from the opposite side of the sheet to the top tool. It is possible to manufacture dies by metal or polymer additive manufacturing to ensure process flexibility is not lost.

2.3.4 ISF Process Parameters

There are several important tooling parameters which can influence the ISF process. Tool size is the diameter of the hemispherical head which is in contact with the sheet during ISF. A small tool radius was shown to concentrate stress at the deformation zone under the tool head whereas a larger radius distributed the strain over an extended area

thereby reducing formability limits (Jeswiet & Young, 2005). Tool sizes typically start at 6 mm and can reach sizes of 100 mm, however most commonly used diameters are 12 mm and 12.5 mm (Jeswiet & Young, 2005). The diameter of the tooling needs to be kept proportional to the dimensions of the features, i.e., forming radii. An investigation into room temperature ISF of commercially pure titanium (CP-Ti) concluded a large contact area between the tool and sheet results in deformation not being localised, which can lower formability levels reached compared to ISF with a smaller tool diameter (Hussain et al., 2008). Another study found higher strains and deformations were achievable when the tool diameter was reduced from 30 mm to 6 mm (Hirt et al., 2002). Despite this, increased tool size has been seen to result in more homogeneous thickness distribution and plastic strain (Han, 2008). In another study, Su et al. (2021) found that as tool radius increased in SPIF the forming limits of aluminium sheet also increased. The feed rate is the speed at which the tool moves across the sheet surface during ISF. A review by McAnulty et al. (2017) into ISF showed higher feed rates reduce formability meaning there is a trade-off between formability and process time. Likewise, sheet formability was shown to increase with a smaller feed rate (McAnulty et al., 2017). Another study performed ISF trials on CP-Ti at room temperature and found work hardening at increased feed rates which led to lower formability (Hussain et al., 2008). However, these results are strongly dependent on the complexity of the geometry or the depth of the forming angle. High rotational speeds of the tool have also been seen to increase frictional heating which softens the sheet material, increasing formability (McAnulty et al., 2017). Likewise, the relative motion between the tool and sheet has been seen to increase formability due to frictional heating (Gatea et al., 2016). Step down is the vertical distance the tool moves after each revolution. The tool step down distance also influences formability, sheet surface roughness and the amount of sheet thinning. Decreasing step down size increased part success rate as stress is kept low which reduces the likelihood of early crack propagation in the neck due to rapid void coalescence (Ham & Jeswiet, 2006). Likewise, reducing step depth has proven to achieve more homogeneous plastic strain and thickness distribution (Han, 2008). Formability has been seen to increase with smaller step sizes and, to a lesser extent,

increased feed rate (Suresh et al., 2018). This result was substantiated in a study by Shafeek et al. (2022). However, Shafeek et al. (2022) also observed that reducing feed rate increased formability during SPIF. Sheet thickness can influence the outcome of ISF. One study found deeper forming depths of conical parts was achievable with smaller initial sheet thicknesses (Fang et al., 2014). In contrast, another investigation into ISF of aluminium sheet found that thinner sheets reduced the achievable wall angle size (Shanmuganatan & Senthil Kumar, 2013). This contradiction may have been a result of the severity of the forming angle which further proves how impactful sheet thickness can be on forming behaviour in ISF.

2.3.5 ISF Forming Mechanics

The unique localised deformation mechanism in ISF exists because of the tool to sheet contact condition. Several forming mechanisms occur to the sheet at this contact zone. The major mechanisms which occur are stretching, bending, shearing, through-thickness compression, and a cyclic effect (Sheng & Long, 2019), Figure 13.

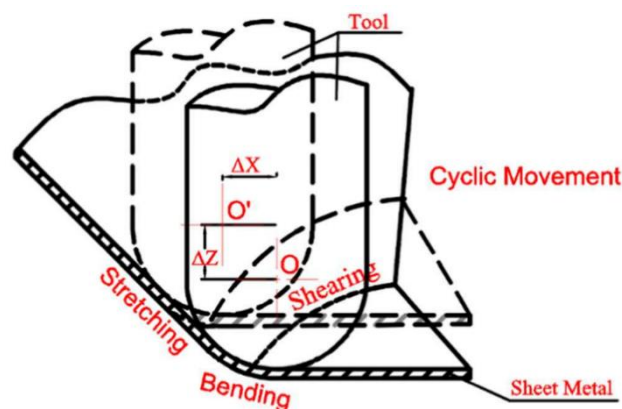


Figure 13 Deformation mechanisms in ISF (Sheng & Long, 2019).

The material in direct contact with the tool end undergoes both contact stress and a bending moment. The plastic deformation results from continuous squeezing of the sheet as the tool moves. Stretching of the sheet occurs along the wall of the formed part, with shear stress developing in the direction of the tool movement. Back pressure from the die, or partial die, supports the sheet during forming and has been shown to increase

geometric accuracy despite increasing process time and costs related to manufacturing the die (Zhao, 2023). The major deformation modes which occur during ISF are plain strain stretching and biaxial stretching. An investigation into ISF forming mechanics witnessed shear parallel to the tool direction, with almost pure bending and stretching perpendicular to the tool direction which caused material to pile up at the centre of the sheet (Jackson & Allwood, 2008). Another investigation suggested that the shearing mechanism is linked to the similarity between ISF and metal spinning, and additionally is responsible for nearly 50% of the plastic work performed by ISF (Maaß et al., 2019). One investigation found stretching with through thickness shear to be the primary forming mechanism in ISF (Jackson & Allwood, 2008). Not only this, the through thickness shear in the tool direction has been attributed to the improved formability of ISF (Allwood et al., 2007). Formability is a measure of the level of strain a material is capable of withstanding before failure. The measure of formability during ISF is the maximum draw angle achievable before thickness reduction results in fracture and subsequent failure of the sheet (Suresh et al., 2018). A major advantage of ISF is its capability of achieving higher levels of formability than conventional forming processes as seen in the FLC (Ai & Long, 2019), Figure 14.

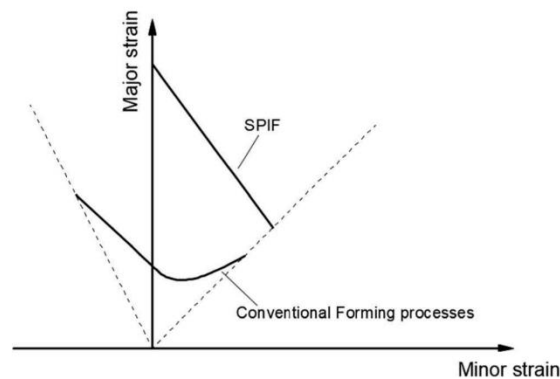


Figure 14 Forming Limit Curve (FLC) of ISF (Ai & Long, 2019).

Conventional forming processes largely operate in tension meaning formability is limited by instabilities. The deformation is typically concentrated in a small region known as the neck. As the neck is localised, small displacements cause high additional

strains which lead to sheet failure. Removing instabilities improve general formability, which is the case in ISF. Formability is maximised under plain strain stretching, which is a prominent forming mechanism in ISF (Nam et al., 2018; Park & Kim, 2003). Another forming mechanism which increases formability in ISF is through-thickness shear. Through-thickness shear demonstrates the principal axes of deformation are not aligned with the sheet, and direct stress at the onset of plastic deformation is lower as a result (Allwood et al., 2007). Another forming mechanism present in ISF is the cyclic effects from the tool which restrict neck growth and, by passing over the same location multiple times, subjects the material to cyclic straining from bending and unbending which improves formability (Emmens & van den Boogaard, 2009). Neck growth is also restricted in ISF by the localised deformation area embedded in a low stress surrounding area meaning the deformation zone is too small for a neck to develop. Finally, compressive hydrostatic pressure from the tool squeezes voids in the material which slows damage development and allows for large levels of strain during ISF (Emmens et al., 2009). Hydrostatic pressure was found to be largest in the region of maximum tool contact (Maaß et al., 2019). The deformation mechanisms present in ISF are responsible for the increase of achievable formability compared to conventional forming processes.

2.3.6 ISF Limitations

There are several drawbacks of ISF which limit its utilisation in industry. One such limiting factor is localised sheet thinning caused by the forming tool squeezing the sheet. Sheet thinning is an indicator of areas where plastic instability is likely to occur which can lead to part failure. Extensive sheet thinning can result in crack propagation, another cause of early part failure (Kilani et al., 2020). One investigation into sheet thinning in ISF showed the equi-biaxial tensile forming mode to be responsible for thinning, unlike the plain strain condition in conventional forming (Ai & Long, 2019). The same study also demonstrated that sheet bending from the tool contact zone increases longitudinal stresses in the transitional zone between the tool contact zone and part wall, resulting in sheet thinning and eventual fracture (Ai & Long, 2019), Figure 15.

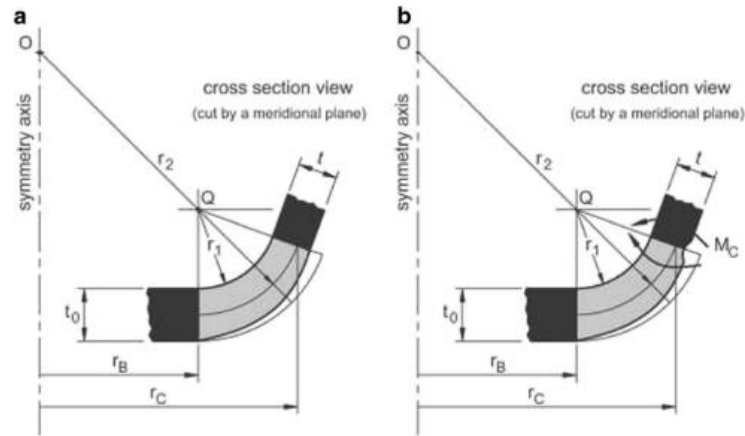


Figure 15 Thinning at transitional zone during ISF (Ai & Long, 2019).

Various research studies have attempted to develop a method for accurately predicting sheet thinning in ISF. Use of the sine law is one method of particular interest, Equation 4. The sine law is described by

$$T_f = T_o \sin (90^\circ - \theta), \quad \text{Equation 4}$$

were T_o is the initial wall thickness, T_f is the final wall thickness and θ equals half of the apex angle (equivalent to the wall angle). Two studies suggested thinning during ISF can be predicted using the sine law (Ai & Long, 2019; Araghi et al., 2009). However, another study found predictions using the sine law resulted in unexpected failure due to the non-uniform thickness distribution in ISF parts (Young & Jeswiet, 2004). What is clear is that sheet thinning increases as the wall angle increases. According to the principle of constant volume, when the wall angle is close to 90° the thickness of the deformed sheet is close to 0. As such, failure (typically cracking) can be avoided by ensuring the wall angle is not too high (Su et al., 2021). Another study showed the shear deformation prominent in ISF is the cause of inaccurate sheet thinning predictions when using the sine law (Yang et al., 2018). Despite this, increasing the wall angle has consistently resulted in greater thinning. This phenomenon was observed in the study by N. Kumar et al. (2019) which investigated thickness reduction during ISF of aluminium sheet, Figure 16.

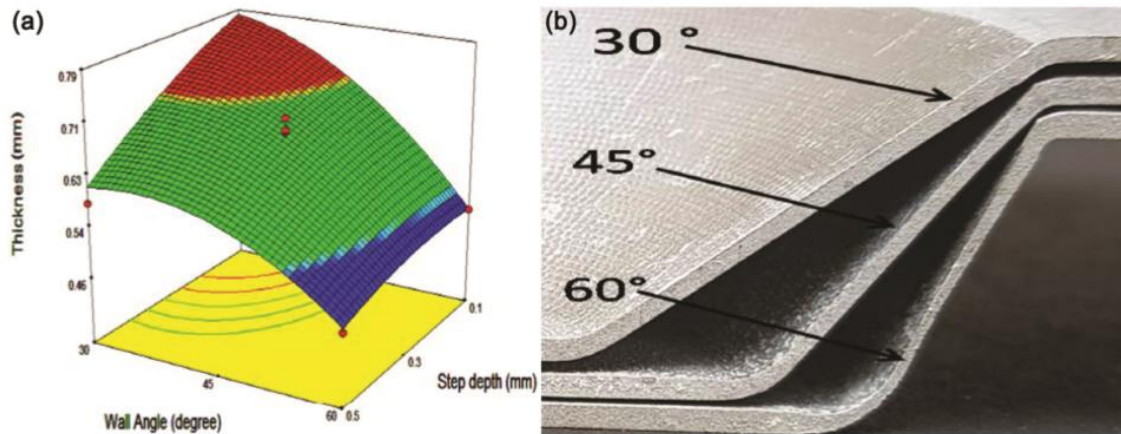


Figure 16 Thinning in response to forming angle (N. Kumar et al., 2019).

The optimal wall angle for ISF of aluminium sheet was shown to be 30° for minimising sheet thinning (Barnwal et al., 2019). Other ISF process parameters have also been shown to affect sheet thinning. Increasing the tool head diameter was shown to increase sheet thinning (Kilani et al., 2020; Yang et al., 2018). Increasing incremental step depth was also shown to increase sheet thinning (Kilani et al., 2020; G. Kumar, 2018). The common result of sheet thinning across many different experimental investigations is early part failure which is why it is such a devastating drawback for ISF. Failure is when the sheet breaks or fractures during forming, particularly in and around the tool contact zone which is considered a weak spot (Ai & Long, 2019). Necking is suppressed by the ISF forming mechanisms, as well as by the mechanism of the “Noodle Theory” which sees more uniform distribution of strain across the ISF sheet part compared to traditional processes, allowing for greater deformation without failure (Malhotra et al., 2012). However, strain will continue to increase until the level of damage propagation in one area eventually causes the part to fail. This often presents as a crack which opens across the sheet surface. The orange peel effect is typically the first indication of material fracture which is the product of different grains having slightly different orientations and hence being better or worse oriented to facilitate slip (Fang et al., 2014). The lifecycle of a crack in a sheet being formed by ISF begins with uniform deformation, followed by damage initiation, damage propagation, and eventually fracture. Shear in

the tool direction has been seen to suppress dimple formation which shows crack propagation initiates from the outer surface and travels to the inner surface of the sheet (Fang et al., 2014). A limitation in ISF is the achievable accuracy of the formed parts. Geometric errors in ISF are definable as any dimensional difference between the designed and formed profile (Micari et al., 2007). The common limitations of ISF which result in this type of geometric error are springback, sheet bending near clamped edges and curvature at the flat base of the curve known as the “pillow effect” (Lu et al., 2019), Figure 17.

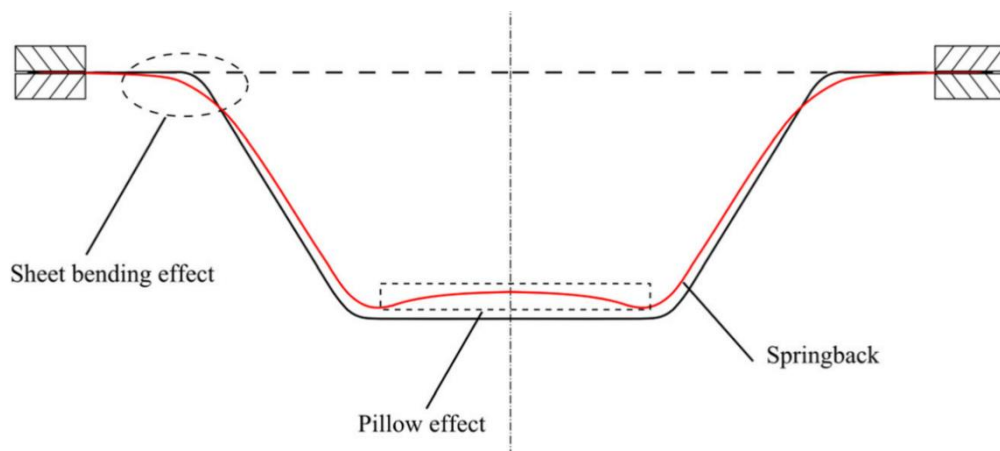


Figure 17 Typical geometric errors in ISF (Lu et al., 2019).

Industry demands high accuracy in all manufactured parts which limits the introduction of ISF in its current capacity. In-situ feedback control and toolpath correction have been shown to be very effective for improving final part accuracy (Lu et al., 2019). Springback is the major contributor to geometric error in ISF parts (Zhang et al., 2016). Springback is elastic recovery after all applied loads are released after forming. There are four variations of springback in ISF (Essa & Hartley, 2011):

1. Local deformation during forming.
2. Springback after unloading the forming tool.
3. Global springback after releasing the formed part from the clamping devices.
4. Springback induced by the trimming process.

ISF of difficult to form materials, such as titanium, results in low accuracy due to springback. One such industrial application is the production of medical devices which demands high accuracy for success. There have been some works indicating that a multistage approach to ISF helped to control and improve the development of the springback effect (Yan et al., 2021). ISF has also been shown to produce parts with poor surface finishes. An investigation into the surface quality of multi-stage ISF aluminium parts found extreme grain deformation in the sheet surface at the tool contact zone which resulted in the removal of material layers (Gupta & Jeswiet, 2019). Another investigation into ISF process parameters and their influence on ISF part quality found that by decreasing step depth, and increasing wall angle, tool diameter and spindle speed, the surface finish can be improved (Barnwal et al., 2019).

2.3.7 ISF fracture

Fractography is used to analyse the topography and morphology of fracture surfaces which can reveal details regarding fracture mechanics and failure mechanisms of a process. Significant plastic deformation is a key property of ductile fracture and dimple elongation typically align with direction of applied stress. Likewise, the expansion of micro-voids which coalesce to generate larger voids indicates ductile fracture. Fractography of SPIF parts showed the presence of significant plastic deformation on the fracture surface with oblate-type (flattened) micro-voids (Jaleel & Narayanan, 2023), see Figure 18.

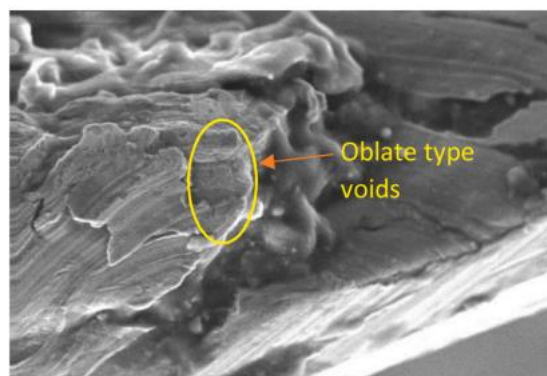


Figure 18 Fracture face of SPIF parts showing oblate-type voids

Shafeek et al. (2022) also concluded that predominately micro voids exhibit in ISF fracture sites which indicate ductile fracture. Additionally, a change in failure mode from void-based mechanism to inter crystalline separation was observed. With regards to the fracture mechanism in ISF, Valoppi et al. (2017) observed tearing in the contact zone (zone III) due to higher stress triaxiality and tapered thickness. Local bending and through-thickness-shear was seen to intensify crack initiation on the outer surface of zone III, which was supported by the direction of dimples, see Figure 19.

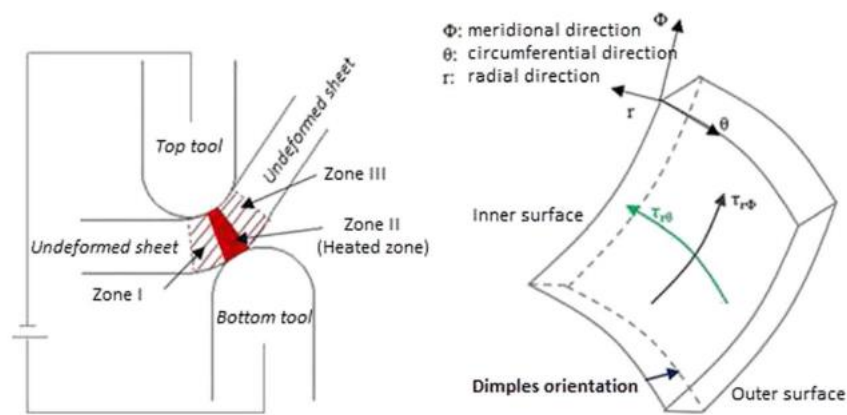


Figure 19 Deformation in DSIF with schematic displaying dimple direction

Crack morphology on the sheet surface can also help better understand ISF fracture mechanics. Hussain et al. (2008) observed micro-cracks above the visible crack on the material surface, and attributed this to the necking-like phenomenon seen in tensile tests, see Figure 20.

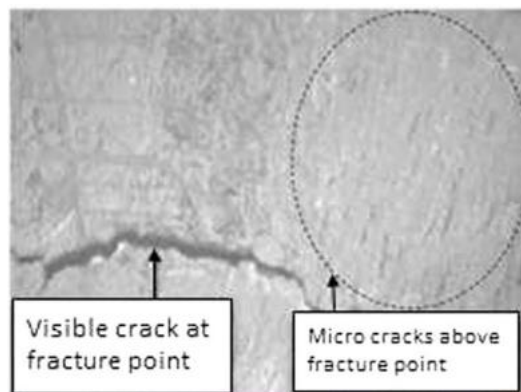


Figure 20 Micro-cracks seen above crack in ISF

A typical type of crack seen in ISF is the zig zag tear-induced crack (Anderson, 2005), Figure 21. This type of crack growth is often observed during ISF, such as in the study by Fang et al. (2014) who saw a zig zag crack appear when incrementally forming a cone shaped part from aluminium sheet. Crack coalescence during ISF is shown to result from plain strain mode I loading and void coalescence typically follows a 45° angle from the crack plane (Ai & Long, 2019; Anderson, 2005). In the study by Maria B Silva et al. (2011) longitudinal tensile stress in the plastically deforming contact zone between sheet and tool was shown to be the primary cause of the zig zag crack.

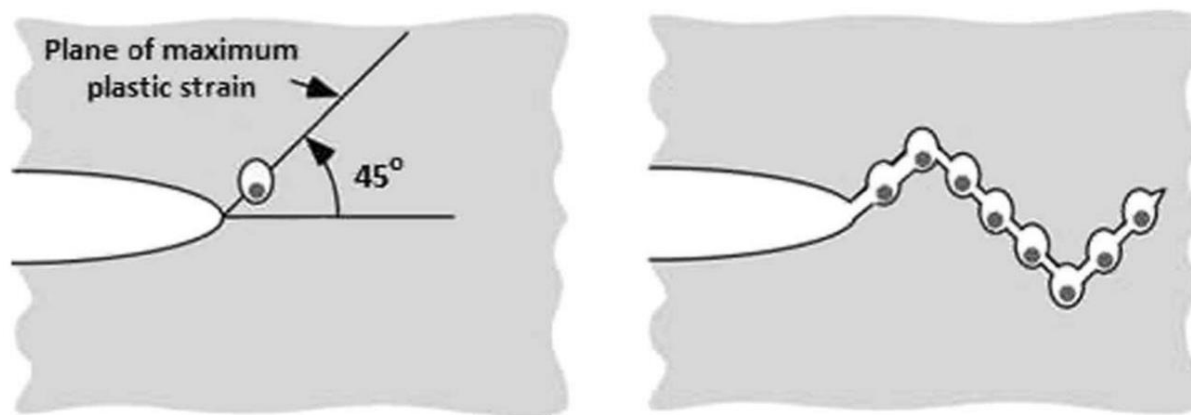


Figure 21 Ductile crack growth (Anderson, 2005).

Regarding the connection between fracture and thinning, Hussain et al. (2007) observed a “transition point” for both CP-Ti and aluminium ISF sheets where thinning became greater than the predicted thinning, indicating that fracture is an intrinsic property of the material, Figure 22.

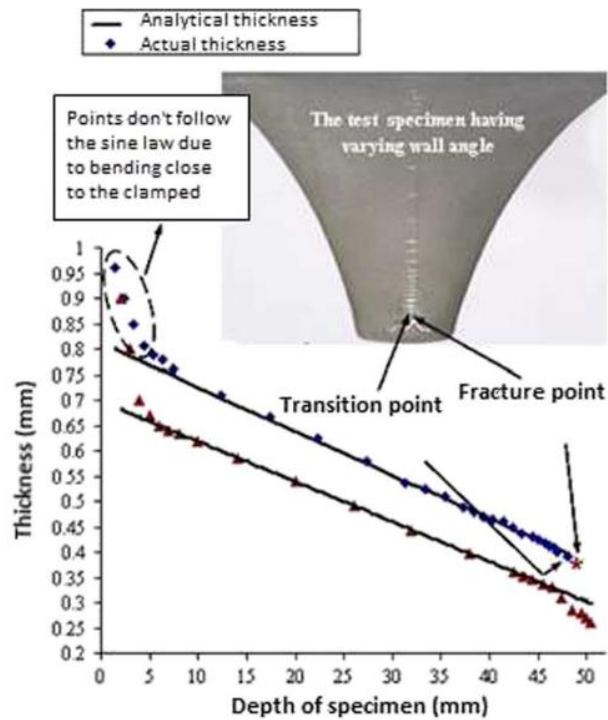


Figure 22 Transition point in CP-Ti ISF part (Hussain & Gao, 2007).

2.3.8 Optimisation of ISF

An essential step in ISF development is process optimisation to satisfy industrial standards. Maqbool & Bambach (2017) developed a modular tooling system to effectively constrain the ISF part for post ISF stress relief heat treatment. This improved the geometric accuracy of ISF parts while maintaining process flexibility which will help realise the economic advantage achievable using ISF over conventional forming. Ambrogio et al. (2009) were able to achieve a 50% improvement in final part accuracy compared to traditional ISF by using a back-drawing strategy which is based on the application of plastic deformation using a simple punch working successively on both sides of the blank, hereby correcting errors arising after the former forming phase, Figure 23. Preforming or stretch forming the sheet to obtain initial thickness distribution, before a final ISF process, was seen to reduce thinning and achieve more uniform sheet thickness distribution (Jagtap & Kumar, 2019).

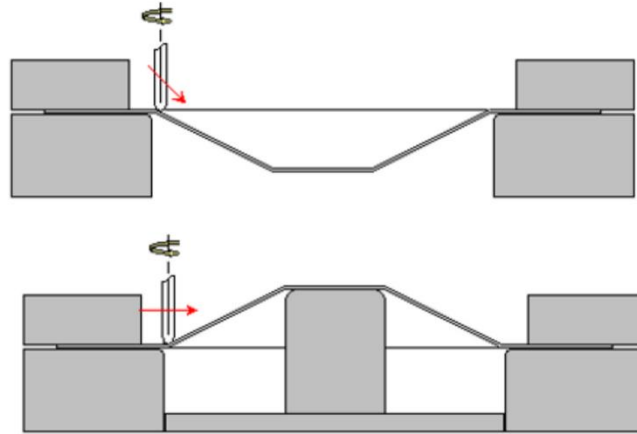


Figure 23 Back-drawing in ISF (G. Ambrogio et al., 2009).

Multi-stage ISF strategies have been able to make parts with higher wall angles than what is achievable by traditional ISF (Gupta & Jeswiet, 2019). Hybrid manufacturing has also been considered to optimise ISF. An investigation by Araghi et al. (2009) into hybrid incremental sheet forming (HISF) showed this strategy could achieve significant process performance improvements. One study used additive manufacturing (AM) to produce backing plates and thickened sheet blanks to improve geometric accuracy in ISF parts by compensating for localised thinning (Ambrogio, et al., 2019). Laser cladding was also seen to improve the stiffness of ISF parts (Bambach, et al., 2017). Use of an optimised tool-path trajectory was explored by Ambrogio et al. (2010) which adapts the tool path to compensate for localised thinning. These optimisation methods offer solutions to the drawbacks of ISF which helps make the aim of industrialising ISF more feasible.

2.4 Hybrid Manufacturing

2.4.1 Hybrid Manufacturing Overview

Hybrid manufacturing is defined as a process which combines two or more established manufacturing processes into a new combined set-up to exploit the advantages of each discrete process (Zhu et al., 2013). The objective aim of hybridising processes is to achieve the “1 + 1 = 3 effect”. So effectively, combining processes more than doubles

the advantages of each single process (Lauwers et al., 2014). Hybrid manufacturing can be used to optimise process capability, production time, and costs (Zhu et al., 2013). The five manufacturing types typically combined for hybrid manufacturing are subtractive, transformative, additive, joining and dividing. Descriptions of each of these five technologies are as follows:

1. Subtractive describes when material is removed from a workpiece to create a new workpiece.
2. Transformative describes when a single workpiece is used to create another without changing the mass.
3. Additive describes when material is added to an existing workpiece to generate a new workpiece and the mass is greater.
4. Joining describes when two or more workpieces are joined to form a new workpiece.
5. Dividing is the opposite to the joining process.

2.4.2 Hybrid Additive Transformative Methods

Combining AM with transformative processes can make parts not typically manufacturable by conventional transformative processes such as forging or forming. Combining sheet forming and AM has been shown to limit material waste by reducing manufacturing steps (M. Bambach et al., 2020). The use of hybrid AM and transformative processes has also been shown to improve geometrical freedom and material efficiency (Merklein et al., 2016). One investigation into AM load adjusted lightweight sheet components found they can help industries produce economic batch sizes thanks to the high geometrical freedom they offer and reduced material use (Merklein et al., 2016). There are two hybrid additive routes commonly used for the production of custom parts. The first is to additively fabricate features such as reinforcement ribs and other functional elements onto formed workpieces. The other is to generate pre-shaped semi-finished parts which are subsequently formed to achieve final part geometry. Hybrid additive ISF (HAISF) is a method of limiting ISF drawbacks which include sheet thinning, springback, low processing speed and poor

accuracy with the addition of an additive step. Hybridising ISF has been shown to improve process performance (Araghi et al., 2011). HAISF has also been seen to improve flexibility for the large scale production of lightweight components with small additive functional parts added by both forming and 3d printing in the same CNC machine using a single clamping device (Tebaay et al., 2020). Another experimental investigation into HAISF added reinforcement and back support to pre-formed sheets with AM which improved process flexibility and achievable geometric complexity (Ambrogio, et al., 2019). An investigation into the laser cladding of formed sheet found it possible to increase part stiffness with the additional additive step (Bambach et al., 2017). However, residual stress was superimposed into the sheet via the thermal input of the additive process which can cause sheet distortion or springback. Residual stress from ISF has been shown to limit the application of additive adjustments post forming (Tebaay et al., 2020), Figure 24. With AM tailored blanks, the bulk deposit and substrate base can typically exhibit different microstructures through its thickness largely as a result of the heat imparted during AM. As a result, through-thickness microstructural development may impact final part performance.

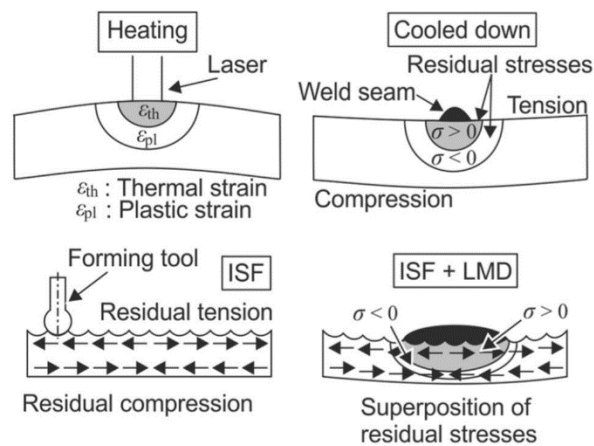


Figure 24 Residual stress after ISF and LMD (Tebaay et al., 2020).

2.4.3 Tailored Sheet Blanks

Tailoring sheet metal blanks is the process of adjusting the sheet properties prior to further fabrication or as a post process, for the purpose of optimising part quality and

process efficiency. Common characteristics of tailored blanks are variable sheet thickness, surface coatings, or variable material properties. The main types and methods of tailoring blanks are as follows (Merklein et al., 2014):

1. Tailor welded blanks – Joining dissimilar materials with a welding process.
2. Patchwork blanks – Reinforcing one blank locally with an additional blank.
3. Tailor rolled blanks – Creating a continuous variation of sheet thickness with a rolling process.
4. Tailored heat treated blanks – Using local heat treatments to adapt material properties.

Tailored blanks have been used for industrial applications, such as the tailoring of an aircraft's load carrying skin with a back-up structure consisting of a grid of stiffening elements. This achieved significant overall weight reduction (Sinke & Zadpoor, 2011). Such trends have led to semi-finished blanks gaining prominence in industry (Bambach, 2017). Another route for tailored blanks is improving product flexibility by designing thicker and stronger material in areas where higher stresses or loading is expected, and thinner material in other areas to reduce part weight and make cost savings without compromising strength (Shunmugam & Kanthababu, 2018). The cost savings achievable by tailored blanks was estimated by General Motors to be \$4.9 million by eliminating dies, weld fixtures and check stands from the production process (Shunmugam & Kanthababu, 2018). Material cost savings of 10% and time/energy savings of 30-40% were shown to be achieved by tailoring blanks due to reduced need for tooling development (Bambach, et al., 2017). Another study investigated local cladding via laser metal deposition (LMD) and found it suited to the tailoring process as precise material deposition on semi-finished or pre-formed blanks is achievable (Bambach, et al., 2017). LMD is well suited to tailoring blanks as the high quality substrate deposit interface limits forming drawbacks such as peeling (Hama-Saleh et al., 2020). One investigation into AM found it possible to improve flexibility by combining AM with sheet forming (Ambrogio, et al., 2019). A major limitation of tailoring blanks is thickness variation which can influence material flow during

forming, reduce formability, and cause springback variation due to thickness inhomogeneity which can necessitate specialised tooling (Bambach, et al., 2017). Dissimilar materials in tailored sheet parts can result in differing material properties which cause unequal stress and strain distribution across the part (Shunmugam & Kanthababu, 2018). Another drawback is poor strength properties in the weld, which is due to the weld cast structure containing large equiaxed grains and columnar grains (Merklein et al., 2014). Limiting material selection to similar materials with pre and post heat treatments has been suggested as a method of improving the performance of AM tailored blanks (Bambach, et al., 2017). AM tailored blanks have been shown to offer better final part properties than bonded patchwork blanks due to the full metallurgical bonding achievable between the deposit and substrate material (Bambach, et al., 2017). LMD was found to be a good AM method to tailor blanks thanks to better heat dissipation, thinner layers, and faster deposition speeds achievable which reduces heat affected zones and limits sheet distortion. It was believed that introducing heat treatments can improve sheet formability by up to 40% by ensuring the microstructures of the metallurgically bonded patches correspond approximately with the substrate material properties (Hama-Saleh et al., 2020). However, in the study by Hama-Saleh et al. (2020) microstructural variation across the sectioned view of the cross-sectional thickness of these samples was observed. The three distinct microstructural regions were as follows:

1. Unchanged cold rolled microstructure of the parent material.
2. Heat affected zone (HAZ) and dilution zone in the interface region.
3. Widmanstatten (cast) microstructure in the deposited layer.

2.5 Additive Manufacturing

2.5.1 Types of additive manufacturing

AM is the building of an object by layering molten material of equal thickness along the objects x-y plane. The deposition direction is controlled using a computer-aided design (CAD) part model which is sliced into 2dimensional layers by a slicing software

which are then used to determine a tool path for the deposition head to follow. Various types of AM exist with the most typical of these using two types of feeding system. These are the powder feed and powder bed systems. In a powder feed system, metal powder is fed through a nozzle to the part surface and melted by a laser. The material solidifies during the cooling phase and forms the final part geometry. The build volume scale up achievable via powder feed AM systems is a significant advantage over other systems such as powder bed (Gebhardt, 2011), Figure 25.

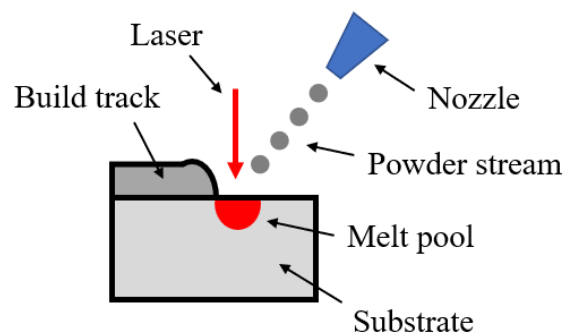


Figure 25 Powder feed system.

In a powder bed system, the metal powder is first spread onto the machine bed and then melted with a laser. The powder particles are fused together. The machine bed drops the height of one layer and another layer of powder is melted on top of the previous layer, generating a part model through this solidification cycle (Acharya et al., 2017). The high resolution features are a major advantage of the powder bed system (Gebhardt, 2011), Figure 26.

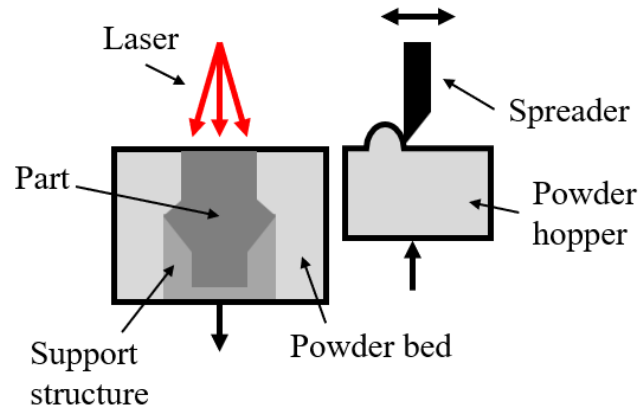


Figure 26 Powder bed system.

2.5.2 Laser metal deposition

Laser metal deposition (LMD) is a laser feed AM system. In LMD a laser forms a melt pool on a substrate surface and the powder is deposited into the melt pool. The powder melts upon entering the melt pool and then cools as the laser moves further along its path. The versatility of LMD makes it possible to fabricate functionally graded objects which makes LMD well suited for the reparation and cladding of valuable parts not possible via traditional methods (Saboori et al., 2017). The material flexibility achievable with LMD means the deposition of pure metals is possible. LMD is capable of generating a very small heat affected zone (HAZ) and good metallurgical bonding with the substrate material which reduces damage in surrounding areas and increases welding speed and process productivity (X. Li et al., 2005). LMD is not as accurate a process as CNC machining meaning post-processing is often required to achieve desirable geometric accuracy. Multiple studies discuss the potential of LMD for the repair of valuable parts and titanium components such as turbine blades (Schulz et al., 2019; Yu et al., 2012). The process parameters for LMD play a significant role in the resultant mechanical and microstructural properties of the final part. A significant parameter to consider during process development is the scanning velocity. The scanning velocity (v) is the speed of the powder deposit and laser and is found by

$$v = \frac{R}{\sin\theta}, \quad \text{Equation 5}$$

were R as the solidification rate and θ the angle between the tangent of the growth vector and scanning direction. Scanning velocity directly impacts the solidification rate of the deposit and informs microstructural properties for the deposit and substrate interface region. Another important LMD parameter is the energy density (which describes the laser energy input into the volumetric unit of powder during deposition. Energy density, E , is found by

$$E = \frac{P}{vht}, \quad \text{Equation 6}$$

were P as the laser power (W), v as the scan speed (mm/s), h as the hatching distance (mm) and t as the layer thickness (t). Laser energy density (LED) greatly impacts density and quality of LMD parts. A higher LED makes a larger melt pool in the substrate (Attar et al., 2014). The powder feed rate is the rate at which the powder leaves the nozzle head (Saboori et al., 2017). Meaning the LED and feed rate can be adjusted to control the size of the build track. The deposition pattern is the shape of the layers deposited which effects various attributes of the deposited part, including the distortion of the material due to the heat distribution. It has been shown that the deposition pattern effects longitudinal bowing and transverse angular distortion, with thin layers along the transverse direction rather than in the longitudinal also seen to decrease substrate distortion (Tebaay et al., 2020). It has been observed that increasing deposit thickness and material selection are the two major influencing parameters to increase LMD part stiffness (Markus Bambach, Sviridov, Weisheit, et al., 2017b). The anisotropic effect of AM parts is a major influencing factor with part mechanical properties. Toughness and tensile ductility have been shown to be higher in the build direction than in the transverse direction (Saboori et al., 2017). Part mechanical properties in the interface region between the substrate and deposit rely on successful integration between the substrate and material powder. An investigation into the interface region of LMD parts showed material solidification begins in the solid-liquid region between the melt pool

and substrate material (Mahamood, 2016). Part quality in LMD is largely influenced by solidification. Solidification is the liquid to solid change of the melt pool and the molten metal powder. During LMD the melt pool begins solidifying immediately after the laser moves away from the melt region (Mahamood, 2016). The scanning speed (velocity of laser) and initial temperature of the substrate material has the largest effect on the solidification rate. Higher scanning speeds are seen to create a smaller melt pool due to a shorter laser interaction time, and low substrate starting temperatures resulted in rapid solidification as the substrate acts like a heat sink and conducts heat away from the melt region. The ductility of a welded component can drop with the introduction of interstitial elements such as oxygen, nitrogen, and hydrogen. Inadequate shielding during deposition can cause this reduction in ductility of welded metal (X. Li et al., 2005). Not only ductility, but hardness varies depending on interstitial elements. The hardness was measured across a weld at different depths which showed hardness variations resulted from the level of diffused oxygen particles in the weld through the surfaces (X. Li et al., 2005). Oxygen content was higher near the surfaces compared to the weld centre, meaning the hardness also increased (X. Li et al., 2005), Figure 27.

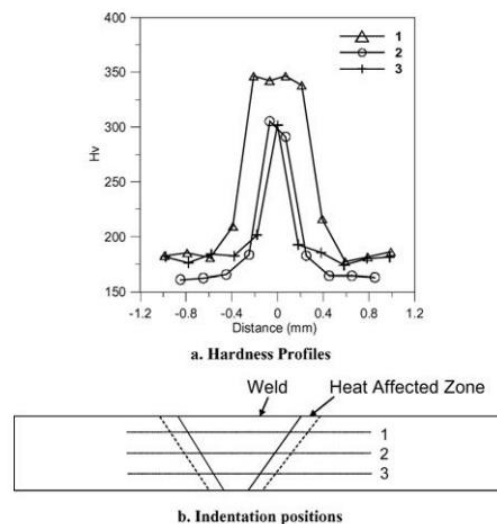


Figure 27 Hardness profiles (X. Li et al., 2005).

There are several properties which influence the microstructural properties of an LMD deposit. Two of these being the solidification rate of a melt (R) and the thermal gradient

at the solid-liquid interface between the melt and the substrate (G). An investigation into this deposition solidification rate and its effect on microstructure showed finer microstructures resulted from higher solidification rates and coarser microstructures from lower cooling rates (Mahamood, 2016). Higher scanning speeds cause smaller melt pools due to shorter dwell time of the laser at each location, which creates parts with fine microstructures. High G/R ratios are seen to promote columnar microstructures and low G/R ratios promoting equiaxed microstructures (Saboori et al., 2017). Three zones are prominent in LMD deposits. The deposition layer, HAZ and the base (or substrate) material. Each zone has different microstructural and mechanical properties. Columnar grains have been observed as the prominent microstructure in the boundary of the melt and base material for Ti-6Al-4V (Ti-64), with a fine dendritic microstructure in the deposited layer (Markus Bambach, Sviridov, Weisheit, et al., 2017b). Crystals (grains) nucleated on the substrate and formed the seed crystal which grows, following the crystallographic orientation in respect to the substrate or preceding layer crystal (Mahamood, 2016). This epitaxial growth occurs perpendicular to the substrate and opposite the heat flow towards the substrate (Mahamood, 2016), Figure 28.

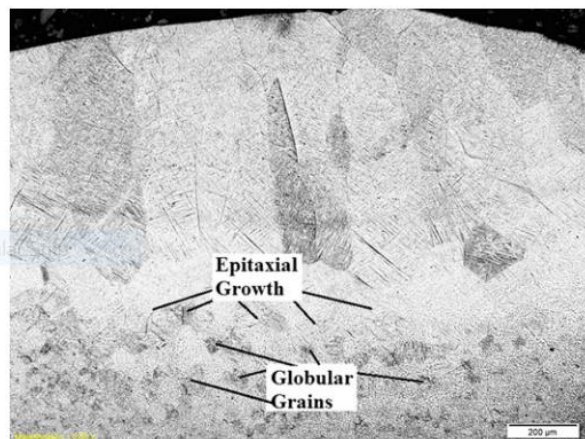


Figure 28 Epitaxial and columnar grain structure in Ti-64 (Mahamood, 2016).

The heat transfer from the melt pool to substrate causes grains to merge and grow which create a globular grain structure localised in the interface area. The globular grain size becomes smaller further from the melt pool site. Adding more layers leads to complex

heterogeneous and anisotropic properties thanks to the thermal history of the interacting layers. Fan et al. (2023) observed heterogeneous nucleation and abnormal formation of equiaxed grains in response to partially melted powder particles, particularly close to the surface of the deposited material, highlighting the importance of correct parameter selection and high powder quality to ensure complete melting.

2.5.3 Advantages and disadvantages of LMD

Geometric freedom gives additive processes an edge over traditional manufacturing processes, such as CNC machining, as such issues as limited tool access are less of an issue with the build layup process (Gebhardt, 2011). LMD can be used for repairs due to its precision and flexibility (Schulz et al., 2019). LMD also has high material diversity which includes pure metals (Gu et al., 2012). A major disadvantage of LMD is residual stresses being imparted into the substrate material during deposition because of heat input into the substrate from the laser and molten deposit material, and the thermal cycle. The thermal cycle for LMD deposition involves initial rapid heating due to the high energy intensity of the laser, followed by rapid solidification with high cooling rates (largely due to the small volume of melt pool) and finally melt-back which involves melting of the top layer as the laser passes over and subsequent remelting of underlying previously solidified layers (C. Li et al., 2018). An initial compressive stress state at the heated zone results from thermal expansion of the material being restrained by surrounding cooler material. The heated zone begins to cool as the laser passes and the material shrinkage is restrained by elastic strain formed during heating, resulting in tensile stress which is balanced by the compressive stresses. This also occurs with previously melted material which experiences remelting, as the solidification process causes material shrinkage which is restrained by previously solidified layers causing a residual tensile stress state. Residual stress results in part distortion which reduces geometric accuracy of the final LMD part. Tebaay et al. (2020) found that for multi-layer depositions the total distortion increased as each layer was added, with a thicker substrate reducing overall distortion. The mechanical properties which occur due to material anisotropy can be considered a disadvantage. It results from the thermal history

of interacting deposited layers. Poor surface quality of LMD parts such as the balling effect, which results in balls of metal being left on the surface after deposition. This can increase surface roughness which can require costly and time-consuming post-processing to achieve desired surface roughness levels. Another limitation of LMD is oxidation and leftover alpha case which are both the result of oxygen-enriched surface phase that is present when titanium is exposed to heated air or oxygen. Argon gas is typically used during LMD to help avoid this from occurring.

2.5.4 LMD of Titanium

The low formability of titanium limits its usability in industry. However, LMD offers an alternative method for fabricating parts from titanium not possible through traditional methods. LMD has the potential to become an economic alternative for manufacturing titanium parts such as turbomachinery or aerospace components (Schulz et al., 2019). The main microstructures observed in LMD of pure titanium components consist of columnar grains, a mix of columnar and equiaxed grains, and fully equiaxed grains. Microstructural evolution in LMD can result in unique features which is attributed to the effect of rapid cooling from the highly localised heat input of the laser and limited volume of the melt pool (Yamanaka et al., 2019b). Abnormal grain growth is seen to occur during LMD of titanium which is sub-boundary-driven, however can be reduced through process optimisation. The microstructure is also dependent on the LMD deposition pattern. Layering multiple tracks and remelting of equiaxed grains in overlapped areas between can result in the solidification of these equiaxed grains into columnar grains (Saboori et al., 2017). A lower depth of melt pool results in higher thermal gradients and higher cooling rates. By increasing melt pool heights, thermal gradients and cooling rates decrease which forms equiaxed grains on top of the melt pool. There are five separate microstructures parallel to the scanning direction in AM builds which are as follows (Meacock & Vilar, 2008), Figure 29:

1. Bulk deposited material, β transformed α platelets.
2. 60 μm thick layer of Widmanstätten structure, characteristic of pure titanium that has undergone the $\beta \rightarrow \alpha$ transformation with oxygen contents higher than 0.3

wt.% oxygen. Layer corresponds exactly to surface of substrate prior to deposition.

3. α platelets indicating substrate material, heated beyond the transus, and quenched
4. Region where the equiaxed structure of annealed and rolled substrate experienced grain growth because of heat dissipation from deposition.
5. Equiaxed α structure (from annealing and rolling) of CP-Ti grade 2 plate.

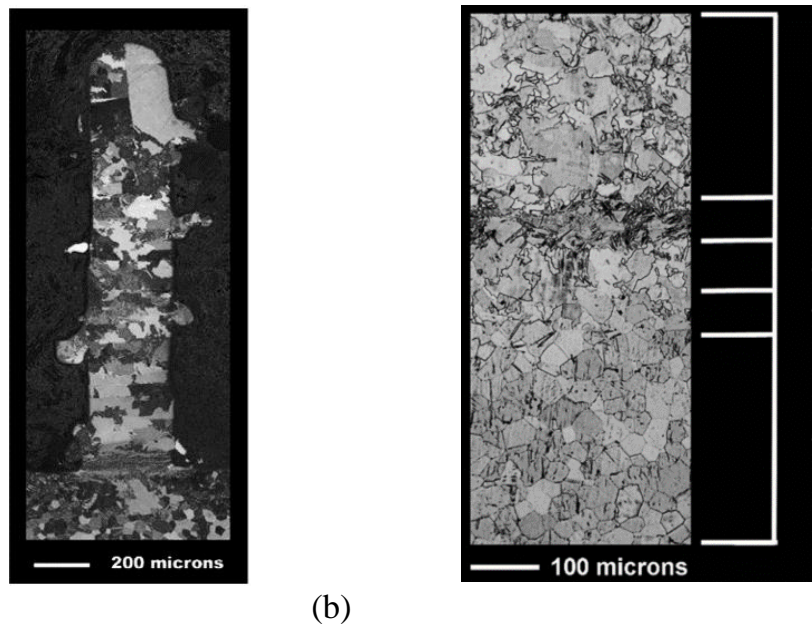


Figure 29 Ti deposit (Meacock & Vilar, 2008): (a) Thin wall; (b) Interface.

The solidification behaviour of the molten pool can determine the type of phase transformation which occurs in CP-Ti microstructure. CP-Ti undergoes an allotropic phase transformation at 882°C , known as the beta transus (β_{T}) temperature, which is a phase change from α -phase hexagonal close-packed (HCP) titanium to β -phase body-centered cubic (BCC) titanium on heating. Increasing scanning speed is shown to transform the phase from $\beta \rightarrow \alpha$ (at 100 mm s^{-1}) to $\beta \rightarrow$ martensitic α' (at 200 mm s^{-1}) (Gu et al., 2012). This phase change is significant as it can change the mechanical properties of the AM part, as well as other outcomes such as microscopic volume expansion which is present during martensitic transformation and can cause stresses at grain boundaries which affect lattice parameters. This α' martensite which forms during AM of CP-Ti is characterised by packets that contain plates (laths) of roughly $1 \mu\text{m}$

thickness (Yamanaka et al., 2019b). These refined α' grains result in improved microhardness and tensile strengths of laser deposited CP-Ti, whilst maintaining ductile properties (Attar et al., 2014). Elongated acicular martensitic α' phase with some basket weave α lathes were discovered in Ti-64 deposited with LMD (Cheng et al., 2021). This was caused by the high cooling rate of the LMD process, with a cooling rate more than 410°C/s resulting in the martensitic microstructure and lower cooling rate between $20^\circ\text{C} - 410^\circ\text{C/s}$ generating a mixed microstructure (Cheng et al., 2021). Serrated clusters of lamellar grains were observed in LMD CP-Ti alloys resulting from the cooling from over the β_T temperature with high (controlled) cooling rates (Barro et al., 2021), Figure 30. Another observation of titanium microstructure developed in response to LMD is the short β columnar grains of a Ti-64 material seen to grow epitaxially in response to $300\ \mu\text{m}$ tall layers deposited via LMD (Cheng et al., 2021). This study is important as it shows the directionality of these grains were driven by heat flux towards the substrate material.

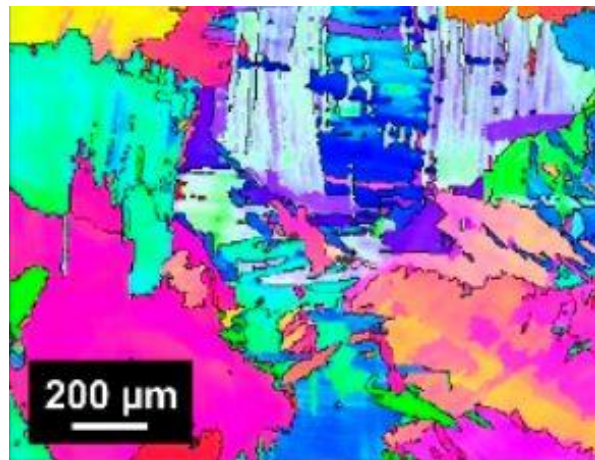


Figure 30 Serrated colonies in LMD sample of pure Ti (Barro et al., 2021).

2.5.5 LMD process parameters for titanium

The selection of appropriate LMD processing parameters will greatly influence build geometry. The geometry of the build track is typically a result of the melt pool size created by the laser and the volume of powder. The process parameters influencing build geometry are the laser power, mass flow rate and laser scanning speed. It is

necessary for the melt pool to maintain constant dimensions during LMD to ensure a consistent cross-section of the deposited track. Laser power is essential to ensure appropriate melting of the powder is achieved. According to Attar et al. (2014) the optimal laser power for melting pure titanium is 165 W, with a laser power of less than 100 W reducing part density and increasing the balling effect due to incomplete melting of the powder. However, other parameters such as laser focus, scan speed and flow rate can be adjusted to optimise the AM process with a low laser power.

2.5.6 Major consideration for the successful LMD of titanium

Some benefits gained from performing LMD on titanium are as follows:

- AM can improve the material properties of titanium largely due to grain refinement and the change from α to α' martensitic microstructures. For example, YS was seen to improve when the α and α' grains were not annealed as the crystals remained elongated (non-equiaxed) with high angle grain boundaries (Attar et al., 2014).
- Strength and ductility of laser sintered CP-Ti grade 2 after annealing at 700°C for 2 hours was seen to be close to that of wrought CP-Ti grade 2 annealed at the same temperature for hot forging (Okazaki & Ishino, 2020).
- Increased residual stress following AM has been shown to enhance strength properties (Attar et al., 2014).

Some difficulties which limit the useability of LMD of titanium parts are as follows:

- LMD titanium parts are weakest in the build direction (perpendicular to the plane axis) largely due to anisotropy (Attar et al., 2014). Anisotropy often results from nucleation, growth, and coalescence of micro-voids, as well as small quasi-cleavage facets in the build direction (Attar et al., 2014).
- Weaknesses in LMD titanium are often the result of incompletely melted powders and porosities in the build material which can result in part fracture.
- Contamination by impurities in the air can lead to environmental elements locating on interstitial sites in the crystal lattice, preventing movement of

dislocations and thereby increasing material hardness and strength, causing embrittlement of the titanium weld (Danielson et al., n.d.). Protective inert gas is needed to prevent microstructural degradation.

- High roughness of LMD parts often require post-processing such as laser polishing to achieve desirable finishes (Dadbakhsh, Hao, & Kong, 2010).
- The high reactivity and low thermal conductivity of titanium is shown to result in poor machinability of titanium which can limit post-processing of AM titanium parts (Saboori et al., 2017).
- The low thermal conductivity and thermal expansion coefficient of titanium is responsible for high inner tensions between the substrate and deposit which creates internal residual stress resulting in distortion and loss of part accuracy (Schulz et al., 2019).
- Temperature oxidation begins at 200°C and becomes critical at 450°C which is an issue as the melt pool temperature for titanium is 1700°C. For micro deposition of titanium, high control of laser power is necessary as heat accumulation in response to building layers is shown to increase the temperature of the material being deposited on for each layer (Meacock & Vilar, 2008).
- Titanium is highly reactive with oxygen which can lead to the deposited material burning or exploding. This is typically avoided by shielding the melt pool with gas. In the powder form there is high potential for titanium to explode as the surface-to-volume ratio is significantly large (Schulz et al., 2019).
- Distortion occurs due to thermal gradients through the parts, specifically the thermal input from the laser or electron beam to form the melt pool on the substrate material. Substrate preheating is often necessary to reduce the distortion for thin titanium substrates, however preheating can increase distortion for thick substrates (Corbin et al., 2018). The rate of distortion was also seen to increase as subsequent layers were deposited (Corbin et al., 2018).

- Powder dispersion during LMD is an environmental contaminant. It is very important to clean parts after AM to prevent any contamination and to avoid damaging machinery (Schulz et al., 2019).

2.6 Gaps and research focus

One of the advantages of ISF over traditional forming techniques is its ability to increase forming limits of difficult-to-form materials, thus making cold forming of titanium possible and reducing process costs. However, a major limitation of cold ISF is sheet thinning, which results in poor final part accuracy and encourages early onset failure by crack propagation and sheet opening (Kilani et al., 2020). Kumar et al. (2019) observed a direct correlation between increasing wall angle and thinning during ISF. Su et al. (2021) agreed with this by showing failure by cracking can be avoided by keeping the wall angle low in ISF. These observations show ISF to be limited to the production of low angled parts, with another study showing the optimum ISF wall angle to be as low as 30° (Barnwal et al., 2019). Some ISF modifications have been investigated to reduce the impact of thinning and improve geometric accuracy at high forming angles. Yan et al. (2021) observed a reduction in springback with multi-stage ISF of titanium sheet. Likewise, Gupta et al. (2019) found it possible to create parts from thicker sheets with multi-stage ISF. Maqbool et al. (2017) showed modular tooling could improve part accuracy. An interesting study by Araghi et al. (2011) showed process improvement was possible by hybridising ISF with AM. Some studies by Ambrogio et al. (2019a; 2019b) showed the use of AM backing plates and localised thickness reinforcement could reduce the impact of thinning in ISF. Despite this, there is no existing research looking into the feasibility of reinforcing thin titanium sheet with additional thickness to minimise localised thinning in high angled parts formed by ISF at low temperatures. Bambach et al. (2017) observed LMD could be used to manufacture sheet blanks thanks to a full metallurgical bonding. Hama-Saleh et al. (2020) also found LMD reduced sheet distortion and size of the HAZ in AM tailored blanks. Thus, a research gap has been identified for testing the feasibility of using LMD to reinforce thin CP-Ti blanks to optimise ISF.

Chapter 3

3 Experimental Approaches and Analysis Methods

3.1 Investigation approach for tailoring CP-Ti sheet with LMD

The approach used in this research was to tailor a thickness of commercially pure titanium (CP-Ti) sheet with Laser Metal Deposition (LMD). The additive LMD process was outsourced to an industry partner. Although it is outside the remit of this work, the economic viability of the LMD process for tailoring CP-Ti sheets for cold forming could be studied by implementing the following experimental approach and analysis methods.

3.2 Engineering Tooling

To successfully perform this investigation into a new hybrid technology it was necessary to first design and manufacture a tooling fixture to support the LMD and Incremental Sheet Forming (ISF) processes in the same process cycle. The major functions of the tooling fixture were as follows:

1. Accurately constrain a titanium sheet along its edges during LMD and ISF.
2. Secure and locate the LMD tailored titanium sheet during post-processing.
3. Position a back support forming die under the titanium sheet during ISF.
4. Facilitate installation of the sheet and die into a 5-axis CNC machine for ISF.
5. Precisely lower the LMD tailored titanium sheet over the die during ISF.
6. Release the fully formed titanium sheet with ease following ISF.

Design for manufacturability and design for assembly were major considerations in the design development and detail design of the fixture. A detailed product design specification (PDS) was developed to guide the design development process, section 3.2.1. Following design development, detail design was performed using SolidWorks and engineering drawings containing critical dimensions for all components and assemblies were created for the supplier and machine operators. Manufacturing and

assembly of the tooling set, which includes both fixtures for hosting the CP-Ti sheet during LMD, the stress relief heat treatment and the ISF operation, were performed by Pascoe Engineering, a Glasgow based precision tooling manufacturer.

3.2.1 Product design specification

A PDS defines the requirements of a new product design according to selected criteria. This PDS was generated to guide the design development stage of the tooling to ensure the previously agreed major functions were satisfied, see Appendix 10.1. Brainstorming and detail design processes were used to aid in the development of the tooling to ensure the final design satisfied the PDS design criteria. Following this, engineering drawings were created to supply the tooling manufacturer with critical dimensions, part and assembly drawings, and a bill of materials. Visits to the manufacturer were made to oversee the manufacture of the tooling. On completion, the final modular tooling fixture consisted of two major modules, the “LMD fixture” and the “ISF fixture”. These modules combined to support the hybrid manufacturing process. A dome shaped die used to support the sheet being formed by ISF was provided for this investigation.

3.2.2 LMD fixture detail design

The development of the LMD fixture is discussed in this section, Figure 31. The purpose of this module is to secure a titanium sheet during LMD and the post stress-relief heat treatment.

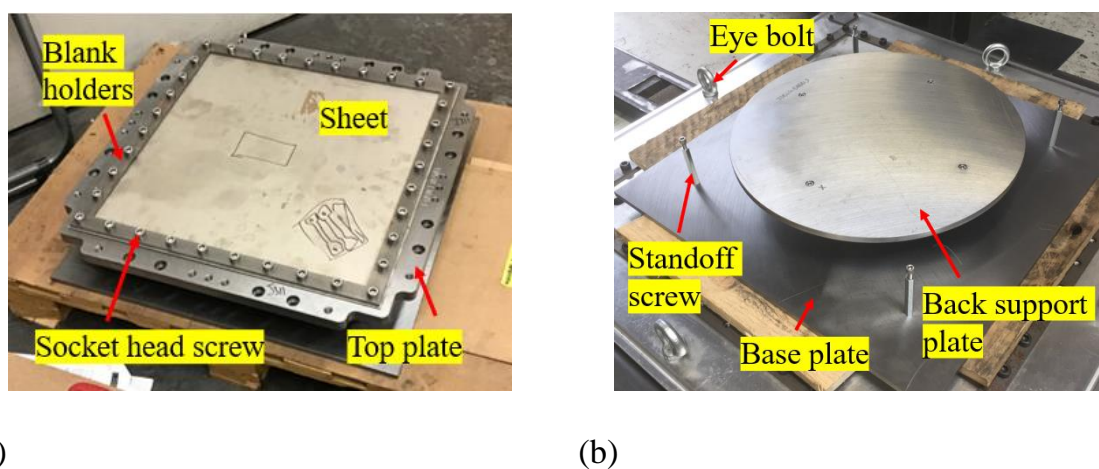


Figure 31 LMD fixture: (a) Fully assembled; (b) Back-support assembly.

The LMD fixture comprises of three parallel plates. A base plate, top plate with a central cavity of 442 mm diameter, and a back support plate. The top plate is lifted by four M6 x 60 standoff bolts for ease of access during assembly. A physical alignment groove at the corner of the top plate ensures repeatable positioning. The back support plate is positioned by four M6 x 70 standoff bolts inside the top plate cavity with a 2 mm edge tolerance. The purpose of the back support plate is to provide pressure to the underside of the sheet during LMD to reduce the likelihood of sheet distortion. Four blank holders of 5 mm thickness hold the sheet in position on the top plate and stop the sheet edges lifting in response to the LMD process. The blank holders are secured to the top plate by thirty-six M10 x 25 socket head screws. All manufactured parts were machined from tool steel satisfying the material requirements specified in the PDS, see Appendix 10.1. The upper half of the LMD fixture (top plate, blank holders, and sheet), Figure 31 (a), is removable from the lower half (base plate, back support plate, and standoff screws), Figure 31 (b). This leaves the cavity within the top plate clear, allowing the die to move through it during forming. The LMD fixture top plate edge is treated as a datum edge to position the deposition head and ensure positional repeatability. The engineering drawing for the LMD fixture design is available in appendix 10.2.

3.2.3 ISF fixture detail design

The ISF fixture was designed and manufactured to locate and guide the movement of the LMD fixture and sheet metal over the forming die during the ISF process, see Figure 32.

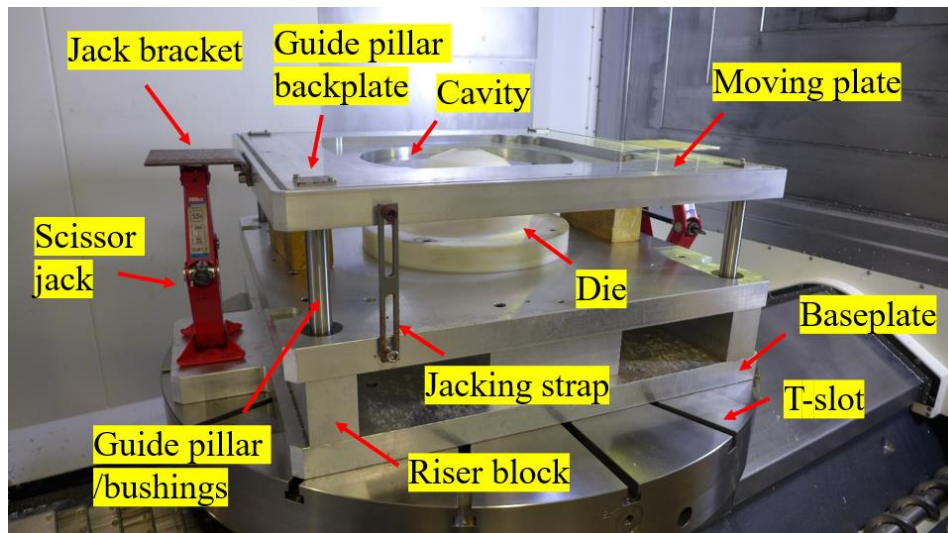


Figure 32 ISF fixture.

The ISF fixture comprises of a top plate named the moving plate, a base plate configuration with riser blocks and two flat plates, and a die-set guiding system containing four guiding pillars and bushing configurations at the four corners. The guiding configuration locates and aligns the moving plate with the base plate to accurately control vertical movement of the moving plate during the forming application. A cavity in the moving plate provides empty space for the die to move within as the moving plate is lowered so the die can provide back support to the sheet as the ISF tool forms the sheet incrementally. The baseplate is designed to be clamped on a T-slot table within the CNC 5-axis machine. The LMD and ISF fixtures are modular in design so are assembled for performing ISF, Figure 33. The engineering drawing for the ISF fixture is available in appendix 10.3.

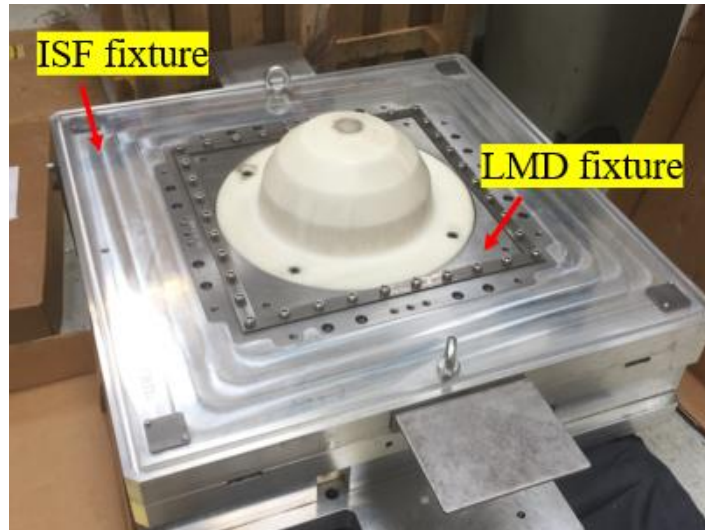


Figure 33 LMD and ISF fixture fully assembled.

Modularity was a key goal for this fixture. The moving plate has a sunken cavity in its surface which the LMD fixture fits into with a slide fit. The LMD fixture is secured by sixteen M10 x 30 socket head screws when in this position. The physical alignment groove of the LMD fixture upper plate is matched with the opposing aligner in the ISF fixture moving plate ensuring accurate and repeatable alignment. Brackets attach to the side walls of the moving plate which sit atop the scissor jacks. The scissor jacks lift the moving plate up by the two brackets during assembly of the fixture pre-ISF. Modularity was essential to facilitate the independent use of the LMD fixture module for LMD and the use as a combined set to perform ISF, Figure 33.

3.3 Experimental setup and material testing

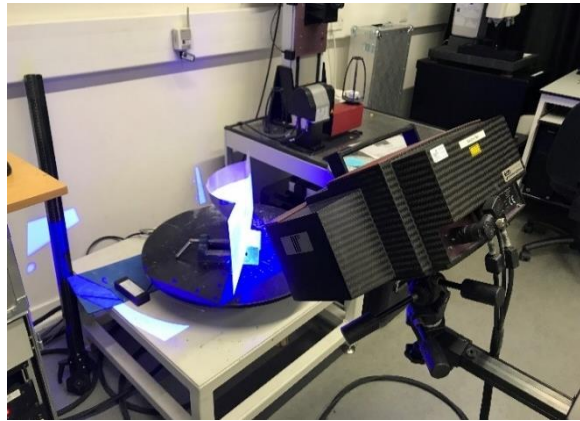
3.3.1 GOM ATOS metrology

A non-contact blue light 3D scanning technique was used to perform 3d scanning using GOM ATOS® software to accurately measure parts. An ATOS Triple Scan sensor was used with a 320 mm³ measuring volume. Two cameras were positioned at 27.9° with focal lengths at 24 mm (camera) and 30 mm (projector), Figure 34. All material samples were cleaned with acetone and sprayed with Adrox 9D1B to minimise light reflection. A calibration panel with several reference markers with specific distance and size from

each other were used to ensure full scanning. The reference markers were measured at different angles and positions from a set distance of 490 mm. The GOM Atos system calculates errors to ensure the scan is working properly. Multiple scans are taken, and a three-dimensional visualisation of the part is generated. The point cloud was polygonised, smoothed, and processed. GOM Inspect was then used to perform the part measurements on the 3d digital model.



(a)



(b)

Figure 34 GOM ATOS system: (a) Dual-camera setup; (b) During scanning.

3.3.2 Laser metal deposition

Laser metal deposition (LMD) was performed at Laser Additive Solutions Ltd (LAS), a laser specialist based in Doncaster, England. LMD was performed using a TRUMPF 2 kW TruDisk Laser and Oerlikon Metco Twin-10-C powder feeder. The laser and powder feed movement were controlled by a 5-axis REIS RL80 Gantry Manipulation System with a 3 x 2.25 x 1.5 (m) work envelope. Programming of the deposition path was performed using Mebitex TopLas3D CAD/CAM software, Figure 35. The material used for LMD was a CP-Ti grade 2 gas atomised powder with a particle size distribution of 45-150 μm .



Figure 35 LMD processing cell.

3.3.3 Development of LMD machine parameters

The LMD machine parameters were developed experimentally on-site by printing tracks on thin titanium sheet and measuring the build dimensions with callipers then adjusting the machine to achieve the desired print geometries. Five separate parameter sets were tested with multiple tracks for each printed to measure track height, width and to ensure the tracks were joined, see Figure 36. The following operator comments were made to justify parameter development decisions:

- For D101 the power was too low.
- For D102 the power was increased to reduce width between the tracks.
- For D103 the separation between tracks was reduced to 2.0 mm and the build height was measured at 0.25 mm.
- For D104 the powder flow rate was reduced, and the desired build height of 0.15mm was achieved.
- D105 was deemed satisfactory.



Figure 36 Developing LMD machine parameters.

The values in bold represent the changes made to the processing parameters. Any changes were decided on from operator experience. A vernier calliper was used to measure the deposit geometry to determine closeness to the desired track topology. The values which were kept constant from D101 were selected on the recommendation of the operator. A logbook was kept by the operator explaining the effect of each parameter change, see Appendix 10.8.

Table 3 LMD parameter development cycle.

Parameter	D101	D102	D103	D104	D105
Carrier pressure (bar)	1.5	1.5	1.5	1.5	1.5
Carrier flow rate (l/min)	4.0	4.0	4.0	4.0	4.0
Powder flow rate (%)	6.0	6.0	6.0	3.5	3.5
Nozzle pressure (bar)	2.0	2.0	2.0	2.0	2.0
Nozzle flow rate (l/min)	10.0	10.0	10.0	10.0	10.0
Nozzle rev(s)	2.0	2.0	2.0	2.0	2.0
Feed rate	15.0	15.0	15.0	15.0	15.0

Dial	8.0	8.0	8.0	8.0	8.0
Laser power	375.0	675.0	675.0	675.0	675.0
Track separation	2.0	2.0	1.4	1.4	1.4

The following LMD machine parameters were selected: laser power (P) of 675.0 W, scanning speed (v) of 15.0 mm/s, track separation of 1.4 mm, and carrier and nozzle shielding gas flow rates of 4.0 l/min and 10.0 l/min respectively. As a result of the machine parameters, a low linear laser energy density (LED) of 45 J/mm was achieved to keep a low heat penetration depth, narrow melt region and small heat affected zone (HAZ), Equation 7.

$$LED = \frac{P}{V} \text{ J/mm} \quad \text{Equation 7}$$

The shielding argon gas carried the metal powder into the laser melt pool where it melted and then cooled and solidified when the laser moved away and stopped providing the thermal loading. The layer height was set at 0.15 mm by adjusting the step height for which the nozzle was lifted between layers. A crosshatch pattern pad of two layers was deposited with the machine parameters from D105. The pad was sectioned, and the quality of the deposit examined by the operator by optical microscopy. Porosity and deposit size were the main concerns of the operator with regards to feedback of process performance. Minimal porosity was seen in the deposit and the machine parameters were approved. To ensure consistency throughout the remainder of the research investigation the selected LMD machine parameters developed were kept consistent.

3.3.4 Residual stress measurements

Residual stress was measured using X-ray diffraction (XRD). This was performed using a Proto LXR2000 machine. XRD is a non-destructive technique used to characterise crystalline materials by providing information on structures, phases, texture, strain, and

other structural parameters (Kohli & Mittal, 2019). It does so by providing XRD peaks which are produced by constructive interference of a monochromatic beam of X-rays scattered at angles from each set of lattice planes in a sample surface. The peak intensities are determined by atomic positions within the lattice planes. The distance between crystallographic planes is used to measure residual stress. This distance, also known as interplanar spacing, increases under tension compared to the unstressed condition. It is calculated using Bragg's Law which is

$$n\lambda = 2d\sin\theta \quad \text{Equation 8}$$

where d is the distance between atomic layers in the crystal, λ is the wavelength of the incident X-ray beam, and θ is the angle of incidence of the reflected X-ray beams. Cu radiation was used. A tube voltage of 30 V and tube current of 30 mA was used, which as exposure time of 3s. XRDWin 2.0 software automatically output the RS measurements. All measurements were performed at ambient temperature.

3.3.5 Heat treatments

A heat treatment to relieve internal residual stress in the prints was performed in a Carbolite LCF furnace, Figure 37. The furnace was selected because of its internal volume being capable of holding the tooling assembly and because it is capable of being purged with gas to limit oxidation of the surface. The furnace is backfilled by argon gas but does not create a complete vacuum meaning slight oxidation of the material surface was unavoidable. There was no access to a furnace with vacuum capabilities, so the decision was made to continue with the Carbolite LCF furnace and acknowledge the possible impact of any oxidation when analysing the results.



Figure 37 Carbolite furnace.

3.3.6 Tensile specimen preparation and geometry

An Agie Charmilles wire electrical discharge machine (Wire-EDM) was used to cut tensile specimens from a sample of material to perform the experimental investigation of tensile properties. The tensile specimen geometry was IAW ASTM-E8/EM “Standard Test Methods for Tension Testing of Metallic Materials” with modified geometry to fit the on-site tooling and to not alter the result of the test, Figure 38. The width of each test specimen was measured using vernier callipers and the thickness measured using a micrometre.

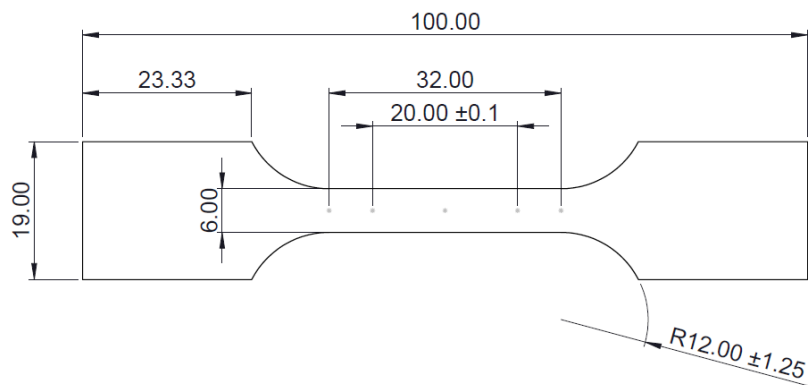


Figure 38 Tensile test specimen geometry.

3.3.7 Mini FLC Nakajima sample preparation and geometry

Mini Forming Limit Curve (FLC) Nakajima test specimens from the LMD tailored material were cut using wire-EDM, Figure 39. The decision to use miniature specimens is explained further in section 8.2.3. The gauge length radius of the FLC specimens was adjusted to test the right side (positive minor strain, ϵ_2) of the Forming Limit Diagram (FLD) for predicting the forming behaviour of the LMD material in response to plane strain, biaxial tension, and equi-biaxial tension.

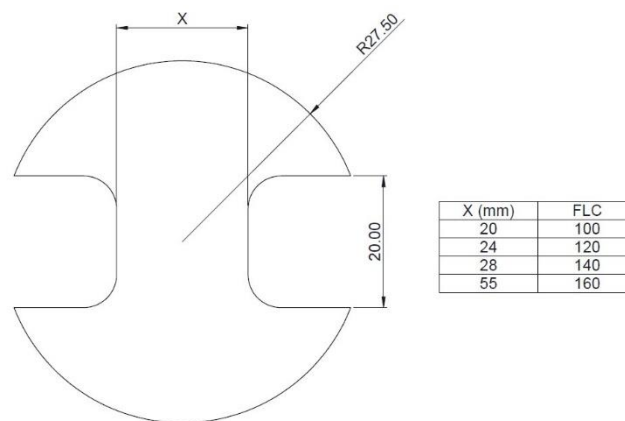


Figure 39 Nakajima FLD specimen geometry for the development of the mini FLC.

3.3.8 Speckle pattern preparation

A stochastic pattern was created on the surface of the tensile and FLC specimens to measure strain distribution, Figure 40. Achieving correct size and distribution of the black dots ensures the DaVis system can accurately track the sample surface displacement to generate the strain map. A good stochastic pattern must have high contrast with varying grayscale intensities and relatively large intensity gradients, randomness, with non-periodic and non-repetitive pattern to facilitate full field displacement mapping, isotropy, and strong stability so it deforms with the surface (Dong & Pan, 2017). A solid white background was sprayed onto the specimen surface. After overnight drying of the white spray, a black spray was used to create a speckle pattern. To do this, the spray nozzle was sprayed at a distance allowing the black paint

to fall in droplets onto the surface. The sprayed surface was illuminated by the monochromatic light during DIC analysis and the stochastic pattern decorated images were obtained (Dong & Pan, 2017).



Figure 40 Stochastic (speckle) pattern on tensile specimen for DIC.

3.3.9 Tensile testing

The tensile testing was conducted to ASTM E8 “Standard Test Methods for Tension Testing of Metallic Materials”. A 150kN Zwick/Roell Z150 load cell tensile testing machine was used to perform room temperature (23°C) uniaxial tensile tests, Figure 41. All tests were carried out at a constant strain rate of 0.001s^{-1} , controlled by testXpert II software. Load and extension were recorded using the testXpert II software and used to determine the stress vs strain data. The load cell evaluates the load on the tensile specimen at any point during testing. An extensometer was used to capture the displacement of the specimen gauge length during the tensile test. This was deemed necessary to validate the extension measured by DIC. The test ended at tensile specimen failure. Tensile behaviour is described using Hooke’s law, Equation 9, and the power law, Equation 10. Both equations are used to calculate the true stress vs strain data for each specimen.

$$\sigma_e = E\varepsilon_e, \quad \text{Equation 9}$$

$$\sigma_y = K(\varepsilon_o + \varepsilon_p)^n, \quad \text{Equation 10}$$

Where σ_e is the stress in the elastic zone, E is the modulus of elasticity, ε_e is the elastic strain, σ_y is the yield stress, K is the strength coefficient, ε_p is the plastic strain and n the strain hardening index.

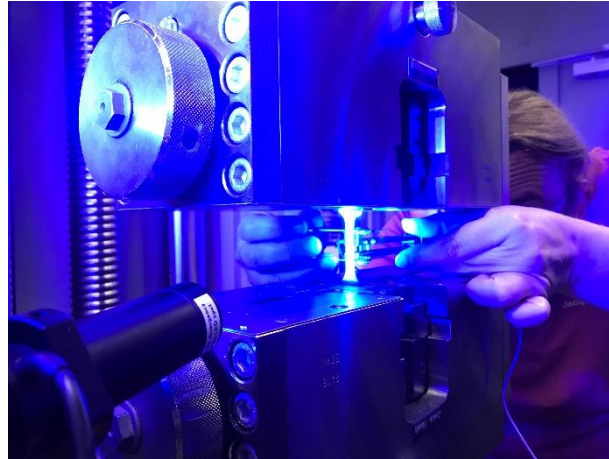


Figure 41 Zwick/Roell Z150 load cell tensile testing machine.

Elastic strain is reversible whereas plastic strain is not. The elastic zone is defined by the calculated yield stress (YS) of the material. Up until reaching the YS the material will return to its original shape when the external force is released, meaning the undergone strain is elastic. However, beyond the YS the material enters the plastic region. If the external force is released within the plastic region, then the material will not return to its original geometry. The final geometry of the test piece is determinable using the materials elastic modulus (EM).

3.3.10 BUP setup and testing

A Zwick BUP 1000 machine was used to test the sheet metal formability, Figure 42. Zwick testXpert II software was used to analyse and present the test results graphically in accordance with BS EN ISO 12004-2:2008. A GOM Aramis system with a 2448 x 2050 camera acquisition mode was used to capture the displacement of the speckle pattern during deformation. A GOM Aramis 5M (GigE) sensor type was used during testing.



Figure 42 Zwick BUP 1000 machine.

3.3.11 Digital Image Correlation

Digital image correlation (DIC) was used to account for surface strain evolution during tensile testing and BUP testing. DIC tracked blocks of pixels to compare digital photographs of a test piece at different stages of deformation. This allowed the material behaviour and fracture initiation of the test specimens during mechanical testing to be tested. The displacement of the randomly placed stochastic pattern was measured at 4 frames per second with two digital cameras at a fixed frequency of 1 Hz. A calibration plate was used to calibrate the system before testing. Successive images were taken of the specimen surface during deformation and stored on the computer. Strain distribution was measured using DaVis 8.0 software supplied by LaVision. A mask was defined over the area for which strain was to be measured on the specimen surface. Seed points were selected in areas of reasonable speckle pattern (roughly 3 features per seed point) which experience low initial deformation.

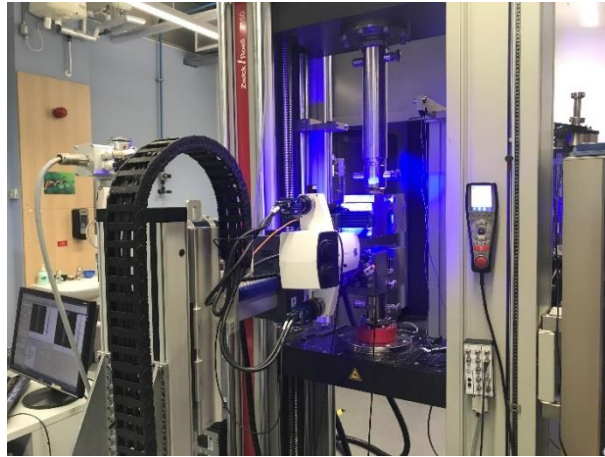
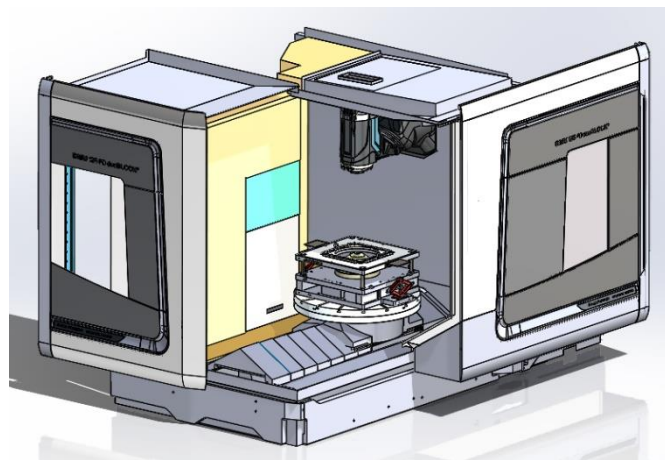


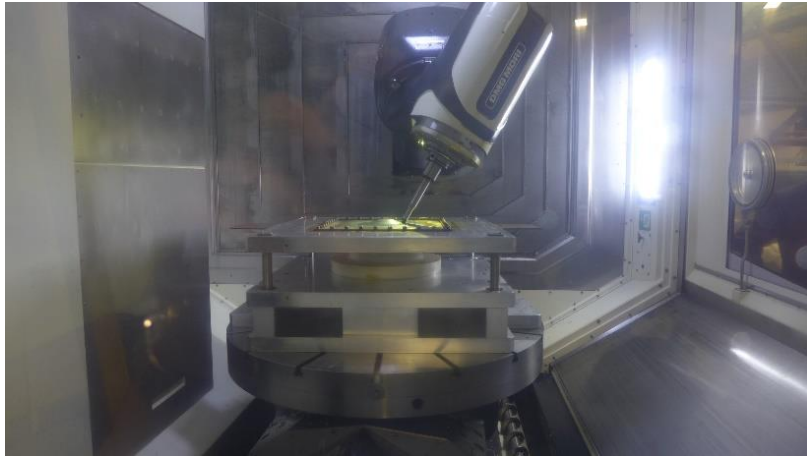
Figure 43 DIC setup during uniaxial tensile test.

3.3.12 Incremental Sheet Forming

ISF was performed using a DMU 125 5-axis CNC machine, Figure 44 (a). The interior of the DMU 125 is large enough to host the ISF fixture and LMD fixture modular system securely during ISF, Figure 44 (b).



(a)



(b)

Figure 44 DMU 125 5-axis CNC: (a) Machine exterior; (b) Machine interior.

3.3.13 Material sample preparation

To conduct microstructure and macrostructure analysis, material samples were taken from testing material and prepared using different preparation methods and specialised equipment. A Buehler Isomet 5000 linear precision saw machine fitted with a standard 7" MetAbrase cut-off abrasive wheel was used to section material samples, Figure 45 (a). Care was taken to ensure no overheating from the cut off wheel as friction from the wheel has potential to alter microstructure. Areas selected for analysis were kept away from cut edges. A single saddle chuck held the sample in place during sectioning. The abrasive wheel was operated at a speed of 4000 rpm with the linear feed of the wheel manually controlled during sectioning. A water hose provided cooling during the cutting process. A Buehler Simplimet 3000 mounting press machine was used for mounting samples, Figure 45 (b). The sectioned samples were mounted in an EpoMet compression mounting compound. These were pressed at a pressure of 29 MPa and heated for 1.5m before cooling for 6m to cure. Grinding and polishing of the samples was performed on a Beuhler Automet 300 Pro grinder and polisher machine, Figure 45 (c). A structured grinding/polishing process was followed to ensure consistent sample surface preparation. Depending on the type of analysis the process was adjusted, Table 4. Silica-carbide abrasive disc grinding papers with grit sizes including: P600, P800,

P1200 and P2500 respectively were used for each grinding step. For polishing, 20 ml of 0.02 μm silica (MasterMet 2 non-crystallising colloidal Silica) was mixed with 100 ml distilled water to form a colloidal suspension used to polish the samples on a ChemoMet polishing cloth.

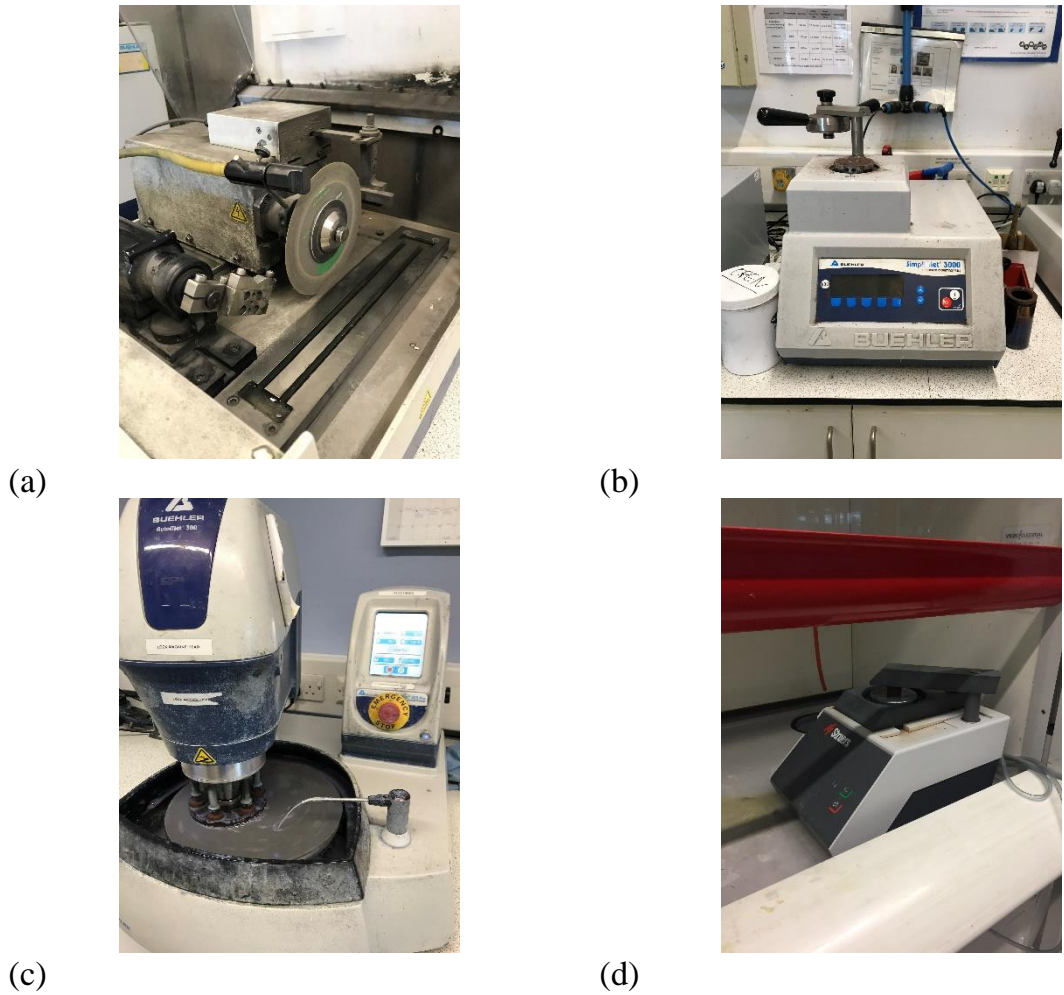


Figure 45 Material preparation equipment: (a) Precision saw; (b) Mounting press; (c) Grinder and polisher; (d) Electrolytic polisher.

Table 4 Material specimen grinding and polishing process for CP-Ti.

Grit paper	Time (min)	Pressure (kN)	Rotation
Follow met prep process for microhardness, optical microscopy and EBSD analysis			
P400	2	20	Same direction

P600	2	20	Same direction
P800	2	20	Same direction
P1200	2	20	Opposite direction
Continue for optical microscopy and EBSD analysis sample preparation step(s).			
P2500	2	20	Opposite direction
P2500	2	10	Opposite direction
Chemomet	6	10	Opposite direction
Chemomet	6	5	Opposite direction
Continue for EBSD analysis sample preparation step(s).			
Perform electropolishing, section 3.3.14.			

3.3.14 Electropolishing

A Struers LectroPol-5 automatic electropolisher machine was used to electropolish the samples for EBSD, Figure 45 (d). A mixture of 600 ml methanol + 360 ml butoxy-ethanol + 60 ml perchloric acid solution (A3 electrolyte) was used as an electrolyte. A polishing current of 0.86 A with a voltage of 35 V was used to polish a 1 cm² area by holding it for 15s at 11°C at a flowrate of 16 m³/s. The polishing unit was setup in a fume cupboard and initial cleaning steps using water and methanol were performed. A transparent mask with an aperture to suit the sample size was selected and installed onto the polishing table. The sample was placed facing down into the aperture of the transparent mask and the anode arm was moved on top of the rear side of the specimen. As the electrochemical process was started, the electrolyte flowed over the sample surface. The current passed through the sample, oxidising and dissolving the surface of the sample in the electrolyte. CP-Ti is difficult to polish because it is soft and retains

cold work, more so than other titanium alloys. Thus, electropolishing as the final step removed residual cold work induced by the polishing step and reduced the surface roughness by levelling micro-peaks and valleys, effectively improving the surface finish of the sample.

3.3.15 Material characterisation

Various material characterisation techniques were used to analyse the macroscopic and microscopic properties of the processed material as an analysis step in this experimental investigation. An optical microscope was first used to characterise the grain structure across the cross-section of the samples. Following this, the material microstructure and failure modes (fractography) were characterised using a Quanta FEG 250 SEM microscope via the acquisition of secondary electrons (SE) to achieve high resolution magnified images, Figure 46. For fractography, a working distance of 10 mm between the lens and the sample surface was employed with magnifications ranging from x250 to x3000. An accelerating voltage of 20 kV and spot size of 4.5 was used. Electron backscatter diffraction (EBSD) was conducted using the Oxford Instruments EBSD detector. EBSD is used to determine the grain structure and texture of the material. A working distance of 13.4 mm was employed, and the sample platform tilted to 70° towards the EBSD detector to increase the contrast in the EBSD pattern. The EBSD detector was inserted to 160 mm. An acceleration voltage of 20 kV was used and spot sizes of 0.1 and 0.2 used depending on the magnification and area of interest. The EBSD pattern is a result of the backscattered electrons escaping the sample and diffracting to form Kikuchi bands which correspond to the lattice diffracting crystal planes.

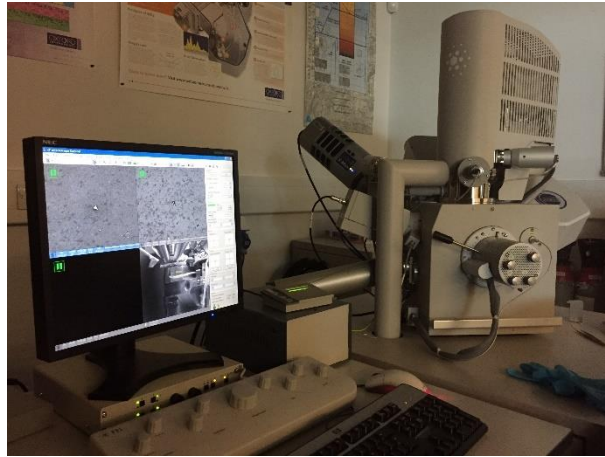


Figure 46 Quanta FEG SEM 250.

A Leica DM 12000M optical microscope was used to examine the surface and edge microstructural morphology of the material samples. A Vickers-Knoop Micro Hardness tester was used for microhardness measurements using a load of 1 kg and a loading time of 15s, Figure 47. A pyramidal diamond indenter was used to form indentations in the material in a straight line down the centre of the gauge length, and a microscope used to measure the diameters of the diamond indent to calculate the Vickers hardness value.

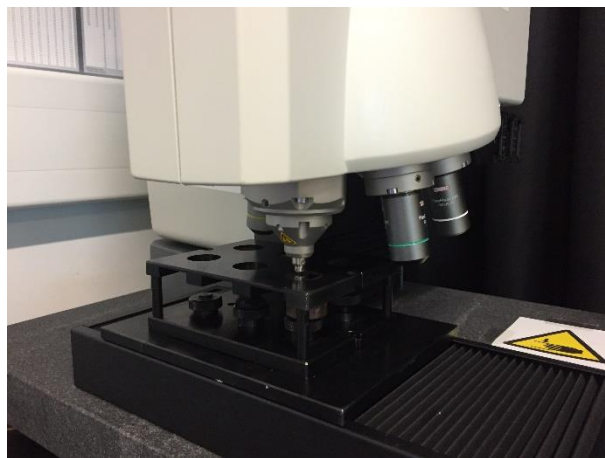


Figure 47 Microhardness tester.

Surface geometry and roughness was analysed using an Alicona Infinite Focus microscope equipped with Alicona measure suite 5.3.1 software, Figure 48. OmniSurf 3D software was used to generate and analyse the 3d visualisation of the sample surface.



Figure 48 Alicona Infinite Focus microscope.

3.4 Results characterisation and analysis

3.4.1 Microstructural analysis in MTEX

A SEM and EBSD detector were used to acquire microstructure maps for analysis of the CP-Ti microstructure. AZtecHKL EBSD software was used for data acquisition and manipulation. After performing the EBSD acquisition, the acquired data was exported as a Common transfer file (CTF) for further analysis in MTEX (a free Matlab toolbox for performing quantitative analysis and modelling of crystallographic textures by means of the EBSD or pole figure data). Matlab R2018b was used to execute the MTEX toolbox. Grain size determination, crystallographic orientation analysis, pole figure generation, grain boundary and misorientation analysis was performed using MTEX. MTEX commands deal with spatial positions and angles typically in reference to crystallographic planes and vectors, also known as Miller indices. Orientations with Euler angles and 3D vectors with Cartesian vectors can also be used to perform this type of analysis. The Miller index defines the orientation of a plane or vector within the crystallographic unit cell. Thus, the Miller index needs the applicable crystal symmetry as input. With pure alpha titanium this is the hexagonal close-packed (HCP) cell. The HCP cell is commonly represented by two equal axes orientated 120° from each other, and a c axis perpendicular to them. Pole figures are stereographic projections used to

display the orientation and distribution of crystallographic lattice planes in any given material.

3.4.2 Finite Element Analysis for Validation

Uniaxial tensile test results were used to validate a material model that was run in Abaqus which is a finite element analysis (FEA) software. Validation concerns how accurately a virtual model can capture the physical behaviour of a real-world scenario (for this research the mechanical properties of an anisotropic CP-Ti grade 2 sheet) with a determinable level of accuracy programmed in. See chapter 5 for the complete description of this process and a discussion on the results, and how these results can be used for further analysis to expand the knowledge base of this research topic.

3.5 Overview of research approach

- Primarily, a modular tooling system has been developed to facilitate the LMD followed by ISF of the LMD tailored material. Design development of the tooling was performed using a PDS to outline major design goals for the system. Manufacture and assembly of each tooling module was outsourced to an independent precision tooling manufacturer. Final assembly of each tooling module was performed on-site at the Advanced Forming Research Centre (AFRC).
- LMD was used to generate material samples and a tailored sheet preform, using a CP-Ti sheet blank supplied by TIMET and CP-Ti powder material supplied by AP&C. LMD was outsourced to a laser specialist. Machine parameters were developed by the LMD specialist and maintained across all LMD trials for this research investigation to ensure consistent results.
- Non-destructive measurement methods, using a GOM Atos scanning system, was used to scan and digitise the formed parts following ISF and the test samples after failure. Polygonisation was conducted to mesh the scanned parts to investigate the thinning evolution.

- A stochastic pattern, in the form of a white background with speckled black dots, was used to compute local surface strains during the uniaxial tensile and Nakajima testing.
- ISF was performed using a DMU 125 5-axis CNC machine on the LMD tailored CP-Ti perform at the AFRC. An existing roller ball tool was used to ensure consistency with respect to previous trials. The programmed toolpath was written in-house using Autodesk Fusion 360 and Vericut was used to ensure no collisions between the roller ball tool, fixture, inner chamber of the CNC machine and fixture occurred during the ISF operation.
- Material preparation and analysis was performed on-site at the AFRC using AFRC-owned equipment. A minimum of three test repeats, when possible, were performed to limit outliers in the results.

Chapter 4

4 Mechanical testing of additively thickened CP-Ti sheet

4.1 Chapter overview

Typically, to form complex components of titanium alloys, elevated temperature forming is required. This is expensive and setup can often be difficult. A potential route for room temperature forming of titanium sheets is Incremental Sheet Forming (ISF). However, sheet thinning during ISF may encourage the early onset of fracture, compromising the part. An additive step prior to ISF has been examined for tailoring a commercially pure titanium (CP-Ti) sheet with additional thickness. This is a potential route to improving ISF with respect to geometric accuracy in formed parts as discussed in section 1.1.1. This chapter documents an experimental trial into the use of Laser Metal Deposition (LMD) for locally thickening a CP-Ti sheet with the goal of generating material samples to analyse the impact of LMD on the properties of CP-Ti. GOM Atos analysis was performed on sheet parts formed by ISF to examine the thinning evolution to inform the location and extent of the additive thickening on the material. Tensile testing with in-situ digital image correlation (DIC) was then used to examine the mechanical behaviour of the LMD tailored material.

4.2 Experimental Procedure

4.2.1 The experimental material

The sheet used to host the LMD layer was an uncoated cold rolled CP-Ti sheet supplied by TIMET with dimensions 1.6 mm x 1 m x 1.6 m (T x W x L) (MatWeb, n.d.). With material properties equivalent to in the ASTM grade 2 CP-Ti standard (TIMET, n.d.). The sheet was cut using a guillotine to 500 mm x 500 mm (W x L). Chemical composition for as received (AR) CP-Ti 50A stock is given in Table 5 (TIMET, n.d.).

Table 5 Chemical composition of CP-Ti50A (TIMET, n.d.).

Constituent elements	Ti	N	C	H	Fe	O
Composition, wt%	Balance	0.03	0.08	0.015	0.30	0.25

According to the TIMET datasheet, the ultimate tensile strength (UTS) of CP-Ti 50A in the AR form is 485 MPa, the yield strength (YS) is 345 MPa and the elongation percentage is 28%, (TIMET, n.d.). Examination of the material using a Scanning Electron Microscope (SEM) showed a microstructure of fine equiaxed grains with an average grain size of 5.4 μm , Figure 49 (a). A true stress vs strain curve of the AR material was generated using uniaxial tensile testing, Figure 49 (b). The material was examined in the sheet rolling direction (RD), transverse to the RD (TD), and 45° to RD (45°), showing anisotropy in the AR CP-Ti50A cold rolled sheet material.

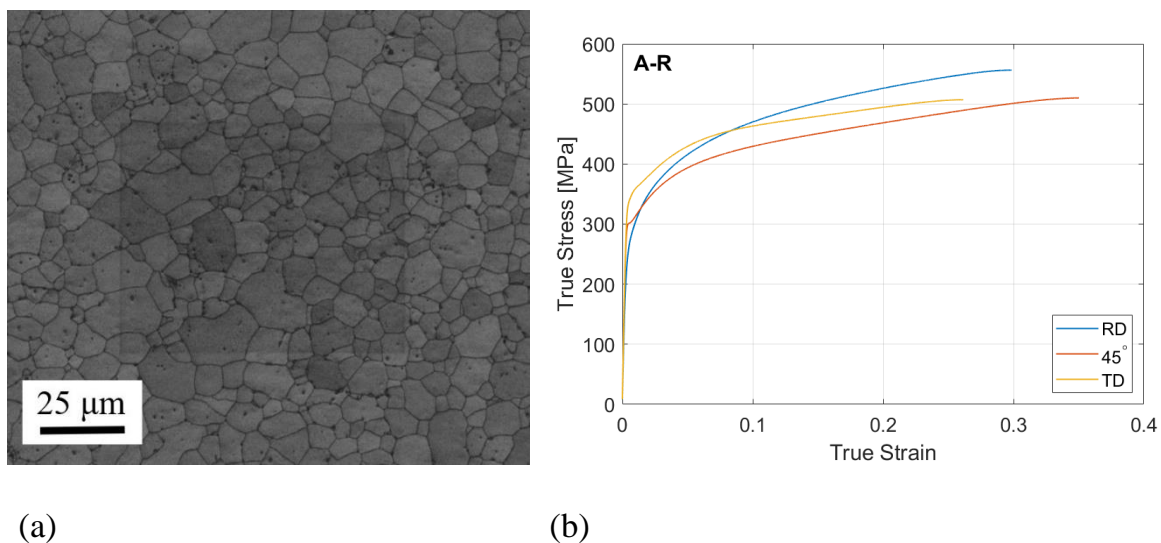


Figure 49 AR CP-Ti material properties: (a) BC map (b) True stress vs strain curves.

The material used for LMD was a CP-Ti grade 2 powder provided by AP&C, Figure 50. It has a particle size distribution of 45 – 150 μm measured by laser diffraction as per ASTM B822. It was gas atomised which ensures a uniform spherical shape for the powder particles. The apparent density of the powder is 2.62 g/cm^3 and oxygen content is 0.16% as listed on the supplier website (Cp-Ti2 | Advanced Powders, n.d.). The

powder was sent directly to the LMD supplier as a batch size of 2.5 kg. The surface of the sheet was cleaned using acetone prior to LMD to ensure the surface condition was high quality, so as to not affect the deposition.

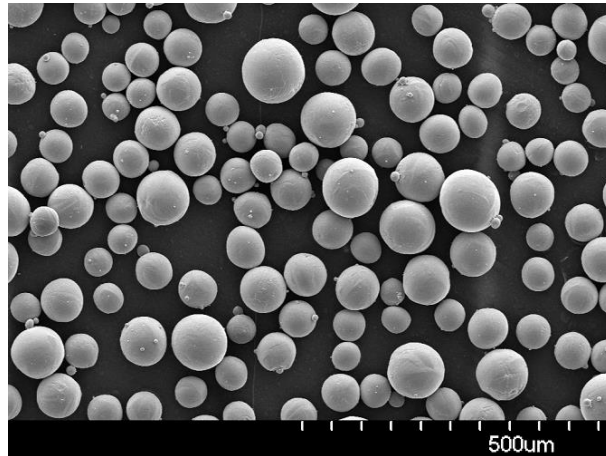


Figure 50 CP-Ti powder (Cp-Ti2 | Advanced Powders, n.d.).

4.2.2 Measuring thickness of CP-Ti ISF formed part

Measuring thickness variation across the formed sheet parts accurately helped define layer thickness (defined by step size), deposit locations, and final thickened sheet thickness morphology. Use of a non-contact blue light 3dimensional (3d) scanning technique was adopted (see section 3.3.1). To begin, a 1.6 mm thick CP-Ti grade 2 sheet part previously formed by ISF was scanned, Figure 51. This sheet was formed by ISF with a back support die. The final part geometry was a dome made of four separate flat angled wall sections angled at 20°, 40°, 60° and 80° to the sheet plane. The AR CP-Ti sheet formed by ISF originally fractured during forming of the wall section at 80° to the sheet plane.

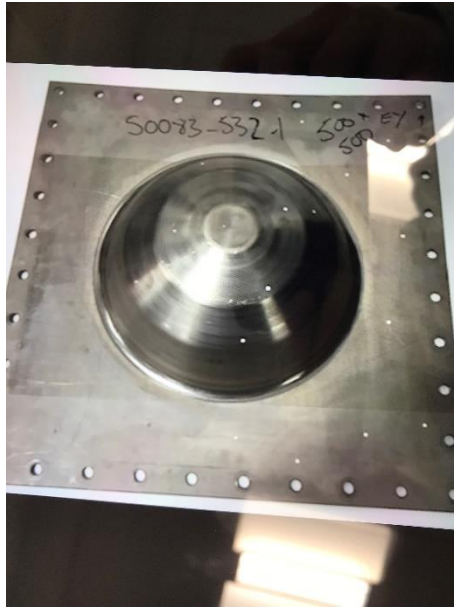


Figure 51 ISF formed titanium part.

GOM ATOS[®] software was used to generate a 3d representation of a section of the part. Prior to the scanning process the material sample was cleaned thoroughly in acetone and sprayed with Adrox 9D1B to minimise light reflection on the material surface. The thickness of the spray coating added approximately 0.05 mm to the thickness measurements. This was considered in the thickness calculations. The sample was clamped on a circular turning table for the scanning process. Reference markers were attached to the sample to ensure full scanning of the material sample. The uniformity of the sprayed layer was verified in the scanning software. The scans were meshed using the GOM Atos software and exported to PAM-STAMP, Figure 52. This mesh was used to generate a part in PAM-STAMP and the thickness change between the top and lower surfaces of the scan was measured, Table 6.

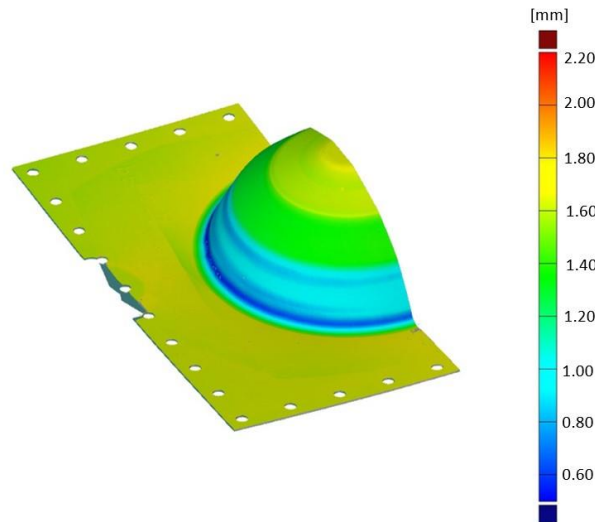


Figure 52 PAM-STAMP thickness measurement.

Table 6 Thickness measurements.

Region	Thickness (mm) \pm 20-40	Standard deviation	Thinning (mm)
$\theta = 0^\circ$	1.60	0.00	N/A
$\theta = 20^\circ$	1.57	0.02	0.03
$\theta = 40^\circ$	1.28	0.03	0.32
$\theta = 60^\circ$	0.84	0.06	0.76
$\theta = 80^\circ$	0.61	0.03	0.99

4.2.3 Deposit and tensile specimen design

Using the measurements from the scanned cut part as reference, a LMD tailored ISF preform sheet was designed with locations assigned for additional material thickening by LMD, Figure 53. The thickening was done with the same material as the AR CP-Ti grade 2 sheet to generate a sheet preform with variable thickness but a singular material alloy. Another reason for selecting the same material as the substrate is to ensure the results clearly represent the impact added thickness has on the thinning during ISF.

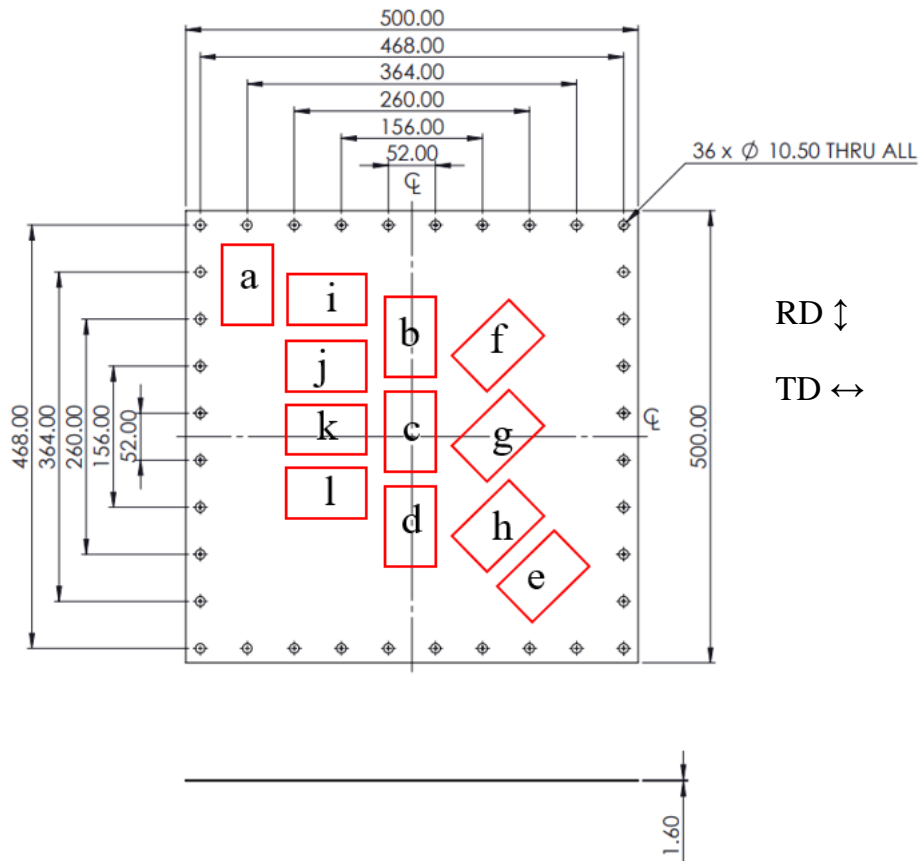


Figure 53 LMD material locations and areas proposed for AR specimen extraction

Designing the sheet with nine LMD deposit locations made it possible to investigate the influence of the LMD build height and orientation on the material's mechanical properties, A further three locations were designated for extraction of AR material specimens.

Table 7. A further three locations were designated for extraction of AR material specimens.

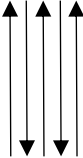
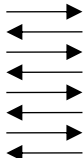
Table 7 Pad location, orientation, and LMD deposit thickness.

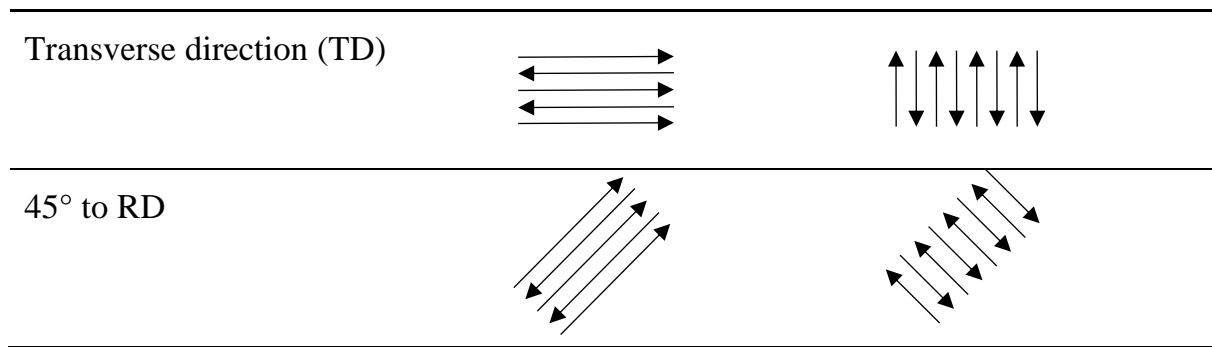
Material Location	Orientation	LMD thickness (mm)
Set a	RD	0
Set b	RD	0.3

Set c	RD	0.6
Set d	RD	0.9
Set e	45° to RD	0
Set f	45° to RD	0.3
Set g	45° to RD	0.6
Set h	45° to RD	0.9
Set i	TD	0
Set j	TD	0.3
Set k	TD	0.6
Set j	TD	0.9

Each deposit measured 111 mm × 71 mm (L × W). Three deposits were orientated with their length parallel to the sheet rolling direction (RD), three at 45° to the RD (45° to RD) and three at 90°, or transverse, to the RD (TD). From each deposit three tensile specimens were extracted. The added thickness in the build direction was achieved by stacking 0.15 mm thick layers of material in a crosshatch pattern. The deposit scan pattern and starting direction is provided in Table 8.

Table 8 Deposit layer patterns and directions

Orientation	Even number layer	Odd number layer
Rolling direction (RD)		



Each pad was designed to the correct dimensions to ensure three tensile specimens could be extracted by wire-EDM with their gauge lengths in-line with the LMD pad length, Figure 54. The tensile specimen gauge length orientation determined its orientation in relation to the sheet RD.

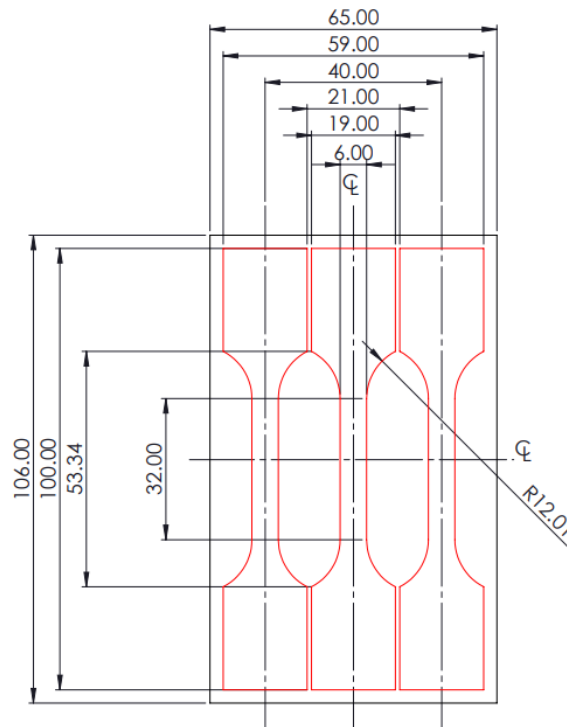


Figure 54 Tensile specimen size and location within LMD pad.

4.2.4 Laser Metal Deposition for material testing

LMD was performed by a commercial supplier using a TRUMPF 2 kW TruDisk Laser and Oerlikon Metco Twin-10-C powder feeder. The laser and powder feed movement were provided with a 5-axis REIS RL80 Gantry Manipulation System with a 3 m x 2.25

m x 1.5 m work envelope. The fixture and sheet assembly were mounted to a T-slot table which rotated around its central axis to position the sheet during LMD, Figure 55.



Figure 55 LMD machine setup.

4.2.5 Post-processing of LMD material

X-ray diffraction (XRD) was performed to measure the residual stress remaining after LMD using a Proto LXR2000 X-Ray stress diffractometer. The results are provided in Table 9.

Table 9 XRD residual stress measurements.

Material location	Measurement direction	Measured stress (MPa)
Set b	TD	137 ± 6.07
	RD	27 ± 3.97
Set c	TD	93 ± 5.25
	RD	75 ± 5.78
Set d	TD	133 ± 5.45

	RD	55 ± 4.51
Set j	TD	-32 ± 6.21
	RD	0 ± 5.13
Set k	TD	51 ± 5.78
	RD	77 ± 5.47
Set l	TD	168 ± 6.69
	RD	10 ± 4.55

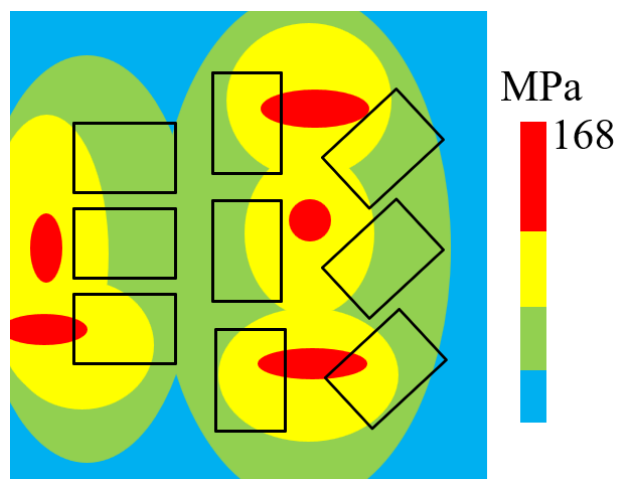
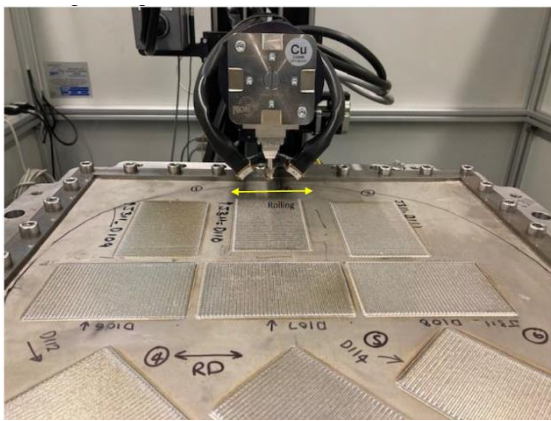


Figure 56 Colour map of known residual stress distribution from XRD results.

A maximum residual stress of 168 ± 6.69 MPa was measured in the TD at a location close to one of the LMD pads which was close to half of the 345 MPa YS of the CP-Ti substrate sheet. Comparably high stresses were measured close to the other LMD deposits. Lower stress was measured in the RD close to the deposit with a maximum stress measurement of 77 ± 5.47 , roughly a fifth of the AR CP-Ti YS. The colour map shows that when there are two neighbouring pads side by side, the stresses indicate the sheet is almost being stretched in the direction of the pads. However, the stress is spread more uniformly in areas of sheet with deposited material at all sides, as if the stress is

balanced. There is a definite difference between the stress measurements in the x and y directions. The first direction of the laser was always along the length which may have influenced this. It was determined that a stress close to half the YS may result in springback of the sheet when releasing the blank holder constraints at the sheet edges. Any sheet distortion will make cutting of the sheet difficult and potentially damage the LMD deposited material. As a precautionary step, a stress relief heat treatment was performed on the tailored blank in a Carbolite LCF furnace, Figure 58.



(a)

(b)

Figure 57 Post-processing equipment: (a) XRD machine; (b) Furnace.

The stress relief heat treatment process is described in Figure 58. To begin, the furnace temperature was raised to 400°C. On reaching 400°C the furnace was purged with argon gas to limit oxidation. The temperature was further raised to 600°C and held at this temperature for 1 hour. The temperature was dropped gradually to 400°C at which point the gas flow was stopped. The temperature of the furnace was lowered at a constant rate for 3-4 hours until the furnace temperature reached 150°C at which point the furnace door was opened and the assembly was left overnight to air cool.

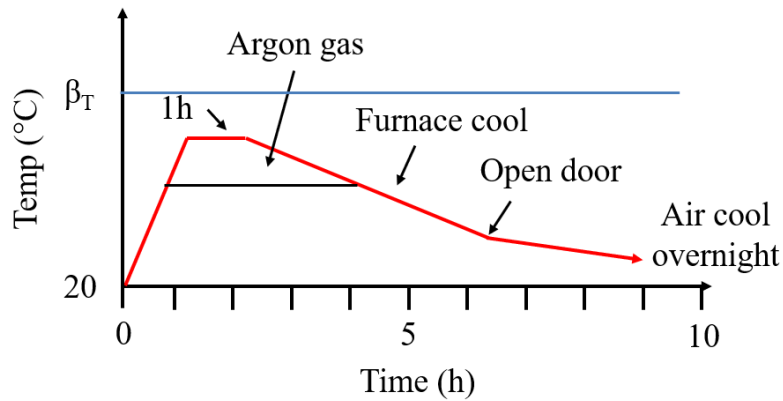


Figure 58 Stress relief annealing process.

A blue oxide layer was observed on the LMD thickened material after the heat treatment signifying shallow penetration of the oxide layer on the material surface, Figure 58. This is likely caused as the Carbolite furnace used to perform the stress relief heat treatment at 600°C is not capable of creating a complete vacuum, meaning minor levels of oxidation were unavoidable. This blue layer indicates the formation of TiO_2 . This is often the case when heat treating CP-Ti in air (unfortunately a result of the incomplete vacuum inside the Carbolite furnace). Despite this, the TiO_2 layer created at temperatures of 600°C is thin and unlikely to have a significant impact on the sheets mechanical properties (T. Chen et al., 2021). Another concern is the cleanliness of the furnace, as furnaces need regular burn out cycles, otherwise particles and other leftover material may stick to the part.



Figure 59 Blue oxide surface following heat treatment.

4.2.6 Tensile specimen geometry

Tensile specimens were extracted by wire electrical discharge machining (Wire-EDM) using an AgieCharmilles CUT 400 Sp machine. The specimens were designed with a gauge length of 20 mm, width of 6 mm and thickness of 1.6 mm plus the added thickness via LMD. The specimens were originally designed to have a gauge length of 25 mm however the DIC setup did not allow a 25 mm extensometer to be installed for displacement measurements, hence a gauge of 20 mm was used and factored into the analysis. A speckle pattern was sprayed on the surface of the tensile specimens for DIC analysis to track surface displacement and generate a strain map. Selected specimens had the speckle pattern applied to the LMD deposit surface and for other specimens the pattern was applied to the opposite side.

4.2.7 Uniaxial tensile testing with in-situ DIC analysis

A 150kN Zwick/Roell Z150 load cell tensile testing machine was used to perform room temperature (23°C) uniaxial tensile tests with in-situ DIC. The test ended at specimen failure. Twelve sets of tensile specimens taken from the LMD tailored blank were tested, each with different configurations of the testing variables (LMD build height and orientation with respect to sheet RD). For each variable set three specimens were used

for test repeats to validate the results. In total, 36 tensile tests were performed. A two-camera setup captured in-situ tensile strain data and strain maps were made across the specimen surfaces.

4.2.8 Fractography

Examination of the fracture face of the tensile specimens was performed using a Quanta FEG 250 scanning electron microscope (SEM) via acquisition of secondary electron images. This technique is known as fractography. The fractography samples were taken from the fracture face of the tensile specimens. The specimens were cut along the gauge length, cleaned thoroughly with acetone, and mounted on a flat platform using adhesive. The edge was coated with a conductive silver suspension, Figure 60. The fracture zone of interest was positioned to face towards the lens within the SEM. High magnifications were used to examine the fracture site. Relevant findings were noted with respect to interesting morphology in the fracture face to better understand the propagation and spread of fracture at specimen failure.

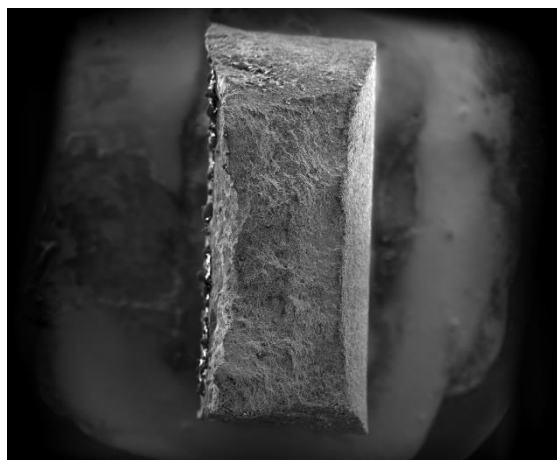
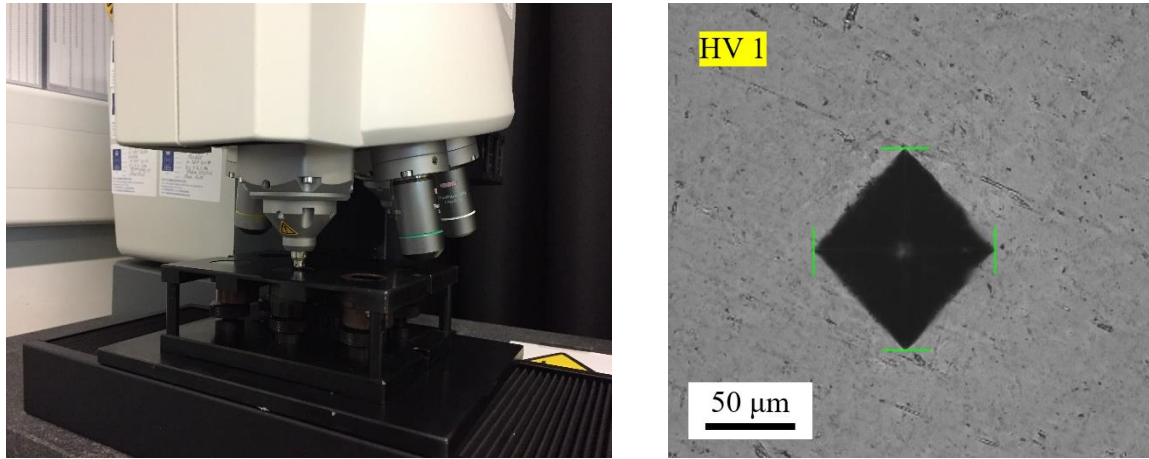


Figure 60 Example of fracture face for fractography.

4.2.9 Microhardness testing

Vickers microhardness measurements were taken using a Vickers-Knoop Micro Hardness tester using a load of 1kg (HV1) and a loading time of 15s. A test indentation was made to help select these settings, Figure 61 (b). For the hardness test a pyramidal diamond indenter was pressed into the material surface, Figure 61 (a). The diameters of

the diamond indent were measured to calculate the Vickers hardness value, Figure 61 (b). Only one indent is shown however a trace was measured along the gauge length of each specimen.



(a)

(b)

Figure 61 Microhardness testing: (a) Machine; (b) Measuring diagonals.

4.3 Results

4.3.1 Mechanical response to LMD tailoring

Room temperature uniaxial tensile testing was performed. The tensile test for each variable combination was repeated three times and averaged. The yield stress (YS), ultimate tensile stress (UTS) and % elongation (E) to 4D was calculated for each specimen, Figure 62 and Figure 63. The AR specimen exhibited anisotropic tensile behaviour with a higher UTS and E in the RD than the specimen at 45° to RD. This anisotropy deformation behaviour is a direct response to the pronounced texture and limited number of slip systems in hexagonally close-packed (HCP) materials such as CP-Ti (Yi et al., 2016). In contrast to the anisotropy of the AR material, the tensile specimens taken from the LMD part exhibited isotropic mechanical behaviour. This is an interesting result which suggests a major change within the material occurred in response to the LMD deposit. Potentially a partial or complete replacement of the cold rolled texture by a new material with a weak or completely random texture component, which would explain the lack of mechanical anisotropy in the tailored material.

Additionally, the LMD layup direction may have been somewhat responsible for the materials newfound isotropic nature. For each specimen, regardless of its orientation to the substrate RD, the even numbered layers were deposited along its length and the corresponding odd numbered layers were printed perpendicular to this, see Table 8. Keeping this consistent across all LMD tailored specimens likely weakened any directionality present in the untransformed CP-Ti sheet mechanical properties. In the RD the LMD had reduced strength and ductility with more abrupt hardening suggesting increased brittleness compared to the AR specimens. The results showed a 2.4% - 5.6% increase in the YS, 4% - 6% reduction in E, and a 6.2% - 9.9% decrease in the UTS compared to the AR material. At 45° to the RD the LMD material exhibited a 5.2% - 9.9% increase in the YS, 11% - 14% reduction in E indicating lower ductility, and similar UTS values of a range 0% - 4.6% higher than the AR material. In the TD there was little change in the mechanical behaviour of the LMD tailored material compared to the AR material with a 1.1% - 2.7% decrease in the YP, 3% - 6% decrease in the E, and a 3.5% - 5.3% decrease in UTS values. Elongation measurements were calculated using a 20 mm extensometer.

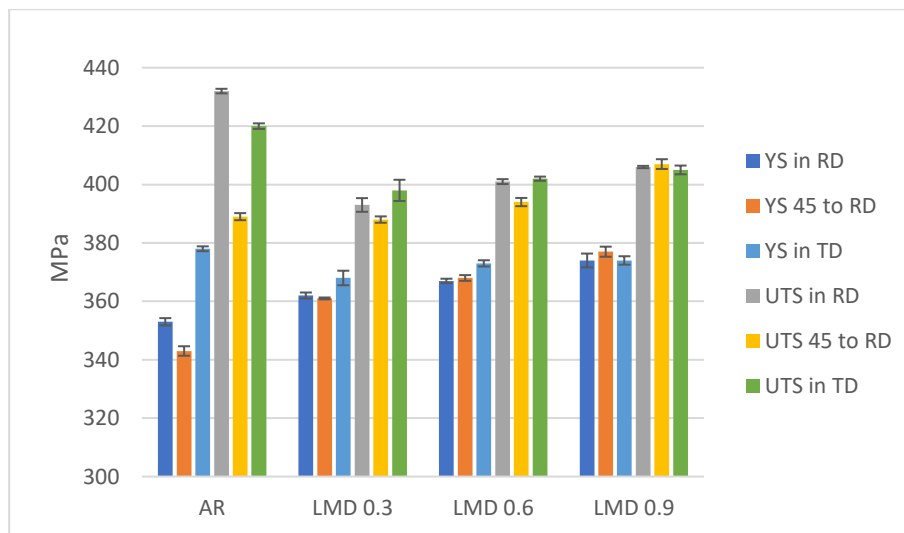


Figure 62 Yield stress and ultimate tensile strength.

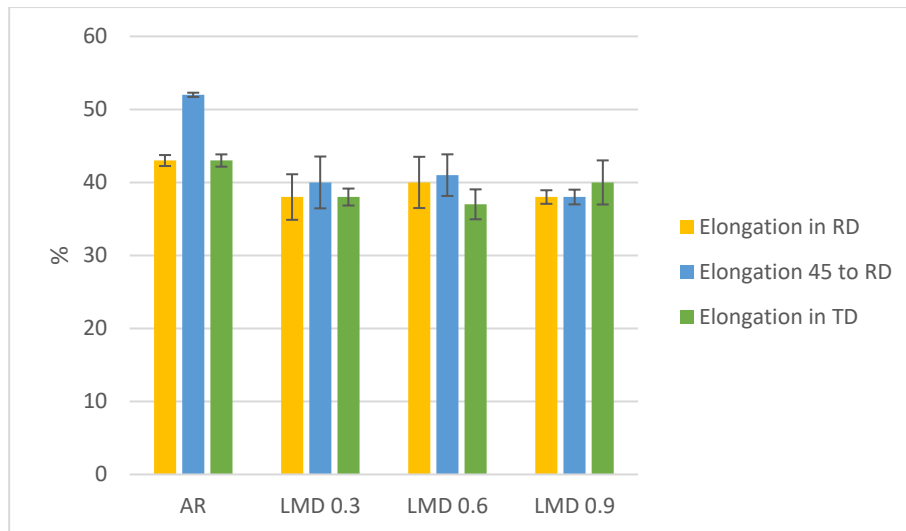


Figure 63 Elongation (%) at break.

The results indicate that LMD thickening reduces elongation and formability in the CP-Ti sheet, see Figures Figure 64 to Figure 66. A larger decrease in ductility was seen in the RD and 45° to RD directions. A noteworthy observation is the lack of influence the number of LMD deposited layers had on the strength properties of the thickened material. The results suggest that the thermal input of the laser changed the materials microstructure through its full thickness which would correlate with the previous discussion on the materials newfound isotropy. Additionally, as the mechanical behaviour is consistent for all deposit thicknesses it would suggest the material development was most likely in direct response to the first laser pass. As such, the major change in the crystallographic microstructure likely occurred at the initial introduction of the LMD material and remained constant despite the deposition of additional layers atop the previous ones. The consistent tensile results indicate there are unlikely to be significant defects, such as pores, in the added LMD material. The LMD thickened material performed well which indicates that LMD is a potential route for tailoring preforms with added thickness to improve thickness homogeneity following room temperature ISF. In summary, the isotropic nature of the LMD tailored material and lack of influence of the LMD build height ensure that anisotropy and geometry are less relevant when designing LMD tailored ISF preforms.

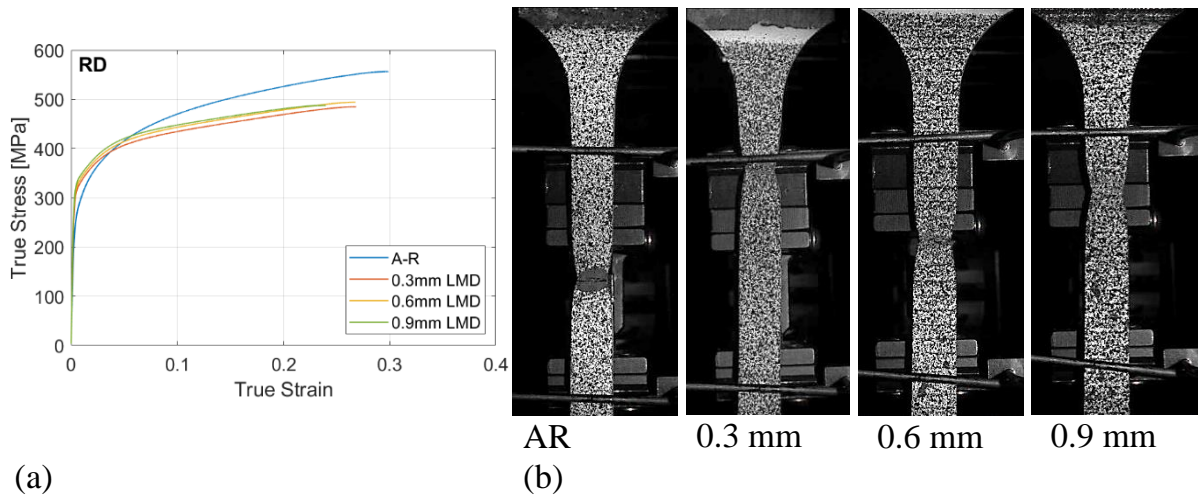


Figure 64 Tensile test results in RD: (a) True stress vs strain; (b) Fractured specimens.

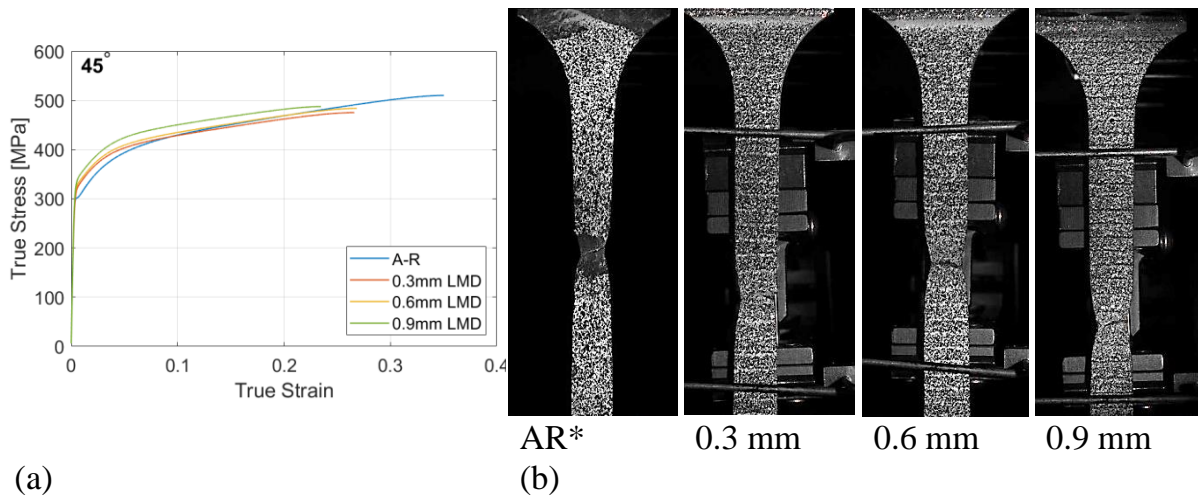


Figure 65 Tensile test results in 45°: (a) True stress vs strain; (b) Fractured specimens.

The extensometer was removed due to the amount of elongation in the AR specimen at 45° to RD and the plot was calculated off the crosshead displacement, Figure 65.

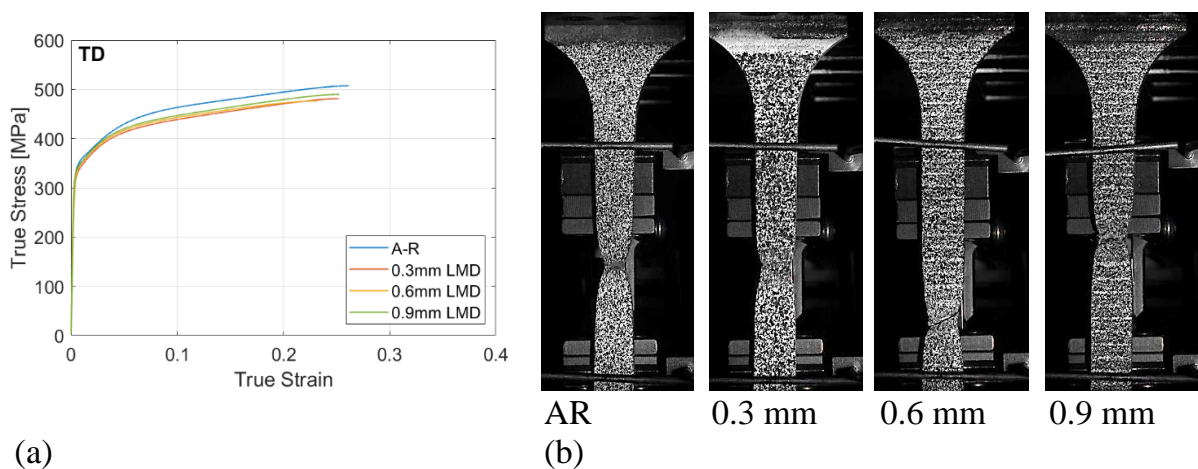


Figure 66 Tensile test results in TD: (a) True stress vs strain; (b) Fractured specimens.

4.3.2 Strain analysis of LMD material

An optical non-contact measurement technique known as digital image correlation (DIC) was used to show effective strain displacement in the plastic region of the tensile specimens during tensile deformation. At 90% (localised) extension in the AR RD sample, strain was seen to concentrate near the gauge centre and localised necking was observed followed by diffused necking and reduction of the gauge width before failure, Figure 67 (a). High strain localisation was seen to initiate at the edge of each sample before failure at the area of crack nucleation and eventual fracture growth across the gauge. The DIC results indicate the necking morphology changed in response to the LMD layer. With the specimens from the LMD part, strain localised in a smaller area during necking and eventual fracture, Figure 67 (b-d). The AR specimen had a diffused neck of 10 mm and localised neck of 5 mm at 90% extension. The LMD tailored specimens in the RD had diffused necks of 5 mm and localised necks of 1 - 1.5 mm at approximately 90% extension. Strain was seen to localise in the direction of the LMD tracks compared to the homogeneous strain distribution across the surface of the AR specimen. Similar strain behaviour was observed for all TD and 45° samples, Figure 68 and Figure 69. This suggests the surface morphology from the LMD tracks influenced strain distribution. The LMD tailored specimens exhibited lower elongation and earlier fracture nucleation and failure compared to the AR specimens as indicated by the true stress vs strain curves. This is likely a result of cracks nucleating from defects in the uneven LMD surface, causing necking to begin at lower strain compared to the AR material.

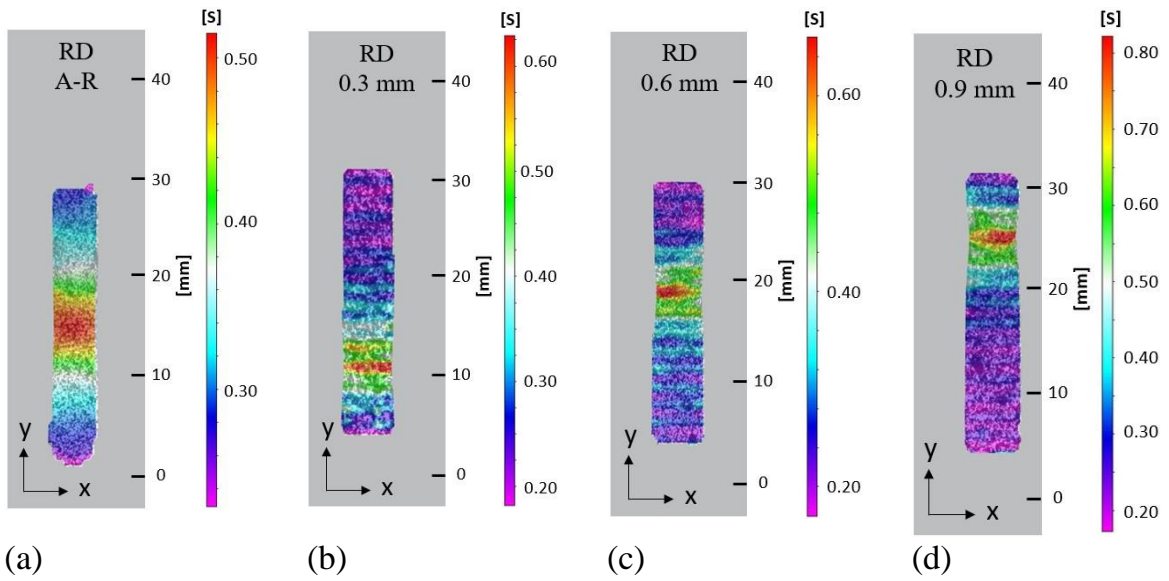


Figure 67 Effective surface strain at 90% extension for RD: (a) AR; (b) 0.3 mm LMD; (c) 0.6 mm LMD; (d) 0.9 mm LMD.

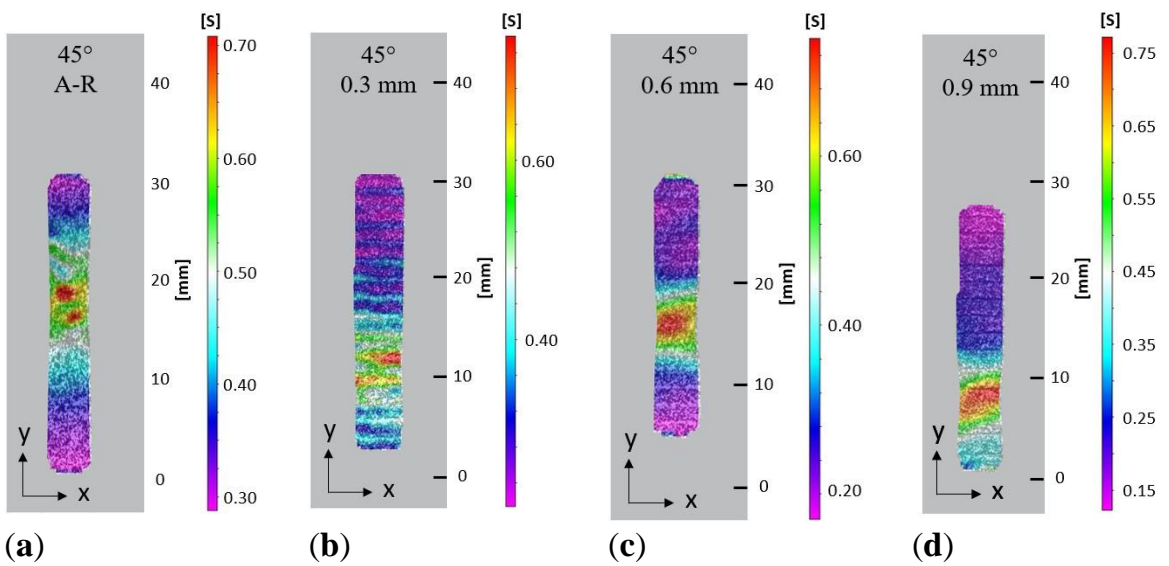


Figure 68 Effective surface strain at 90% extension for 45° (a) AR; (b) 0.3 mm LMD; (c) 0.6 mm LMD; (d) 0.9 mm LMD.

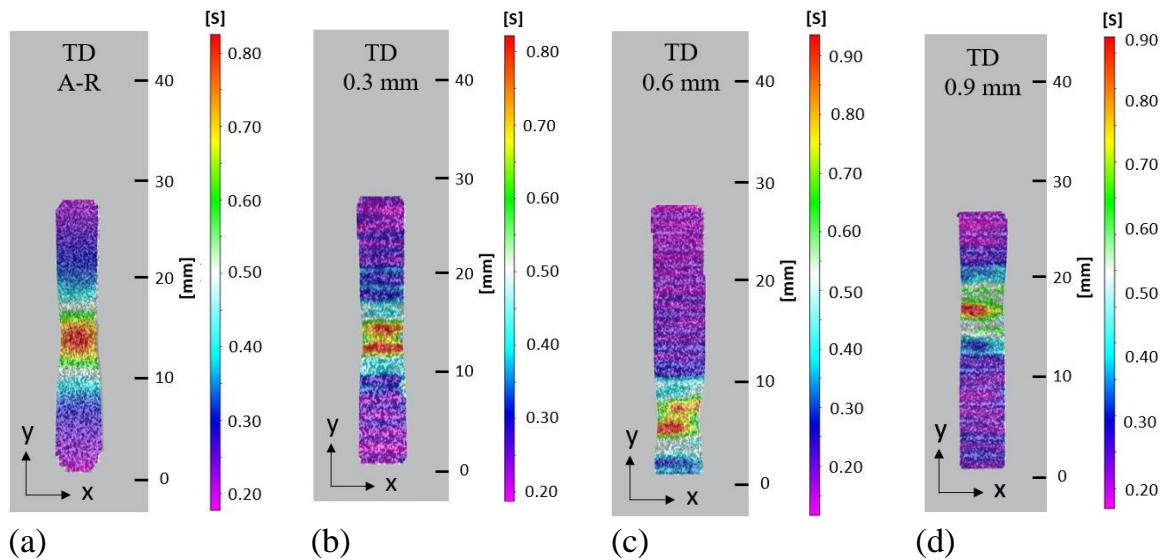


Figure 69 Effective surface strain at 90% extension for TD: (a) AR; (b) 0.3 mm LMD; (c) 0.6 mm LMD; (d) 0.9 mm LMD.

A speckle pattern was sprayed on the reverse side of selected specimens to compare the strain distribution on the LMD surface (front) to the reverse side with no LMD (back). At 90% extension the diffused neck measured 5 mm on both the front and back of the RD and TD specimens with 0.9 mm added LMD material, Figure 70. Despite the same diffused necking, high strain in response to localised necking was localised to an area of 1 - 2 mm across the front and 3 - 4 mm on the back for the RD and TD specimens. This indicates surface morphology likely impacted surface strain distribution. Higher surface strain at 90% extension occurred on the front compared to the back, with 0.80 and 0.90 strain values for front RD and TD specimens respectively, compared to 0.72 and 0.675 strain values for the back of the RD and TD specimens, respectively. It is thought this is happening because the lower ductility of the LMD material makes it less resistant to plastic deformation, resulting in quicker degradation of the material in response to the tensile forces. Eventually resulting in crack propagation and fracture starting first on the LMD side, and propagating through the thickness until eventual full cleavage of the tensile specimen.

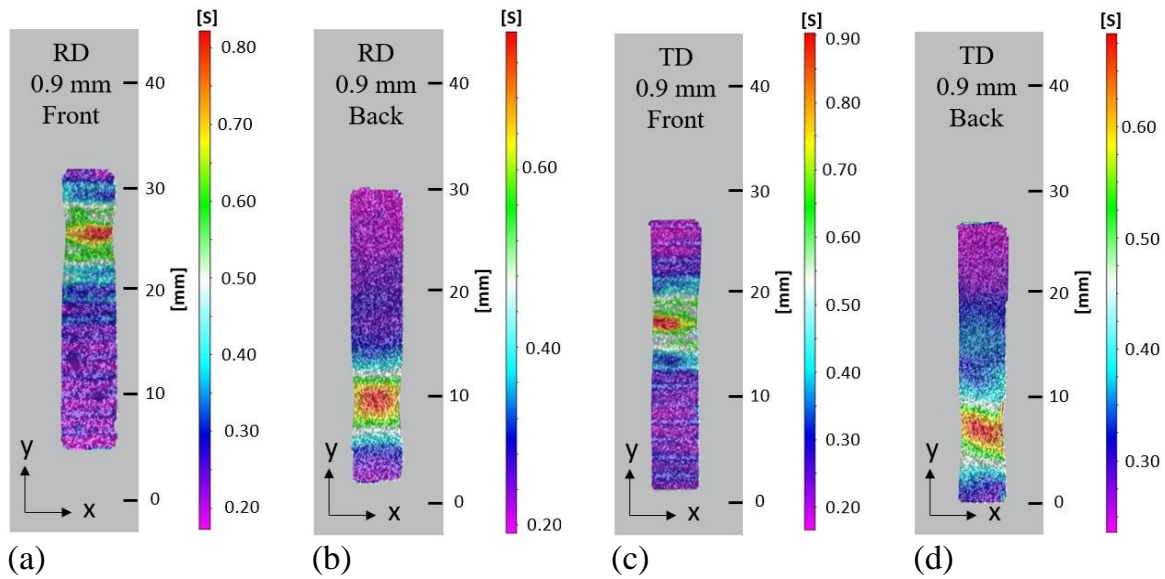


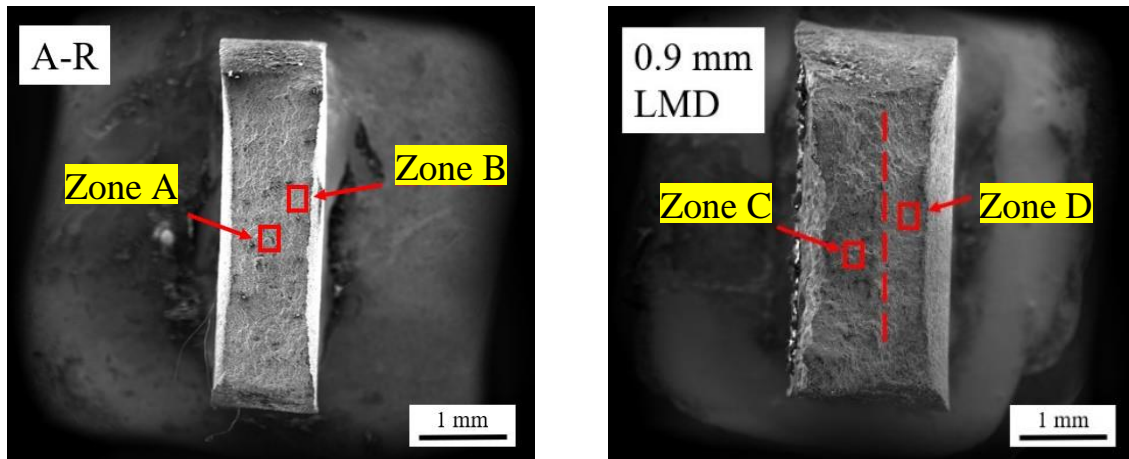
Figure 70 Effective surface strain at 90% extension on opposing sides (a) RD 0.9mm LMD side; (b) RD 0.9 mm substrate side; (c) TD 0.9 mm LMD side; (d) TD 0.9 mm substrate side.

It proved difficult to determine from the DIC imagery if the strain propagated on or between the LMD grooves. It is recommended for future work to confirm which is correct, and to determine if the increased strain was solely a material effect or a by-product of the measurement technique. It should be noted that a fair tensile test should have all specimen surface finishes equal. However, the testing was performed as described to further understand the strain behaviour of the as-printed deposit. From this, the results may be used to develop optimal process which could include a surface finishing step.

4.3.3 Fracture behaviour during tensile deformation

Fractography was performed using the FEI Quanta 250 FEG SEM at high magnification to help understand the fracture mechanics in the tailored material in response to uniaxial tensile forces. Analyses were performed on the fracture face of extracted samples taken from the failure location in each specimen gauge lengths orientated in the sheet RD. Fractography was first performed on the AR tensile specimen fracture face, Figure 71 (a), followed by the sample with 0.9 mm LMD added thickness, Figure 71 (b). From the low magnification images, it is difficult to pin-point the exact fracture location. It is

however evident from the morphology of the fracture face that the substrate stretched beyond the LMD deposit indicating greater elongation in the material zone, and so exhibiting properties similar to the AR CP-Ti base material.

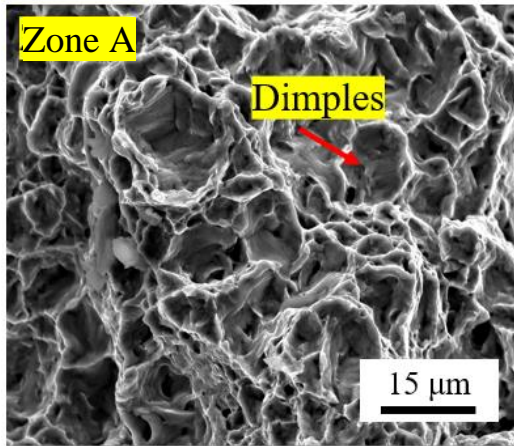


(a)

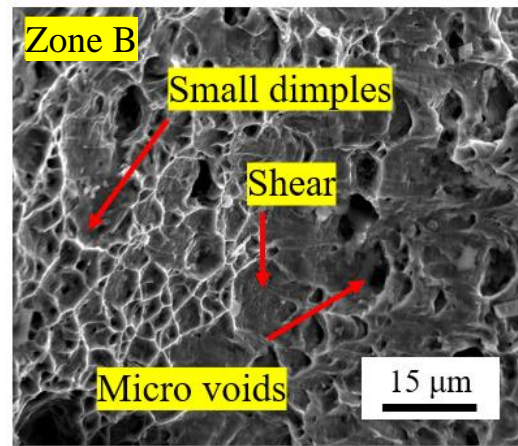
(b)

Figure 71 Fractography sample surfaces: (a) AR material; (b) LMD layer.

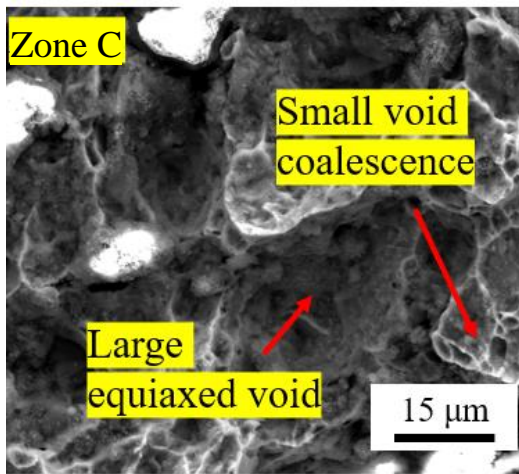
High magnification images were taken to analyse the fracture surfaces in greater detail, Figure 72. The centre of the fracture face on the AR sample (Zone A) had a fine dimple texture accompanied by microscopic voids typical of ductile fracture. The edge of the AR sample (Zone B) had small dimples, micro-voids, and evidence of shear. The LMD surface (Zone C) and non-transformed substrate material (Zone D) both had distinct fracture morphologies. No delamination of the LMD material was evident with good bonding across the interface region of Zone C and Zone D. Within Zone C there were large equiaxed voids with groups of coalesced microscopic voids at their base.



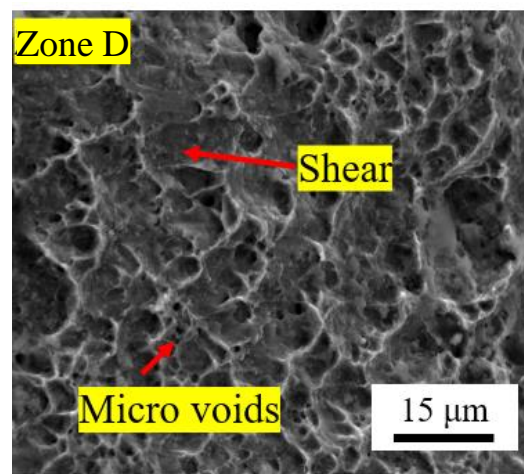
(a)



(b)



(c)



(d)

Figure 72 Fractography analysis: (a) Zone A AR; (b) Zone B AR; (c) Zone C LMD; (d) Zone D LMD.

Typically, the ductile fracture mechanism is preceded by substantial plastic deformation and includes the growth and coalescence of microscopic voids. Zone D had similar fracture morphology as Zone B in the AR specimen, showing micro-voids propagating in the direction of the stress axis and visible surface shear, suggesting the microstructure in Zone D was not altered significantly by LMD. However, the mechanical performance of the LMD material counters this. It may suggest that there is no overheating of the base substrate material and the AR microstructure and mechanical properties are somewhat preserved. Alternatively, it could suggest that the laser heat input has not fully transformed the AR microstructure so it continues to behave in a ductile manner.

4.3.4 Microhardness measurements

Vickers hardness testing of the AR and LMD part was performed on the LMD side of the samples, Figure 73. For the in-plane measurements an average depth of 280 μm was removed by grinding to measure the microhardness of the added LMD layer. The hardness results for the AR material were highly repeatable with a mean of 153 ± 3 HV. The hardness results for the tailored materials exhibited more scattering than the AR material. It is possible this was caused by inhomogeneous grain sizes resulting from abnormal grain growth (AGG) in the tailored material (Yamanaka et al., 2019a). The mean hardness values for the tailored materials were in the range of 159 – 166 HV with significant overlap of the standard deviation error bars showing the difference was not statistically significant, Figure 73 (a). This indicated the hardness was consistent across the tailored material despite the difference in LMD build thickness. Microhardness measurements were taken along the gauge length of the fractured tensile samples, from the top grip region towards the fracture site. A rise in microhardness across the gauge to approximately 173-182 HV was observed across all material samples, Figure 73 (b). A concern is the inhomogeneous grain size of the LMD material affecting the microhardness results. This concern should be acknowledged for future work.

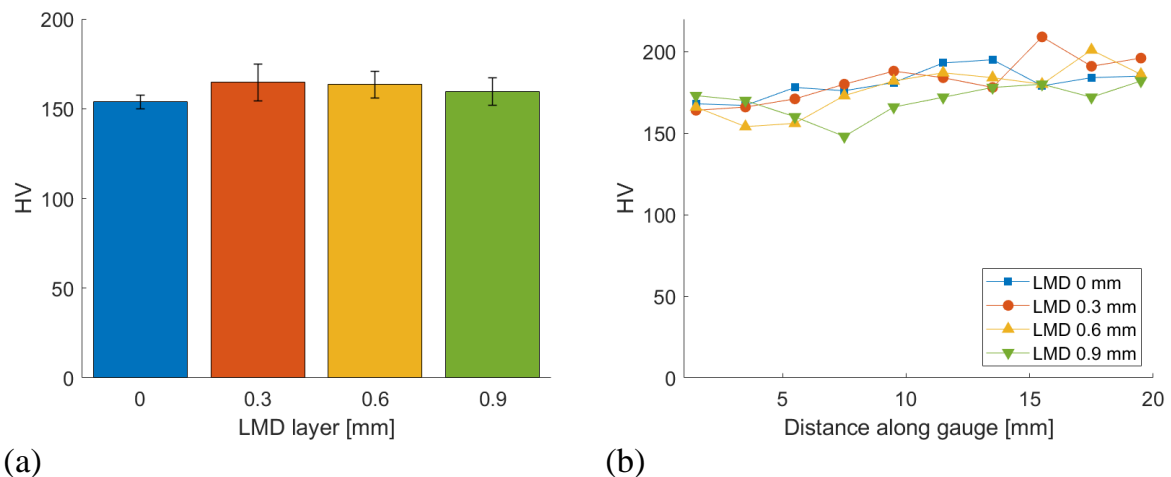


Figure 73 Vickers hardness results: (a) LMD surface; (b) Along gauge.

4.4 Summary

Mechanical response has indicated a major change occurred in the material in response to the LMD step. It is expected that the heat input from the laser and melted material deposits transformed the texture component of the original AR material resulting in the newly isotropic mechanical properties of the tailored sheet. Investigation of the microstructure is required to showcase this and link it to the altered mechanical behaviour of the sheet following LMD. The formability of the material with the LMD thickening is lower than the AR material. Mechanical behaviour is consistent for all specimens with the level of thickening having little to no effect, which suggests the first laser pass may have fully transformed the material across its full thickness. As such, it is possible the subsequent laser passes and cyclic temperature flux had mitigating effect on the final output material. However, the ductile fracture behaviour on the non-transformed side of the tailored specimens suggests the base material maintained some of the properties of the base material. It is necessary now to perform material characterisation of the tailored material to investigate the microstructural development, and link this with the results of the mechanical testing from this chapter. In summary, with respect to the experimental results the following conclusions were made:

- Isotropic material properties were observed in the LMD tailored blank material. This contrasted with the anisotropy of the AR CP-Ti parent material. The LMD added thickness was seen to reduce the ductility and formability of CP-Ti sheet.
- The LMD build height appeared to have little influence on the strength. As such, an ISF preform with the LMD tailored blank may be designed without significant consideration of its directionality or the thickness added via LMD.
- In-situ DIC analysis performed during tensile testing showed the LMD surface morphology impacted the effective strain distribution across the sample surfaces, with surface strain propagating in the direction of the LMD builds. This differed from the homogeneous strain distribution across the AR specimens.

- Fractography was used to determine the resulting fracture behaviour within the failed gauge section of the tensile specimens. A fine dimple texture accompanied by microscopic voids, typical of ductile fracture, was observed in the AR sample.
- Ductile fracture behaviour was observed at the substrate side of the LMD thickened material sample. Analysis of the LMD side showed a population of dimples and fine microscopic cracks accompanied by large equiaxed voids with internal coalesced microscopic voids. 3d scanning of the fracture face is recommended for future work to better understand the fracture mechanism.
- AGG occurs when CP-Ti is exposed to a focused heat source during additive manufacturing (Yamanaka et al., 2019b).
- No delamination was observed between the LMD layer and substrate material which indicated good bonding.
- Microhardness values were seen to be statistically equal despite the LMD added material.

5 Finite element analysis of a uniaxial tensile test

5.1 Chapter overview

5.1.1 Introduction

Finite element analysis (FEA) is a numerical tool used to solve complex engineering problems in the fields of structural analysis, heat transfer, and fluid flow amongst others. In engineering problems there are basic unknowns, and in the case of solid mechanics these unknowns are typically displacements. By dividing the solution into small parts (finite elements) the unknowns can be expressed in terms of assumed approximating functions. Within each element there are nodal points thus, in solid mechanics, displacement of the nodes is used to express the field unknowns which are then calculated using interpolation functions. The force vs displacement (stiffness characteristic) of each individual element is calculated and used to assemble global properties. Boundary conditions are imposed and the solutions of the simultaneous equations gives the nodal unknowns, which are used to find stresses, strains, and moments in solid mechanics problems (Pidaparti, 2017). FEA is an incredibly valuable tool and is of direct importance to this investigation as it can allow for testing to be performed on non-physical systems. This can significantly reduce the cost and time of experimental research. An accurate model of the uniaxial tensile test was designed and verified using the experimentally developed stress vs strain curve from the previously performed room temperature uniaxial tensile test, section 4.2.7. This chapter documents the process of modelling this and presents the verified results. The purpose of creating the FE model of the uniaxial tensile test setup is to develop material properties for the AR CP-Ti anisotropic material. The original goal was to generate a material model for the LMD tailored material also, and model the ISF operation using both the AR and tailored material properties. However, this was not achievable due to time constraints and has been suggested for future investigations. This chapter details the process of modelling the room temperature tensile test of the as received (AR) CP-Ti material and presenting the results.

5.1.2 Aim and Objectives

Aim: Verify material properties for CP-Ti material using FEA method.

Objectives:

1. Develop material model for CP-Ti material.
2. Perform uniaxial tensile test in modelling environment.
3. Verify results against known material properties from lab-based tensile test.

5.2 Experimental approach

5.2.1 Non-linear simulation

Physical nonlinearity is being modelled for the uniaxial tensile test. This is because during tensile deformation the specimen experiences plastic flow. Plastic flow is when permanent deformation occurs beyond a limiting stress known as the yield stress (YS) (Wriggers, 2014). In physical nonlinearity the stiffness of the structure changes as it deforms. This is calculated by breaking the simulation into time increments which are updated incrementally. In an implicit analysis, equilibrium is sought between applied external force and internal reaction force after each increment. Equilibrium is when net force acting on the body and at all nodes is zero. The increment size is determined by the FE software. Having the time increments small makes it possible to achieve an accurate solution to the nonlinear finite element equations but if the increments are too small the analysis will require significant processing power and time to complete.

5.2.2 Pre-processing – Part geometry and meshing

The model of the physical problem was graphically realised in the Abaqus/CAE 3dimensional (3d) modelling space. The part was embedded in an XYZ cartesian coordinate system. The geometry of the tensile specimen used in the experimental investigation was first sketched with the gauge length in the y-direction and thickness in the x-direction. Idealisation of the geometry helped to reduce both the model and mesh complexity. To decide on the method of idealisation it was necessary to consider both the geometry and operation of the lab-based testing, Figure 74. Both grip sections

of the tensile specimen were fixed by the machine grips throughout. The top grip moved positively in the y-direction which deformed the specimen. A compression force from the grips in the direction of the red arrows, Figure 74, held the specimen grip sections to stop the specimen from slipping during the test. This compression force was deemed negligible as the assumption is made that the material in the grip section at each end returns to its original shape after the grip forces are released and has no impact on the deformation behaviour of the gauge section. This assumption justified removing the grip sections of the specimen from the part model. The necking region is key to the tensile simulation so was included in the part model. The reduced shoulder sections experience deformation and are likely to impact the deformation behaviour of the gauge during specimen elongation (green arrows) so were maintained as part of the model.

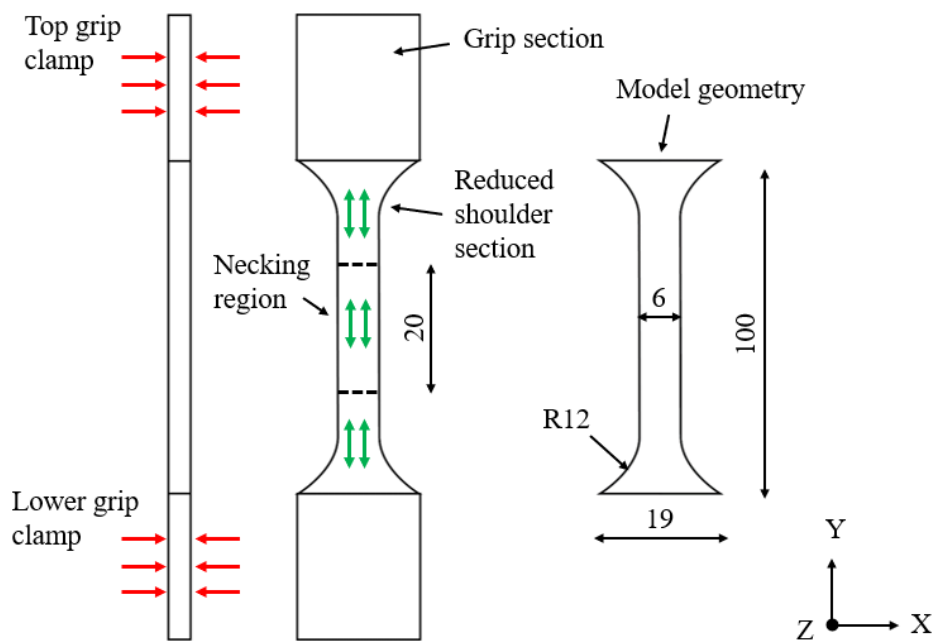


Figure 74 Geometry simplification and final model geometry (units in SI).

The idealised specimen geometry was drawn and extruded by 1.6 mm in the thickness (Z) direction. The gauge was partitioned to create a gauge length of 20 mm, Figure 76 (a). Five regions were selected and boundary conditions were assigned to them. In the FE software these regions are named sets. These are the top and bottom surfaces of the specimen, nodes at the top and bottom of the gauge section, and finally the entire model.

After defining the boundary conditions a mesh was applied to the entire model. Global seeds were created along the edges of the model to specify the target mesh density and the mesh was generated according to the seed points, Figure 75. Continuum solid elements with a 3d hexahedron linear element type were selected for the mesh. This was because it is a stress-displacement simulation. This element type is denoted as C3D8 which defines the element shape and number of nodes. For this stress/displacement simulation the translation of the nodes was calculated in all directions by linear interpolation. The mesh was refined in the gauge region as it was known from the experimental tensile test that this region will experience greater deformation and so will require a fine mesh to ensure convergence. Mesh refinement was kept to a minimum to reduce model complexity.

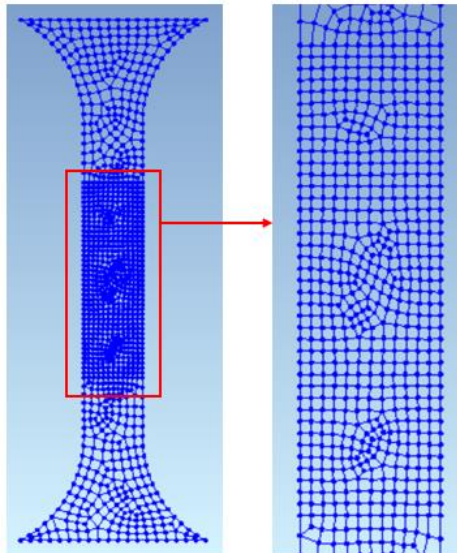


Figure 75 Meshed tensile specimen with refined mesh in necking region.

The mesh was exported, and an artificial weakness was made at the centre of the gauge section by manipulating the location of a node. This is representative of a small impurity in the material. This is a common technique used to encourage the material to fail in the centre of the gauge. Also, as perfect materials do not exist in the real world, without manually creating this imperfection in the mesh the simulated material behaviour would be unrealistic.

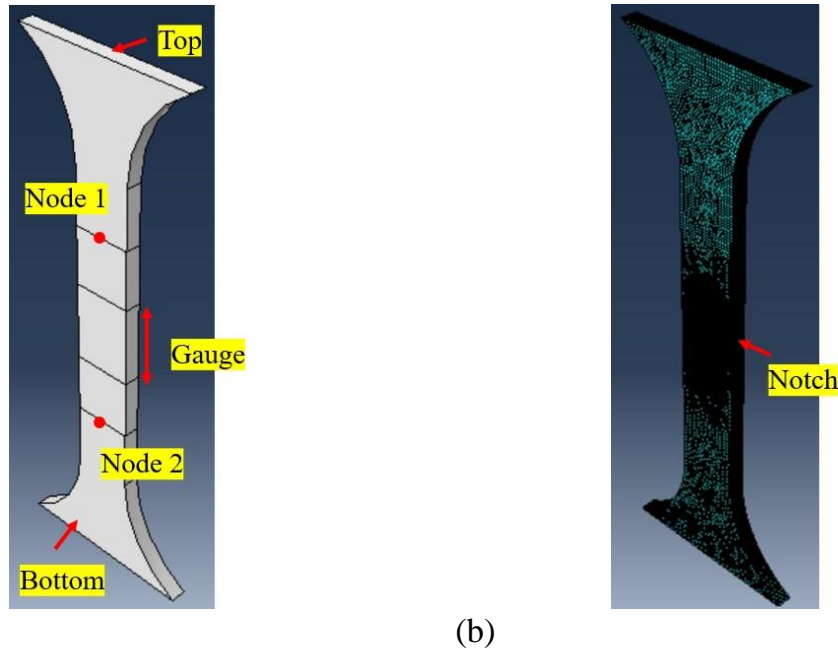


Figure 76 Abaqus pre-processing: (a) Part model with sets; (b) Mesh.

5.2.3 Pre-processing – Material definition

A separate FEA software known as PAM-STAMP was used to perform the uniaxial tensile simulation because it has the facility of modelling anisotropic material built in which means less setting up is involved. To begin, an input file (INP.) was exported from Abaqus which contained the nodal information for the meshed model and imported into PAM-STAMP using a MATLAB script, see Appendix 10.12. This generated the part model in PAM-STAMP which included the previously generated mesh and sets. The model was assigned an object type ‘volume blank’ and a material property ‘CP-Ti’. The rolling direction (RD) was set in the vertical (Y) direction. To create the CP-Ti material property the yield criteria was first calculated. An excel macro was used to determine the accuracy of various plasticity laws to model the anisotropic behaviour of the CP-Ti material. Experimental data was input into the macro. This included R-values and YS ratios in three directions with respect to RD, see Table 10 and Table 11. The R-values were taken from in-house test results of the same material and the yield stress data was gathered from the previously performed experimental uniaxial tensile test. An extensometer to measure thickness change in the tensile specimen was not fitted during tensile testing due to its interference with the DIC

cameras, justifying the use of R-values calculated from previous tensile testing of specimens extracted from the same CP-Ti grade 2 1.6 mm thick material batch.

Table 10 Plastic anisotropy coefficient.

R0	R45	R90
0.84	2.44	2.77

Table 11 Uniaxial and biaxial yield stress factor.

SIG0	SIG45	SIG90
1	1.10	1.22

It was determined that the Barlat 91 plasticity law would model the anisotropic material with sufficient accuracy (Barlat et al., 1991). There was good agreement between the experimental data from the anisotropic CP-Ti material and the Barlat 91 yield function with an accuracy of 85.87%. The yield stress and R-value variations showed good agreement with respect to the tension direction, see Figure 77. Other yield functions were Hill 48 with 84% accuracy, and VegterLite with 99% accuracy. However, the VegterLite yield function was not available in the FE modelling software used.

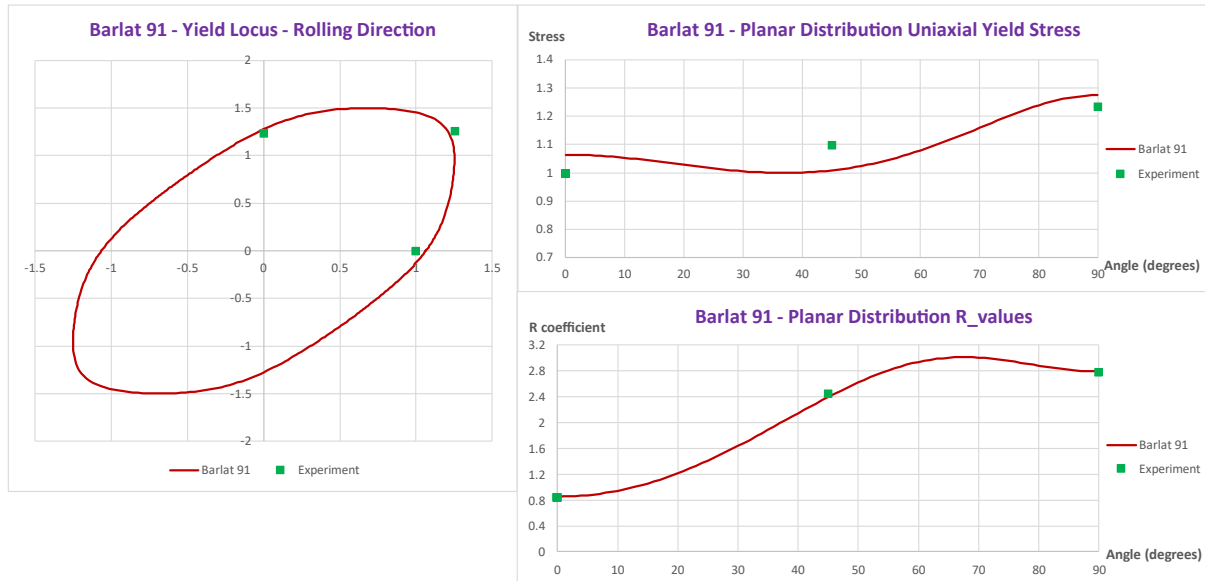


Figure 77 Barlat 91 yield function results.

The function parameters determined were input into the material window in PAM-STAMP, see Appendix 10.17. All material property values were input as SI (mm). An elastic modulus (E) of 105 GPa which represents the materials stiffness measured as a materials resistance to elastic strain (Shackelford, 1988). The Poisson's ratio was input as 0.32. Poisson's ratio is a unitless value which represents the ratio of a materials contraction perpendicular to extension caused by a tensile stress (Shackelford, 1988). Finally, the materials density (ρ) was input as 4.5×10^{-6} tonne/mm³ (MatWeb, n.d.). Material hardening data was calculated from the experimental uniaxial tensile test to accurately simulate its behaviour in the plastic region of the stress vs strain curve, Figure 78. This was achieved by first interpolating the experimental stress vs strain data from the uniaxial tensile test of the AR CP-Ti samples. Interpolation is a process used to estimate data values between points and is useful for cleaning and reducing data to make it easier to manipulate. For this analysis it was necessary to perform curve fitting. New data points were fitted along the interpolated data up to the point of severe necking and failure of the specimen from excessive strain beyond the materials UTS. This was appropriate as the actual fracture of the material is not being simulated. The fitted hardening curve (otherwise known as flow curve) was imported into the PAM-STAMP

CP-Ti material definition. This was the final information required by the solver to model the anisotropic material accurately.

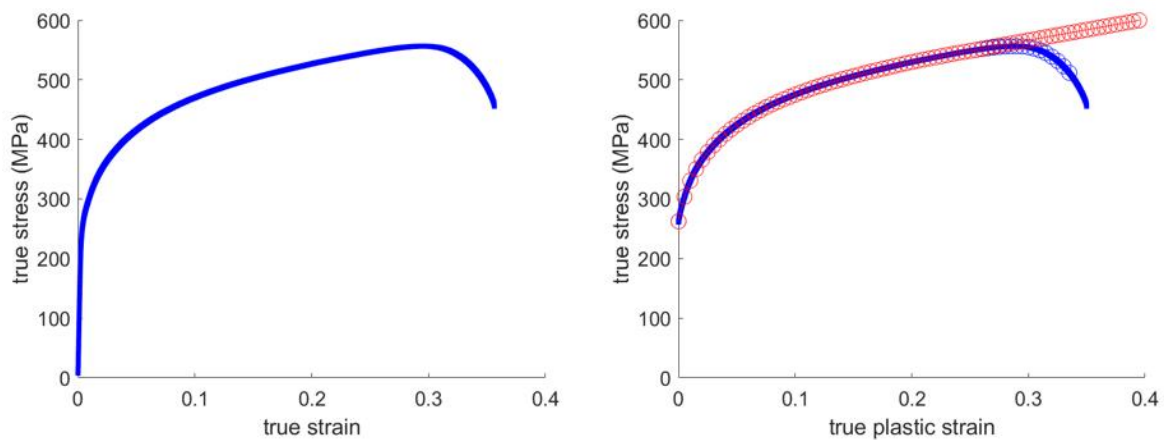


Figure 78 Fitting to experiment data to generate material hardening curve.

5.2.4 Pre-processing – Boundary conditions and output data

After creating the material model, the boundary conditions were assigned to the models sets, Figure 74. The set named ‘bottom’ had its translation and rotation locked in the X Y and Z directions. The set titled ‘top’ had its translation in the X and Z directions locked and free in the Y direction to allow for displacement. The set titled ‘top’, rotation was locked in the X Y and Z direction. The translation vector titled ‘disp’ was assigned in the positive Y direction. Finally, the section force and node history were recorded for post analysis. These boundary conditions were selected to simulate as accurately as possible the experimental tensile test by mimicking the setup of the test and mechanism of the machine in the simulation environment.

5.2.5 Running the FE simulation

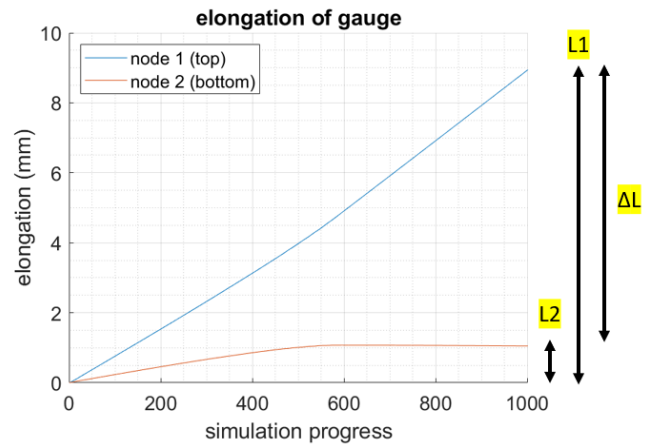
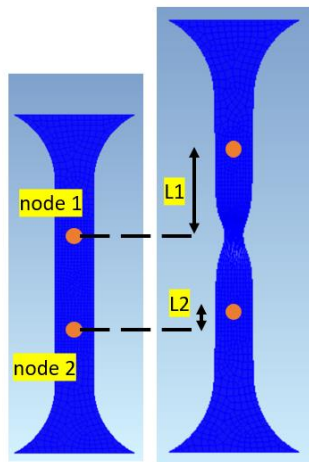
Following pre-processing, the output data was selected to gather relevant information to define the material properties and validate the model against the experimental data. For the sets ‘node top’ and ‘node bottom’ the node history was recorded for post analysis. From this, the displacement data was extracted to calculate the change in elongation of the gauge section. The uniaxial force applied to the specimen was taken

at the top and recorded as a function of displacement. In actual practice, the force is recorded from the displacement between the grips of the testing machine. However, this is not possible as the machine grips were not modelled for this simulation. From the output data sets a force-elongation curve was generated. The force-elongation curve was used to generate accompanying stress vs strain curves to calculate the E, YS and UTS values, as well as validate the simulation.

5.3 Results

5.3.1 Extracted data from FE simulation

Following the pre-processing steps, the simulation was run and the resulting data output was analysed. In this section, the resulting data is reviewed and compared to the results of the experimental room temperature uniaxial tensile test of the same material, see section 4.3.1. Firstly, the displacement data of two nodes located at the top and bottom of the 20 mm gauge section were plotted. The uniform elongation of the gauge which occurs in the elastic region of the stress vs strain curve was 1.1 mm. This value was derived by the vertical displacement of node 2 (L2), see Figure 79 (b). Beyond the yield point necking ensued which resulted in all strain localising in the necking region. This caused the lower half of the gauge below the neck to stop stretching. Elongation beyond the yield point was found by subtracting the displacement of node 2 from the displacement of node 1 (L1), found to be 8.9 mm respectively. Node 1 was in the upper half of the gauge section above the neck meaning it continued to move in the direction of extension even as the neck grew. From this, the final gauge elongation (ΔL) was found to be 7.8 mm.

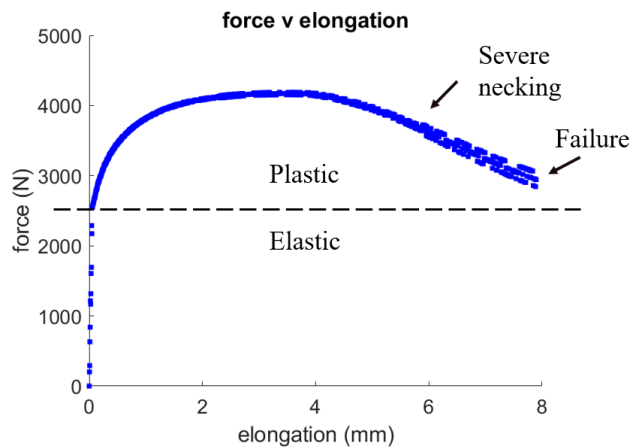
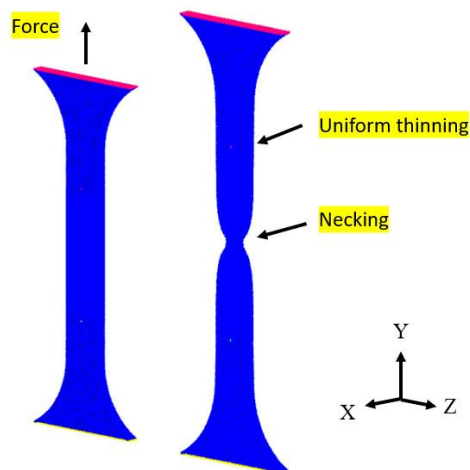


(a)

(b)

Figure 79 Elongation of gauge (ΔL): (a) node displacement; (b) elongation.

The uniaxial tensile force was taken from the top surface set of the specimen, Figure 80 (a). This was plotted against the sample elongation to generate the corresponding force-elongation curve, Figure 80 (b). From the curve, the elastic and plastic regions are identifiable before and after the yield point, respectively. The moment of severe necking and ultimate material failure are also identifiable.



(a)

(b)

Figure 80 Simulation result: (a) tensile specimen; (b) force-elongation curve.

5.3.2 Stress vs strain curve comparison

The engineering and true stress vs strain curves for the FE simulation were plotted alongside the experimental stress vs strain curves for comparisons to be made, Figure 81. The purpose being to assess the numerical prediction of the CP-Ti material hardening properties and ensure good confidence in the simulation output. Due to the repeatability of the experimental tensile test specimens only the average experimental values across the three samples were used for this comparison. To quickly summarise, engineering stress is defined as F/A where F is the axial load and A_o is the initial transversal area and the engineering strain or elongation is computed as $(L-L_o)/L_o$, with L and L_o being the final and starting extensometer lengths, respectively. At high levels of elongation, the stress and strain distributions are no longer uniform due to necking, therefore a true stress vs strain curve was generated which is the natural logarithm of the ratio of the instantaneous gauge length to the original length. True stress vs strain is only accurate during uniform strain, so the curves were not extrapolated beyond the materials UTS.

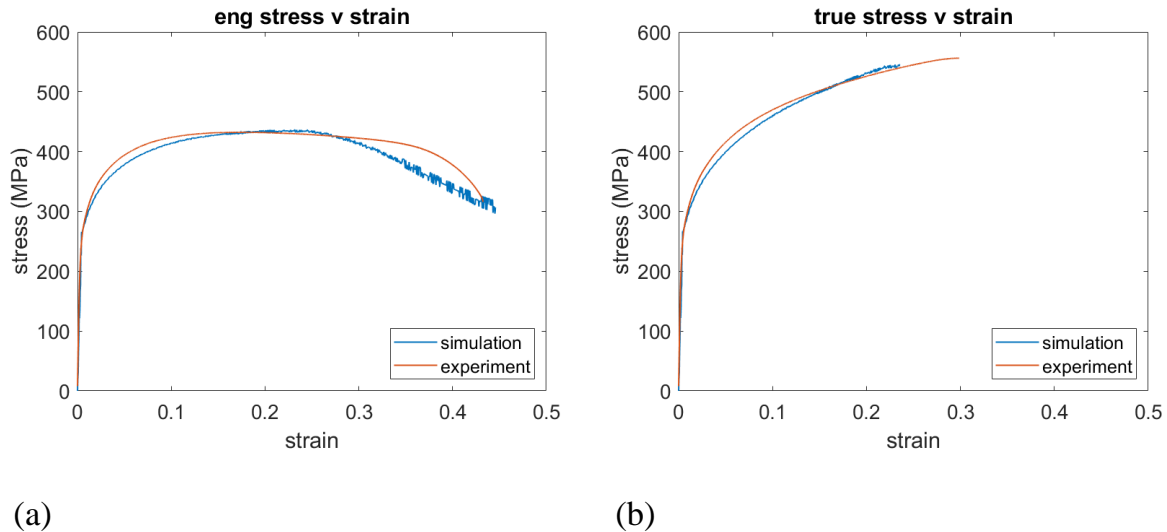


Figure 81 Stress v strain comparison: (a) Engineering curve; (b) True curve.

Table 12 Material properties extracted from the engineering stress vs strain curves.

Source of results	YS (0.2% proof) (MPa)	E (%)	UTS (MPa)
Experiment	353 ± 1.25	43 ± 0.75	432 ± 0.78
Simulation	337	44.6	436.5

Material properties extracted from the engineering stress vs strain curves are provided in Table 12. Overall good agreement between the simulation and the experimental values can be observed. This is particularly apparent at low levels of strain in the elastic region. However, the simulated reduction rate of the gauge section is unrealistically underestimated. This is apparent in the early stage as the simulated yield stress of 337 MPa is lower than the experimentally derived yield stress of 353 MPa. However, the divergence of results is more significant in the final stage of the engineering stress vs strain curve, see Figure 81 Stress v strain comparison: (a) Engineering curve; (b) True curve. (a). There seems to be problems in predicting the non-linear strain of the tensile specimen during severe necking. This is potentially linked to inadequate mesh convergence. A finer mesh in the necking region is a potential route to ensure the system response converges to a repeatable solution at high levels of non-linearity. When comparing the true stress vs strain curves, it seems that although the simulation was computed up until approximately the same elongation of the experiment, 44.6% and 43% respectively, the corresponding logarithmic strains for the simulation and experiment are different, 0.24 and 0.3 respectively, see Figure 81 Stress v strain comparison: (a) Engineering curve; (b) True curve.. However, the numerical results fit the experimental results reasonably well, despite the divergence beyond the point of severe necking. Fracture analysis was not performed for this simulation.

5.3.3 Further FE work

These results show that the material input parameters used to model the AR CP-Ti material are reasonable and in good agreement with the experimental data as proven in

the stress vs strain curve comparison. There is an unpredictability in the development of a neck and the artificial weakness may not have been representative of the actual situation. Potential future work would be to run a sensitivity study to understand whether this made much of a difference in the result. However, the result suggests it will be possible to use this material definition for further FE analyses, potentially to model ISF or to define the material properties for the LMD deposit and interface region. To improve the accuracy of the simulation it is recommended to perform further mesh refinement at the gauge centre. A future model would also need to consider surface finish and its impact on the LMD tailored materials strain behaviour.

Chapter 6

6 Material analysis of additively thickened CP-Ti sheet

6.1 Chapter overview

The material microstructure of the LMD tailored blank was characterised to investigate the underlying impact of the additional AM step on the microstructure of CP-Ti thin sheet. This chapter will include a breakdown of the experimental procedure followed by a discussion of the results.

6.2 Experimental Procedure

6.2.1 Material

The material generated in the previous LMD procedure was examined with respect to its changed microstructure. Material samples were extracted via wire electric discharge machining (wire-EDM) and the previously described preparation process was followed to prepare material samples for microstructural characterisation, section 3.3.13. There are several key zones highlighted for investigation, Figure 82. To test these areas, samples were first extracted from the as received (AR) material samples and then from the added LMD layer, the heat affected zone (HAZ), and the parent (substrate) material of the LMD tailored material samples with varying final thicknesses (T_f). To ensure the heat input from the cut off saw did not affect the microstructure the microstructural examination was performed at the centre of each sample away from the cut edge.

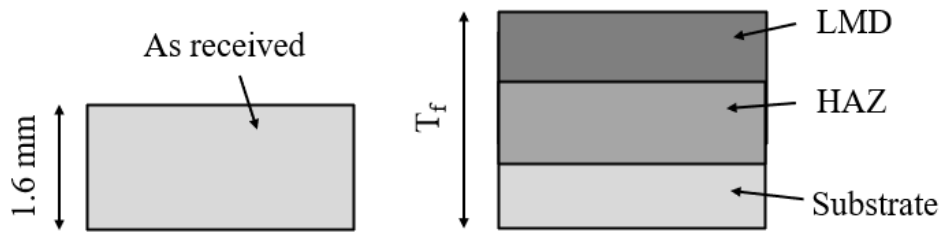


Figure 82 Key material zones in material study.

6.2.2 Surface analysis

The surface morphology of the LMD layer was characterised using the Alicona Infinite Focus microscope equipped with Alicona measure suite 5.3.1 software, Figure 83. All measurements performed with the Alicona 3D InfiniteFocus optical microscope conformed to ISO 4287 and ISO 4288 metrology standards. 3 dimensional (3d) representations of the LMD tracks were generated first using the OmniSuf 3D software. Three measurements were made along a 10 mm section of each built section, perpendicular to the tracks, to determine the surface profile of the LMD material. The waviness profile was calculated from the scanned data and imperfections which included cracks, scratches, and dents were ignored. The waviness profile was then generated in the OmniSurf 3D software by a phase compensation filter of cut-off values λ_f and λ_c being applied to the primary profile of the sample surfaces. This method helped determine the track peaks and depth of valleys between tracks. A MATLAB script was used to generate the profiles for analysis, see Appendix 10.11.



Figure 83 Alicona Infinite Focus microscope.

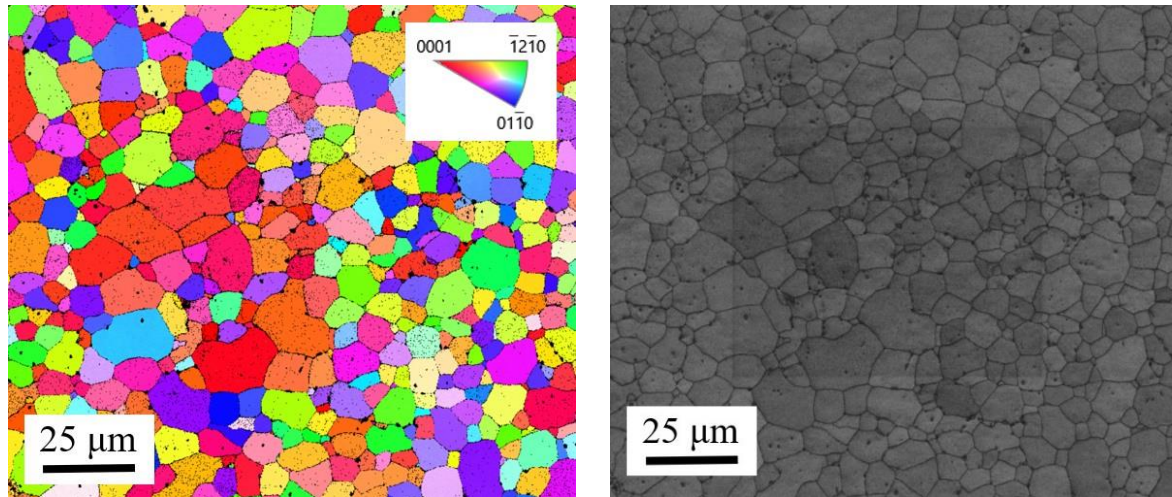
6.2.3 Optical microscopy

Low magnification micrographs were taken from a Leica DM 12000M optical microscope across the edge of mounted material samples. The samples were mounted, polished, and etched using Kroll's reagent for 3 - 10s to expose the internal grain boundaries (Danielson et al., n.d.). The samples were then examined under the optical microscope. The evolution of the material microstructure was examined across the thickness of the extracted material samples.

6.2.4 Electron backscatter diffraction

Electron backscatter diffraction (EBSD) was used to image the internal microstructure at higher magnification than achievable with optical microscopy. Samples were prepared using the standard CP-Ti polishing procedure. An electropolishing step was then introduced to prepare the material sample surfaces for microstructural examination. A polishing current of 0.14 A and voltage 35 V was used to polish a 1 cm² area with A3 electrolyte. A Quanta FEG 250 SEM microscope performed EBSD. EBSD was performed with step size 0.2 μm to observe the material microstructure using an SEM operated with an accelerating voltage of 20 kV. An EBSD orientation map with its accompanying distribution of the coloured inverse pole figure (IPF) map of the AR material in the rolling direction (RD) was generated, Figure 84. The standard stereographic triangle with colour codes red (0001), blue (01 $\bar{1}$ 0) and green ($\bar{1}$ 2 $\bar{1}$ 0) are

representative of the crystallographic orientations of the grains. The AR material micrograph revealed a fine equiaxed alpha grain structure with an average grain size of 5.38 μm , calculated using the interference method according to ASTM E112-12 “Standard Test Method for Determining Average Grain Size”, with misorientation angles below 15° and partial grains on the map edge not considered, Figure 84 (a). Indexing of 90% was achieved.



(a)

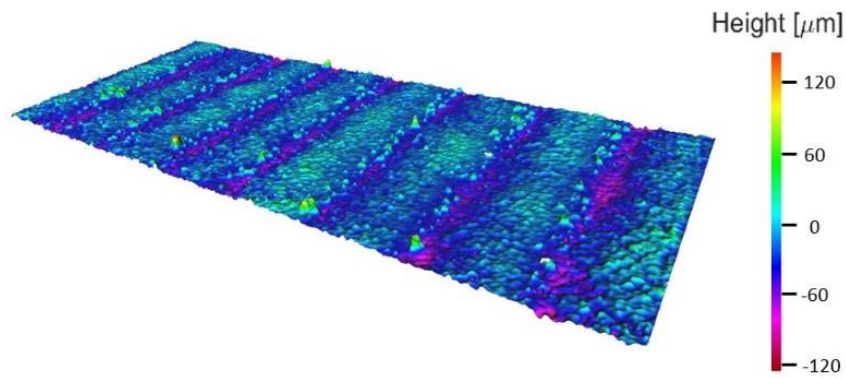
(b)

Figure 84 AR CP-Ti EBSD maps: (a) IPF; (b) BC map.

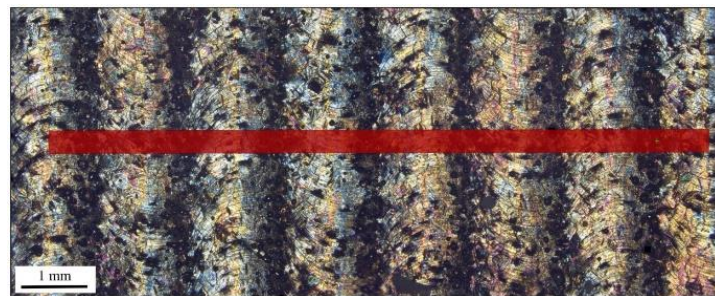
6.3 Results

6.3.1 Surface morphology analysis

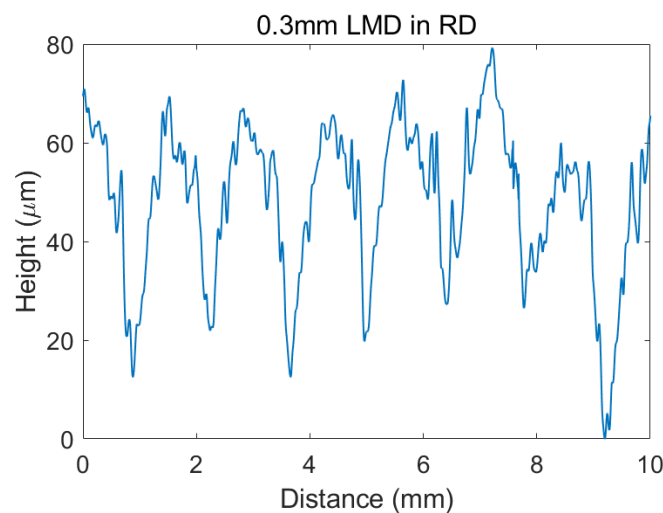
An Alicona microscope was used to measure the depth of grooves between each LMD track following the experimental procedure described in section 6.2.2. The 3d representation and surface profile of a sample surface are shown in Figure 85 (a) and (b). Alicona diagrams are provided only for the 0.9 mm LMD thickened material sample only, however the same data was created and examined for all sample surfaces.



(a)



(b)



(c)

Figure 85 Surface morphology of 0.3mm LMD sample: (a) 3d representation; (b) Top surface; (c) Surface profile.

All sample surface morphology results are provided in Table 13. The average groove depth across all LMD surfaces was $73.5 \mu\text{m}$ with a standard deviation (SD) of $10.6 \mu\text{m}$ showing relative closeness of the results. Black dots of approximately $100 \mu\text{m}$ in diameter were seen to have collected in the valleys between the build tracks. These are possibly collections of unconsolidated, partially melted, CP-Ti powder, see Figure 85

(b). A study by Sutton et al. (2020) showed that particles being ejected from the melt pool, known as spatter, can adhere to other powder particles at contact. Spatter during LMD likely caused this to occur resulting in ejected powder to become fixed to the material surrounding the melt pool. These unconsolidated powder particles may have functioned as surface defects leading to premature crack nucleation and early onset fracture. Laser scanning is suggested as a post-LMD step to smooth out the grooves. It is a method of smoothing an additively deposited surface with an intense beam to achieve high precision polished surfaces (Krishnan, 2019).

Table 13 Groove depths of LMD material samples.

Material sample variables	Average peak height (μm)
Set b	58.7
Set c	73.3
Set d	88.8
Set f	65.3
Set g	86.2
Set h	60.7
Set j	73.9
Set k	69.5
Set l	85.4

6.3.2 Microstructure development in response to LMD

Optical microscopy was used to observe the microstructural development across the cross-sectional thickness of the LMD tailored material samples, with the building direction in the y-axis and the optical image taken in the x-direction parallel to the RD.

Different cross sectional microstructural development is observed between the 0.6 mm and 0.9 mm LMD thickened samples, Figure 86 and Figure 87 respectively.

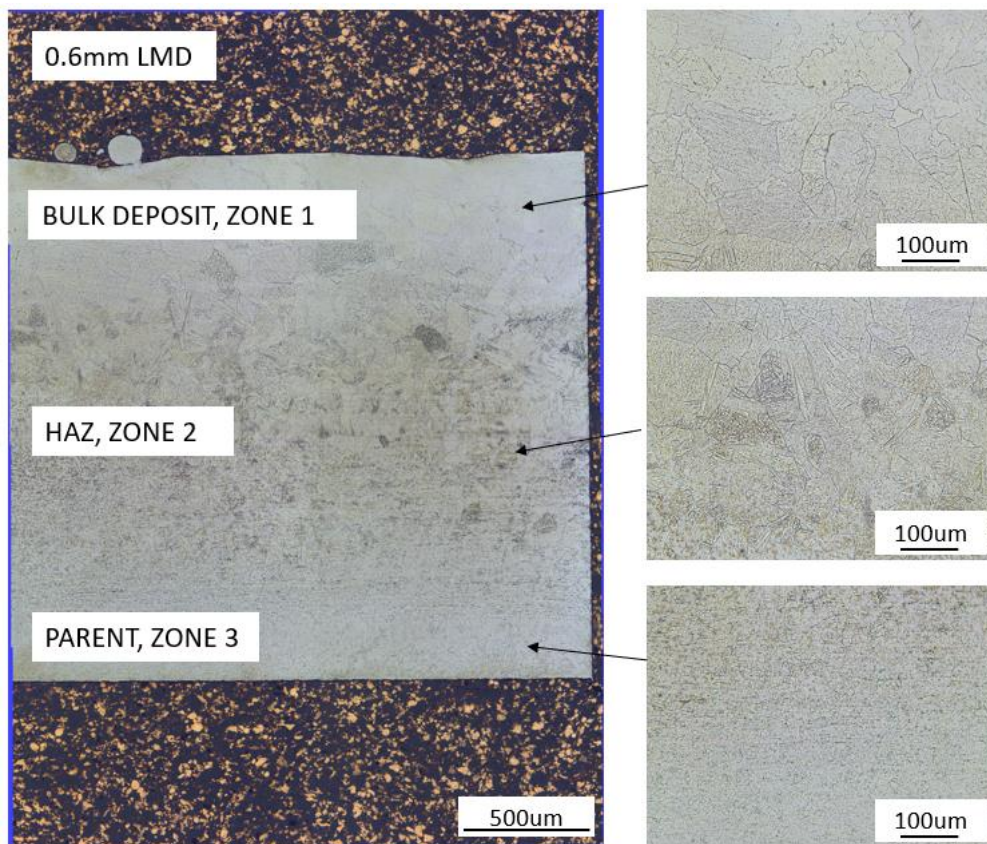


Figure 86 Cross section of 0.6mm thickened LMD material

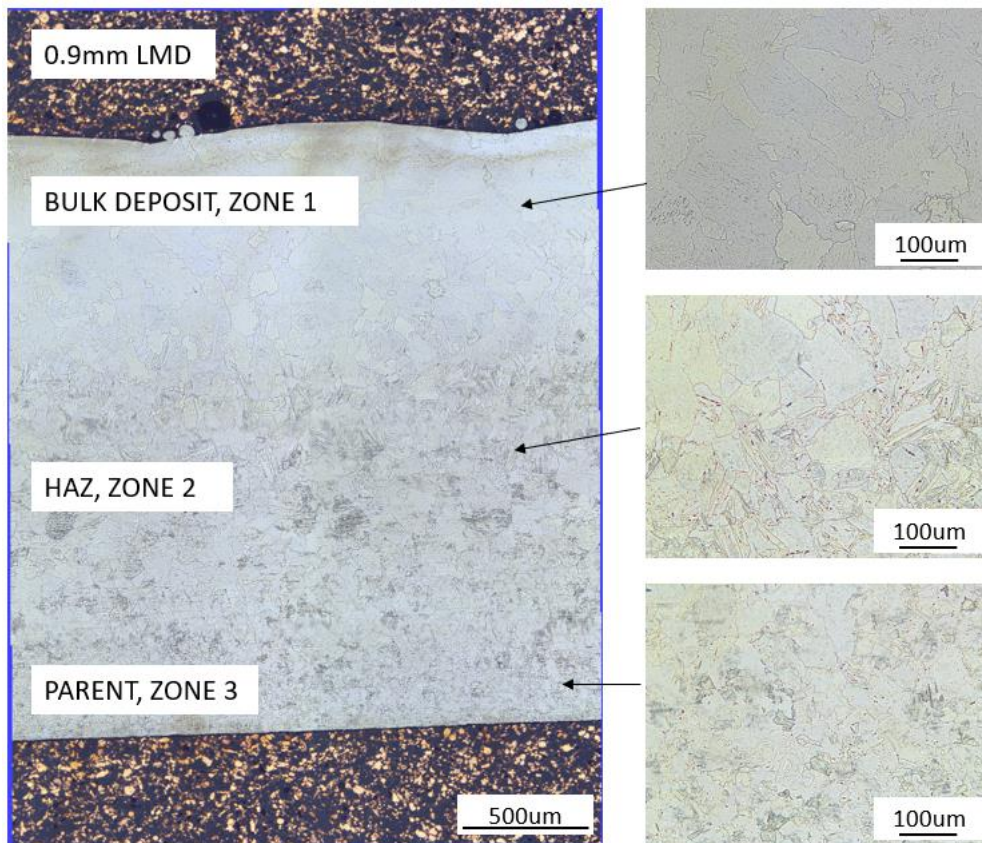


Figure 87 Cross section of 0.9mm thickened LMD material

Near-surface grain growth was observable in the LMD bulk material (Zone 1) for both samples. Near the base of the 0.6 mm thickened sample there was fine equiaxed microstructure which is indicative of the non-transformed parent material (Zone 3). However, zone 3 in the 0.9 mm thickened sample shows a microstructure closer to that of the HAZ in zone 2. This suggests more deposit layers result in deeper heat penetration through the thickness of the sheet substrate. It was not possible to measure the temperature during LMD to confirm this. However, these results suggest the HAZ depth can be used as an indication of the degree of heat penetration from the laser and melted layers during LMD. An accumulation of serrated colonies composed of fine lamellar grains, caused by the cooling over the β_T temperature with high cooling rates, is observed in the HAZ for both samples. This microstructural change is typical of pure titanium which has underwent this type of thermal history (Bignon et al., 2021). In the bulk material significant grain growth is observed.

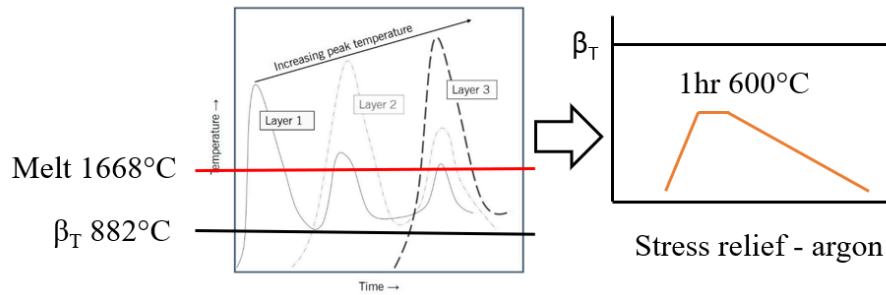


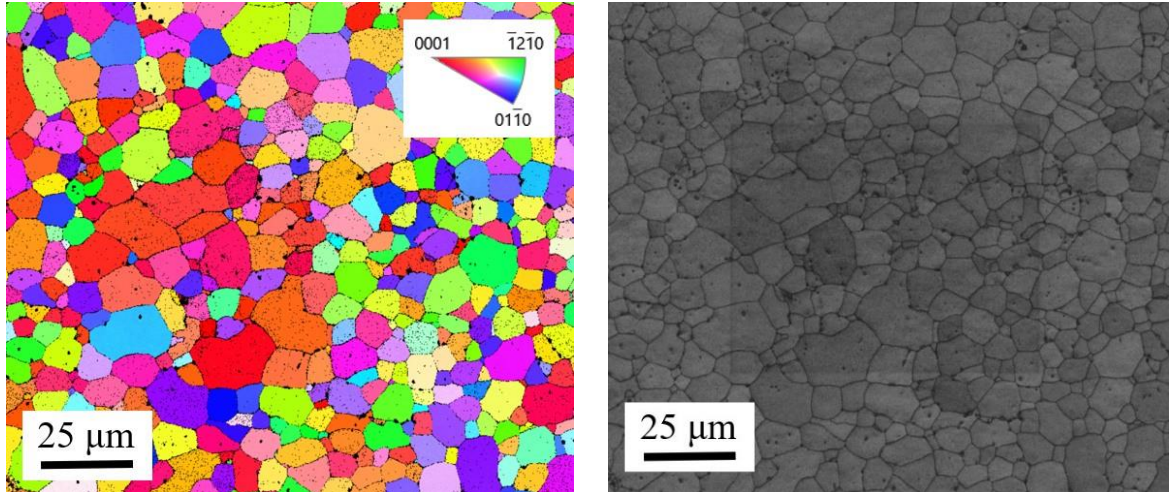
Figure 88 Thermal cycle of LMD and post-print stress relief on tailored material

Thermal loading from the laser and subsequent cooling as the laser moves away from the heated area is the likely cause for the $\alpha \rightarrow \beta \rightarrow \alpha$ phase change of the microstructure. Dass et al. (2019) showed the thermal history in LMD to be complex, with a direct correlation between increasing peak temperature and increasing layer number, as well as the accumulation of thermal energy as more layers are built up, and very fast cooling rates to the order of 10^3 to 10^5 K/s, Figure 88. It is likely that during the LMD process the laser heated the melt pool above the CP-Ti melt temperature (1668°C) and, as the laser moved away, the melt pool cooled rapidly to below the β_T temperature of 882°C . This same material will have subsequently been re-melted and later solidified as the laser passed over again. Furthermore, as the number of layers increased the peak temperature likely increased causing greater heat penetration to transform the fine equiaxed microstructure closer to the base material into a microstructure like that in the HAZ. The extent of grain growth and microstructure formed is an indication of thermal behaviour during LMD, with a study by Bermingham et al. (2020) showing that low temperature gradients and high cooling rates are favourable conditions for the formation of equiaxed grains.

6.3.3 Microstructural analysis of LMD deposited material

Electron Backscatter Detection (EBSD) is used for in-depth grain analysis. Grinding of the material samples to depths of 0.3-0.6 mm below the top surface exposed the microstructure within the LMD layer. Inverse pole figure (IPF) maps were created using MATLAB, section 10.13. The RGB colour code, red for (0001), green for $(1\bar{2}\bar{1}0)$ and

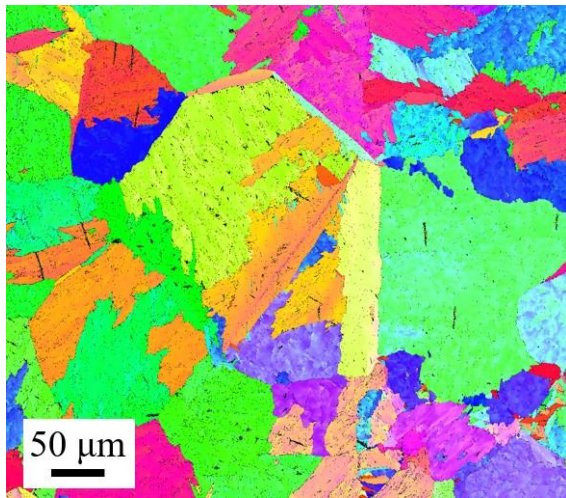
blue for $(01\bar{1}0)$ as shown in the standard stereographic triangle, corresponds to the crystallographic orientation of each grain. As a benchmark, an IPF map of the AR material was generated to compare the newly formed microstructures in response to LMD. The AR material exhibits equiaxed grains with some directionality thanks to the cold rolling operation.



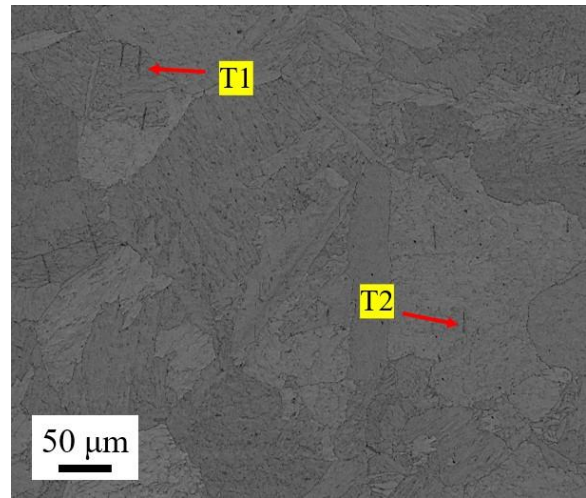
(a) (b)
Figure 89 AR CP-Ti EBSD maps: (a) IPF; (b) BC.

In contrast, the colour of the grains in the IPF maps for the LMD tailored material show random grain orientation which may help explain the isotropic nature of the tensile test results, see Figure 90. However, the size of grains and SEM capability meant insufficient grains could be captured to produce pole figures for texture analysis. Low magnification maps were used to measure the average grain size of the LMD tailored material using the intercept method. The 0.3 mm thickened material had an average grain size of $54.5 \mu\text{m}$ and size range of $8.1 \mu\text{m}$ - $250 \mu\text{m}$ ($\text{SD} = 56.9$). The 0.9 mm thickened material had an average grain size of $39 \mu\text{m}$ and size range of $2.2 \mu\text{m}$ - $326.2 \mu\text{m}$ ($\text{SD} = 57.7$). The AR material had an average grain size of $5.4 \mu\text{m}$ ($\text{SD} = 3.3$). Grain growth of approximately ten-fold was observed in response to LMD. The increased SD value for the LMD tailored microstructures suggest a greater spread in grain sizes in contrast to the AR material. Band contrast (BC) maps were used to show twinning in the microstructure of the LMD tailored material, Figure 90 (b, d). Twins were seen to either

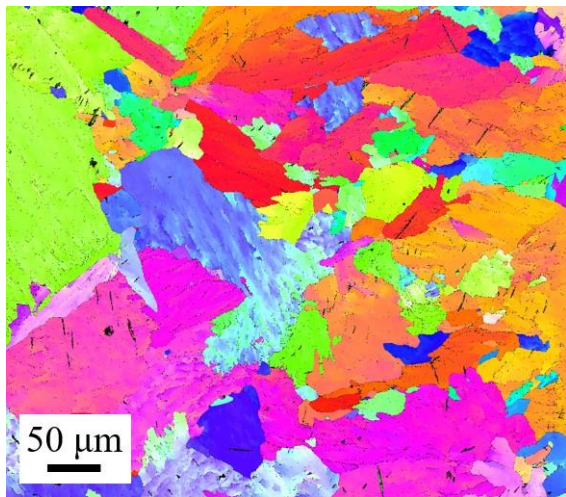
nucleate and terminate on grain boundaries (T1 and T3) or nucleate on the boundary and terminate within the grain (T2 and T4).



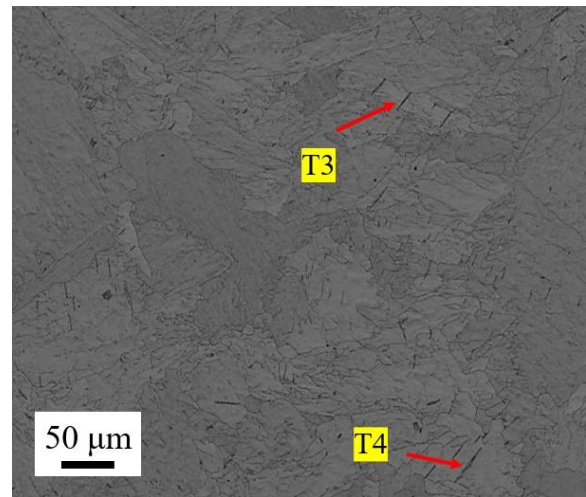
(a)



(b)



(c)



(d)

Figure 90 LMD microstructures: (a) IPF map 0.6 mm; (b) BC map 0.6 mm; (c) IPF map 0.9 mm; (d) BC map 0.9 mm.

A coloured inverse pole figure (IPF) map at high magnification was performed for the 0.9 mm LMD thickened material sample to examine the microstructure in greater detail, Figure 91 (a). The image contained several single grains and a fragmented large grain with intragranular misorientations.

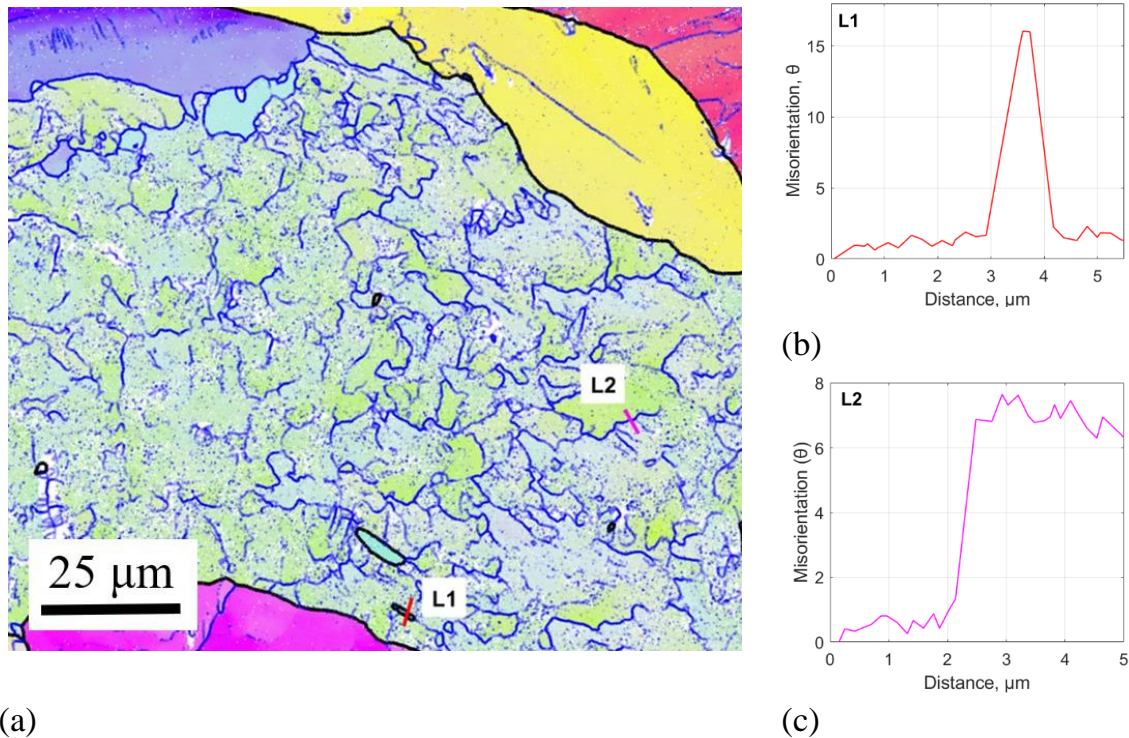


Figure 91 EBSD analysis of 0.9 mm LMD sample: (a) x2000 IPF map; (b) misorientation of enclosed HAGB; (c) misorientation of segmented LAGB.

The single grains were presumed to be the microstructure of the melted deposit material. The fragmented grain had an internal substructure containing partially and fully enclosed grains with low angle grain boundaries (LAGB) with a misorientation below 15° (represented by blue lines) and several fully enclosed grains with high angle grain boundaries (HAGB) with misorientation over 15° (represented by black lines). The substructure had a single crystal orientation as determined by the IPF colouring. A misorientation angle measurement across a fully enclosed HAG grain, labelled L1, revealed that the misorientation was just over 15° which confirmed the internal HAGB's evolved from LAGB's with the accumulation of dislocations, Figure 91 (b). An incomplete LAGB misorientation, labelled L2, had a misorientation of just under 8° which suggested the further accumulation of dislocations may result in a fully enclosed LAB grain and potentially lead to the creation of a HAB grain, Figure 91 (c). The size and shape of the LAB segments were close to the fine equiaxed microstructure of the

AR CP-Ti material. The occurrence of incomplete grains was a strong indication that continuous dynamic crystallisation (CDRX) occurred (Tamimi et al., 2020).

6.3.4 Impact of altered microstructure on plastic deformation

Typically, the strength and hardness of metallic materials is enhanced in microstructures which have smaller average grain size (Whang, 2011). Smaller grains create larger amounts of grain boundaries which leads to grain-boundary strengthening thanks to boundaries acting as pinning points to prevent further propagation of dislocations. Additionally, grain boundaries have a high degree of disorder and introduce a large number of dislocations which obstructs continuous movement of dislocations within slip planes, enhancing yield strength and hardness. From this, it can be deduced that the altered microstructure in the LMD deposit region of the specimen exhibits with lower overall yield strength thanks to the enlarged grains from the thermal input of the laser and melted layers. As such, the tailored specimens would theoretically exhibit lower resistance to plastic deformation on the deposit side of the specimen compared to the untransformed AR microstructure on the substrate side, which would affirm that premature crack propagation and failure of the enhanced blank would begin in the bulk deposit region. This mechanism was likely enhanced thanks to the morphology of the deposit surface. Lamellar microstructure, as seen in the build region of the tailored specimens, exhibits with moderate strength and low ductility compared to equiaxed microstructure, as seen in the AR CP-Ti sheet pre-LMD. Likewise, the lower ultimate tensile strength (UTS) will have led to premature plastic strain. It will have been preferable for the tailored material to have maintained the original equiaxed microstructure of the AR CP-Ti material to ensure high formability during ISF. As such, greater research into the control of thermal behaviour during LMD is necessary as well as in-depth study into post-LMD heat treatments and its impact on the materials microstructural development.

6.4 Summary

From the microstructural analysis, it is seen that the cyclic heat input from the laser has caused microstructural development in the sheet. A HAZ is evident in the cross-section which presents with enlarged fragmented grains and intragranular high and low angle misorientations, see Figure 91. The HAZ is more dominant in the 0.9 mm thickened samples as more deposited layers increase the peak temperature reached in the material resulting in greater heat penetration, see Figure 88. In summary, with respect to the experimental results the following conclusions were made:

- Analysis of the LMD track surface morphology and subsequent measuring of the track peaks showed strain to localise on the deposit surface in alignment with the LMD deposited tracks.
- 3d representations of the LMD deposit surfaces showed reasonably similar surface morphologies across all samples regardless of the number of LMD layers.
- High strain values in the valleys between LMD tracks may help explain why the LMD samples failed at a lower elongation than the AR samples.
- Surface machining, grinding, or polishing are potential post-processing operations which could help improve surface flatness levels for homogeneous strain distribution across the material surface, and reduce overall strain levels on the LMD surface. However, additional LMD thickness to accommodate this and the associated costs and processing times this will demand must be considered.
- Analysis of the cross-section across the extracted material samples revealed three reasonably distinct regions. These were the non-transformed parent material, an interface region containing a mixture of refined and larger grains, and the LMD deposit on the top surface.
- Grain growth in the LMD section was made visible by EBSD. This is likely to be a direct response to the thermal input from the laser during LMD. The large grains were found to be fragmented with intragranular LAB misorientations and fully enclosed HAB grains.

Chapter 7

7 ISF of an additively tailored CP titanium preform

7.1 Chapter overview

In this chapter, the development of a Laser Metal Deposited (LMD) tailored preform and subsequent back supported Incremental Sheet Forming (ISF) of the sheet preform is documented. The goal being to tailor a commercially pure titanium (CP-Ti) preform with additional thickness in areas of predicted thinning to achieve thickness homogeneity in the final sheet part. Through-thickness thinning during room temperature ISF is a major problem which compromises the sheet part and leads to failure by fracture. The pre-forming additive step offers a solution to this, however testing is required. This chapter describes preparing of and performing the ISF trial, and a discussion regarding the results.

7.2 Experimental procedure

7.2.1 Materials and equipment used

A CP-Ti grade 2 sheet with 1.6 mm thickness was provided by TIMET (Titanium Metals Corporation) for use as the substrate material for LMD. LMD was performed by a laser specialist to tailor the preform sheet with areas of added thickness. The CP-Ti sheet was from the same material stock used in the previous investigation, section 4.2.1. The sheet was trimmed with a guillotine, holes were drilled for the hex screws to tighten the blank holders in place, and then assembled and fixed into the LMD fixture for delivery to the laser specialist. CP-Ti grade 2 powder was used as the material to be deposited by LMD.

7.2.2 ISF fixture design

The main module of the tooling was designed to host the LMD fixture with the tailored ISF preform material still constrained. This is named the “ISF fixture”, Figure 92. This was designed to accurately locate the sheet and keep it securely constrained during LMD, the post-LMD heat treatment, and the ISF process. The full design development including a design specification is provided in section 3.2.3. The engineering drawing is given in appendix 10.3.



Figure 92 ISF fixture.

The main feature of the ISF fixture is the moving top plate. This has a cavity which fits the LMD fixture sub-module. The top plate is lifted by two scissor lifts to position the sheet over the die. The top plate lowers the sheet over the die and the sheet is formed into the shape of the die by a CNC controlled roller ball tool. Four sets of guide pillars and bushings maintain accurate placement of the top plate. The guiding assembly components were outsourced. The guiding pillars and bushings have slide fits and are highly toleranced, which gives the tooling the high accuracy it demands. The ISF fixture fits into the 5-axis CNC machine and is constrained to a T-slot table.

7.2.3 ISF tool

The tool which was used to perform the ISF operation has three main parts. The mount for mounting the tool within the CNC machine tool holder, the arm which fits into the mount, and the ball bearing which is held within a chamber at the end of the arm, Figure

93 (a). The ball bearing measures at 25.4 mm in diameter and has the freedom to rotate 360° around its axes, Figure 93 (b).

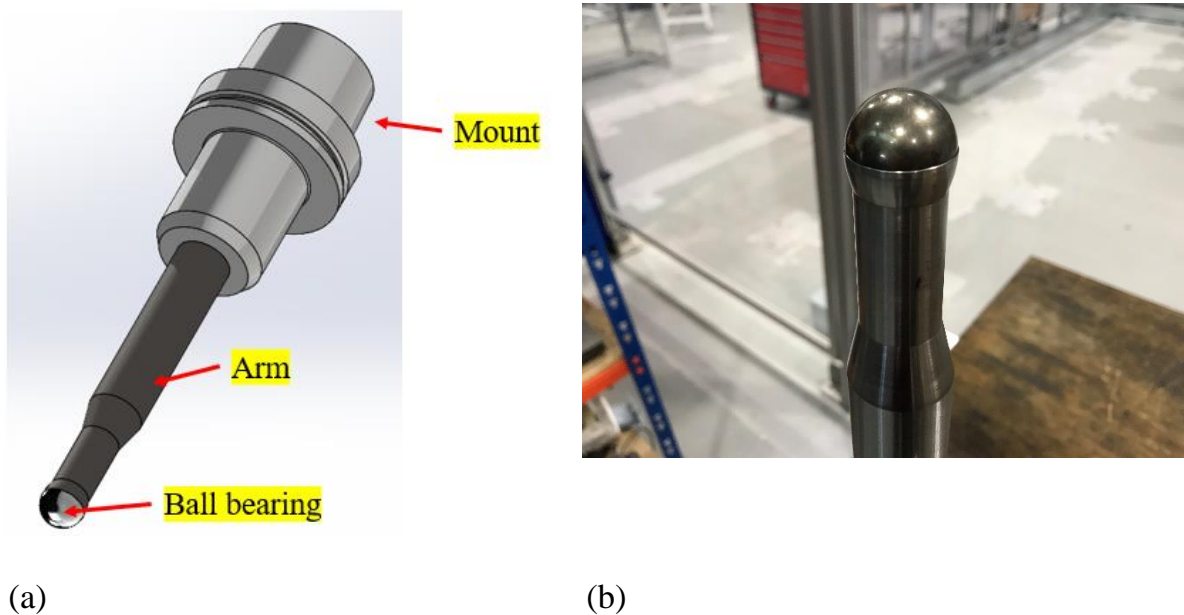


Figure 93 Roller ball tool: (a) Tool assembly; (b) Ball bearing within chamber.

The tool was designed to be installed into a CNC 5-axis machine, Figure 94. The arm is inserted into a mount which fits into a tool holder within the CNC machine chamber. The movement of the tool holder is controlled by the motor system within the CNC machine. It moves the tool along the pre-programmed toolpath to form the sheet.

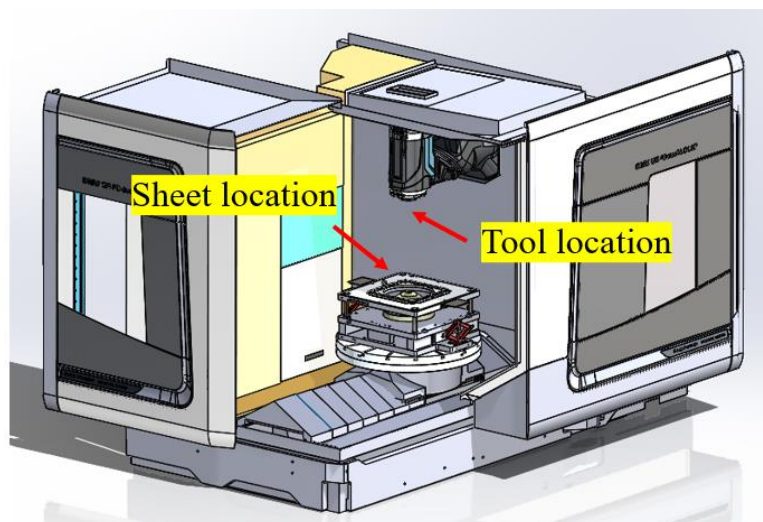


Figure 94 CNC 5-axis machine with tool/sheet location.

7.2.4 LMD preform design

The strategy of thickening the sheet where the thinning was expected is hoped to result in a more homogeneous thickness distribution across the ISF part. Scanning the previously made ISF parts has proven that thinning is prevalent in the wall sections formed at high angles with respect to the sheet plane. A dome with flat wall sections angled at 20°, 40°, 60° and 80° to the sheet plane was used to inform the design of the LMD thickening for the ISF preform. A 3-dimensional (3d) representation was generated by exporting the mesh from the GOM Atos software and making a representative model using PAM-STAMP, Figure 95 (a). The GOM ATOS® two camera setup was used to create the original 3d model which contained the original mesh. A MATLAB script was then used to export/import the mesh, see appendix 10.12. The meshed part in PAM-STAMP was split into two surfaces (top and bottom) and the distance between these two surfaces provided the thickness measurement. A colour scale bar was used to visualise the thickness across the formed sheet, Figure 95 (a). Extra thickness by the powder, used to lessen the reflective surface of the sheet, likely impacted the measurement. However, it is to be assumed that any thickness change from the spray is equal across the entire sheet.

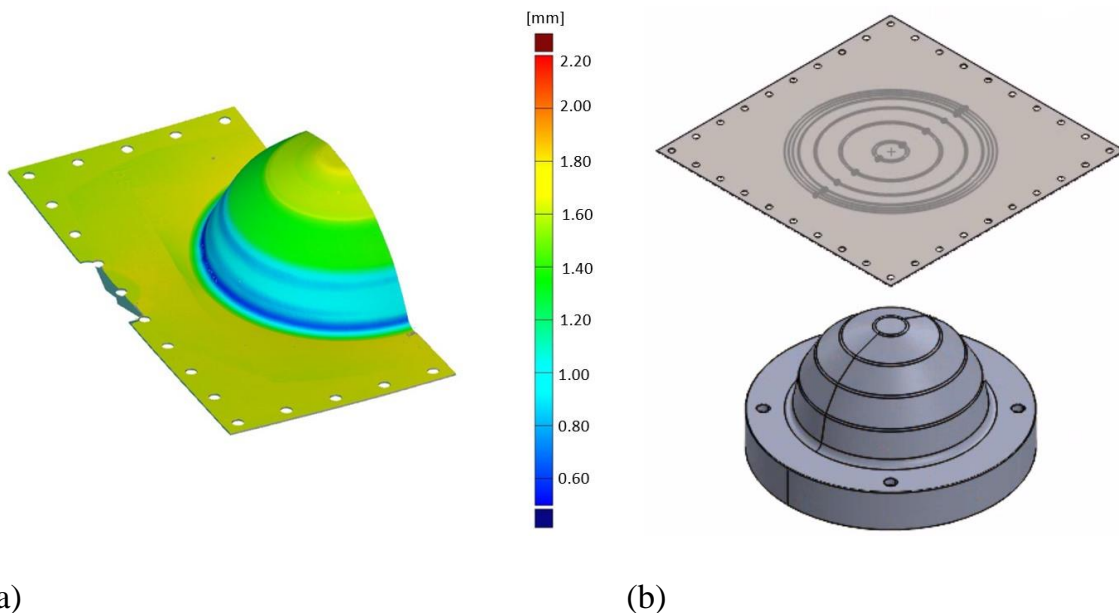


Figure 95 Design of LMD added thickness: (a) 3dimensional representation of ISF formed part; (b) Informing thickening area using die projection.

Firstly, to determine if the sine law is useful for predicting the level of thinning by ISF final thickness predictions were made based off the initial sheet thickness of 1.6 mm and the forming angle of each wall section with respect to the horizontal, Equation 4. The results of this are given in Table 14.

Table 14 Final thickness predictions using sine law (in mm).

Angle	0°	20°	40°	60°	80°
Result	1.6	1.5	1.23	0.8	0.28

The GOM thickness measurements were extracted from the 3d representation, collated, and used to calculate the level of thinning of each angled wall section, Table 15.

Table 15 GOM thickness measurements of ISF CP-Ti sheet (in mm).

Location	0°	rad	20°	rad	40°	rad	60°	rad	80°	Rad1	Rad2
1	1.60	1.63	1.54	1.52	1.24	1.11	0.84	0.77	0.66	1.12	1.44
2	1.60	1.63	1.56	1.53	1.26	1.08	0.75	0.78	0.57	1.11	1.42
3	1.60	1.65	1.56	1.56	1.29	1.1	0.78	0.78	0.58	1.11	1.43
4	1.60	1.66	1.58	1.57	1.30	1.12	0.90	0.8	0.61	1.11	1.45
5	1.60	1.67	1.61	1.59	1.32	1.14	0.91	0.88	0.63	1.15	1.45
Average	1.60	1.65	1.57	1.55	1.28	1.11	0.84	0.8	0.61	1.12	1.44

The sine law thickness predictions are good up until the 60° wall section. The sine law is assuming the material is in an approximate plane strain state in the direction of the tool movement. It is possible that on reaching the 80° wall angle, because of the severity of the forming angle, the acting strain state changes which is why the sine law begins

to break down. Possible strain states the sheet is put under could be biaxial or equibiaxial stretching which would impact the predictability of the thinning.

Table 16 Required LMD thickening calculations.

Location	0°	rad	20°	rad	40°	rad	60°	rad	80°	Rad1	Rad2
Thinning (mm)	0	0	0.07	0.09	0.32	0.54	0.76	0.85	0.99	0.53	0.21
Closest Fit	0	0	0.15	0.15	0.3	0.6	0.75	0.9	0.9	0.6	0.3
Layers	0	0	1	1	2	4	5	6	6	4	2

The necessary added thickness was calculated by subtracting the final thickness from the original thickness, Table 16. The thinning distances were used to inform the design of the tailored preform as the areas of added thickness correspond with the geometry of the die, Figure 95 (b). Despite the sine law not predicting the thinning across the entire part a definite relationship was seen between the forming angle and the thinning distance from the measurements, as thinning increased steadily as the forming angle increased. This means the flat sections with higher wall angles led to increased thinning so the added thickness by LMD effectively reinforces the sheet against over-thinning. The same LMD machine parameters as the previous experiment were used to ensure consistency in LMD build geometry and properties, see section 3.3.3. The individual layer height of 0.15 mm was used. The closest fit to the expected thinning distance was selected in increments of 0.15 mm. Attempting to deposit exact thickness to match the thinning value would require new machine parameters to be developed which would be time consuming and costly, so this best-fit strategy was deemed the most effective route to preform creation. The angled sections from the die used during ISF were mapped on to the flat sheet using SolidWorks, Figure 95 (b). It was expected the sheet will be squeezed and stretched outward during ISF, so the projected angled sections were not expected to align perfectly during the ISF process. However, it was also assumed the

sheet movement would be minor and would not significantly impact the quality of the part geometry. A 2d sketch was created using projected geometry from the 3d CAD model of the forming die. The 2d sketch elements were copied on the top surface of a 3d model of the preform sheet. The 2d sketch elements were then extruded to the desired thickness. Each extrusion was made to 0.15 mm in the y-direction to model the new thickness of the deposit layer. These layers were extruded on top of each other to create the LMD preform in SolidWorks. The solid 3d model was then imported into a 2d engineering drawing template. Part information including weight, shape, dimensions, material type and deposit material volume was noted on the engineering drawing, see section 10.5. The LMD deposit time was calculated by comparing material volumes to the previous experimental trial. Time stamps were taken from the previous LMD experimental trial and used to estimate the new LMD deposit time. The drawing and evaluated processing times were passed to the manufacturer to help with the LMD process design and cost calculations.

7.2.5 Laser Metal Deposition of CP-Ti sheet for ISF

Using the same laser specialist as the previous experimental trial ensured consistency in the material generated, see section 3.3.2. The LMD machine parameters were kept consistent with the previous LMD trial, see section 3.3.3. As before, 0.15 mm layers of CP-Ti grade 2 powder were deposited on the sheet substrate by the LMD process. To generate areas of greater thickness more layers were deposited. This layering strategy allowed the same tool feed and powder flow rate to be used in areas of different build heights which simplified the procedure. The main difference between this experimental trial and the previous was the deposit pattern. The new pattern required a new toolpath programme to be generated by the operator. Before, the LMD shape of the deposits were achieved using a crosshatch pattern. The build pattern was changed into a spiralling path which generated a circle with a centre hole, Figure 98. The tool path was changed from the cross-hatch pattern from the previous experiment as, instead of simply printing samples for testing, the shape of the deposit had to reinforce in the areas of predicted thinning which were shaped as concentric rings of increasing diameter. As

such, a circular tool path was optimal for achieving a uniform and complete deposit in these areas, Figure 96. The deposit started at the centre of the sheet and spread outwards with concentric rings of increasing diameter.

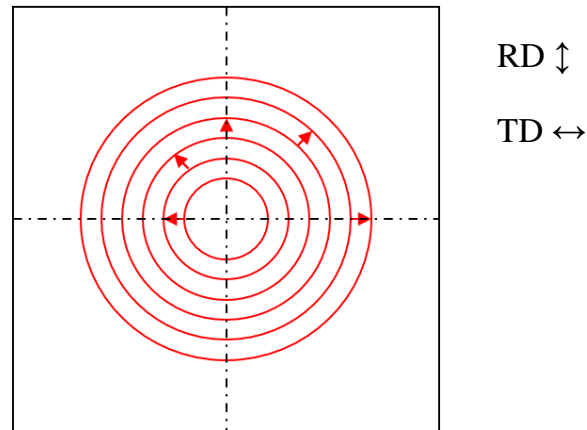
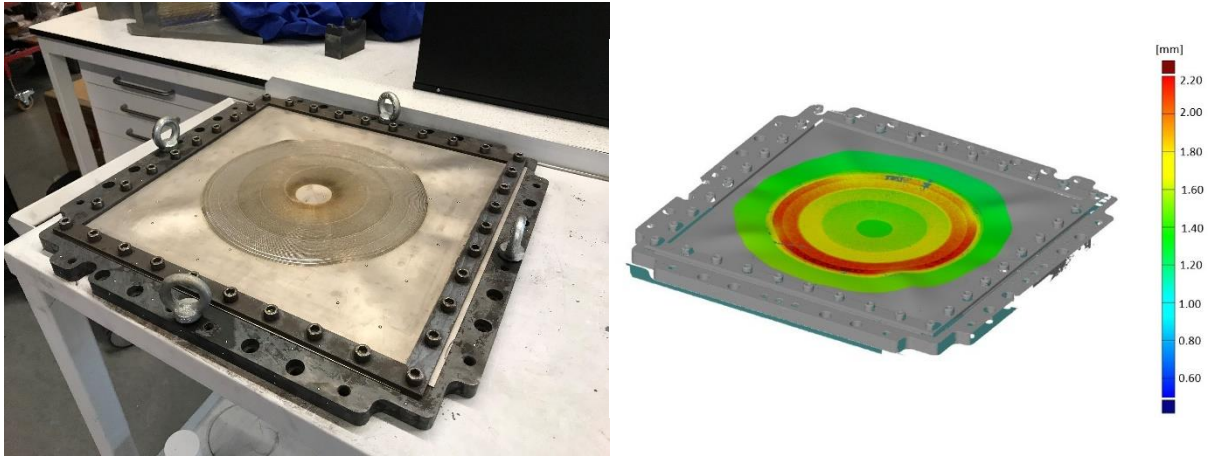


Figure 96 Circle tool path pattern (not drawn to scale).

The LMD fixture was clamped to a table in the workshop of the laser specialist. The nozzle head was centred on the sheet and lifted to 12 mm above the sheet material. A laser spot size of 3 mm was made on the substrate surface. The nozzle followed the toolpath in a clockwise direction. The laser melted the substrate, and the nozzle deposited CP-Ti powder into the newly generated melt pool. As the laser moved along its programmed path the temperature drop caused the melt pool and molten powder material to solidify leaving a solid build track across the sheet. On completing the layer, the nozzle was lifted 0.15 mm and the same process was performed in the shape of the laser path. The laser re-melted the previously deposited layer and powder was then fed through the nozzle by the argon gas stream into the melt pool. On solidification, a new layer was left on top of the previous layer increasing the overall build height by an additional 0.15 mm. This process was repeated until all layers were successfully deposited. After completing the LMD operation the sheet was kept clamped to avoid part distortion. The sheet was palletised and returned for post-process heat treating and ISF, Figure 97 (a).



(a)

(b)

Figure 97 LMD tailored preform for ISF: (a) Post LMD; (b) 3d representation.

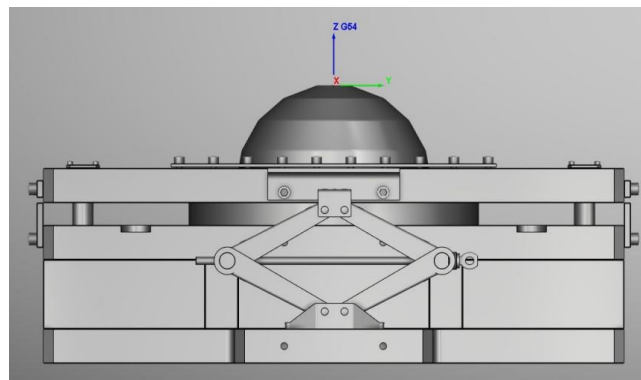
A 3d representation was generated for the LMD tailored preform using the GOM Atos system to examine the new part geometry, Figure 97 (b). Wrinkling was observed in the sheet corners. This was likely caused by the sheet expanding during LMD in response to the thermal input and moving outwards. The material expanding into the blank holders may have resulted in the wrinkling effect. However, this is not considered a major issue because the pressure applied to the sheet by the tool during ISF will flatten the sheet against the die during forming.

7.2.6 Post-processing of material

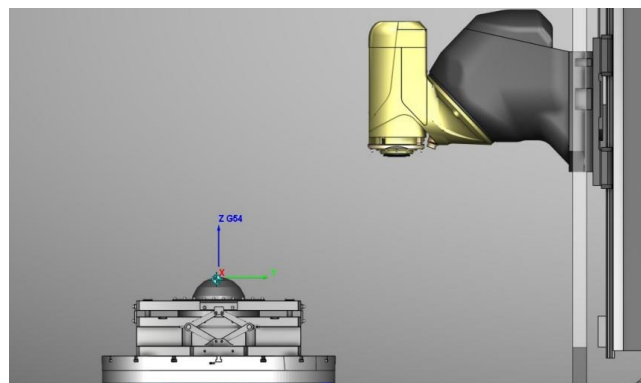
The same stress relieving heat treatment used for the previous trial was repeated to remove residual stress from the sheet from the thermal loading of the laser. The same Carbolite LCF furnace was used for the heat treatment operation. An argon gas tank was connected to the furnace. The fixture and sheet were placed in the furnace and the furnace turned on early in the morning to warm the parts to the resting temperature of the furnace. The temperature was raised to 400°C. Upon reaching 400°C the furnace chamber was flooded with argon gas to limit the amount of oxidation on the material surface. The temperature was raised to 600°C and held for 1 hour. After 1 hour the temperature was lowered to 400°C and the gas was stopped. The furnace was left to cool overnight, see section 3.3.5.

7.2.7 Machine and setup for ISF

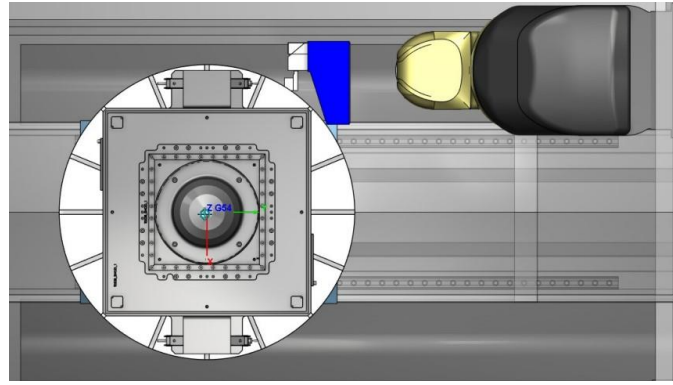
ISF was performed using the DMU 125 FD Duo Block 5-axis CNC machine at the Advanced Forming Research Centre. The ISF fixture was lifted into the CNC machine using a forklift. The bottom plate was secured to the machine bed table by a series of hex bolts and centred within the CNC, see Figure 98 (a). Two scissor jack lifts lifted the top plate into position. The LMD fixture with LMD preform was installed and the scissor lifts removed. The sheet was left in contact with the top of the die. The sheet contact with the die supported the top plate. This was designed so that as the sheet is formed over the die the top plate and sheet move downward together. A sensor was used to locate the centre of the sheet. The toolpath origin was set to the top of the die, Figure 98 (b). From this, the tool was lifted 1.6 mm to compensate for the thickness of the sheet. The die contained five angled sections at 0° , 20° , 40° , 60° and 80° to the sheet plane. The purpose of the die was to support the sheet during forming.



(a)



(b)



(c)

Figure 98 ISF setup: (a) LMD/ISF fixture assembly (closed); (b) Assembly in machine; (c) Fixture and tool holder/controller.

The toolpath was designed to accommodate the sheet areas with increased thickness. The tool was orientated perpendicular to the sheet surface during the ISF operation. Between operations, the temperature of the ball bearing was measured using a temperature gun. Coolant was brushed on the ball bearing to keep its temperature below 60°C as allowing the tool temperature to rise too much risked damaging the tool and sheet. It may have also lead to the ball bearing becoming locked within the tool chamber due to heat expansion which could result in catastrophic damage to the tool and sheet if forming continued in this situation.

7.2.8 ISF Programming

The toolpath was programmed using Autodesk Fusion 360. 3d models of the LMD tailored sheet, LMD and ISF fixtures, and the Dmu 125 CNC were imported into Fusion 360 to orientate all the components and ensure no parts collided. After this, the program went through Vericut to ensure no collisions or other incidents would occur. It was then uploaded to CIMCO and made available to the machine operator on the control device. The tool was programmed to return to the toolpath origin after forming 10 mm and the CNC machine door was unlocked automatically by the program to allow for inspection, cleaning, and re-application of lubricant to the sheet for cooling. The visual inspection during operation breaks was also important to check for cracks in the sheet. The tool

began at a central point and followed a spiral path in concentric circles, deforming the material incrementally.

7.2.9 Performing ISF

Room temperature ISF was performed on the LMD tailored preform sheet. The sheet and fixture were installed into the CNC machine as described in section 7.2.7, see Figure 100. Utilisation of all 5-axes of the CNC machine was necessary to keep the tools central axis perpendicular to the sheet surface throughout forming. The tool was installed into the CNC machine. A tool controller switched between the tool and touch sensor. The touch sensor was used to locate the sheet centre and provide a Z_0 coordinate for the toolpath program. The tool followed a pre-programmed tool path at a feed rate of 1800-3750 mm/min. The sheet was formed over a die which was constrained within the ISF LMD fixture assembly. As the sheet was formed over the die it began to fit the shape of the die and the moving plate was moved downwards in a controlled manner along with the outer edges of the sheet. The top plate was located by four guiding pillars and guide bushings which facilitated accurate movement in the negative vertical axis of the top plate without the risk of lateral movement.

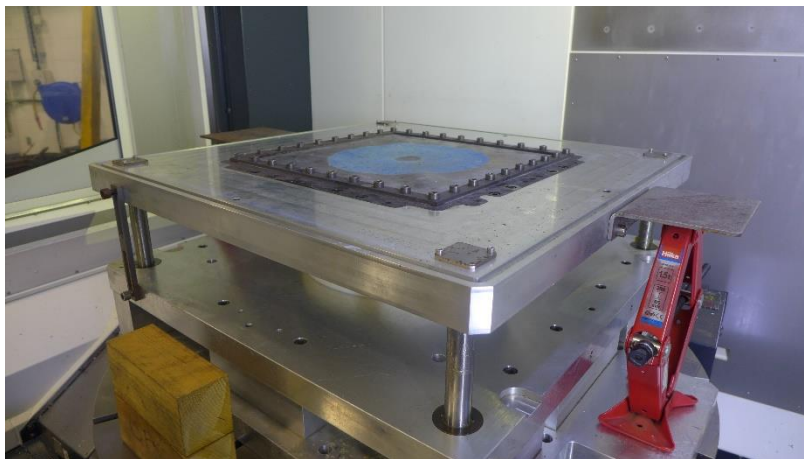





Figure 99 Fixture assembly with sheet installed for ISF.

The ISF operation was eventually stopped after an open crack was spotted in the sheet surface. The crack was noticed following the operation step titled ‘60DEG_CW_64.77’. The first part of this operation title refers to the wall angle of the section (60° measured

from the XY plane of the fixture and substrate), Figure 98. Forming did not continue after the crack appeared. Stopping ISF was important to ensure the sheet, ISF tool, fixture assembly, and/or the CNC machine were not damaged. The final part shape progression is visually documented in Table 17. As can be seen, the final part shape is near completion.

Table 17 ISF progress documentation.

Operation name	Photograph
TOP_FLAT_CW	
RAD1_CCW	
20DEG_CW_20.17	

20DEG_CCW_40.34



20DEG_CW_60.51



20DEG_CCW_80.68



20DEG_CW_100



RAD2_CCW



40DEG_CW_22.09



40DEG_CCW_44.19



40DEG_CW_66.28



40DEG_CCW_88.38



40DEG_CW_100



RAD3_CCW



60DEG_CW_21.59



60DEG_CCW_43.18



60DEG_CW_64.77

(Crack circled in red)



7.2.10 GOM analysis of LMD/ISF part

A GOM scanner was used to generate a 3d digital representation of the LMD tailored preform before and after the stress relief heat treatment, and after ISF. The purpose of scanning the preform before and after the stress relief operation was to ensure no significant change in the sheet shape occurred which could impact the ISF operation.

The part was released from the fixture to perform the scanning. It is possible there was some distortion of the sheet part on release from the fixture. However, it is the thickness variation of the tailored sheet post-ISF which is the key parameter being measured by the scanner, so distortion was not a real issue. Additionally, releasing the part from the fixture made transporting the sheet and orientating it during scanning easier. The previous scanning operation was repeated, see section 3.3.1. However, the sheet was held in a custom holder because of its shape, Figure 100. The holder was rotated after scanning the top surface to scan the underside. Reference markers were positioned across the sheet part so the software could accurately stitch the scans together into a full 3d image. A mesh of the scanned model was generated and imported into PAM-STAMP to measure the thickness distribution across the sheet. These measurements were used to determine the extent of thinning from the ISF operation and compare thickness homogeneity of both formed parts with and without the pre-forming additive step.



Figure 100 ISF LMD part scanning procedure.

7.2.11 Material characterisation

To perform material characterisation material samples were extracted from the deformed material and prepared with consideration of the characterisation method. Samples were extracted from each angled section including the area containing the crack. Fractography analysis was performed on the face of the crack which propagated on the 60° angled wall section. The area of the sheet containing the crack was first

removed by Wire-EDM. The extracted sample was then cut using the abrasive saw to split the crack into an upper and lower half, Figure 101 (a). The upper half was cleaned, mounted on a flat platform, and the edge touching the platform was coated with conductive silver suspension, Figure 101 (b). The fracture face of each sample was viewed using the Quanta FEG 250 under magnifications of 250x to 3000x. Areas of interest were photographed for further analysis.



(a)

(b)

Figure 101 Fractography sample preparation: (a) Section; (b) Mounted sample.

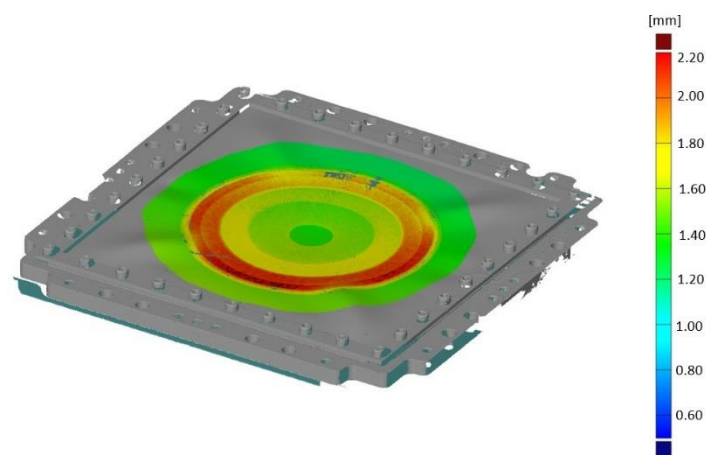
Following fractography, the surface roughness of the LMD surface was measured. The arithmetical mean roughness value (R_a), root-mean-square (R_q), maximum peak (R_t) and maximum valley (R_v) were calculated using the Alicona Infinite Focus microscope. The surface roughness of each angled section from the sectioned part was measured to determine if there was a relationship between the forming angle and the surface texture. First, samples were extracted from the angled sections and with the Alicona microscope the surface was scanned. The Alicona measure suite 5.3.1 software was used to measure the roughness across each surface. Three sections were measured across each sample surface to calculate an average roughness value. According to EN ISO 4287 surface imperfections such as cracks, scratches, and dents are not to be included as part of the profile so for this analysis were ignored. A MATLAB script was used to display the roughness data, Appendix 10.11. Following surface analysis, microstructural analysis of the material samples extracted from the formed sheet was performed. First, the samples were cut from the removed sections of the sheet and mounted. Grinding and

polishing was performed to remove enough material to expose the desired area for analysis, section 3.3.13. For the EBSD analysis an average of 1.2 ± 0.12 mm thickness was removed to ensure the scan was taken inside the LMD material region. A Scanning Electron Microscope (SEM) was then used to perform microstructural examination of the LMD tailored material specimens. Electron back scatter diffraction (EBSD) was used to examine the materials internal microstructure. EBSD was performed at 4000x magnification with step size $0.1 \mu\text{m}$ and an accelerating voltage of 20 kV. The sample was tilted at 70° within the SEM chamber while collecting the EBSD data. The resulting data was exported in the form of a CRC file and, using a MATLAB plug-in called MTEX, the microstructural data was analysed. Analysis included generating inverse pole figure (IPF) coloured maps which describe grain orientation and size.

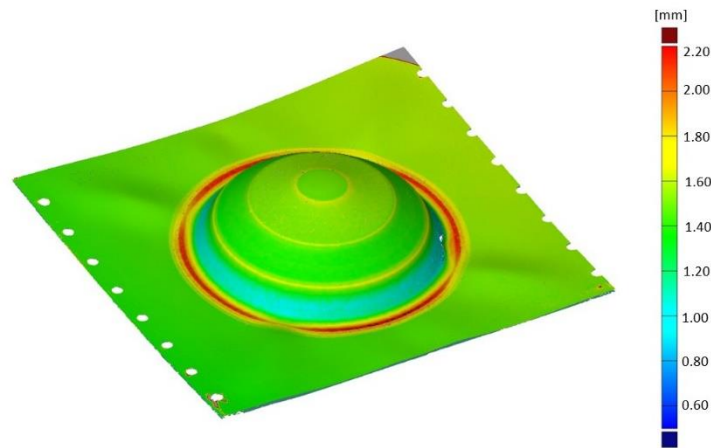
7.3 Results

7.3.1 Thickness distribution of LMD/ISF part

On completing the ISF process the sheet was removed from the fixture for analysis. A 3d representation of the LMD/ISF preform and formed part “LMD/ISF part”, were generated, Figure 102 (a-b). From this, thickness measurements could be made using the PAM-STAMP software, section 4.2.2.



(a)



(b)

Figure 102 LMD part scans: (a) LMD tailored preform; (b) LMD/ISF part

The results show the rate of thinning is roughly the same for the AR and LMD tailored sheets during ISF, Figure 103. This is expected as the ISF operation is unchanged and the material mechanical properties under tensile strain are largely unchanged as shown in the previous tensile testing, section 4.3.1. The final thickness of each wall angle section is closer to the desired 1.6 mm thickness in the LMD tailored sheet than the AR sheet. This suggests the thickness distribution was improved by thickening the sheet preform prior to ISF which proves the feasibility of the hybrid ISF/LMD process. However, despite this promising result the LMD thickened CP-Ti sheet fractured when forming the 60° angled section. The AR sheet could be formed to 80° with respect to the horizontal until failure. Different deformation mechanisms dominate ISF at different forming angles largely because of the contact condition between the sheet and forming tool. As such, the LMD type microstructure performed poorly under the deformation mechanism type at the higher angled sections. The likelihood of forming sheet parts to this extent with ISF is relatively low. The results suggest limiting room temperature ISF of LMD tailored CP-Ti parts to part geometries with wall angles of 40° and less is the best guarantee to produce quality parts using the LMD/ISF hybrid process.

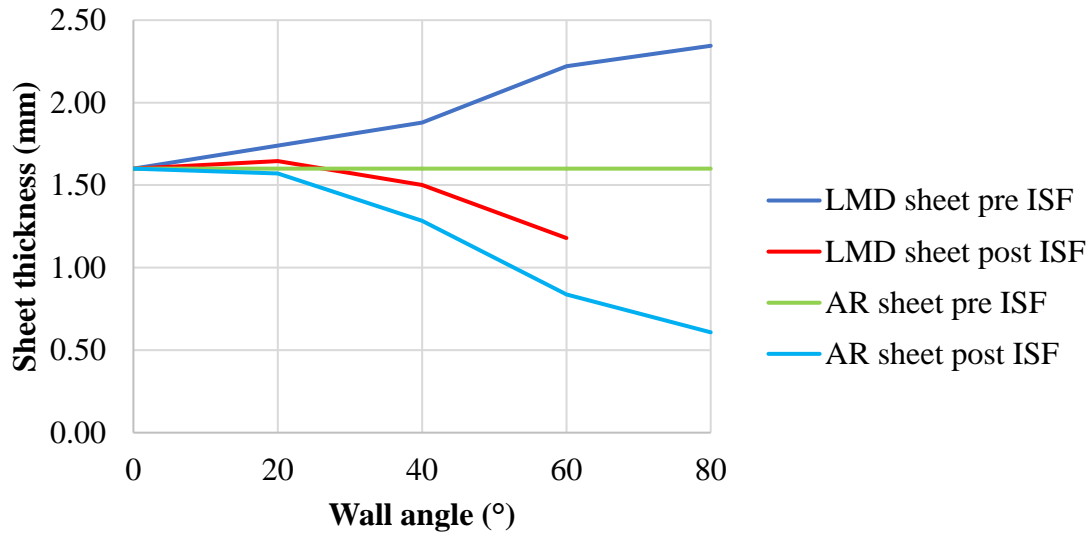


Figure 103 Thinning rate of the AR and LMD sheets during ISF

7.3.2 Surface roughness analysis

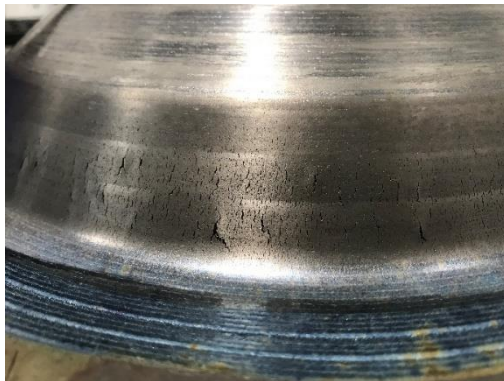
Surface roughness measurements were then performed on extracted material samples from the ISF part. The LMD built tracks on the 20° angled wall were visible after forming was completed, Figure 104 (a). In contrast, the surfaces of the 40° and 60° wall sections were observably smoother suggesting the increasing forming angle affected the surface roughness, Figure 104 (b-c). A possible reason for this is the material stretched during forming, reducing groove depth and build height of the LMD deposit surface. Also, burnishing by the forming tool. An oxidation colour was seen to reduce in intensity on the high angled wall sections, suggesting the oxidised surface was stretched and distributed over a greater surface area, causing the blue colour to fade. Nucleation and subsequent development of cracks in the forming depth direction were observed in the 60° angled wall. This speaks about exhaustive stretching and the material perhaps lacking the capability to be formed to such an extent. It needs to be determined if failure is a response to the stress state when forming at 60° with respect to the horizontal. Or else it may well be a frictional problem related to the sheet to tool contact relationship damaging the surface, possibly cyclically as the tool passes over the same area multiple times, which may have led to micro-cracking of the deposit surface, micro-cracks coalescing, and eventually a rupture.



(a)



(b)

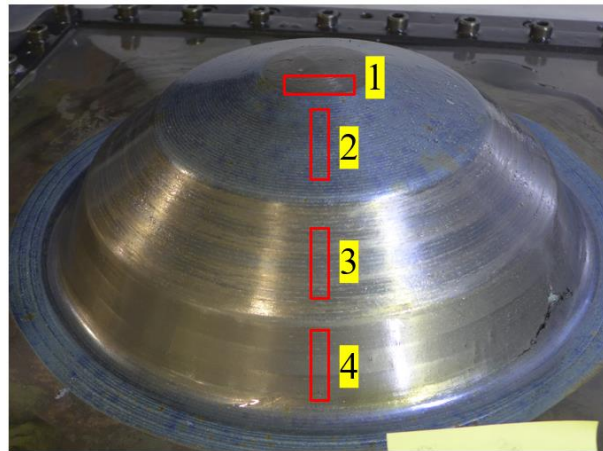


(c)

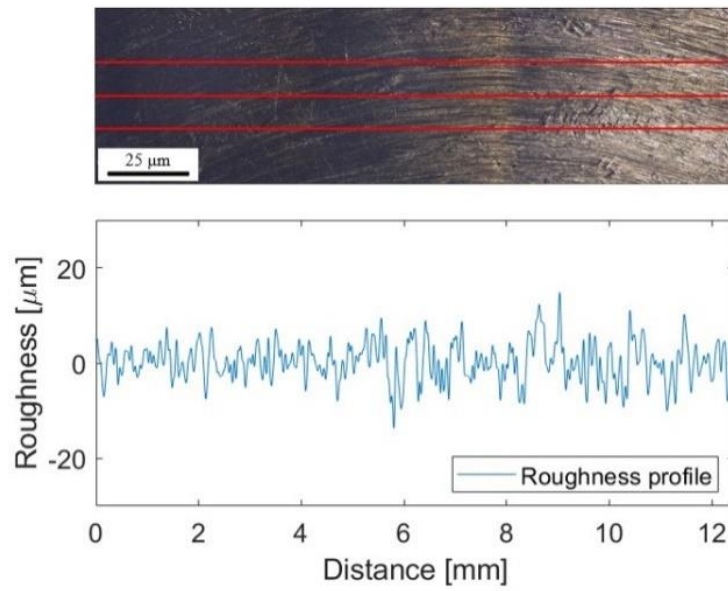
Figure 104 Surface roughness: (a) 20° section; (b) 40° section; (c) 60° section.

A correlation between the forming angle and surface roughness was observed. The roughness reduced as the wall angle increased. The average roughness (Ra) for the AR unformed section was 4.74 μm , Figure 105 (a). For the 20° wall angle section Ra was 9.72 μm , the 40° wall angle Ra was 6.92 μm , and for 60° wall angle Ra was 6.23 μm , Figure 105 (b-d). A sample was first taken from the area with no LMD material (sample 1). Samples for roughness measurements were then taken perpendicular to the LMD track direction from each angled section. From 20° wall angle section (sample 2), 40°

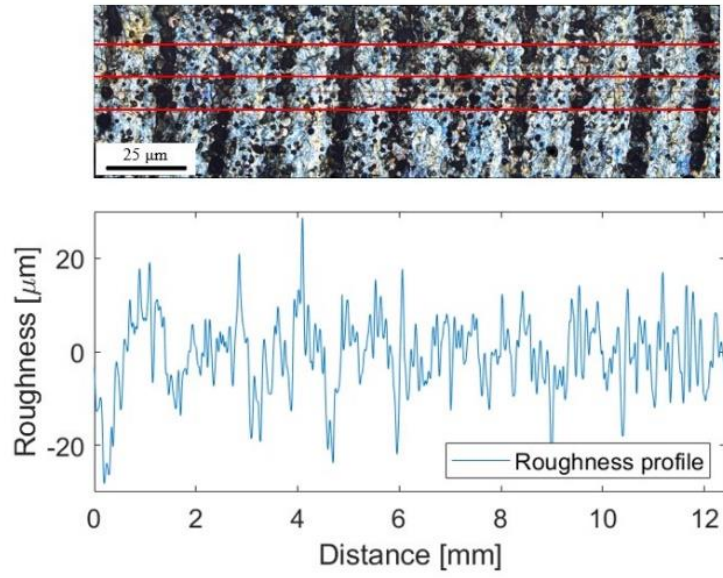
(sample 3), and 60° (sample 4). Despite care being taken when positioning the section lines on the 60° section, surface micro-cracks may have impacted the Ra value.



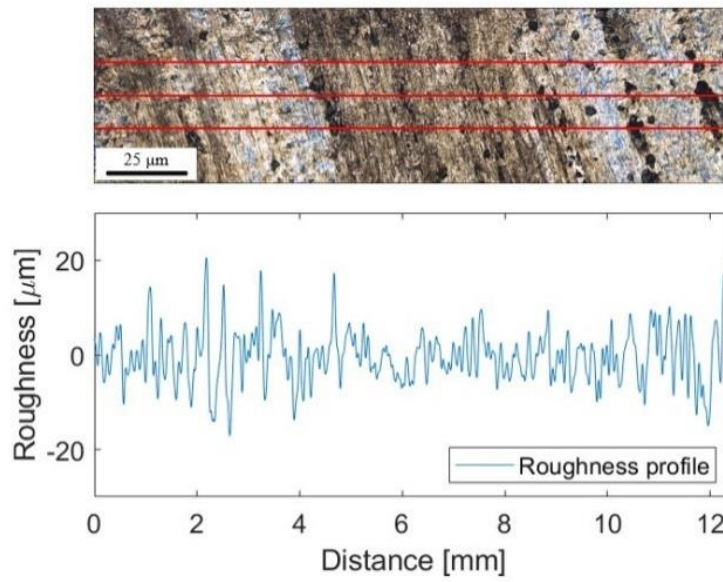
(a)



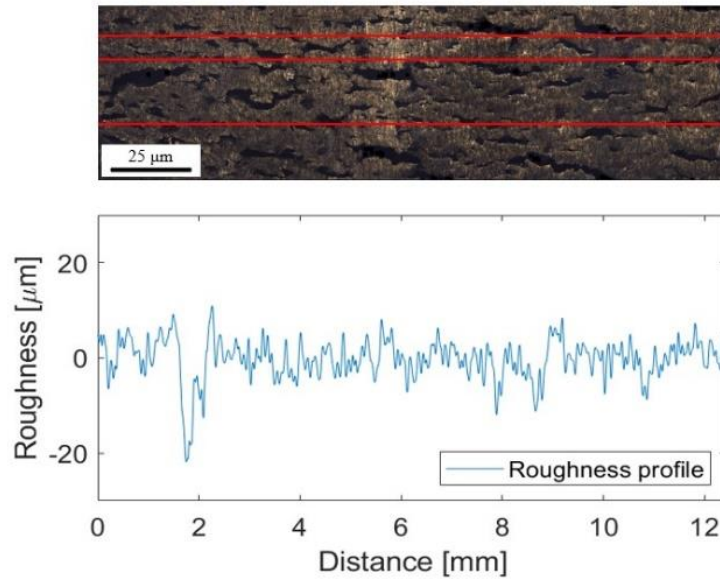
(b)



(c)



(d)



(e)

Figure 105 Surface roughness (Ra) calculations: (a) Sample orientations; (b) Sample 1; (c) Sample 2; (d) Sample 3; (e) Sample 4.

7.3.3 Micro-cracks on 60-degree wall.

On the 60° angled wall micro-cracks appeared on the surface, Figure 106. These micro-cracks were seen to nucleate from the top surface of the tailored preform. Also, micro-cracks were seen to coalesce and form larger cracks approximately 1-2 mm in length. The cracks stretched in the tool movement direction with their length perpendicular to the forming depth direction.

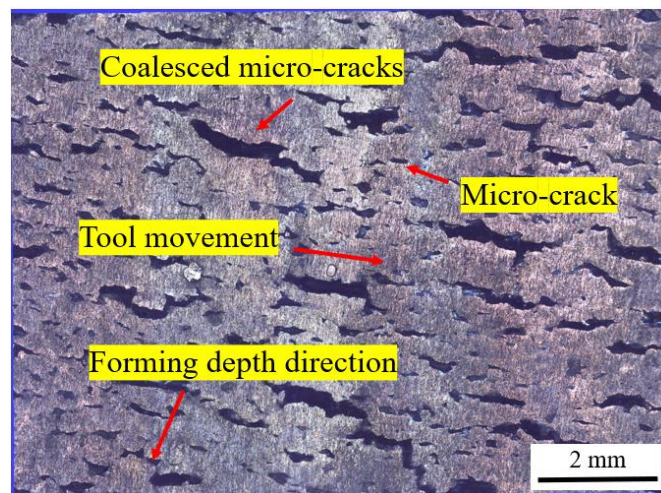


Figure 106 Micro-cracks and propagated cracks on surface of sample 4.

A higher quality surface was observed on the un-changed substrate side of the formed part. During the tensile test it was seen that the substrate material stretched at a greater rate than the LMD surface and effectively pulled the LMD surface apart. This was likely a result of the lower formability of the LMD material. It makes sense this happened to the LMD tailored sheet during ISF. Another observation during tensile testing was the cracks growing from the grooves of the deposit meaning crack propagation was largely controlled by the deposit morphology. It is possible this same phenomenon led to the crack formation during ISF. However, the act of the ISF forming tool stretching the sheet and flattening the grooves likely lessened the influence of the LMD deposit morphology on crack propagation. Another possible influence which may have impeded forming and led to premature cracking of the sheet is alpha case ingrained in the deposit surface, a possible side effect of the stress relief heat treatment of the sheet prior to ISF. Alpha case would result in premature cracking of the sheet during forming as the higher oxygen level would make the surface more brittle. There exists a research opportunity to repeat the LMD/ISF process with two key changes. First, polishing the LMD side to achieve a smooth surface. Second, form the material from the substrate side. However, to justify this further work it must be established if indeed it is the surface condition or microstructure which is the main influencing factor on the formability of the LMD tailored CP-Ti sheet.

7.3.4 Fracture, zig-zag crack on 60-degree wall

Part failure was noted when a crack opened and spread across the sheet thickness when forming the 60° wall section. The crack spread in a zig-zag pattern, see Figure 107. This is typical of tension induced failure under Mode I loading condition and plane strain condition (Anderson, 2005). Maximum plastic strain occurs at 45° to the crack plane due to tensile forces, Figure 107. This would normally be in the direction of the crack, however global constraints from the surrounding material does not allow this. The crack reconciles with these competing requirements to remain in its original plane by growing in a zig-zag pattern. This is the ductile crack growth theory (Anderson, 2005). The wrinkles produced due to in-plane compressive forces likely induced crack propagation

leading to the crack opening in this manner. This may explain why the crack formed close to the wrinkle location, Figure 107.

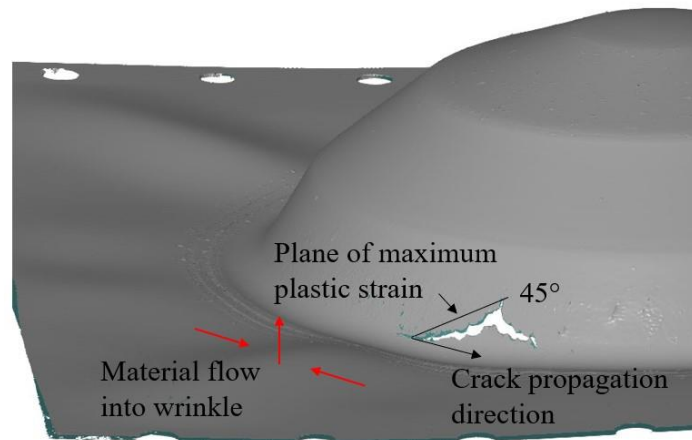


Figure 107 Analysis of crack formation and shape.

Fractography analysis was used to investigate the fracture in greater detail. In the microscopic image across the cross-section of the fracture face several key areas were identified, Figure 108.

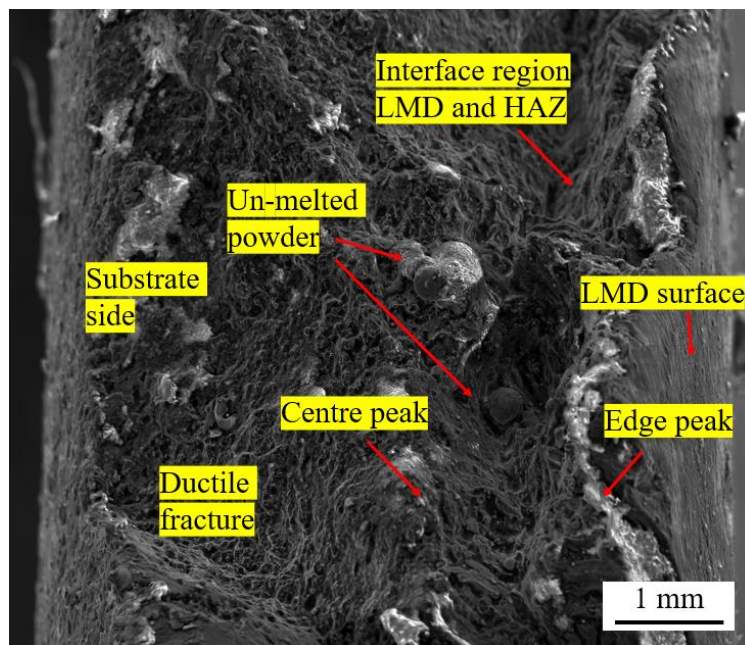
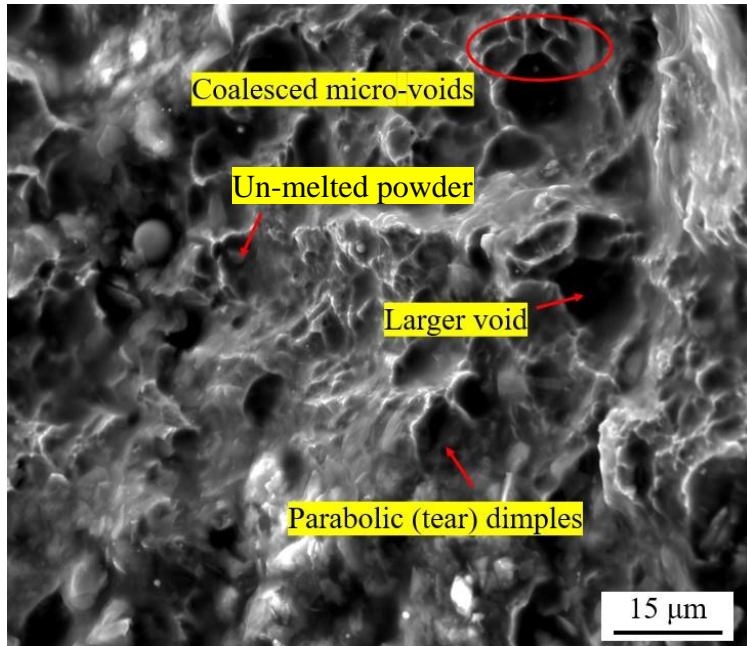
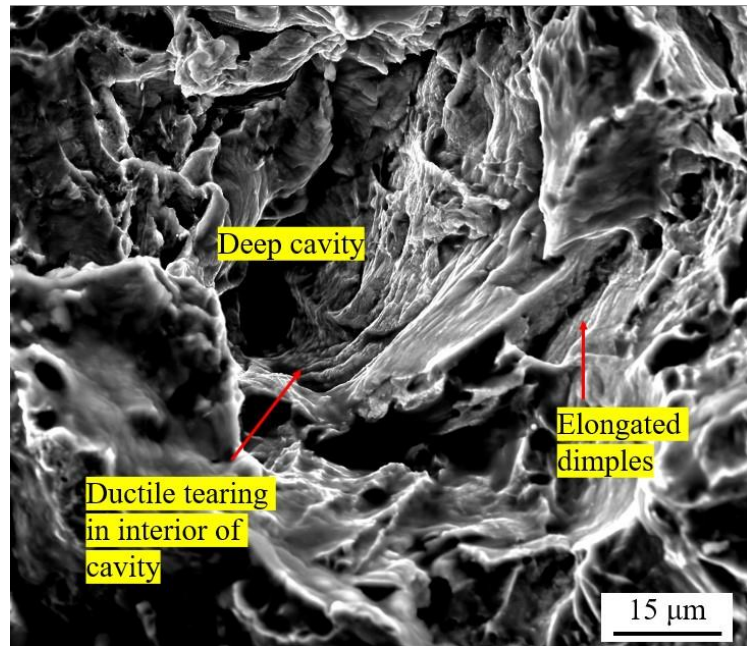


Figure 108 Fractography of fracture face on zig-zag crack.

Higher magnification images were taken at different areas on the fracture surface, Figure 109. On the substrate side the typical ductile fracture mode occurred. Un-melted powder was seen to have settled into the fracture face which likely will have both reduced the material properties being an internal defect, and acted as stress propagators leading to early fracture. The size of the un-melted powder particle is not representative of the 45-90 μm powder size distribution of the virgin powder used in the LMD operation. This may be a result of the powder not being in focus during imaging. The surface of the fracture also contained many small dimples packed together. These dimples will have nucleated as voids from inclusions and linked up by local internal necking which will have led to void coalescence as seen in the captured micrograph, Figure 108. Parabolic dimples were observed in the fractured material at the substrate side of the specimen. These parabolic dimples occur when there is a gradient to the axial opening stress, such as when bending is a dominant fracture mechanic (Pineau et al., 2016). These parabolic dimples are directed towards the centre of the specimen, Figure 109 (a). On the LMD side of the fracture face the effect of the larger grains on the failure evolution was visible. This presented as deep cavities with ductile tearing in the cavity interior, Figure 109 (b). The large cavities formed from smaller voids linking together. The dimples were elongated which likely corresponds to the original crystal orientation. It was likely that trans-granular fracture (fracture through the grain) occurred due to the size of the grains in the LMD microstructure. However, this was not clear from the images. Grain cleavage on the face of the LMD added material suggests the additive material was a quasi-brittle material rather than fully ductile, Figure 109 (c).



(a)



(b)

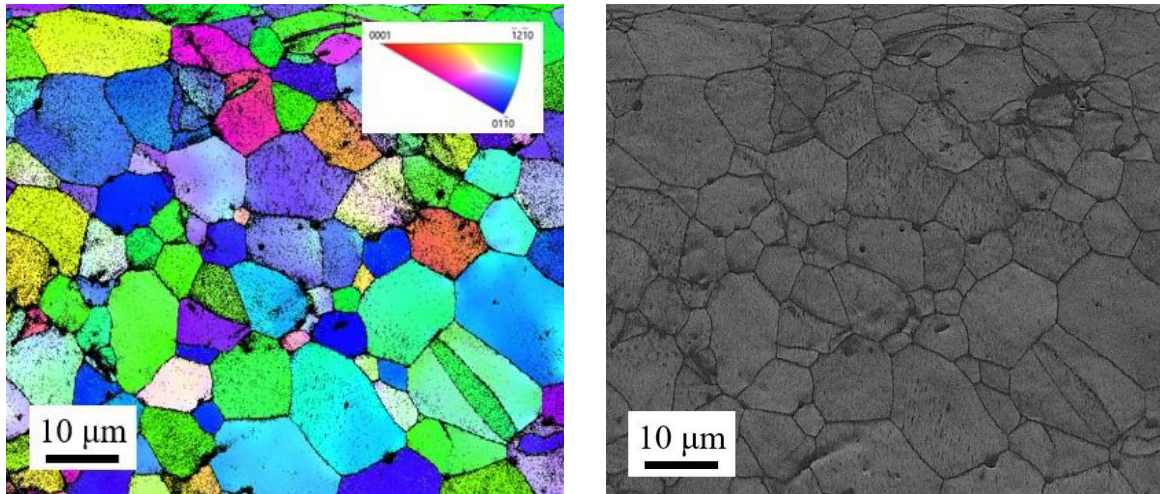


(c)

Figure 109 Fractography images: (a) Substrate side of LMD sample; (b) Fracture within LMD layer; (c) Grain cleavage on surface of LMD layer.

7.3.5 Microstructure of LMD material post-ISF

Samples were taken from the 20° and 60° wall angles sections for microstructural analysis. These material samples were prepared to a mirror finish for EBSD. This involved cutting, mounting, grinding, polishing, and a final electropolishing step. The material was analysed using the SEM as described in section 3.3.15. High magnification images of the material microstructure were taken for analysis. Firstly, from the 20° formed wall, see Figure 110, then from the 60° formed wall, see Figure 111.

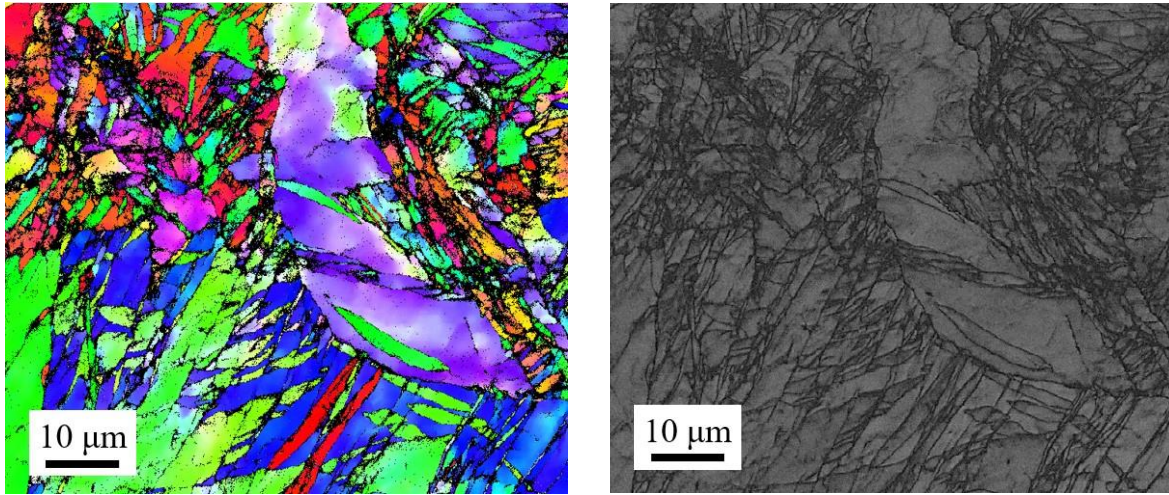


(a)

(b)

Figure 110 Microstructure images of 20° section: (a) IPF map; (b) BC map.

The material within the 20° wall angle section had one 0.15 mm layer of LMD added material making this section 1.9 mm in thickness before forming, Table 15. The total material removed during the material preparation process was 1.49 mm of the 1.75 mm original thickness (T_0). So, the microstructure map was taken from a region somewhere within the interface between the HAZ and the unchanged substrate material. This was determined using the measurements of the optical images from the previous LMD tailored material, section 6.3.2. For the 20° microstructure no significant grain growth was observed. The grain growth in the previously tailored material was seen closer to the surface containing the LMD material. This was likely because the heat input from the laser did not penetrate deep enough into the material for long enough to cause any major grain growth effect. The grains were equiaxed with average size of 4.5 μm , close to the AR materials grain size of 5.4 μm . Some twinning was observed in the microstructure of the formed material. It is possible the twins resulted in a smaller average grain size calculation as the intercept method can sometimes include twins as boundaries. A relatively random crystal orientation was observed with slight preference for a (1210) and (0110) crystal texture, Figure 110 (a).



(a)

(b)

Figure 111 Microstructure images of 60° section: (a) IPF map; (b) BC map.

The second EBSD image was taken from the 60° wall angle section. This microstructure was representative of the material at its highest deformation before failure. The material sample extracted from the 60° wall angle section contained five layers, so 0.75 mm, of added material making the sheet thickness in this area 2.35 mm prior to forming. The total material removed during the material preparation process was 1 mm meaning the microstructure under investigation was at the interface region between the LMD layer and HAZ. This area was chosen for analysis to further investigate the interface between the deposit and substrate. This analysis used the optical images across the thickness of the etched material samples from the earlier work in this research, see Figure 87 (b). Grain growth was a direct consequence of the thermal input from the laser. A single coarse grain in the tailored material measured at approximately 40-50 μm in length, Figure 111 (a). Intragranular misorientation was observed in this grain as evidenced by the IPF colouring, Figure 90 (a) and (c). The low angle intragranular misorientation in this grain is likely a result of the accumulation of dislocations during deformation. There is severe grain refinement across the microstructure with fine high angle grain boundary (HAGB) twins.

7.3.6 LMD preform surface optimisation

A potential defect which may have been an influencing factor for the early fracture of the tailored sheet blank during ISF was the surface morphology of the LMD build. It is possible that improving the surface by reducing surface roughness could improve the performance of the material during ISF, as suggested in section 6.4. As such, introducing machining or polishing of the surface post-printing and pre-forming as an additional processing step could improve the LMD/ISF hybrid operation. A surface with lower roughness could reduce friction between the surface and the ball bearing in the forming tool. Grinding and polishing of the surface of material samples extracted from the LMD material was performed to test the possibility of this processing step. Samples with 0.6 mm and 0.9 mm thickness added via LMD were taken and, using 250 grit grinding paper, the surface manually ground until the surface had no evidence of the LMD build tracks. Three measurements of the sample thickness before and after polishing were taken and the average thickness calculated to measure the material removed, Table 18.

Table 18 Surface grinding depth to flatten LMD builds.

Sample	Before (mm)	After (mm)	Removed (mm)
0.6 mm LMD	2.23	2.07	0.16
0.9 mm LMD	2.53	2.40	0.13

0.16 mm was removed from the 0.6 mm LMD sample by grinding and polishing before a flat surface free of surface undulation from the LMD built tracks was reached. Effectively, a full 0.15 mm layer was removed in the process. Likewise, for the 0.9 mm LMD sample 0.13 mm of material was removed. It was concluded an entire 0.15 mm layer of build material needs to be removed to create a flat surface following LMD. This necessitates an additional 0.15 mm layer to be deposited which could potentially lead to increased processing time, more waste material, and higher costs. Increasing the number of layers to be deposited may also increase the likelihood of sheet distortion

during LMD. However, if it can improve the surface finish this should be a legitimate consideration for post-LMD processing. Further work in this area is recommended for future work. Despite this, another potential route to improve surface finish is the optimisation of LMD machine parameters to flatten the surface and lessen the impact of the friction between roller ball and LMD surface. Scanning the laser over the surface to re-melt the powder without adding more powder could fully melt partially melted and unconsolidated powder on the surface. This would be cheaper and faster than a post-grind operation. However, excess heating could potentially impart extra residual stress into the sheet. Further consideration and testing of post-LMD surface finishing is suggested.

7.4 Summary

- The material generated by LMD was shown to have distinctive microstructures in regions through its thickness. At the base of the sheet is the AR cold rolled CP-Ti with fine equiaxed microstructure. In the middle interface region is the HAZ which contains a mixture of coarse and refined grains. At the top is the LMD layer which contains large grains with internal misorientations.
- When tested under uniaxial loads the tailored material presented with lower ductility and formability than the AR material, section 4.3.1. The performance of the LMD tailored sheet under ISF was however poorer than expected based off the uniaxial testing results.
- The LMD tailored preform failed when forming the 60° wall in contrast to the AR material which could form walls at angles up to 80° to the sheet plane before fracture.
- Micro-cracks propagated in the LMD surface and coalesced to form larger openings which eventually opened at the substrate side of the sheet, resulting in complete through-thickness failure. Further testing is required to determine the mechanical performance of the LMD tailored material under the biaxial tensile

stress states, which were suggested to have been prevalent when forming the high angled walls.

- ISF of the additively tailored CP-Ti preform was useful although the results did not meet the expectation. More investigations should be conducted in the future.

Chapter 8

8 Biaxial testing of additively tailored CP-Ti blanks

8.1 Chapter Overview

The early onset fracture of the additively thickened commercially pure titanium (CP-Ti) sheet during Incremental Sheet Forming (ISF) was a surprising outcome of the experimental trial considering the tensile behaviour of the laser metal deposited (LMD) thickened material when tested previously, see section 4.3.1. The LMD CP-Ti tensile specimens did not present with significantly lower formability than the as received (AR) CP-Ti tensile specimens under room temperature uniaxial tension. As such, further experimental analysis was undertaken to explain why the LMD tailored material failed earlier than expected during ISF. The LMD CP-Ti sheet specimens with thickness 1.9 mm were put under biaxial strain conditions in a Nakajima test to create a forming limit diagram (FLD). An FLD for 1.6 mm thick CP-Ti sheet specimens in the AR condition (cold-rolled with no additional LMD thickening) was experimentally generated to compare the material properties. The Nakajima test has been used in prior studies to produce a fracture forming limit curve (FFLC) identical to that constructed from incremental sheet forming (ISF) tests for pyramidal and conical truncated parts (Isik et al., 2014). Considering this, the Nakajima test was used to examine the forming behaviour of LMD CP-Ti specimens to better understand the materials performance when formed under the prominent deformation modes present in ISF, see section 7.2.9. This chapter will describe the experimental procedure for the Nakajima test and provide a discussion on the results.

8.2 Experimental procedure

8.2.1 Nakajima test setup

The Nakajima test consists of a hemispherical punch, blank holders, lubricant, and a camera setup, see the schematic in Figure 112. A stochastic pattern is applied to the surface of the sheet specimen and the deformation is recorded by cameras. The specimens are then deformed at ambient room temperature until fracture. This method is used to measure the strain evolution across the surface of the deformed specimens.

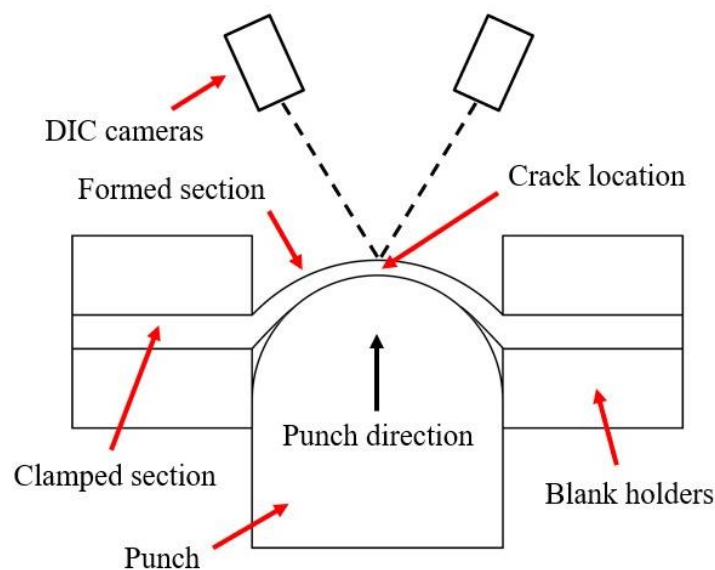


Figure 112 Nakajima test schematic.

The forming behaviour and work hardening of a material are investigated using the Nakajima test. Material samples are exposed to significantly larger strain levels than during a uniaxial tensile test (Banabic, 2020). Different deep draw and stretch forming conditions are achieved by varying the size of the specimen gauge (Paul, 2013). A FLD is generated by analysing the strain evolution across the surface of the specimen up to, and beyond, fracture. The points for major and minor strain (ϵ_1 and ϵ_2 , respectively) in the FLD determine the materials safe forming limit. Using the strain data, a forming limit curve (FLC) is created to determine the extent to which a material can be deformed

by any combination of drawing and stretching assuming a linear strain path (Paul, 2013), Figure 113. A FLD is split into two branches:

- The left branch for positive strain, ϵ_1 and negative strain ϵ_2
- The right branch for positive ϵ_1 and ϵ_2 .

For this study, the FLC was generated for the AR and LMD CP-Ti specimens solely within the right branch of the FLD. This covers strain ratios from plane ($\alpha = 0$) strain to full equi-biaxial ($\alpha = 1$) stretching. A comparison of the resulting FLC will be used to investigate the failure behaviour of the LMD CP-Ti material to explain the early failure of the tailored sheet during ISF.

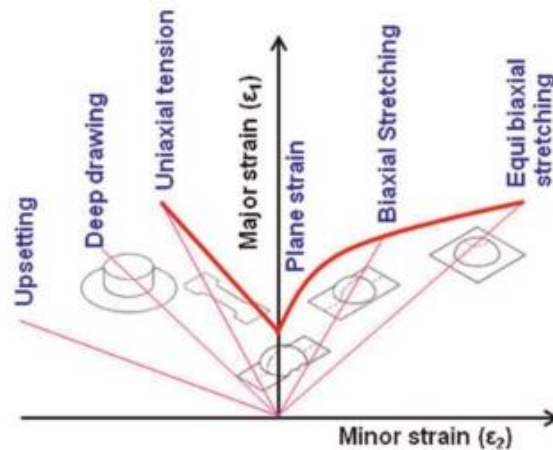


Figure 113 FLC schematic (Paul, 2013).

8.2.2 Nakajima test variables

The Nakajima test variables were selected with consideration of the previous uniaxial tensile results and the availability of equipment and materials with the goal of simplifying the design of experiment (DoE). The uniaxial tensile results showed that increasing the quantity of LMD layers had little impact on the strength properties of the tailored material, see section 4.3.1, so the LMD build thickness was not selected as relevant test variable. Likewise, the isotropy of the LMD tailored CP-Ti material justified the decision to not include gauge orientation as a test variable. The CP-Ti material was thickened to a single build height using LMD and the impact of deposit orientation was assumed to be negligible. The test specimens were subjected to three

strain states during testing. These were plane strain, biaxial, and equi-biaxial stretching. Failure by fracture in incremental sheet forming (ISF) with suppression of necking is typically governed by the fracture forming line (FFL) in the principal strain space (Maria B Silva et al., 2011). Pyramidal (flat polygon base with four flat triangle lateral faces rising to a single point) and conical (flat circular base with curved face rising to a single point) parts of 0.7 mm thick grade 1 titanium sheet were formed by ISF. The ϵ_1 was seen to rise above the FFLC only in the right branch of the FLD indicating failure occurred only under some form of biaxial stretching (Gatea et al., 2018), Figure 114. This justified the decision to only generate strain data in the right branch of the FLD.

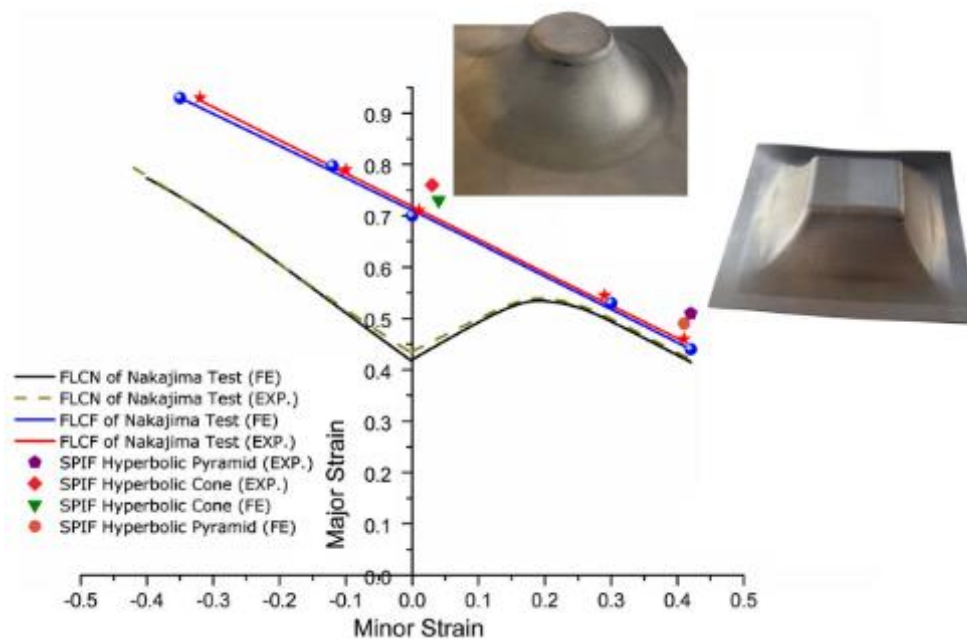
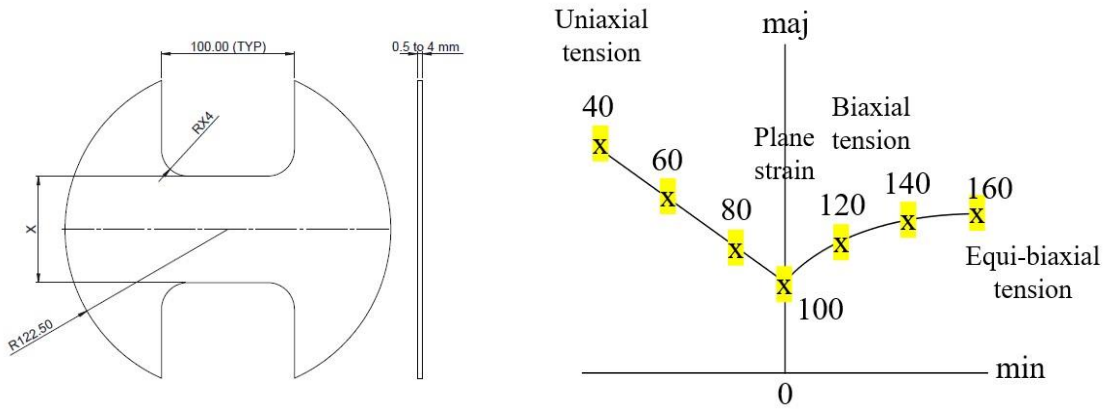


Figure 114 Strain values for ISF of titanium above the FFLC (Gatea et al., 2018).

8.2.3 Dimensioning Nakajima test specimens

The geometry and design of the Nakajima sheet specimen is typically governed by ISO 12004-2:2021, see Figure 115 (a). In accordance with the ISO standards the specimen was designed circular in shape with a gauge section and thickness was kept in the threshold of 0.5 mm to 4 mm. The width (X) of the gauge section was adjusted to test the material across the different strain states in the FLD ($X = 40$ to 160 mm), Figure 115 (b).



(a)

(b)

Figure 115 Nakajima test piece geometry: (a) Dimensions; (b) Correlation between gauge width (X) and strain state.

However, because of material limitations miniature specimens each with a diameter of 55 mm were created for this experimental Nakajima test, see Figure 116. It was not possible to prepare enough 245 mm diameter specimens to test strain across the entirety of the FLD right branch with the available material. A study by Casari et al. (2006) showed good agreement between the strain path imposed when testing the standard specimen compared to specimens which accommodated a punch size down to a 50 mm punch. This was used to justify the use of the smaller specimen size. The selected gauge widths of the miniature specimens for testing are provided in Table 19.

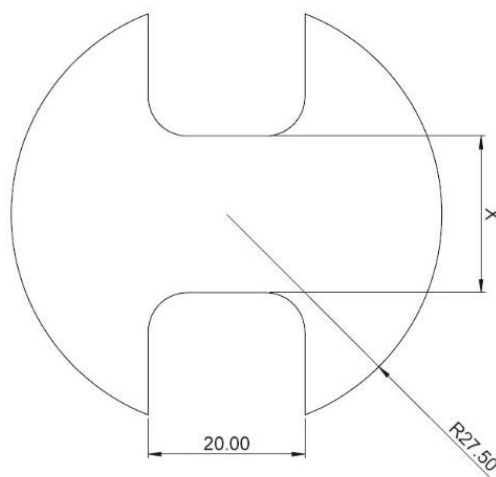


Figure 116 Adapted miniature FLC specimen.

Table 19 New specimen gauge width and testing strain state.

Gauge width according to ISO12004-2:2021 (mm)	Gauge width of miniature specimen (mm)	Strain state
100	20	Strain plane
120	24	Biaxial strain
140	28	Biaxial strain
160	55	Equi-biaxial strain

8.2.4 Design of LMD material and Nakajima test specimens

SolidWorks was used to model the sheet substrate and the LMD deposit. Consideration of specimen locations ensured sufficient LMD material was deposited in the correct location. Engineering drawings were created for the laser specialist, see Appendix 10.6. By switching to the miniature specimen design three test repeats for each variable configuration was possible to ensure possible outliers in the data did not impact the strain results. A design of experiments (DoE) was made for the Nakajima test, see Table 20. Each specimen ID number coincided with the specimen location.

Table 20 Design of Experiments for Nakajima test.

Specimen ID #	Gauge width (mm)	Thickness (mm)	Strain state	Speed (mm/s)	Repeats
1	20	1.9	Plane strain	1	3
2	24	1.9	Biaxial strain	1	3
3	28	1.9	Biaxial strain	1	3
4	55	1.9	Equi-biaxial strain	1	3

5	20	1.6	Plane strain	1	3
6	24	1.6	Biaxial strain	1	3
7	28	1.6	Biaxial strain	1	3
8	55	1.6	Equi-biaxial strain	1	3

8.2.5 Performing laser metal deposition

A LMD thickened CP-Ti sheet was manufactured for generating the Nakajima test specimens. To maintain consistency, the same laser specialist was used to perform the LMD and the LMD machine parameters and setup conditions were kept consistent as previous LMD trials, see section 7.2.5. The CP-Ti LMD sheet again was clamped into the LMD fixture, fixed to a pallet, and transported to the laser specialist. LMD build layers of 0.15 mm were created on the top surface of the CP-Ti substrate sheet. CP-Ti Grade 2 gas-atomised powder from the same material stock as before was fed through the nozzle into the laser generated melt pool. Two layers were deposited in a spiral pattern across the sheet adding 0.3 mm of additional thickness to the CP-Ti sheet, Figure 117. The LMD fixture was clamped directly to the T-slot table to avoid movement during LMD which could risk reducing part quality. The toolpath programme for Layer 1 of the LMD preform was run twice to achieve a uniform deposit of 0.3 mm across the sheet substrate, see section 4.2.3.

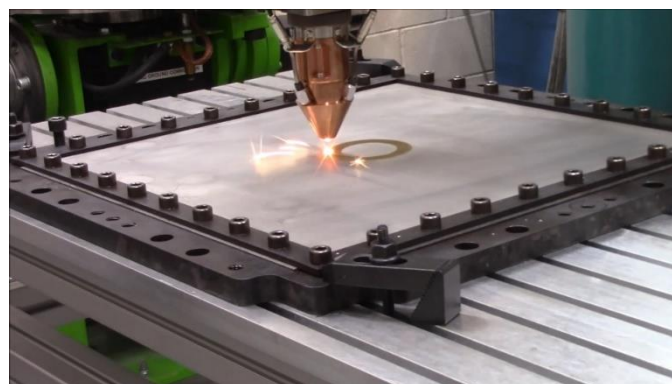


Figure 117 Generating LMD tailored sheet for Nakajima test.

The decision to deposit a layer of 0.3 mm equal thickness across the sheet was made for three reasons:

1. To limit thermal input from the laser.
2. To limit the volume of powder used.
3. Thickness was shown to have little to no effect on the mechanical properties.

Limiting the amount of thermal input from the laser reduced the likelihood of sheet distortion. Any sheet distortion would make wire-EDM difficult to perform and potentially damage the deposited material. Also, limited budget meant no new powder was purchased. This meant a limited volume of leftover virgin powder and some recycled powder collected from the LMD machine hopper was available to generate the thickened Nakajima specimens. The laser specialist was asked to prioritise use of virgin powder unless necessary to reduce the likelihood of powder impurities impacting LMD part quality.

8.2.6 Preparing Nakajima test specimens

The AR CP-Ti sheet was cut to size using a guillotine and sent to the laser specialist to perform LMD. Following LMD a residual stress heat treatment was performed using the same procedure and equipment as the previous trial, see section 3.3.5. A 3d scan of the LMD sheet was performed using the same procedure and equipment as the previous trial, see section 3.3.1. Maintaining consistency in testing ensures consistency in the quality of results. With an Agie Charmilles wire-EDM machine the sheet metal specimens were cut from the tailored CP-Ti material. Wire-EDM ensured a high-quality edge condition on the specimens was achieved to avoid influencing the fracture mechanism during the Nakajima test. Engineering drawings for the test specimen cutting strategy are available in Appendices 10.6 and 10.7. A white coat of paint was spray painted on the surface of each specimen and dried overnight. The following day a black paint was sprayed on the surface in a speckle formation to create a stochastic pattern for strain analysis, see section 3.3.8 for information on these preparation steps. This method was chosen in place of engraving a deterministic grid of precise

dimensions because of equipment availability and time restrictions. A potential risk of using a stochastic speckle pattern is the paint peeling or cracking during forming which can impact the quality of strain measurement. Proper application of the base layer was ensured to reduce the likelihood of this occurring. The fundamental method of strain analysis is best described by imagining a circle on the specimen surface. In response to deformation of the specimen the circle will change shape and the new dimensions of the major (d_1) and minor (d_2) axes of the circle can be used to calculate values of ϵ_1 and ϵ_2 using Equation 11 and Equation 12, see Figure 118. Using the same principle, the DIC system measures the surface strain using the stochastic pattern. Unlike a single gauge which measures a single strain direction, such as during uniaxial tensile testing, the speckle pattern allows for many virtual strain gauges in all directions for measuring strain.

$$\epsilon_1 = \ln \frac{d_1}{d_0} \quad \text{Equation 11}$$

$$\epsilon_2 = \ln \frac{d_2}{d_0} \quad \text{Equation 12}$$

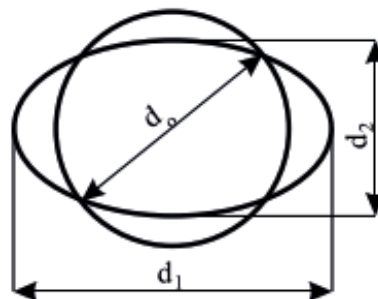


Figure 118 Strain determination (J Adamus et al., 2015).

8.2.7 Test equipment

A Zwick/Roell BUP 1000 sheet metal testing machine was used to perform the Nakajima test, Figure 119 (a). The ISO 12004-2:2021 standard was followed to ensure proper determination of the FLC. A hemispherical punch with accompanying die set formed the sheet specimens, Figure 119 (b). A lubricant was applied to the punch and

specimen before forming to minimise friction. A GOM Aramis system captured the displacement of the stochastic pattern and measured strain on the specimen surface.



(a)



(b)

Figure 119 Nakajima test setup: (a) BUP machine; (b) Hemispherical punch.

8.2.8 Performing the Nakajima test

The Nakajima test was performed at ambient room temperature. The Nakajima test specimens were placed within the Zwick/Roell BUP machine, Figure 120 (a), and deformed by the rising punch until failure, Figure 120 (b). Appropriate failure to gather the correct strain results is the crack propagating on the centre of the specimen and spreading outwards. Some specimens cracked on their edge at the point of contact with the die so these measurements were rejected. Due to the novelty of the material properties this occurred with some of the early specimens formed until the test procedure was refined as discussed in section 8.3.2.

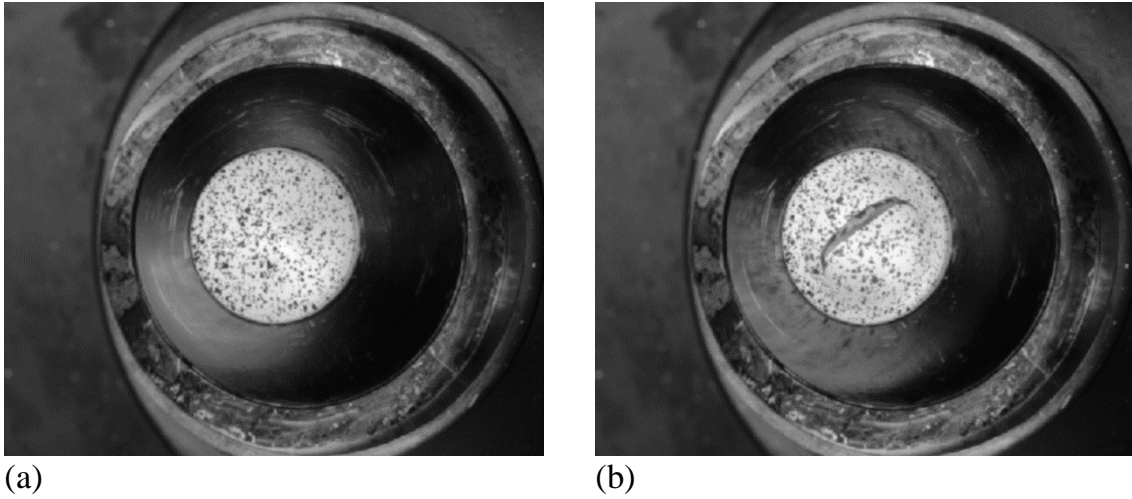


Figure 120 Successful Nakajima test sample: (a) Before; (b) After.

8.2.9 Determination of strain values

A series of strain maps were generated across the specimen surface for the complete forming operation using the GOM analysis software package. For each Nakajima specimen the strain map of the surface at the moment of crack initiation was selected. Three section lines were then drawn across the surface perpendicular to the crack opening, see Figure 121. The ϵ_1 and ϵ_2 values were measured across the section lines. The strain map images were cycled to the frame preceding the fracture initiation to measure strain at the moment of failure.

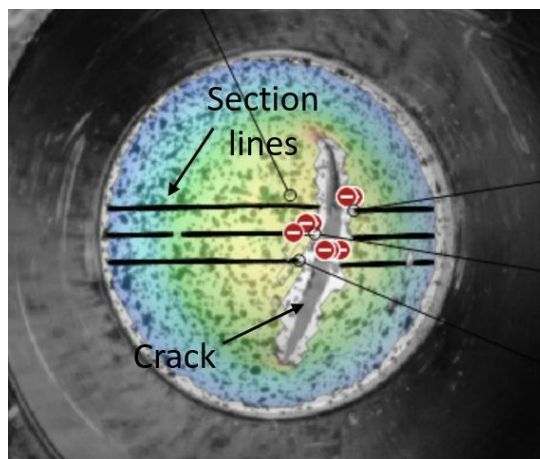


Figure 121 Section lines perpendicular to the fracture opening.

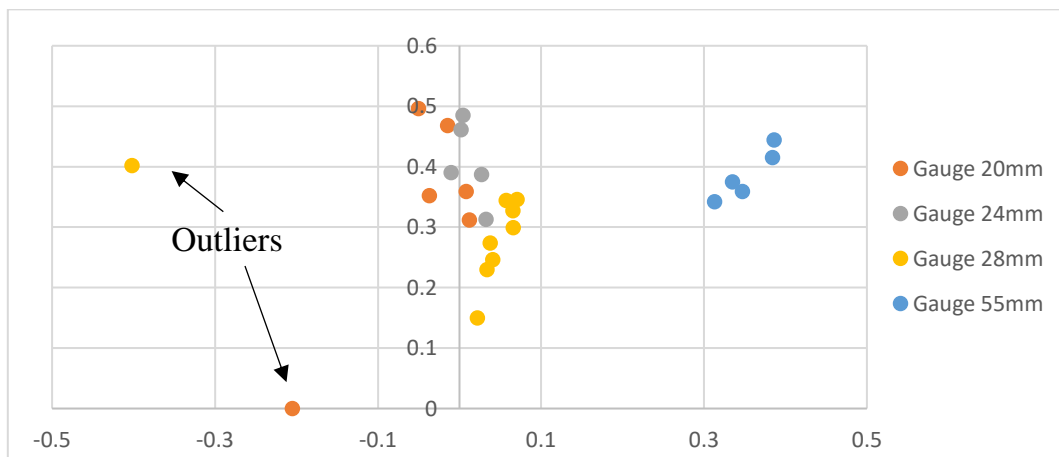
8.3 Calculating strain

8.3.1 Traditional method

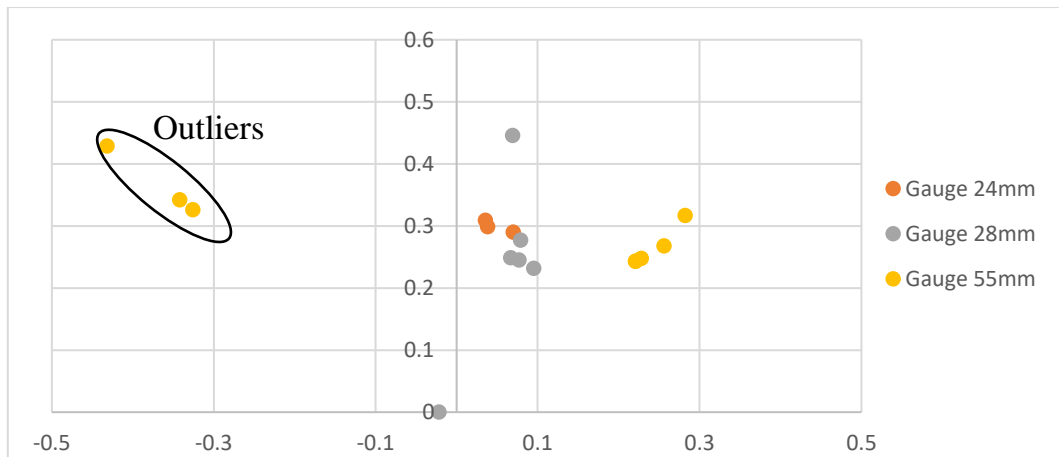
Typically, strain measurement for the Nakajima test is performed according to ISO 12004. The crack position is determined by best fit to a parabola using Equation 13 and the centre of the range is given by the highest value of ϵ_1 .

$$f(x) = ax^2 + bx + c \Rightarrow f''(x) = 2a \quad \text{Equation 13}$$

The second derivative is calculated using a range of 3 points ($x_1, y_1; x_2, y_2; x_3, y_3$) taken from the strain curve to create a parabolic fit of the ϵ_1 data without smoothing or filtering. This is done at both sides of the crack. The position of the highest of all peaks is determined within a range of 6 mm from the edge of the crack. The “filtered” second derivative is repeated for the ϵ_1 data using a range of 5 points for the parabolic fit. A curve regression is defined which is seen as a bell-shaped curve, from which a pair of ϵ_1 and ϵ_2 values is determined. FLC’s were generated using this method for the AR and LMD CP-Ti blanks, see Figure 122.



(a)



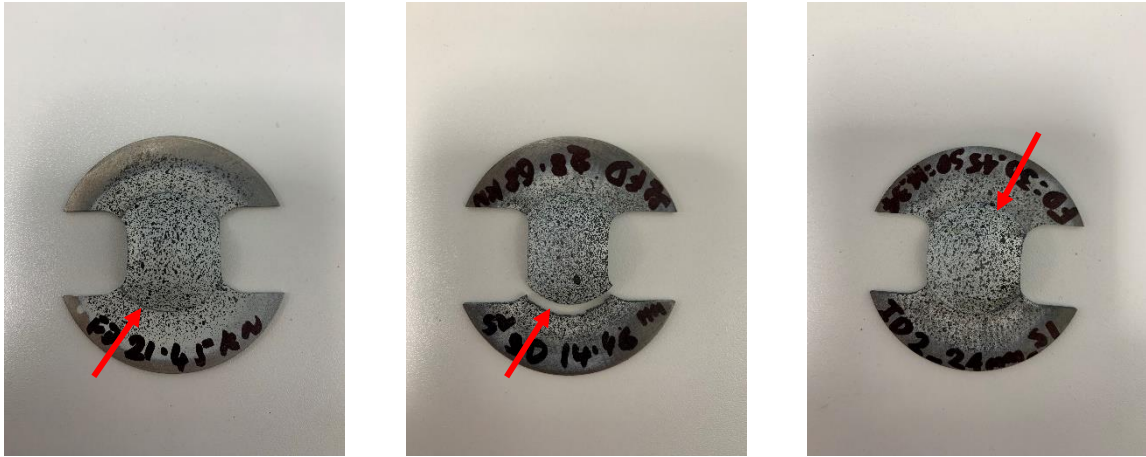
(b)

Figure 122 Forming limit diagrams (FLD's) containing forming limit curves (FLC's): (a) AR CP-Ti blanks; (b) LMD CP-Ti blanks.

However, some issues with these results were noted. Firstly, there is incomplete data as the plane strain specimens failed, meaning a complete FLC was not possible, Figure 123 (b). Secondly, outlying results were measured which would not allow a correct curve to fit the FLC. Performing further data analysis was necessary to clean the strain data before analysis.

8.3.2 Reasons for errors in measurements

Some common problems arose which seemed to have caused the measurement errors. The first was the location of the crack opening. When the crack started at the edge of the specimen in contact to the die edge this made the strain measurement either void or not measured by the system, see Figure 123. The void measurement is because the specimen contacting the die likely influenced the initiation of the crack, rather than the strain imparted to the specimen by the hemispherical punch. The material properties of the LMD tailored specimens were also novel to the machine operators meaning correct machine setup and test parameters were unknown prior to testing. This led to in-situ adjustments of the machine parameters and setup which included adding extra lubricant and a rubber gasket layer.



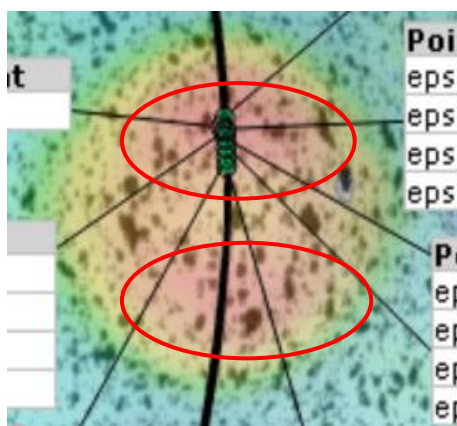
(a)

(b)

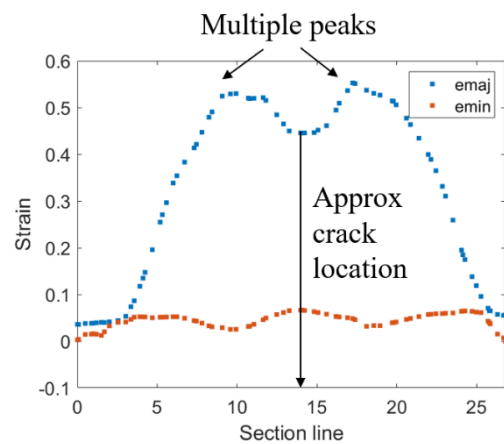
(c)

Figure 123 Cracks propagating at edge of sample resulting in void result.

The second and most prevalent error across the entirety of the test blanks was multiple peaks appearing in the ϵ_1 strain curve. Multiple peaks in data are typically caused by excess friction between the specimen and die resulting in inhomogeneous deformation of the specimen. This presents as two or more areas of high strain instead of a single peak to appear at either side of the crack, Figure 124. The common method of curve fitting using the 2nd order derivative does not allow for accurate strain calculation for a bell-curve with multiple peaks, resulting in unrealistic FLC values due to inaccurate best-fit approximations which underestimate the limit strain.



(a)



(b)

Figure 124 Multiple peaks: (a) Areas of split high strain readings; (b) The resulting strain curve.

8.3.3 Approximation of the strain curve

Two methods of data adjustment were tested to improve the accuracy of the strain results in response to the multiple peaks in the strain distribution data:

1. Perform multiple curve fitting to generate a single bell-curve which provides a more accurate reading of the max-min strain values at the sample center.
2. Calculate strain state values at independent points along each section line and average these at the point of necking and crack opening.

The above two methods of data manipulations were performed for specimen ID #2 to test their applicability before committing to the entirety of the test results. The sheet metal blank with ID #2 had a gauge width of 24 mm and was formed under biaxial strain. First, the multiple curve fit method of data manipulation was used to approximate the major-minor strain values for the sample in question. The strain data from the half containing the largest curve was extracted, see Figure 125 (a). This data was cleaned by interpolation and mirrored to form a bell curve, see Figure 125 (b).

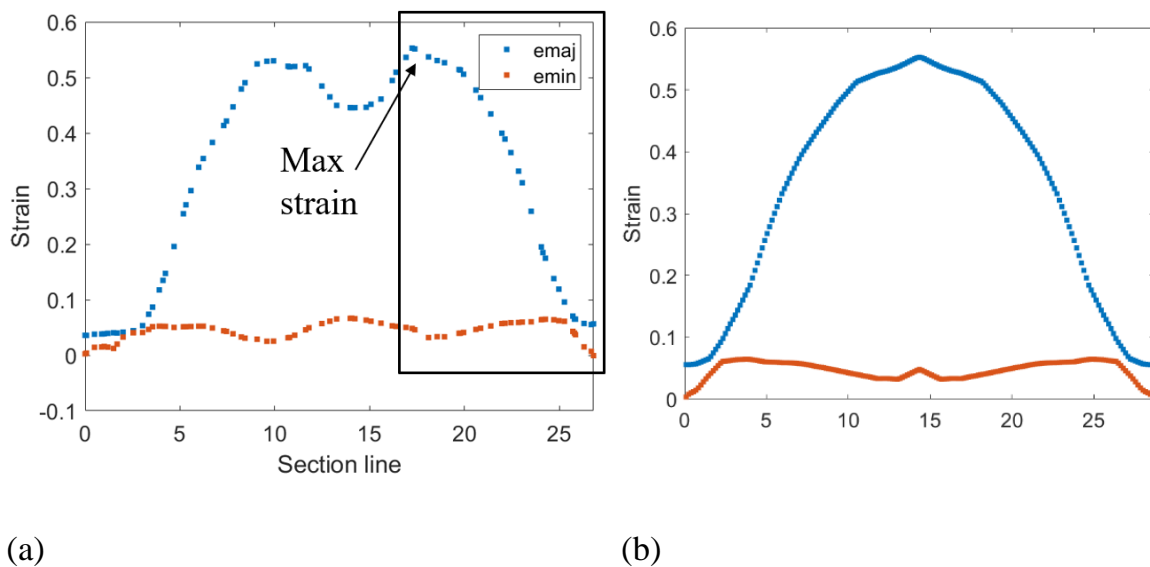


Figure 125 Interpolating data to solve for multiple peaks: (a) Maximum curve; (b) Interpolation and mirroring of data.

Curve fitting of the newly generated bell curve, using the method described in section 8.3.1, identified the new major-minor strain values, see Figure 126. Strain values are

provided in Table 21. The MATLAB script for performing this multiple curve fit is provided in Appendix 10.14.

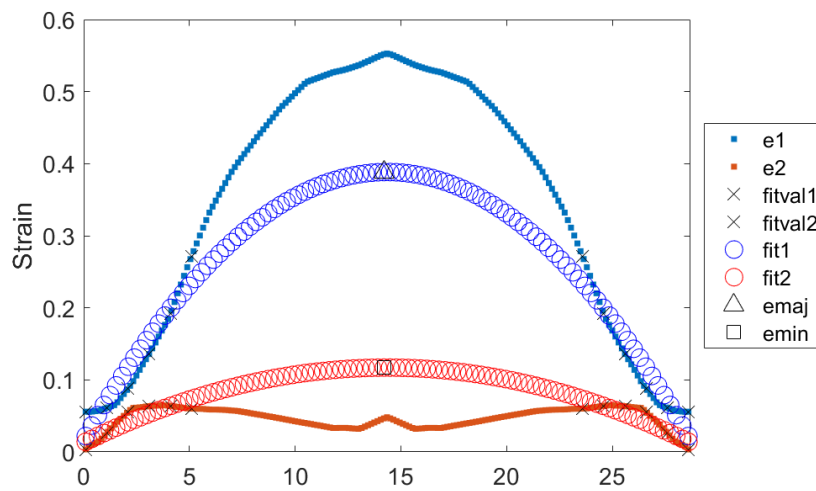


Figure 126 Final fitted curve from treated data.

The second data manipulation method for calculating accurate major-minor strain values makes use of the temporal analysis of the major strain distribution and its first-time derivative for a series of points selected along a section line drawn perpendicular to the crack. Point A is at the boundary of the instability region and is defined by the points on either side of the crack that cease to strain and reach zero strain as the crack appears, and point B is the fracture point and is identified as the point which exhibits the maximum strain evolution, Figure 127 (M B Silva et al., 2015).

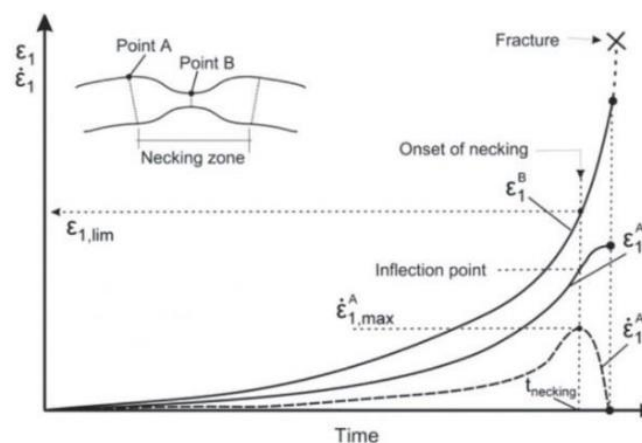


Figure 127 Scheme of time-dependent methodology (M B Silva et al., 2015).

This second method of strain data manipulation was performed again on specimen ID #2. Using GOM analysis the moment of strain was found on the specimen surface, see Figure 128 (a). The image one frame prior to fracture was selected and the two reference points defined by the time-dependent method were selected and the resulting ϵ_1 and ϵ_2 values were measured, see Figure 128 (b).

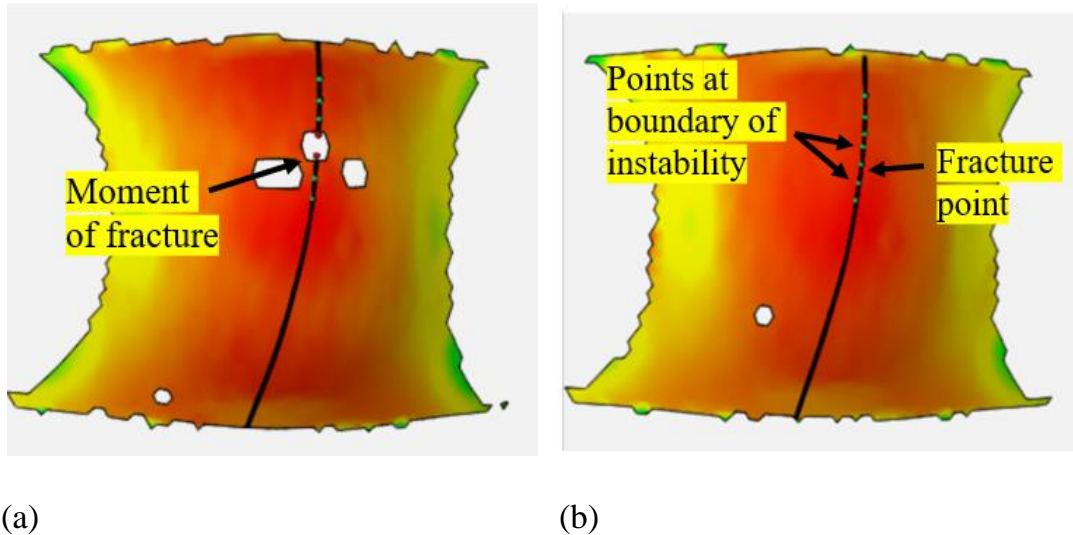


Figure 128 Time-dependant strain calculation: (a) Fracture; (b) Strain points.

This was performed across three section lines on the specimen and the average values calculated to avoid inaccuracies impacting the results. All strain values for each strain approximation method are provided in Table 21.

Table 21 Strain approximation results comparison for sample ID#2

Strain approximation method	ϵ_1	ϵ_2
Multi-curve fitting	0.38	0.12
Time-dependent strain	0.4	0.06

For both strain approximation techniques, the values for ϵ_1 were close with only a difference of 0.02 mm measured. Both stress values aligned with the raw data value of $\epsilon_1 = 0.3$ for sample ID #2. However, the values for ϵ_2 were not close suggesting an error in one of the strain approximation methods. Some concerns regarding the path of

the fitted curve on the ϵ_2 data were raised due to the high strain at the location of the 5 points taken for the parabolic fit. This was considered to have returned an unrealistically high value for ϵ_2 . Also, it was suggested that mirroring the data at the high strain location did not return an appropriate representation of the strain across the crack. Raw data for sample ID #2 returned a strain of 0.05 for ϵ_2 . As such, the time-dependent approximation method seemed to provide a more realistic value for ϵ_2 . Also, the multi-curve fitting returned a dramatically increased strain value which mirrored the concerns raised previously about the curve fitting method. As such, the time-dependent strain approximation method was selected to approximate the remaining strain data.

8.4 Results

After completing the Nakajima test the usable data was extracted and the strain values determined using the time-dependent strain approximation method. From the twenty four specimens formed by the punch during the Nakajima test a total of seven were rejected due to the strain data being unreadable. The rejected data was a result of the errors discussed in section 8.3.2. FLD's were generated for the AR CP-Ti and LMD CP-Ti specimens and compared to determine to what extent LMD thickening impacted the forming behaviour of the CP-Ti sheet.

8.4.1 Forming limit diagrams

The Nakajima test was performed on the AR CP-Ti specimens and strain data was measured across the specimen surface using DIC with respect to the strain state and the gauge width of each specimen. This strain data is provided in Table 22.

Table 22 Results of Nakajima test for AR CP-Ti test specimens.

ID #	Specimen #	Strain state	Gauge width	Section line #	Major strain (ϵ_1)	Minor strain (ϵ_2)
5	1	Plane strain	100	1	0.43	-0.01
5	1	Plane strain	100	2	0.43	-0.01

5	1	Plane strain	100	3	0.4	-0.02
5	2	Plane strain	100	1	0.41	-0.01
5	2	Plane strain	100	2	0.42	0
5	2	Plane strain	100	3	0.39	-0.02
5	3	Plane strain	100	1	0.43	-0.04
5	3	Plane strain	100	2	0.43	-0.01
5	3	Plane strain	100	3	0.43	0
6	2	Biaxial tension	120	1	0.37	0.01
6	2	Biaxial tension	120	2	0.39	0.03
6	2	Biaxial tension	120	3	0.39	0.04
6	3	Biaxial tension	120	1	0.39	0.01
6	3	Biaxial tension	120	2	0.41	0.02
6	3	Biaxial tension	120	3	0.51	0
7	1	Biaxial tension	140	1	0.34	0.04
7	1	Biaxial tension	140	2	0.36	0.05
7	1	Biaxial tension	140	3	0.41	0.05
7	2	Biaxial tension	140	1	0.35	0.07
7	2	Biaxial tension	140	2	0.33	0.08
7	2	Biaxial tension	140	3	0.4	0.07

7	3	Biaxial tension	140	1	0.36	0.05
7	3	Biaxial tension	140	2	0.39	0.07
7	3	Biaxial tension	140	3	0.38	0.06
8	1	Equi-biaxial tension	160	1	0.29	0.27
8	1	Equi-biaxial tension	160	2	0.32	0.27
8	1	Equi-biaxial tension	160	3	0.33	0.27
8	2	Equi-biaxial tension	160	1	0.32	0.29
8	2	Equi-biaxial tension	160	2	0.33	0.28
8	2	Equi-biaxial tension	160	3	0.33	0.28
8	3	Equi-biaxial tension	160	1	0.33	0.3
8	3	Equi-biaxial tension	160	2	0.34	0.29
8	3	Equi-biaxial tension	160	3	0.34	0.3

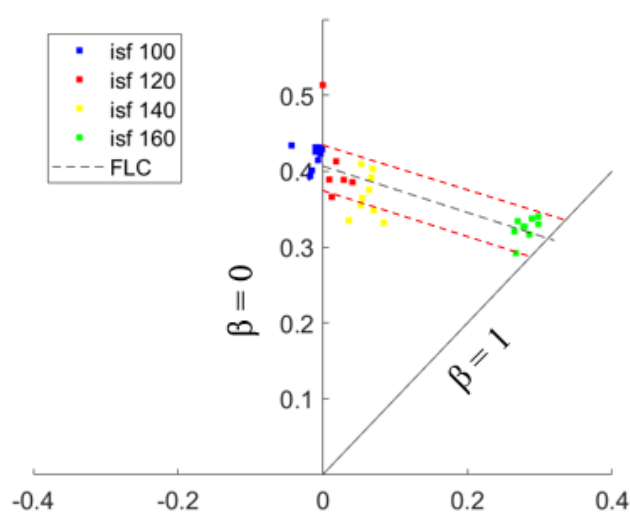


Figure 129 FLC curve for the AR CP-Ti material.

A FLD was generated which represents the forming behaviour of the 1.6 mm thick AR CP-Ti specimens, Figure 129. It contains the collected data points in the right branch of the FLD. Three specimens were tested for each strain state with separate ϵ_1 and ϵ_2 values taken across three section lines. The FLC was fitted across this data using a first order derivative. The FLC presented as a negative slope of -0.3 in the right branch of the FLD. The intercept location of the FLC on the major strain axis, known as the strain-hardening component, was 0.41. Typically, the FLC is offset with a safety margin of 10% for which strain values should fall within (Paul, 2013). This safety margin provides a safe region to accommodate slight changes in the material properties or process conditions (J Adamus et al., 2015). A safety margin of 10% was added above and below the FLC (red dotted lines), Figure 129. One data point for the FLC120 biaxial tension specimen was lying outside the safety region so was not used when calculating the FLC. Following this, the strain data for the LMD CP-Ti specimens was extracted and compiled in Table 23.

Table 23 Results of Nakajima test for LMD thickened CP-Ti test specimens.

ID #	Specimen #	Strain state	FLC	Section line #	Major strain (ϵ_1)	Minor strain (ϵ_2)
2	3	Biaxial tension	120	1	0.4	0.06
2	3	Biaxial tension	120	2	0.41	0.07
2	3	Biaxial tension	120	3	0.4	0.05
3	2	Biaxial tension	140	1	0.35	0.07
3	2	Biaxial tension	140	2	0.38	0.08
3	2	Biaxial tension	140	3	0.37	0.08
3	3	Biaxial tension	140	1	0.38	0.08

3	3	Biaxial tension	140	2	0.37	0.09
3	3	Biaxial tension	140	3	0.38	0.08
4	1	Equi-biaxial tension	160	1	0.23	0.19
4	1	Equi-biaxial tension	160	2	0.25	0.20
4	1	Equi-biaxial tension	160	3	0.24	0.21
4	2	Equi-biaxial tension	160	1	0.27	0.24
4	2	Equi-biaxial tension	160	2	0.26	0.23
4	2	Equi-biaxial tension	160	3	0.26	0.24
4	3	Equi-biaxial tension	160	1	0.26	0.23
4	3	Equi-biaxial tension	160	2	0.25	0.24
4	3	Equi-biaxial tension	160	3	0.26	0.24

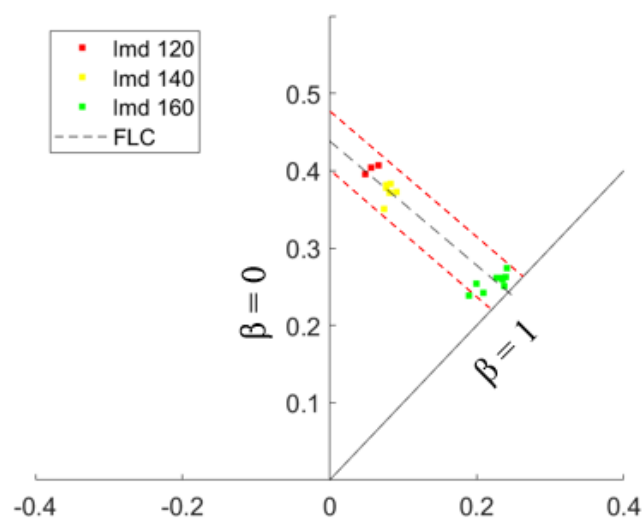


Figure 130 FLC for the LMD thickened CP-Ti material.

A FLD was created using the strain data from Table 23. This FLD describes the forming behaviour of the 1.9 mm thick LMD CP-Ti specimens in the biaxial and equi-biaxial strain modes, see Figure 130. Strain data for the LMD thickened samples in the plane strain state are not included in this FLD as the software was not able to read the strain data. As such, the FLD is likely not a completely reliable representation of the LMD thickened specimens forming behaviour. Despite the incompleteness of the data, a first order derivative line was fitted to the remaining data points and a FLC was generated with a negative slope of -0.8 across the right side of the FLD. The strain-hardening component was measured at 0.41.

8.5 Summary

The FLC's generated from the strain specimens represent failure by fracture of the sheet. According to these diagrams the key difference between the LMD thickened CP-Ti material and AR CP-Ti material is the LMD tailoring seemingly resulted in a lower critical strain limit in the equi-biaxial strain state. The equi-biaxial strain state is when tension is distributed equally in all directions and was achieved in testing by forming circle blanks with no gauge section. This change in critical strain limit contrasts with the closely aligned strain values in the plane strain and remaining biaxial strain states. The results suggest that additively thickening the sheet material by 0.3 mm by LMD weakened the material to this strain state. Considering this, it is possible that stretching during ISF put the material under equi-biaxial tension resulting in the material being subjected to strains above its critical limit which led to necking and eventual fracture. As the fracture appeared in the 60° wall angle section it is conceivable that the described failure is invariably linked to the angle of forming. This may explain why the AR CP-Ti preform was formed beyond the 60° wall angle because, according to its FLC, its critical limit in the equi-biaxial state is higher than the CP-Ti sheet containing the LMD thickened layer, see Figure 129. Stretching has been shown to be the governing mode of deformation in ISF rather than vertical shear (Allwood et al., 2007). Biaxial stretching is predominant when forming corners with ISF (M. B. Silva et al., 2008). This is caused by an increase in the meridional stress from increased contact surface

area between the forming tool and sheet surface at corners which increases friction at the forming tool-sheet contact interface. As such, the observed behaviour in the Nakajima forming test may be a direct response to the contact condition between the sheet and forming tool when forming at 60° angle to the sheet plane. However, this is unlikely because of the forming tool orientation during the previous ISF trial, see Figure 131.

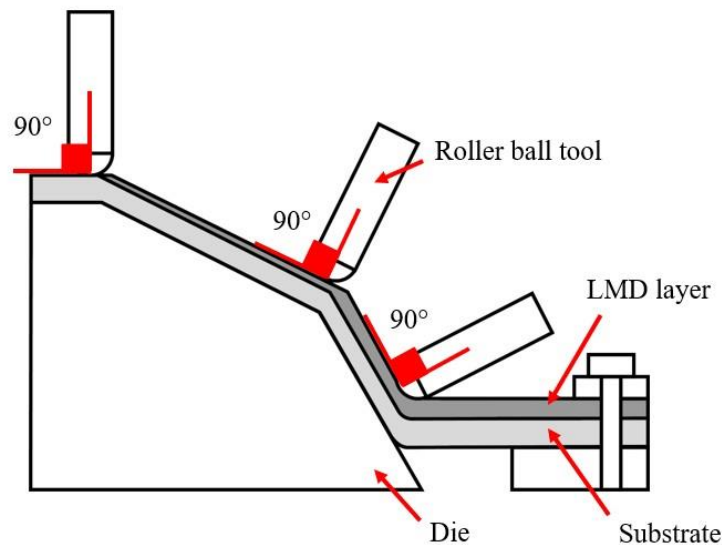


Figure 131 Change in angle of roller ball tool during back supported ISF.

The angle between the central axis of the forming tool and the sheet surface plane was kept perpendicular throughout ISF, ensuring the forming tool maintained a 90° offset between its central axis and the sheet plane. Texture is another possible reason for the better strength properties of the AR CP-Ti material under equi-biaxial tension. The pole figures for cold-rolled CP-Ti and LMD thickened CP-Ti were taken to analysis the texture, see Figure 132.

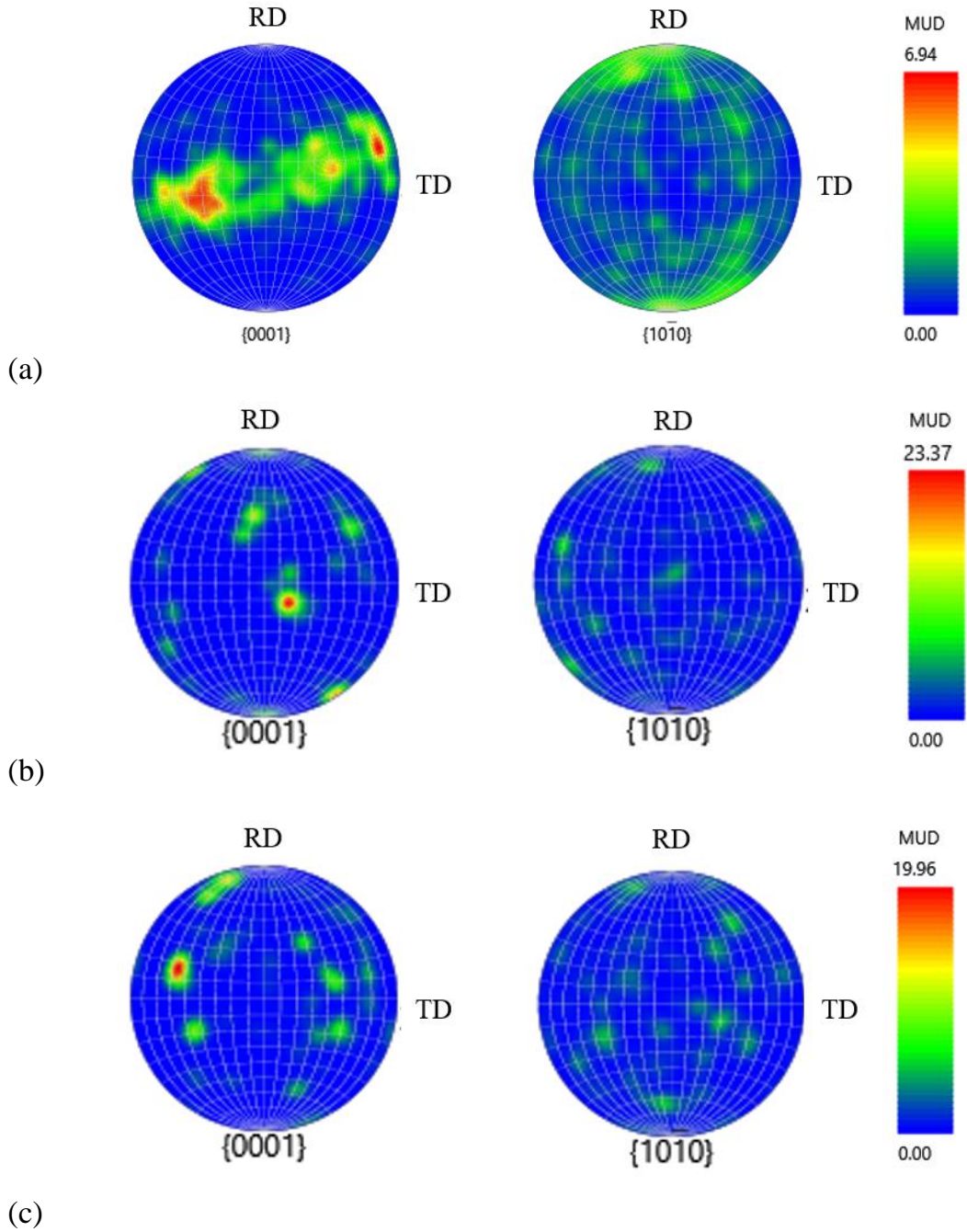


Figure 132 Pole figures: (a) AR CP-Ti; (b) 0.3 mm LMD; (c) 0.9 mm LMD.

Split-basal texture of cold-rolled CP-Ti sheet has been seen to improve yield strength and result in biaxial strengthening, also known as texture hardening (Srinivasan et al., 2016). This was examined by Babel (1967) who found two anisotropic Ti alloys exhibiting split-basal texture to impart biaxial strengths higher than isotropic materials. However, the pole figures did not give a clear representation of the texture. This is

because not enough grains were sampled. However, according to the study by Babel (1967) the isotropic tensile behaviour of LMD CP-Ti material is a possible reason for its inferior biaxial strength compared to the AR CP-Ti material. Possible future work is required to conduct further study into the impact of the additive thickening on the texture component of CP-Ti and determine if it changes the strength properties under biaxial and equi-biaxial tension. Despite this analysis, it must be kept in consideration that the difference in FLC's could simply be the result of inaccurate test results caused by the incompleteness of the test data rather than a fundamental property of the material.

Chapter 9

9 Conclusions and future research

In this chapter, the major findings of this research study are summarised and reflected upon. The main contributions to knowledge are discussed. To conclude, recommended future research projects to advance our understanding and capability in the fields of additive manufacturing and incremental sheet forming are given.

9.1 Major findings

The goal of this experimental investigation was to successfully reinforce a commercially pure titanium (CP-Ti) sheet with added thickness using laser metal deposition (LMD) to counter sheet thinning during room temperature incremental sheet forming (ISF). With respect to this, a hybrid LMD/ISF process was developed and tested, and the experimental data reviewed to determine its effectiveness in achieving this goal. The major findings are as follows;

- The LMD thickened CP-Ti material exhibited isotropic mechanical properties in contrast to the anisotropic nature of the as-received (AR) CP-Ti sheet. The quantity of deposited layers had little influence on its strength properties.
- Strain was seen propagating in thin lines parallel to the LMD tracks during tensile testing. Likely in response to the undulating surface of the LMD deposit as strain was evenly distributed across the relatively flatter surface of the AR specimens in response to uniaxial tension. The quantity of deposited layers had little influence the measured roughness of the deposit surface.
- The fracture face of the LMD thickened specimens were populated with small dimples, microscopic cracks, and large equiaxed voids with internal coalesced microscopic voids synonymous with ductile fracture. There was no delamination of the deposited layers from the substrate which suggests good bonding of the LMD layer to the substrate sheet.

- Microstructural analysis of the LMD added material found abnormal grain growth (AGG) to be predominant in the deposited thickness.
- The large grains were shown to be fragmented with a network of intragranular low angle grain boundary misorientations with some fully enclosed high angle boundary grains the same shape and size as observed in the AR material.
- Microscopic analysis through the thickness of the LMD thickened sheet showed a variation in microstructure. This consisted of fine grains at the substrate side reminiscent of AR cold rolled CP-Ti, a heat-affected zone (HAZ) in the interface region made up of platelet alpha microstructure typical of CP-Ti cooled from the β -phase field, and AGG in the LMD deposit.
- During ISF, the LMD thickened sheet exhibited micro-cracking followed by the opening of a zig zag crack resulting in catastrophic part failure. The sheet failed when forming at 60° to the sheet plane, earlier than the AR sheet which failed when forming at 80° .
- LMD blanks reduced the level of thinning as intended and therefore suggest hybrid LMD\ISF is a feasible option to improve thickness homogeneity of titanium sheet parts formed by low temperature ISF. However, the use of LMD blanks is limited to forming parts with maximum angles of 40° .
- Investigation into the biaxial strain mechanism found the LMD thickened material exhibited with lower formability under equi-biaxial strain, a stress state observed during high angle ISF.

9.2 Contributions to knowledge

A peer reviewed journal paper was published thanks to the investigative work of this doctorate study, see Publications section. As such, a successful contribution to knowledge has been made. The key contributory findings and their novelty are reflected upon in detail.

9.2.1 Material analysis of LMD tailored CP-Ti sheet

The tailored material exhibited isotropic tensile behaviour in contrast to the anisotropy of the AR cold-rolled CP-Ti material, see section 4.3.1. This material change was consistent for all tensile test specimens despite varying the quantity of deposited layers, proving this test parameter had little impact on its strength properties, see section 4.3.1. The only major difference in the material was its microstructure, with significant grain growth found close to the surface containing the LMD deposit. However, the microstructure change had little impact on its tensile behaviour, see section 6.3.3. The consistency in the tensile results, and lack of delamination of the LMD layers, supports the use of LMD to thicken sheet preforms in areas of predicted thinning prior to forming, see section 4.3.3. Despite this, strain was shown to localise along the grooves formed by the undulating LMD tracks, unlike the homogeneous strain distribution across the relatively flatter AR specimen surfaces, see section 4.3.2. The track height stayed consistent even as more layers were added, see section 6.3.1. As such, future researchers should consider introducing an operation after LMD thickening to reduce surface roughness to minimise high stress points during forming. Some suggestions for post-processing of the surface are machining, polishing, or a final laser scan to fully melt partially melted powder and flatten the build tracks.

9.2.2 Incremental sheet forming of LMD tailored CP-Ti sheet

Early opinion, based off the evidence from the preliminary evidence based results, was that the LMD material should behave almost the same as the AR CP-Ti sheet during ISF. Indeed, the LMD thickening was shown to be effective in improving thickness homogeneity in the ISF part, see section 7.3.1. However, the tailored sheet seemed to break down once the forming angle increased above 40°, with micro cracks appearing on the sheet surface eventually leading to a zig zag crack and premature part failure, see sections 7.3.1 to 7.3.4. The results suggest the microstructure was not the main cause of this failure as the tailored sheet behaved normally during ISF in the 20° and 40° wall angle regions. It is also unlikely either the surface roughness or oxidation from the heat

treatment were responsible as the ISF tool seemed to smooth the sheet surface during forming and brittle increase was minimal so unlikely to impact formability.

9.2.3 Biaxial testing of LMD tailored CP-Ti sheet

With respect to these conclusions, and because the material behaved as expected when put under the uniaxial strain mechanism, it became important to examine the biaxial strain mechanism to understand how the tailored material behaved in this more complex strain distribution. Nakajima testing found the LMD thickened material had lower formability than its parent material when put under biaxial tension. As such, the materials poor performance during ISF can be somewhat linked to the forming mechanism present when forming at an angle greater than 40° to the sheet plane, see section 8.4.1. This experimental investigation proves the criticality of the forming angle to the success of incrementally forming LMD thickened CP-Ti sheet at room temperature. It also proves LMD as a viable option for tailoring CP-Ti sheet with extra material to improve post-ISF thickness homogeneity. However, further work to optimise LMD and heat treatments is suggested to optimise the tailored materials microstructure.

9.3 Reflections and future work

Such industries as defence would benefit from a rapid prototyping operation capable of manufacturing thin sheet titanium components with minimal setup costs and design adaptability. Especially in front line applications were transportability and process flexibility are critical. With respect to succeeding in industrial implementation, further research into the hybrid LMD/ISF process is required to better understand the mechanisms responsible for the premature failure, and eventually refine the process to mitigate this. A major focus of future research should be on improving the LMD added material, e.g., improving heat treatment, or using a mechanical approach. Additionally, alternative methods for increasing local thickness of the sheet metal should be tested. Thanks to this feasibility study, there is a strong case to be made for the future use of hybrid LMD/ISF for manufacturing thin sheet titanium components at low

temperatures. With reflection, the following areas of research have been suggested as a continuation of this work;

- i. Investigate alternative methods of thickening the preform, such as the removal of material by machining or other forms of additive manufacturing.
- ii. Develop and test LMD thickened CP-Ti with an additional post-LMD operation to reduce surface roughness and flatten the LMD tracks. This could be by machining or polishing the sheet surface, and a laser scan of the surface post-LMD to fully melt any leftover partially melted or unmelted powder and flatten the deposited tracks.
- iii. Build a finite element (FE) material model of the LMD tailored CP-Ti material using the FE material model and experimental material data from this research study to support its development.
- iv. Develop an FE model of the ISF operation to investigate other processing parameters such as part geometry, tool speed, lubrication effects, amongst others.

References

- Acharya, R., Sharon, J. A., & Staroselsky, A. (2017). Prediction of microstructure in laser powder bed fusion process. *Acta Materialia*, *124*, 360–371. <https://doi.org/10.1016/j.actamat.2016.11.018>
- Adamus, J. (2006). Characteristic of Shaping Titanium Sheets by Cold Working Methods. In *Int. J. of Applied Mechanics and Engineering* (Vol. 11, Issue 4).
- Adamus, J., Dyja, K., & Motyka, M. (2015). Experimental and theoretical determination for forming limit curve. *Archives of Metallurgy and Materials*, *60*(3). <https://doi.org/10.1515/amm-2015-0321>
- Adamus, Janina. (2016). *Investigation of sheet-titanium drawability Investigation of sheet-titanium drawability*. April.
- Ai, S., & Long, H. (2019). A review on material fracture mechanism in incremental sheet forming. *International Journal of Advanced Manufacturing Technology*, 33–61. <https://doi.org/10.1007/s00170-019-03682-6>
- Allwood, J. M., Shouler, D. R., & Tekkaya, A. E. (2007). The Increased Forming Limits of Incremental Sheet Forming Processes. *Key Engineering Materials*, *344*, 621–628. <https://doi.org/10.4028/www.scientific.net/KEM.344.621>
- Ambrogio, G., de Napoli, L., & Filice, L. (2009). A novel approach based on multiple back-drawing incremental forming to reduce geometry deviation. *International Journal of Material Forming*, *2*(SUPPL. 1), 9–12. <https://doi.org/10.1007/s12289-009-0498-5>
- Ambrogio, Giuseppina, Gagliardi, F., Muzzupappa, M., & Filice, L. (2019). Additive-incremental forming hybrid manufacturing technique to improve customised part performance. *Journal of Manufacturing Processes*, *37*(March 2018), 386–391. <https://doi.org/10.1016/j.jmapro.2018.12.008>
- Ambrogio, Giuseppina, Gagliardi, F., Serratore, G., Ramundo, E., & Filice, L. (2019). SPIF of tailored sheets to optimize thickness distribution along the shaped wall.

- Procedia Manufacturing*, 29, 80–87. <https://doi.org/10.1016/j.promfg.2019.02.109>
- Anderson, T. . (2005). *Fracture Mechanics - Fundamentals and Applications* (3rd ed.).
- Araghi, B. T., Göttmann, A., Bambach, M., Hirt, G., Bergweiler, G., Diettrich, J., Steiners, M., & Saeed-Akbari, A. (2011). Review on the development of a hybrid incremental sheet forming system for small batch sizes and individualized production. In *Production Engineering* (Vol. 5, Issue 4, pp. 393–404). <https://doi.org/10.1007/s11740-011-0325-y>
- Araghi, B. T., Manco, G. L., Bambach, M., & Hirt, G. (2009). Investigation into a new hybrid forming process: Incremental sheet forming combined with stretch forming. *CIRP Annals - Manufacturing Technology*, 58(1), 225–228. <https://doi.org/10.1016/j.cirp.2009.03.101>
- Attar, H., Calin, M., Zhang, L. C., Scudino, S., & Eckert, J. (2014). Manufacture by selective laser melting and mechanical behavior of commercially pure titanium. *Materials Science and Engineering A*, 593, 170–177. <https://doi.org/10.1016/j.msea.2013.11.038>
- Babel, H. W. (1967). *The Biaxial Textured Titanium*.
- Bambach, M., Sizova, I., Sydow, B., Hemes, S., & Meiners, F. (2020). Hybrid manufacturing of components from Ti-6Al-4V by metal forming and wire-arc additive manufacturing. *Journal of Materials Processing Technology*, 282. <https://doi.org/10.1016/j.jmatprotec.2020.116689>
- Bambach, Markus, Sviridov, A., & Weisheit, A. (2017). Stiffness management of sheet metal parts using laser metal deposition. *AIP Conference Proceedings*, 1896. <https://doi.org/10.1063/1.5008094>
- Bambach, Markus, Sviridov, A., Weisheit, A., & Schleifenbaum, J. H. (2017a). Case Studies on Local Reinforcement of Sheet Metal Components by Laser Additive Manufacturing. In *Metals* (Vol. 7, Issue 4). <https://doi.org/10.3390/met7040113>
- Bambach, Markus, Sviridov, A., Weisheit, A., & Schleifenbaum, J. H. (2017b). Case

- studies on local reinforcement of sheet metal components by laser additive manufacturing. *Metals*, 7(4). <https://doi.org/10.3390/met7040113>
- Banabic, D. (2020). *Advances in anisotropy of plastic behaviour and formability of sheet metals*. 749–787.
- Barlat, F., Lege, D. J., & Brem, J. C. (1991). A six-component yield function for anisotropic materials. *International Journal of Plasticity*, 7(7), 693–712. [https://doi.org/10.1016/0749-6419\(91\)90052-Z](https://doi.org/10.1016/0749-6419(91)90052-Z)
- Barnwal, V. K., Chakrabarty, S., Tewari, A., Narasimhan, K., & Mishra, S. K. (2019). Influence of Single-Point Incremental Force Process Parameters on Forming Characteristics and Microstructure Evolution of AA-6061 Alloy Sheet. *Journal of Materials Engineering and Performance*. <https://doi.org/10.1007/s11665-019-04446-9>
- Barro, Ó., Arias-González, F., Lusquiños, F., Comesaña, R., Del Val, J., Riveiro, A., Badaoui, A., Gómez-Baño, F., & Pou, J. (2021). Improved commercially pure titanium obtained by laser directed energy deposition for dental prosthetic applications. *Metals*, 11(1), 1–15. <https://doi.org/10.3390/met11010070>
- Bedinger, G. M. (2013). Titanium. *Mining Engineering*, 2013(July), 92–95. <http://pubs.er.usgs.gov/publication/70047016>
- Bignon, M., Bertrand, E., & Rivera-díaz-del-castillo, P. E. J. (2021). Martensite formation in titanium alloys_ Crystallographic and compositional effects. *Journal of Alloys and Compounds*, 872, 159636. <https://doi.org/10.1016/j.jallcom.2021.159636>
- Boyer, R. R., & Briggs, R. D. (2005). *The Use of Titanium Alloys in the Aerospace Industry*. 14(December), 681–685. <https://doi.org/10.1361/105994905X75448>
- Casari, F., Tassan, M., Messina, A., & Molinari, A. (2006). Effect of punch diameter, grid dimension, and lubrication on forming limit diagram. *Journal of Testing and Evaluation*, 34(1), 24–30. <https://doi.org/10.1520/jte12669>

- Chen, F. K., & Chiu, K. H. (2005). Stamping formability of pure titanium sheets. *Journal of Materials Processing Technology*, 170(1–2), 181–186. <https://doi.org/10.1016/j.jmatprotec.2005.05.004>
- Chen, T., Koyama, S., Nishida, S., & Yu, L. (2021). Mechanical properties and frictional wear characteristic of pure titanium treated by atmospheric oxidation. *Materials*, 14(12). <https://doi.org/10.3390/ma14123196>
- Cheng, D., Zhang, J., Shi, T., Li, G., Shi, J., Lu, L., & Fu, G. (2021). Microstructure and mechanical properties of additive manufactured Ti-6Al-4V components by annular laser metal deposition in a semi-open environment. *Optics and Laser Technology*, 135. <https://doi.org/10.1016/j.optlastec.2020.106640>
- Chun, Y. B., Yu, S. H., Semiatin, S. L., & Hwang, S. K. (2005). Effect of deformation twinning on microstructure and texture evolution during cold rolling of CP-titanium. *Materials Science and Engineering A*, 398(1–2), 209–219. <https://doi.org/10.1016/j.msea.2005.03.019>
- Clemens, H., Mayer, S., & Scheu, C. (2017). *Microstructure and Properties of Engineering Materials*.
- Corbin, D. J., Nassar, A. R., Reutzel, E. W., Beese, A. M., & Michaleris, P. (2018). Effect of substrate thickness and preheating on the distortion of laser deposited ti-6al-4v. *Journal of Manufacturing Science and Engineering, Transactions of the ASME*, 140(6). <https://doi.org/10.1115/1.4038890>
- Cottrell, A. (1967). *An Introduction to Metallurgy*. Edward Arnold (Publishers) Ltd.
- Cp-Ti2 | Advanced Powders. (n.d.). Retrieved November 5, 2021, from <https://www.advancedpowders.com/powders/titanium/cp-ti2>
- Danielson, P., Wilson, R., & Alman, D. (n.d.). *Microstructure of Titanium Welds*.
- Den, N., & Carless, L. (2012). *Advanced metal-forming technologies for automotive applications*.
- Dong, Y. L., & Pan, B. (2017). A Review of Speckle Pattern Fabrication and

- Assessment for Digital Image Correlation. *Experimental Mechanics*, 57(8), 1161–1181. <https://doi.org/10.1007/s11340-017-0283-1>
- Emmens, W. C., & van den Boogaard, A. H. (2009). An overview of stabilizing deformation mechanisms in incremental sheet forming. In *Journal of Materials Processing Technology* (Vol. 209, Issue 8, pp. 3688–3695). <https://doi.org/10.1016/j.jmatprotec.2008.10.003>
- Emmens, W. C., Van Der Weijde, D. H., & Van Den Boogaard, A. H. (2009). The FLC, Enhanced Formability, and Incremental Sheet Forming. *International Deep Drawing Research Group IDDRG*.
- Essa, K., & Hartley, P. (2011). An assessment of various process strategies for improving precision in single point incremental forming. *International Journal of Material Forming*, 4(4), 401–412. <https://doi.org/10.1007/s12289-010-1004-9>
- Fang, Y., Lu, B., Chen, J., Xu, D. K., & Ou, H. (2014). Analytical and experimental investigations on deformation mechanism and fracture behavior in single point incremental forming. *Journal of Materials Processing Technology*, 214(8), 1503–1515. <https://doi.org/10.1016/j.jmatprotec.2014.02.019>
- Firat, M., Kaftanoglu, B., & Eser, O. (2008). Sheet metal forming analyses with an emphasis on the springback deformation. *Journal of Materials Processing Technology*, 196(1–3), 135–148. <https://doi.org/10.1016/j.jmatprotec.2007.05.029>
- Gammon, L. M., Briggs, R. D., Packard, J. M., Batson, K. W., Boyer, R., & Domby, C. W. (2004). *Metallography and Microstructures of Titanium and Its Alloys*. 9. <https://doi.org/10.1361/asmhba0003779>
- Gatea, S., Ou, H., & McCartney, G. (2016). Review on the influence of process parameters in incremental sheet forming. *International Journal of Advanced Manufacturing Technology*, 87(1–4), 479–499. <https://doi.org/10.1007/s00170-016-8426-6>
- Gatea, S., Xu, D., Ou, H., & McCartney, G. (2018). Evaluation of formability and fracture of pure titanium in incremental sheet forming. *International Journal of*

Advanced Manufacturing Technology, 95(1–4), 625–641.
<https://doi.org/10.1007/s00170-017-1195-z>

- Gebhardt, A. (2011). Characteristics of the Additive Manufacturing Process. In *Understanding Additive Manufacturing* (pp. 21–91).
- Gu, D., Hagedorn, Y. C., Meiners, W., Meng, G., Batista, R. J. S., Wissenbach, K., & Poprawe, R. (2012). Densification behavior, microstructure evolution, and wear performance of selective laser melting processed commercially pure titanium. *Acta Materialia*, 60(9), 3849–3860. <https://doi.org/10.1016/j.actamat.2012.04.006>
- Gupta, P., & Jeswiet, J. (2019). Manufacture of an aerospace component by single point incremental forming. *Procedia Manufacturing*, 29, 112–119. <https://doi.org/10.1016/j.promfg.2019.02.113>
- Ham, M., & Jeswiet, J. (2006). Single point incremental forming and the forming criteria for AA3003. In *CIRP Annals - Manufacturing Technology* (Vol. 55, Issue 1). [https://doi.org/10.1016/S0007-8506\(07\)60407-7](https://doi.org/10.1016/S0007-8506(07)60407-7)
- Hama-Saleh, R., Weisheit, A., Schleifenbaum, J. H., Ünsal, I., Sviridov, A., & Bambach, M. (2020). Formability Analysis of Micro-Alloyed Sheet Metals Reinforced by Additive Manufacturing. *Procedia Manufacturing*, 47, 1023–1028. <https://doi.org/10.1016/j.promfg.2020.04.317>
- Han, F. (2008). Numerical simulation and experimental investigation of incremental sheet forming process. *Journal of Central South University Technology*, 15, 581–587. <https://doi.org/10.1007/s11771>
- Hirt, G., Junk, S., & Witulski, N. (2002). Incremental sheet forming: quality, evaluation and process simulation. *Proceeding of the 7th ICTP Conference*.
- Hussain, G., Gao, L., & Zhang, Z. Y. (2008). *Formability evaluation of a pure titanium sheet in the cold incremental forming process*. 920–926. <https://doi.org/10.1007/s00170-007-1043-7>
- Isik, K., Silva, M. B., Tekkaya, A. E., & Martins, P. A. F. (2014). Formability limits by

- fracture in sheet metal forming. *Journal of Materials Processing Technology*, 214(8), 1557–1565. <https://doi.org/10.1016/j.jmatprotec.2014.02.026>
- Jackson, K., & Allwood, J. (2008). The mechanics of incremental sheet forming. *Journal of Materials Processing Technology*, 209(3), 1158–1174.
- Jagtap, R., & Kumar, S. (2019). An experimental investigation on thinning and formability in hybrid incremental sheet forming process. *Procedia Manufacturing*, 30, 71–76. <https://doi.org/10.1016/j.promfg.2019.02.011>
- Jeswiet, J., & Young, D. (2005). Forming limit diagrams for single-point incremental forming of aluminium sheet. *Proceedings of the Institution of Mechanical Engineers, Part B: Journal of Engineering Manufacture*, 219(4), 359–364. <https://doi.org/10.1243/095440505X32210>
- Kilani, L., Mabrouki, T., Ayadi, M., Chermiti, H., & Belhadi, S. (2020). Effects of rolling ball tool parameters on roughness, sheet thinning, and forming force generated during SPIF process. *International Journal of Advanced Manufacturing Technology*, 106(9–10), 4123–4142. <https://doi.org/10.1007/s00170-019-04918-1>
- Kim, T. J., & Yang, D. Y. (2000). *Improvement of formability for the incremental sheet metal forming process*. 42, 1271–1286.
- Kohli, R., & Mittal, K. L. (2019). Methods for Assessing Surface Cleanliness. In *Developments in Surface Contamination and Cleaning, Volume 12* (pp. 23–105). Elsevier. <https://doi.org/10.1016/b978-0-12-816081-7.00003-6>
- Kumar, G. (2018). An Experimental Study on Single-Point Incremental Forming of AA5083 Sheet Using Response Surface Methodology. In *Advances in Forming Machining and Automation*. <http://www.springer.com/series/15734>
- Kumar, N., Belokar, R. M., & Agrawal, A. (2019). Multi-objective optimization of quality characteristics in single point incremental forming process by response surface methodology. In *Indian Journal of Engineering & Materials Sciences* (Vol. 26).

- Lauwers, B., Klocke, F., Klink, A., Tekkaya, A. E., Neugebauer, R., & McIntosh, D. (2014). Hybrid processes in manufacturing. *CIRP Annals - Manufacturing Technology*, 63(2), 561–583. <https://doi.org/10.1016/j.cirp.2014.05.003>
- Leyens, C. (Christoph), & Peters, M. (Manfred). (2003). *Titanium and titanium alloys : fundamentals and applications*. Wiley-VCH.
- Li, C., Liu, Z. Y., Fang, X. Y., & Guo, Y. B. (2018). Residual Stress in Metal Additive Manufacturing. *Procedia CIRP*, 71, 348–353. <https://doi.org/10.1016/j.procir.2018.05.039>
- Li, X., Xie, J., & Zhou, Y. (2005). Effects of oxygen contamination in the argon shielding gas in laser welding of commercially pure titanium thin sheet. *Journal of Materials Science*, 40(13), 3437–3443. <https://doi.org/10.1007/s10853-005-0447-8>
- Lu, H., Liu, H., & Wang, C. (2019). Review on strategies for geometric accuracy improvement in incremental sheet forming. *International Journal of Advanced Manufacturing Technology*, 102(9–12), 3381–3417. <https://doi.org/10.1007/s00170-019-03348-3>
- Lutjering, G., & Williams, J. C. (2007). Titanium. In B. Derby (Ed.), *Springer* (2nd ed.). Springer. <https://link.springer.com/content/pdf/10.1007%2F978-3-540-73036-1.pdf>
- Maaß, F., Hahn, M., Tekkaya, A. E., Dobecki, M., Poeche, A., Brömmelhoff, K., & Reimers, W. (2019). Forming mechanisms-related residual stress development in single point incremental forming. *Production Engineering*, 13(2), 149–156. <https://doi.org/10.1007/s11740-018-0867-3>
- Mahamood, R. M. (2016). Laser Metal Deposition Process. In *3D Printing*. <https://doi.org/10.4018/978-1-5225-1677-4.ch009>
- Malhotra, R., Xue, L., Belytschko, T., & Cao, J. (2012). Mechanics of fracture in single point incremental forming. *Journal of Materials Processing Technology*, 212(7), 1573–1590. <https://doi.org/10.1016/j.jmatprotec.2012.02.021>

- Maqbool, F., & Bambach, M. (2017). A modular tooling set-up for incremental sheet forming (ISF) with subsequent stress-relief annealing under partial constraints. *AIP Conference Proceedings*, 1896. <https://doi.org/10.1063/1.5008090>
- Marciniak, Z., Duncan, J. L., & Hu, S. J. (2002). *Mechanics of sheet metal forming*. Butterworth-Heinemann.
- MatWeb. (n.d.). *TIMET TIMETAL® 50A CP Titanium (ASTM Grade 2)*. Retrieved February 8, 2022, from <http://www.matweb.com/search/datasheet.aspx?matguid=247af0c81c8a4a9da817bafa791d20bf&ckck=1>
- McAnulty, T., Jeswiet, J., & Doolan, M. (2017). Formability in single point incremental forming: A comparative analysis of the state of the art. *CIRP Journal of Manufacturing Science and Technology*, 16, 43–54. <https://doi.org/10.1016/j.cirpj.2016.07.003>
- Meacock, C., & Vilar, R. (2008). Laser powder microdeposition of CP2 Titanium. *Materials and Design*, 29(2), 353–361. <https://doi.org/10.1016/j.matdes.2007.01.033>
- Merklein, M., Johannes, M., Lechner, M., & Kuppert, A. (2014). A review on tailored blanks - Production, applications and evaluation. *Journal of Materials Processing Technology*, 214(2), 151–164. <https://doi.org/10.1016/j.jmatprotec.2013.08.015>
- Merklein, M., Junker, D., Schaub, A., & Neubauer, F. (2016). Hybrid additive manufacturing technologies - An analysis regarding potentials and applications. *Physics Procedia*, 83, 549–559. <https://doi.org/10.1016/j.phpro.2016.08.057>
- Micari, F., Ambrogio, G., & Filice, L. (2007). Shape and dimensional accuracy in Single Point Incremental Forming: State of the art and future trends. *Journal of Materials Processing Technology*, 191(1–3), 390–395. <https://doi.org/10.1016/j.jmatprotec.2007.03.066>
- Nam, S., Cho, H., Kim, C., & Kim, Y.-M. (2018). Effect of Process Parameters on Deposition Properties of Functionally Graded STS 316/Fe Manufactured by Laser

- Direct Metal Deposition. *Metals*, 8(8), 607. <https://doi.org/10.3390/met8080607>
- Okazaki, Y., & Ishino, A. (2020). Laser-Sintered Commercially Pure Ti and Ti-6Al-4V. *Materials*, 13(609).
- Ortiz Ortega, E., Hosseinian, H., Rosales López, M. J., Rodríguez Vera, A., & Hosseini, S. (2022). *Characterization Techniques for Morphology Analysis*. https://doi.org/10.1007/978-981-16-9569-8_1
- Park, J. J., & Kim, Y. H. (2003). Fundamental studies on the incremental sheet metal forming technique. *Journal of Materials Processing Technology*, 140(1-3 SPEC.), 447–453. [https://doi.org/10.1016/S0924-0136\(03\)00768-4](https://doi.org/10.1016/S0924-0136(03)00768-4)
- Paul, S. K. (2013). Theoretical analysis of strain- and stress-based forming limit diagrams. *Journal of Strain Analysis for Engineering Design*, 48(3), 177–188. <https://doi.org/10.1177/0309324712468524>
- Pidaparti, R. M. (2017). Engineering Finite Element Analysis. *Synthesis Lectures on Mechanical Engineering*, 1(1), 1–267. <https://doi.org/10.2200/s00761ed1v01y201703mec001>
- Pineau, A., Benzerga, A. A., & Pardoën, T. (2016). Failure of metals I: Brittle and ductile fracture. *Acta Materialia*, 107, 424–483. <https://doi.org/10.1016/j.actamat.2015.12.034>
- Rauch, E. F. (1998). Plastic anisotropy of sheet metals determined by simple shear tests. In *Materials Science and Engineering* (Vol. 241).
- Richard, H. A., & Kuna, M. (1990). Theoretical and Experimental Study of Superimposed Fracture Modes I, II and III. In *Engineering Fracture Mechanics* (Vol. 35, Issue 6).
- Roylance, D. (2001a). *Introduction to Fracture Mechanics*.
- Roylance, D. (2001b). *STRESS-STRAIN CURVES*. 1–15.
- Saboori, A., Gallo, D., Biamino, S., Fino, P., & Lombardi, M. (2017). An overview of additive manufacturing of titanium components by directed energy deposition:

- Microstructure and mechanical properties. *Applied Sciences (Switzerland)*, 7(9).
<https://doi.org/10.3390/app7090883>
- Schulz, M., Klocke, F., Riepe, J., Klingbeil, N., & Arntz, K. (2019). Process optimization of wire-based laser metal deposition of titanium. *Journal of Engineering for Gas Turbines and Power*, 141(5).
<https://doi.org/10.1115/1.4041167>
- Shackelford, J. F. (1988). *Introduction to Materials Science for Engineers*.
- Shafeek, M., Namboothiri, V. N. N., & Raju, C. (2022). Materials Today : Proceedings Formability analysis on titanium grade2 sheets in multi point incremental forming process. *Materials Today: Proceedings*, xxxx.
<https://doi.org/10.1016/j.matpr.2022.06.578>
- Shanmuganatan, S. P., & Senthil Kumar, V. S. (2013). Metallurgical analysis and finite element modelling for thinning characteristics of profile forming on circular cup. *Materials and Design*, 44, 208–215. <https://doi.org/10.1016/j.matdes.2012.07.042>
- Sheng, A., & Long, H. (2019). A review on material fracture mechanism in incremental sheet forming. *The International Journal of Advanced Manufacturing Technology*, 104, 33–61.
- Shunmugam, M. S., & Kanthababu, M. (2018). Advances in Simulation, Product Design and Development. *Editors Proceedings of AIMTDR*.
<http://www.springer.com/series/15734>
- Silva, M. B., Skjoedr, M., Atkins, A. G., Bay, N., & Martins, P. A. F. (2008). Single-point incremental forming and formability-failure diagrams. *Journal of Strain Analysis for Engineering Design*, 43(1), 15–35.
<https://doi.org/10.1243/03093247JSA340>
- Silva, M B, Centeno, G., Vallellano, C., & Martins, P. A. F. (2015). Recent Approaches for the Determination of Forming Limits by Necking and Fracture in Sheet Metal Forming Recent approaches for the determination of forming limits by necking and fracture in sheet metal forming. *Procedia Engineering*, 132(January 2016), 342–

349. <https://doi.org/10.1016/j.proeng.2015.12.504>

- Silva, Maria B, Nielsen, P. S., Bay, N., & Martins, P. A. F. (2011). Failure mechanisms in single-point incremental forming of metals. *International Journal of Advanced Manufacturing Technology*, 56, 893–903. <https://doi.org/10.1007/s00170-011-3254-1>
- Sinke, J., & Zadpoor, A. A. (2011). Tailor made blanks for the aerospace industry. In *Tailor Welded Blanks for Advanced Manufacturing* (pp. 181–201).
- Soeiro, J. M. C., Silva, C. M. A., Silva, M. B., & Martins, P. A. F. (2015). Revisiting the formability limits by fracture in sheet metal forming. *Journal of Materials Processing Technology*, 217, 184–192. <https://doi.org/10.1016/j.jmatprotec.2014.11.009>
- Srinivasan, N., Velmurugan, R., Kumar, R., Singh, S. K., & Pant, B. (2016). Deformation behavior of commercially pure (CP) titanium under equi-biaxial tension. *Materials Science and Engineering A*, 674, 540–551. <https://doi.org/10.1016/j.msea.2016.08.018>
- Stjohn, D., & Nie, J. (2017). *Titanium alloys*. <https://doi.org/10.1016/B978-0-08-099431-4.00007-5>
- Struers. (n.d.). *Vickers Hardness Testing*. Retrieved November 7, 2022, from <https://www.struers.com/en/Knowledge/Hardness-testing/Vickers#introduction>
- Su, C., Lv, S., Wang, R., Lv, Y., Lou, S., Wang, Q., & Guo, S. (2021). Effects of forming parameters on the forming limit of single-point incremental forming of sheet metal. *International Journal of Advanced Manufacturing Technology*, 113(1–2), 483–501. <https://doi.org/10.1007/s00170-020-06576-0>
- Suresh, K., Priyadarshini, A., & Kotkunde, N. (2018). Analysis of formability in incremental forming processes. In *Materials Today: Proceedings* (Vol. 5). www.sciencedirect.com/www.materialstoday.com/proceedings2214-7853
- Sutton, A. T., Kriewall, C. S., Leu, M. C., Newkirk, J. W., & Brown, B. (2020).

- Characterization of laser spatter and condensate generated during the selective laser melting of 304L stainless steel powder. *Additive Manufacturing*, 31(November 2019), 100904. <https://doi.org/10.1016/j.addma.2019.100904>
- Suwas, S., & Ray, R. K. (2014). *Crystallographic Texture of Materials*. <http://www.springer.com/series/4604>
- Tamimi, S., Sivaswamy, G., Siddiq, M. A., Leacock, A., & Blackwell, P. (2020). Mechanical response and microstructure evolution of commercially pure titanium subjected to repetitive bending under tension. *Materials and Design*, 193. <https://doi.org/10.1016/j.matdes.2020.108814>
- Tebaay, L. M., Hahn, M., & Tekkaya, A. E. (2020). Distortion and Dilution Behavior for Laser Metal Deposition onto Thin Sheet Metals. *International Journal of Precision Engineering and Manufacturing - Green Technology*. <https://doi.org/10.1007/s40684-020-00203-9>
- TIMET. (n.d.). *TIMETAL 50A*. Retrieved January 22, 2021, from www.timet.com
- Wang, Y. N., & Huang, J. C. (2003). Texture analysis in hexagonal materials. In *Materials Chemistry and Physics* (Vol. 81, Issue 1, pp. 11–26). [https://doi.org/10.1016/S0254-0584\(03\)00168-8](https://doi.org/10.1016/S0254-0584(03)00168-8)
- Weiss, I., & Semiatin, S. L. (1998). Thermomechanical processing of alpha titanium alloys. *TMS Annual Meeting*, 147–161.
- Wriggers, P. (2014). *Peter Wriggers Nonlinear Finite Element Methods*. May. <https://doi.org/10.1007/978-3-642-56865-7>
- Yadav, P., & Saxena, K. K. (2019). Effect of heat-treatment on microstructure and mechanical properties of Ti alloys: An overview. *Materials Today: Proceedings*, 26, 2546–2557. <https://doi.org/10.1016/j.matpr.2020.02.541>
- Yamanaka, K., Saito, W., Mori, M., Matsumoto, H., Sato, S., & Chiba, A. (2019a). Abnormal grain growth in commercially pure titanium during additive manufacturing with electron beam melting. *Materialia*, 6, 100281.

<https://doi.org/https://doi.org/10.1016/j.mtla.2019.100281>

- Yamanaka, K., Saito, W., Mori, M., Matsumoto, H., Sato, S., & Chiba, A. (2019b). Abnormal grain growth in commercially pure titanium during additive manufacturing with electron beam melting. *Materialia*, 6. <https://doi.org/10.1016/j.mtla.2019.100281>
- Yan, Z., Hassanin, H., El-sayed, M. A., Eldessouky, H. M., Rizki, J., Djuansjah, P., Alsaleh, N. A., Essa, K., & Ahmadein, M. A. (2021). *Multistage Tool Path Optimisation of Single-Point Incremental Forming Process*.
- Yang, M., Yao, Z., Li, Y., Li, P., Cui, F., & Bai, L. (2018). Study on Thickness Thinning Ratio of the Forming Parts in Single Point Incremental Forming Process. *Advances in Materials Science and Engineering*, 2018. <https://doi.org/10.1155/2018/2927189>
- Yi, N., Hama, T., Kobuki, A., Fujimoto, H., & Takuda, H. (2016). Anisotropic deformation behavior under various strain paths in commercially pure titanium Grade 1 and Grade 2 sheets. *Materials Science and Engineering A*, 655, 70–85. <https://doi.org/10.1016/j.msea.2015.12.081>
- Young, D., & Jeswiet, J. (2004). Wall thickness variations in single-point incremental forming. *Journal of Engineering Manufacture*, 218, 1453–1459.
- Yu, J., Rombouts, M., Maes, G., & Motmans, F. (2012). Material Properties of Ti6Al4V Parts Produced by Laser Metal Deposition. *Physics Procedia*, 39, 416–424. <https://doi.org/https://doi.org/10.1016/j.phpro.2012.10.056>
- Zhang, Z., Zhang, H., Shi, Y., Moser, N., Ren, H., Ehmann, K. F., & Cao, J. (2016). Springback Reduction by Annealing for Incremental Sheet Forming. *Procedia Manufacturing*, 5, 696–706. <https://doi.org/10.1016/j.promfg.2016.08.057>
- Zhu, Z., Dhokia, V. G., Nassehi, A., & Newman, S. T. (2013). A review of hybrid manufacturing processes - State of the art and future perspectives. *International Journal of Computer Integrated Manufacturing*, 26(7), 596–615. <https://doi.org/10.1080/0951192X.2012.749530>

10 Appendices

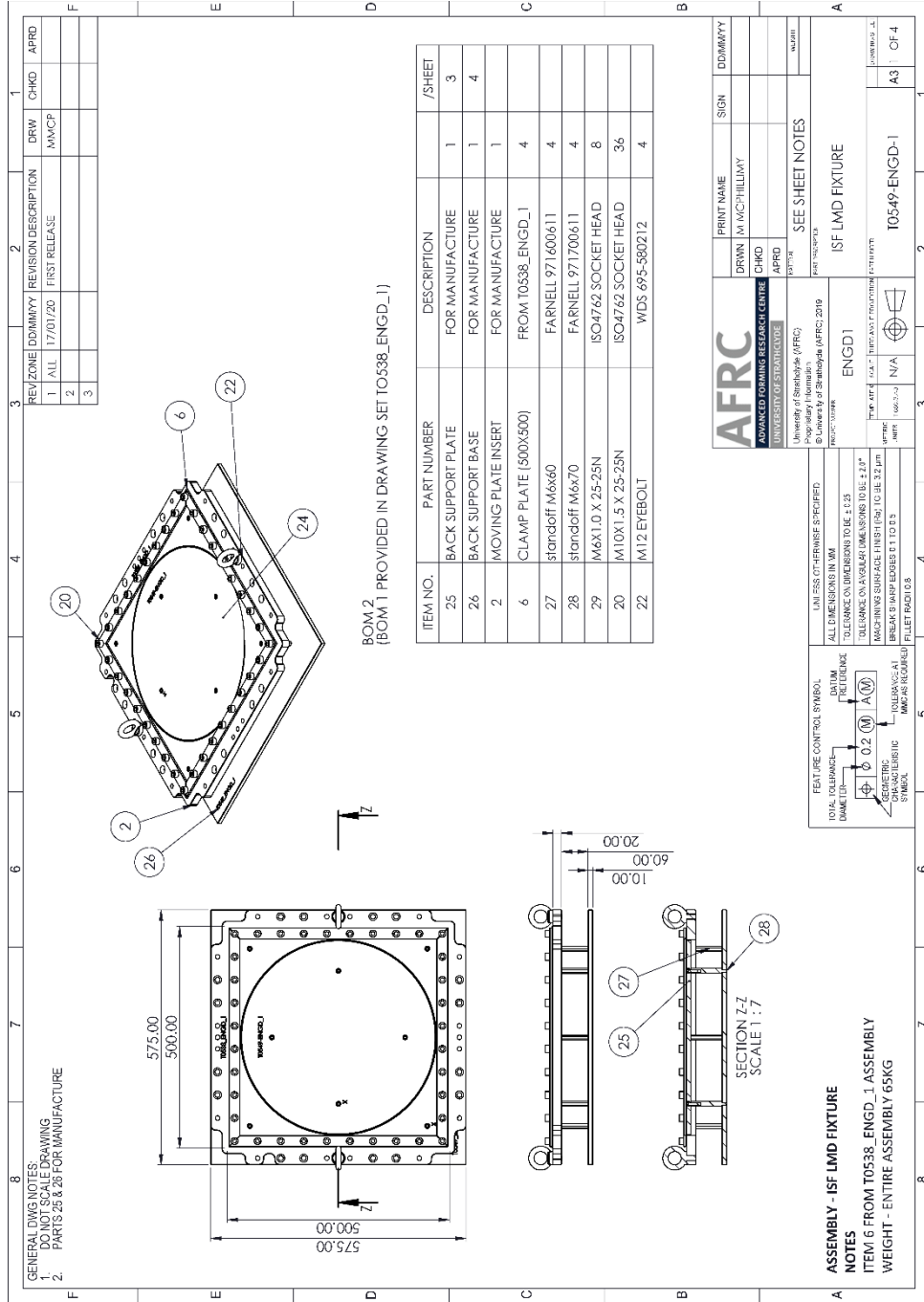
10.1 Product Design Specification for Fixture Design

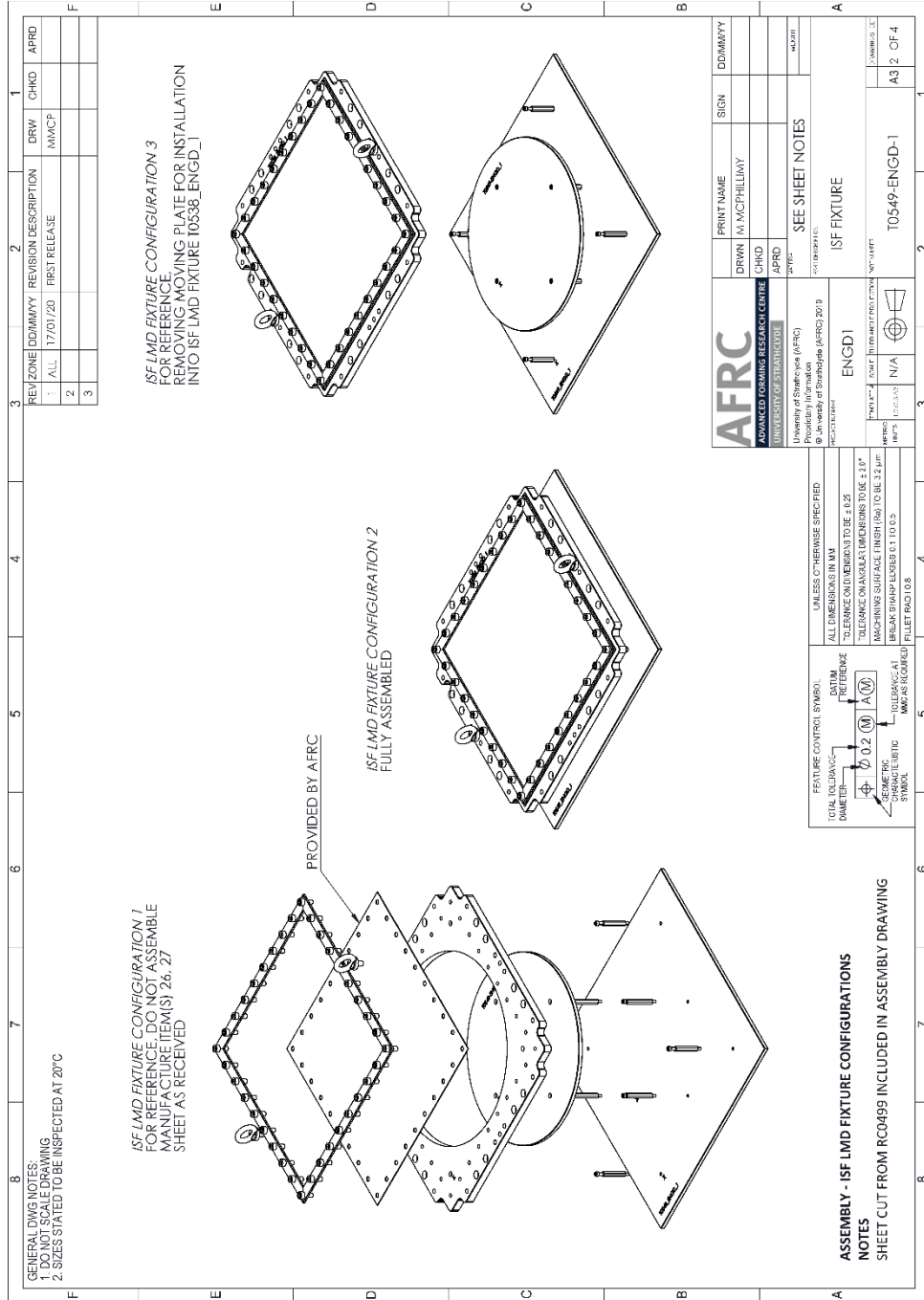
No.	Criteria	Requirement(s)
1	Performance	<ul style="list-style-type: none">• Sheet must be constrained on all sides.• Sheet must have under-side supported during LMD.• Sheet must not move.• Sheets must be kept parallel to the table surface.• Must be no risk of collisions.• Sheet must be open to the back-support die.• Sheet must be open to tool from above.• Sheet must be lowered over die.
2	Environment	<ul style="list-style-type: none">• Gas flow must not be restricted during LMD and heat treatment.• Must perform up to 600°C.
3	Maintenance	<ul style="list-style-type: none">• Guiding elements must be accessible for lubrication.• Sheet must be accessible during ISF.
4	Target product cost	<ul style="list-style-type: none">• Cost must be kept within project budget.
5	Component availability	<ul style="list-style-type: none">• Must use standard parts when possible.

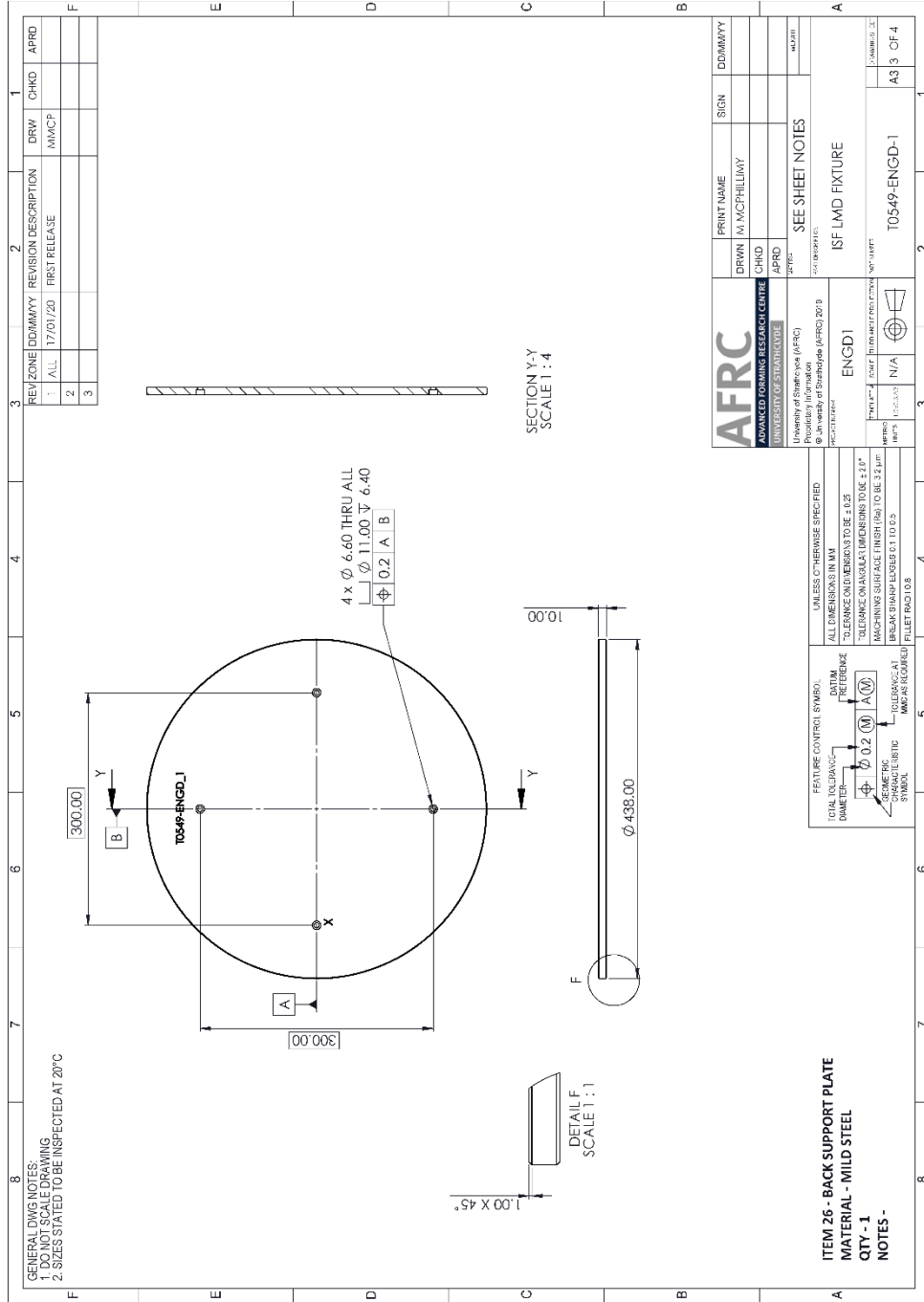
		<ul style="list-style-type: none"> • Must have reliable source for bought parts.
6	Transportation	<ul style="list-style-type: none"> • Sheets must be protected. • Must be kept as lightweight as possible.
7	Manufacturing Facilities	<ul style="list-style-type: none"> • Must be easily manufacturable.
8	Size and weight	<ul style="list-style-type: none"> • Must be within the size limit of laser specialist LMD cell. • Must fit inside DMU250 CNC at AFRC.
9	Finish	<ul style="list-style-type: none"> • All edges must be burred. • Back-support must not damage sheet.
10	Materials	<ul style="list-style-type: none"> • Materials must be machinable. • Must be readily available. • Must meet basic requirements. • Must be able to withstand 600°C.
121	Quality and reliability	<ul style="list-style-type: none"> • Must perform during entire process cycle. • Movement of parts must be uninhibited and controllable. • Must always maintain accuracy.
12	Processes	<ul style="list-style-type: none"> • Design for manufacturability of non-standard components to be performed. • Non-standard parts to be machined.
13	Safety	<ul style="list-style-type: none"> • Full risk assessment must be prepared. • Assembling sub-components must not put operator at risk.

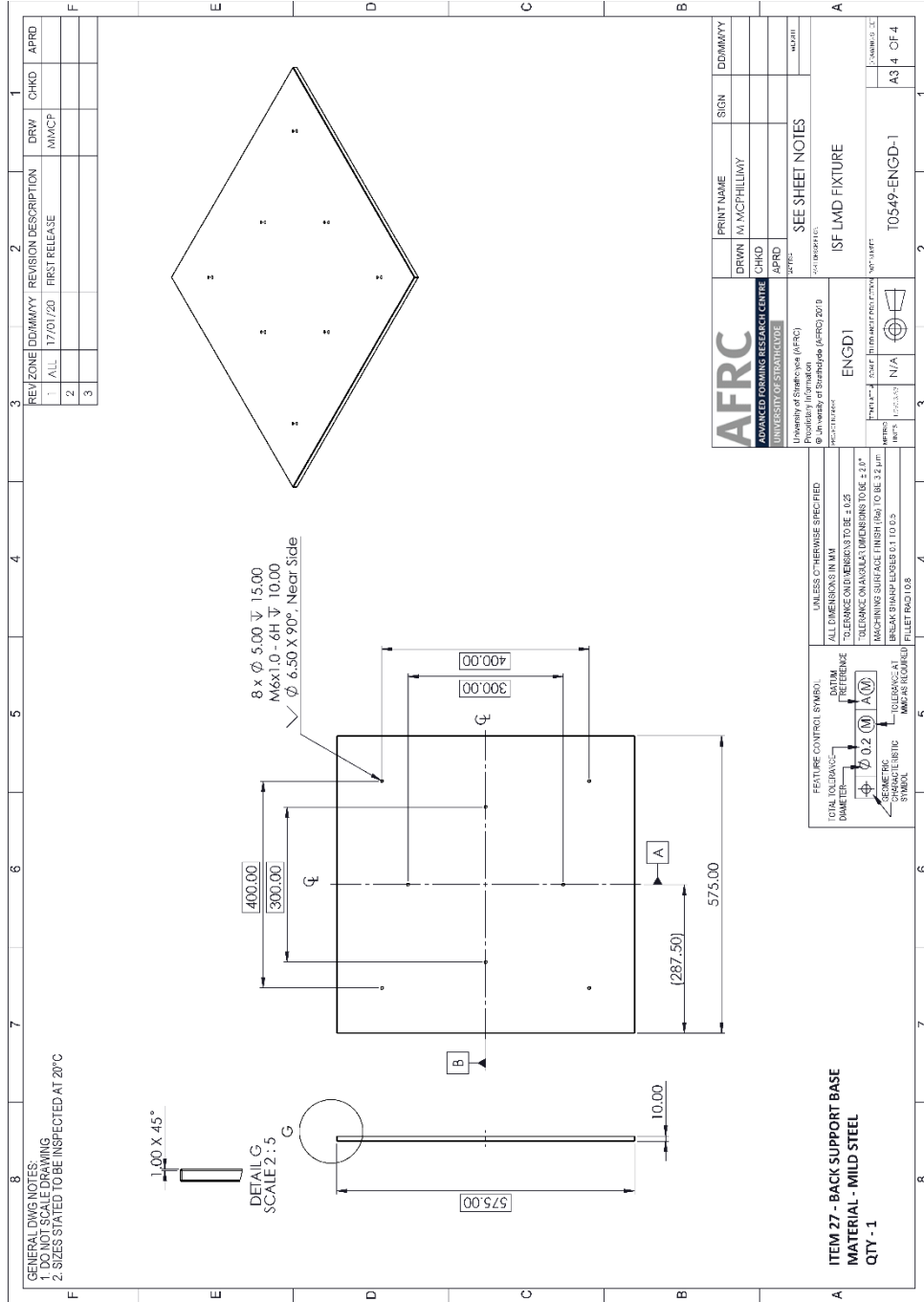
		<ul style="list-style-type: none">• Installing sheet must not put operator at risk.• All edges must be de-burred.
14	Company constraints	<ul style="list-style-type: none">• Must be easy to store.• Must be operable in company machinery.
15	Patents	<ul style="list-style-type: none">• Research into patents must be performed prior to detail design.
17	Installation, operation	<ul style="list-style-type: none">• Detailed description of assembly and disassembly must be provided.• Assembly and disassembly must be performable with standard tools.• Standard fixings must be used for assembly and installation.• Operation must be controlled remotely.

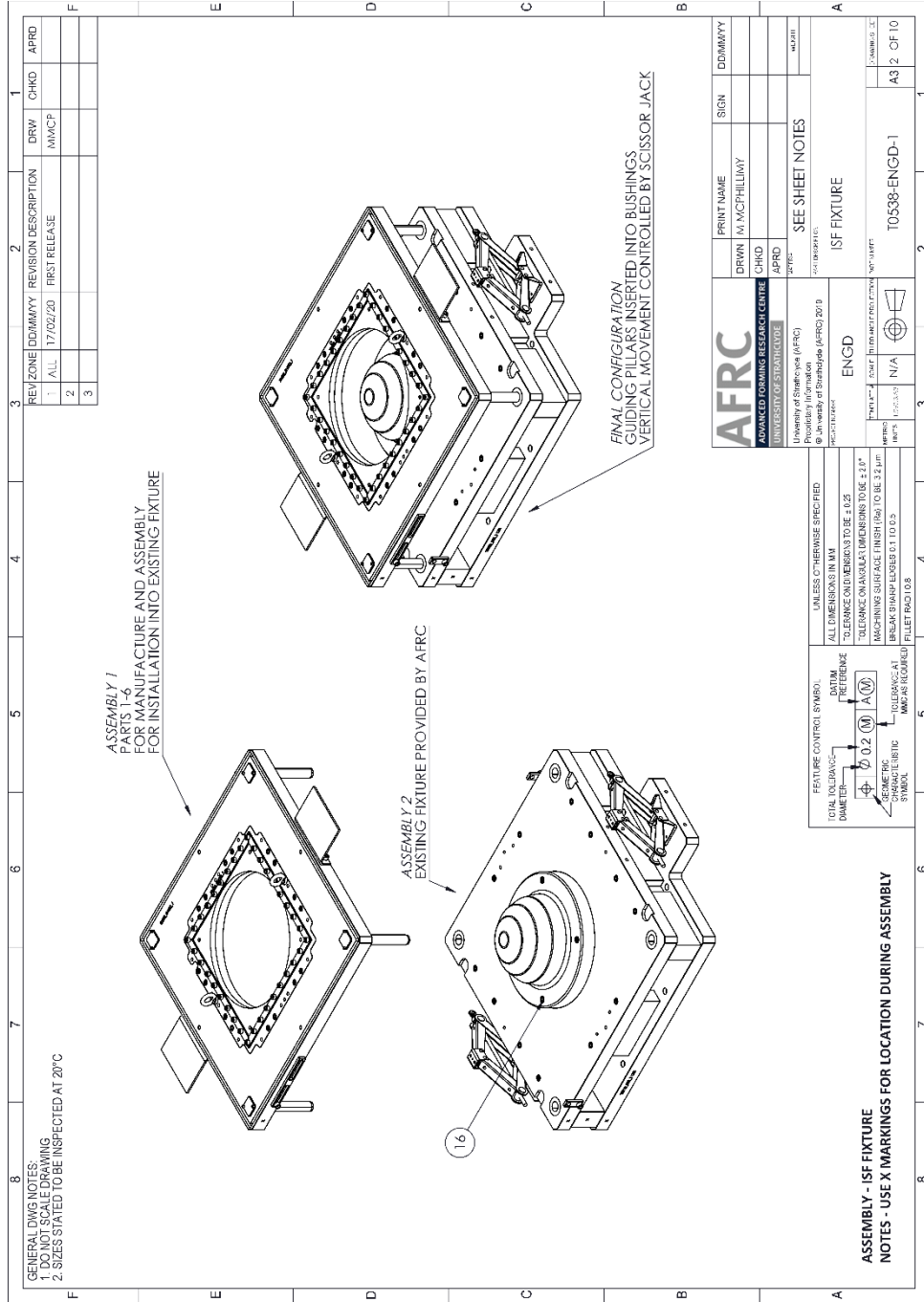
10.2 Engineering Drawings, LMD Fixture









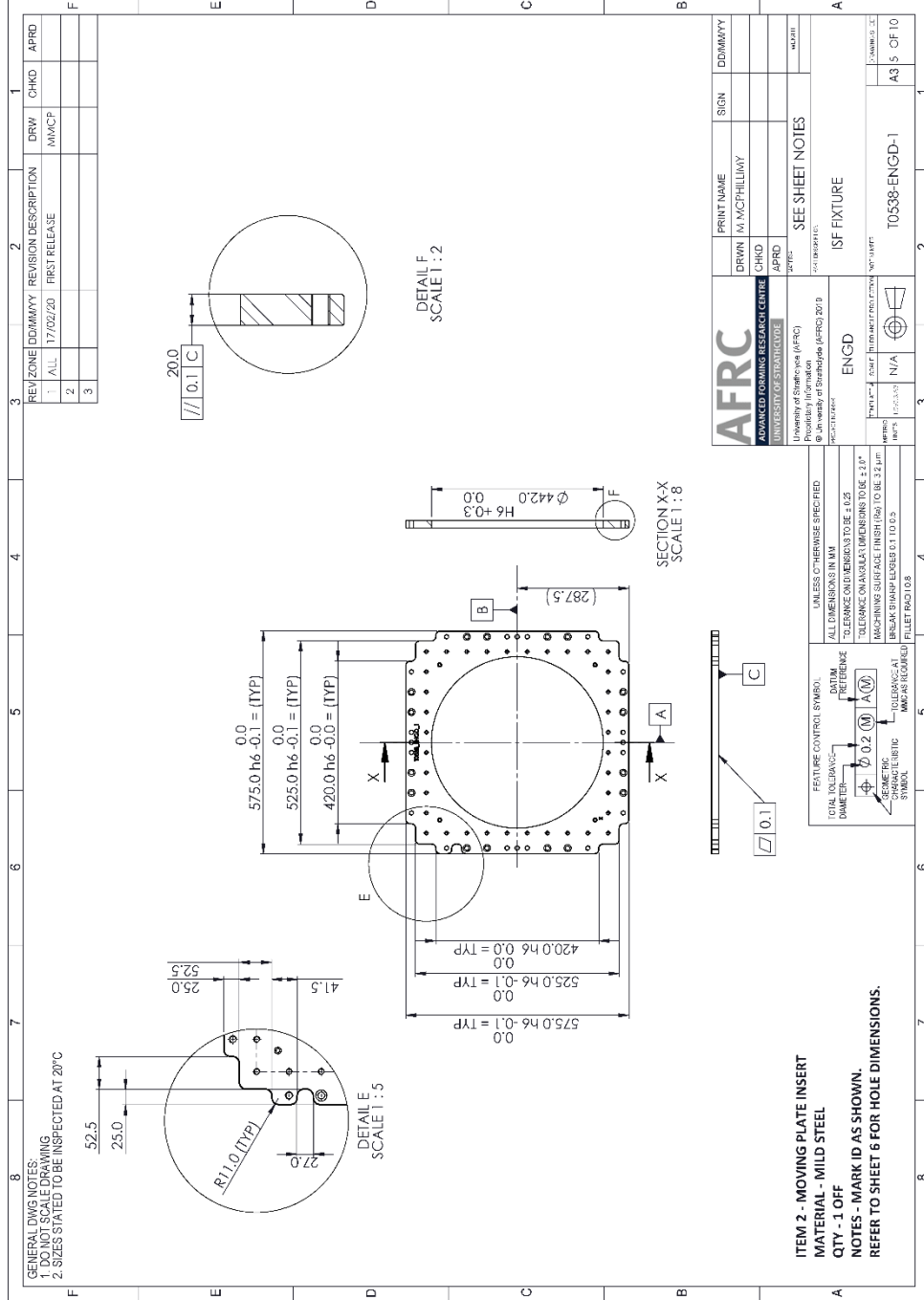


ASSEMBLY - ISF FIXTURE
NOTES - USE X MARKINGS FOR LOCATION DURING ASSEMBLY

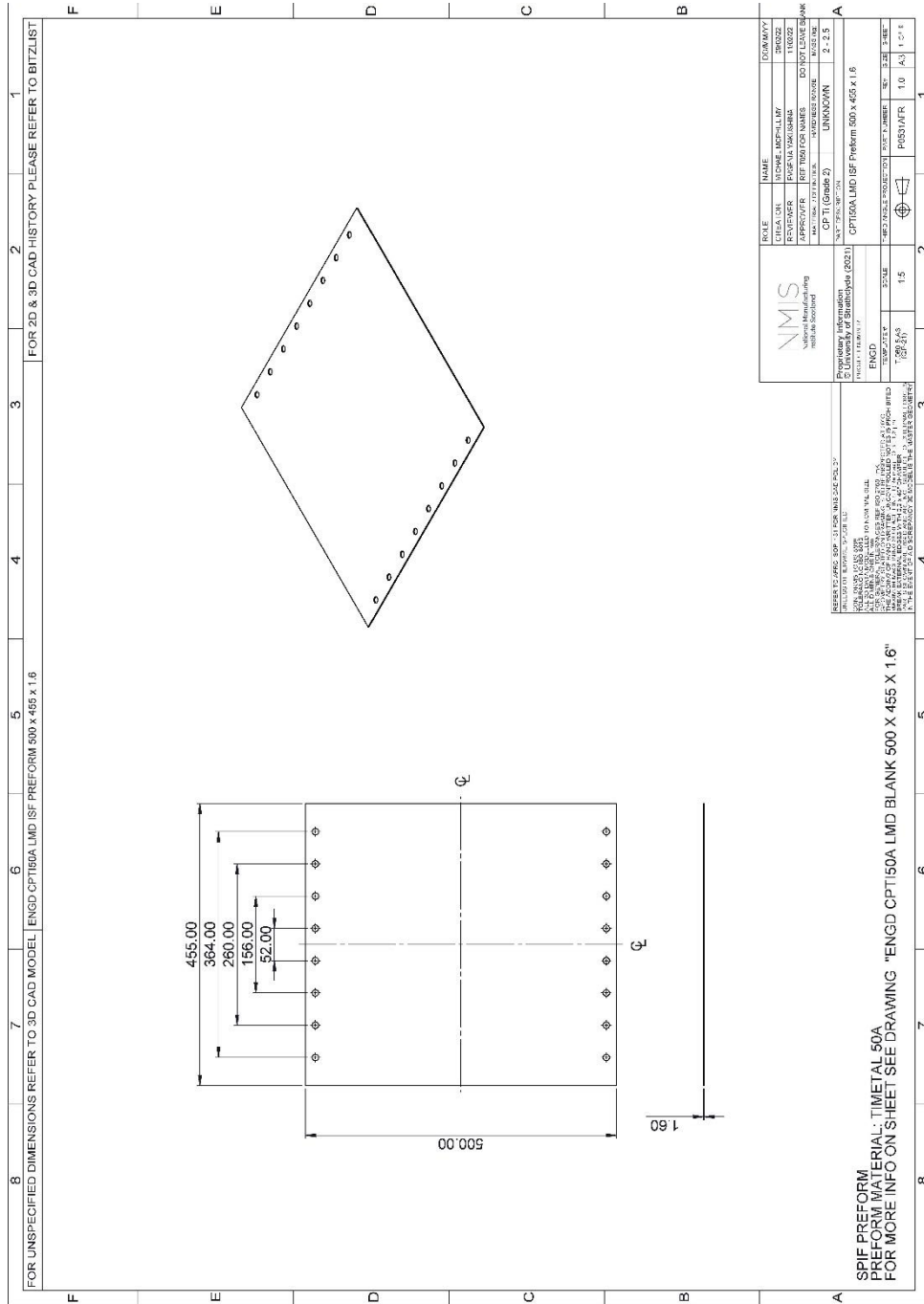
FEATURE CONTROL SYMBOL	UNLESS OTHERWISE SPECIFIED
TOTAL TOLERANCES	ALL DIMENSIONS IN MM
DIMETER	TOLERANCE ON DIMENSIONS TO BE ± 0.25
Ø 0.2	TOLERANCE ON ANGLES DIMENSIONS TO BE ± 3.0°
Ø 0.2 (M)	MACHINING SURFACE FINISH (Ra) TO BE 1.2 µm
Ø 0.2 (A)	BREAK CHAMF USES 0.1 TO 0.25
Ø 0.2 (S)	TOLERANCES AT ANGLES TO BE ± 0.5°
Ø 0.2 (R)	TOLERANCES AT ANGLES TO BE ± 0.5°
Ø 0.2 (T)	TOLERANCES AT ANGLES TO BE ± 0.5°
Ø 0.2 (U)	TOLERANCES AT ANGLES TO BE ± 0.5°
Ø 0.2 (V)	TOLERANCES AT ANGLES TO BE ± 0.5°
Ø 0.2 (W)	TOLERANCES AT ANGLES TO BE ± 0.5°
Ø 0.2 (X)	TOLERANCES AT ANGLES TO BE ± 0.5°
Ø 0.2 (Y)	TOLERANCES AT ANGLES TO BE ± 0.5°
Ø 0.2 (Z)	TOLERANCES AT ANGLES TO BE ± 0.5°

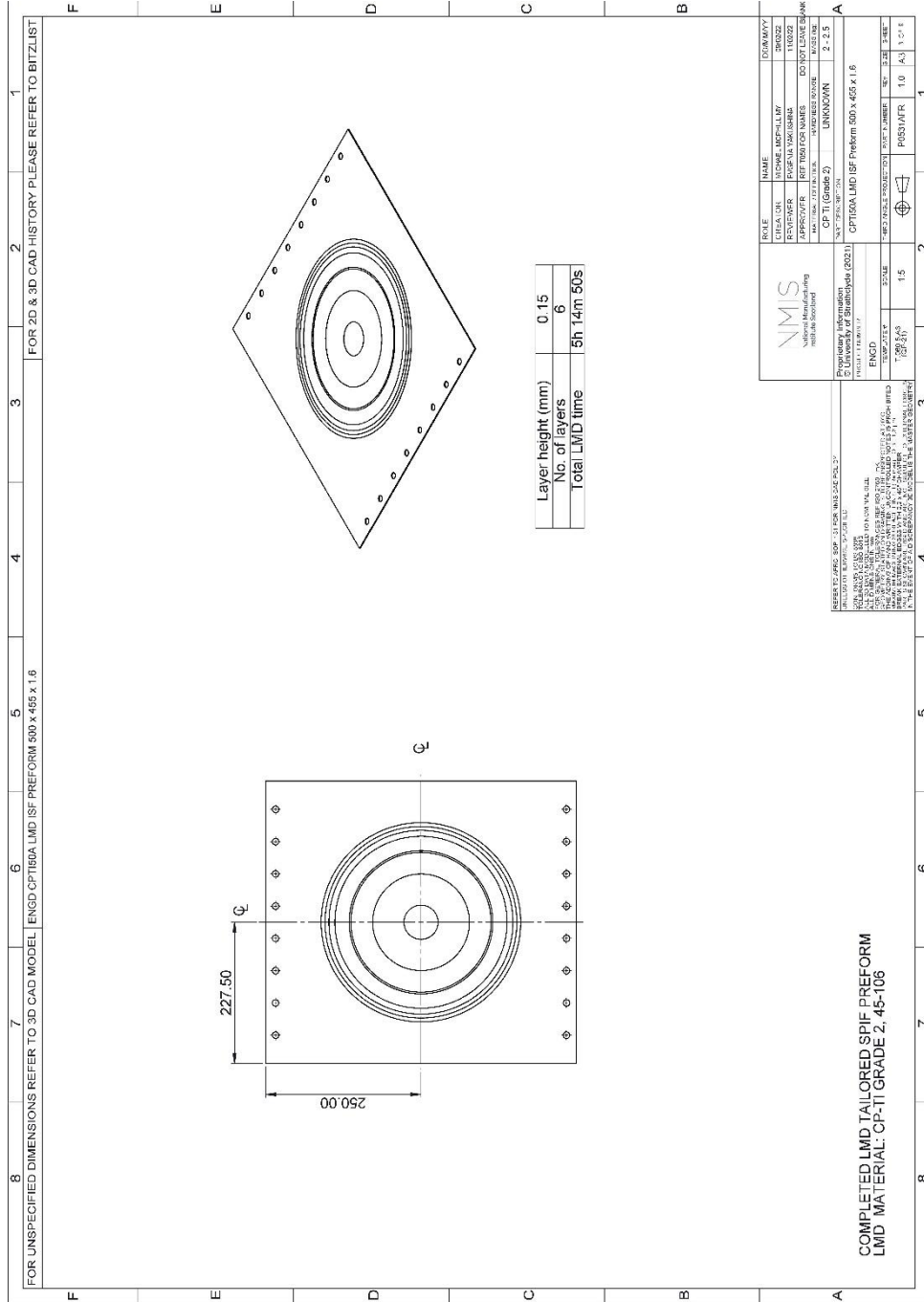
AFRC
ADVANCED DRAWING RESEARCH CENTRE
 UNIVERSITY OF STRATHCLYDE
 University of Strathclyde (AFRC)
 Provisional Information
 © University of Strathclyde (AFRC) 2010

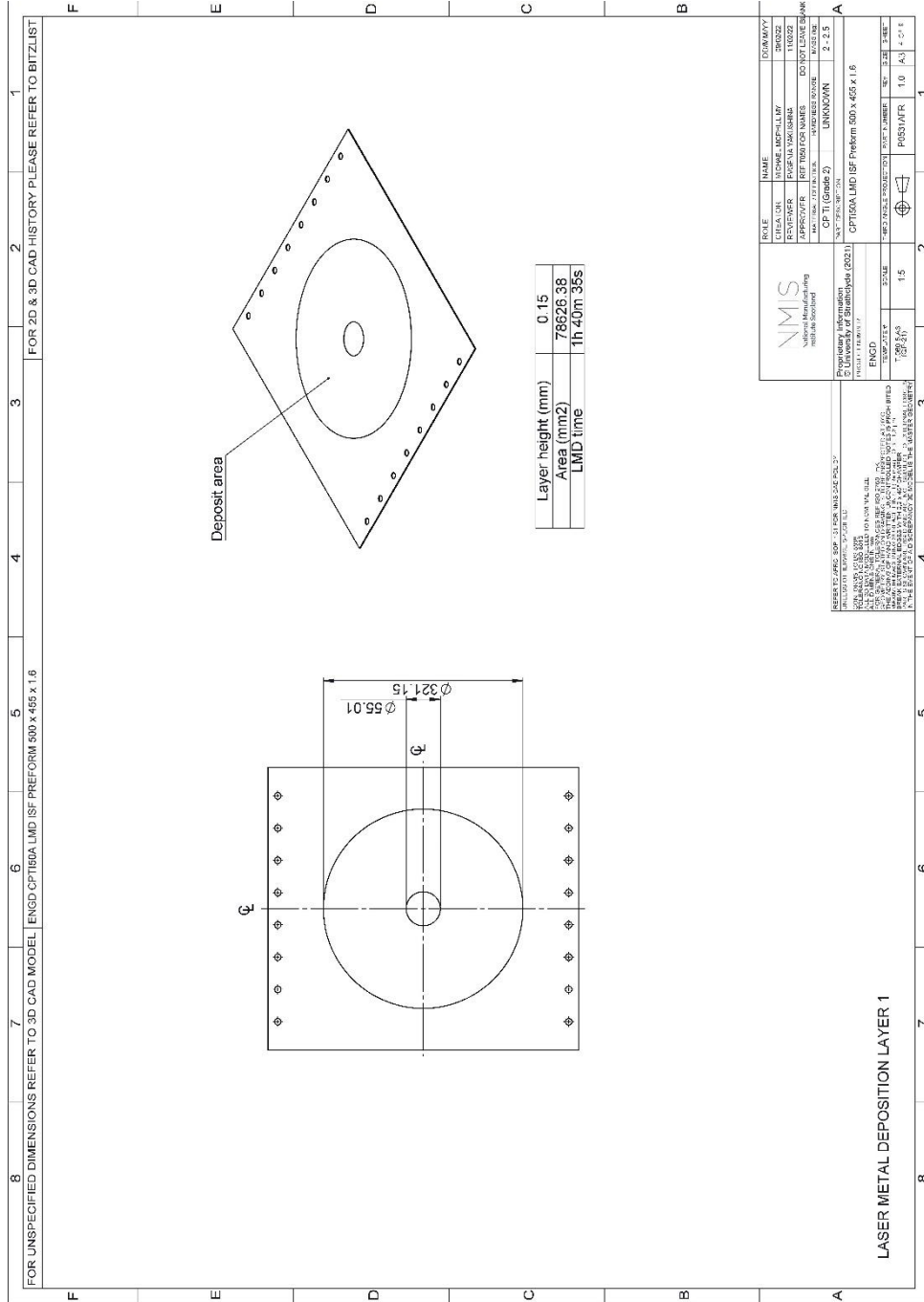
PRINT NAME	SIGN	DDMMYY
DRWN M. MCPHILLWAY		
CHKD		
APRD		
SEE SHEET NOTES		
ISF FIXTURE		
T05389-ENGD-1		A3 2 OF 10

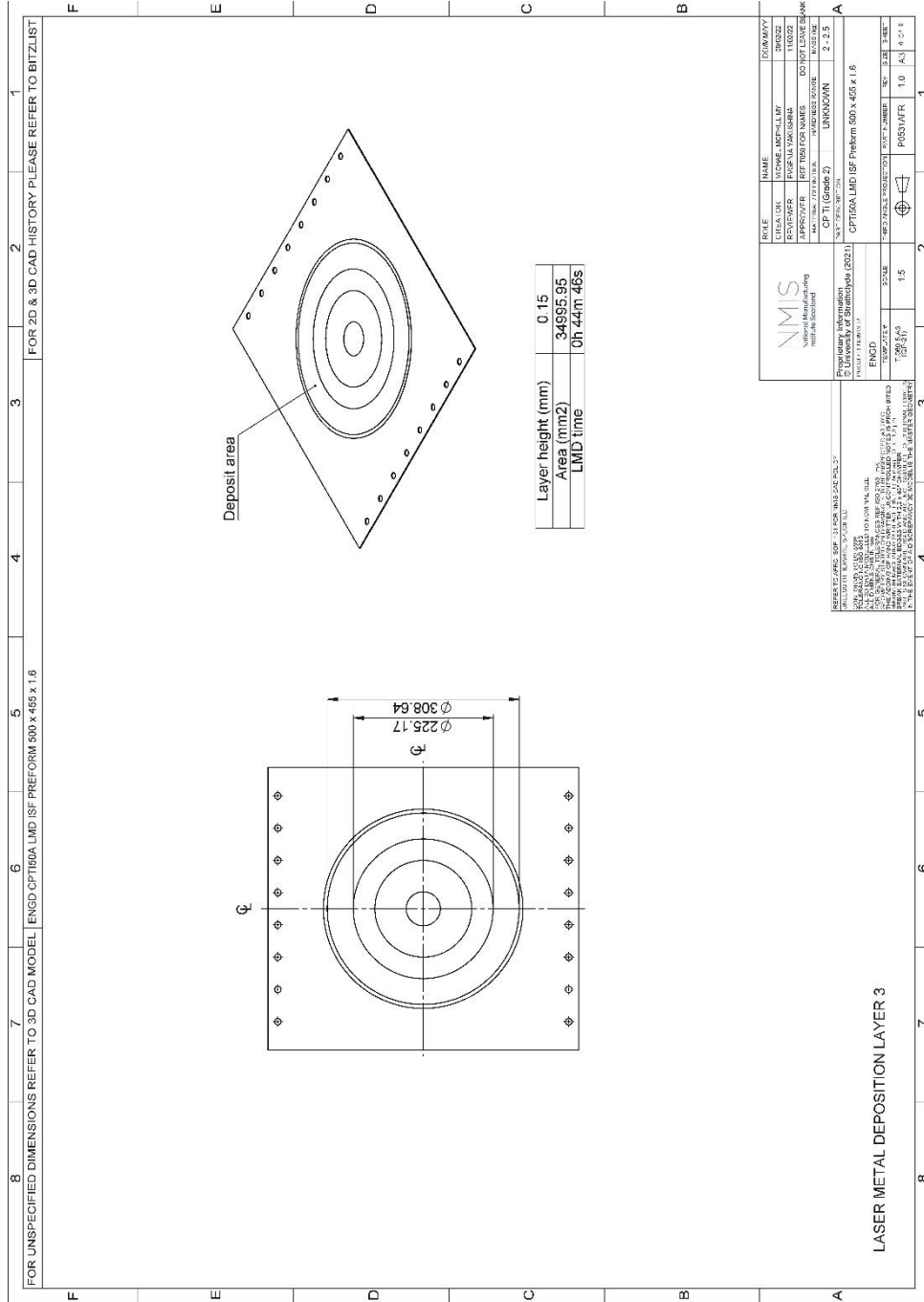


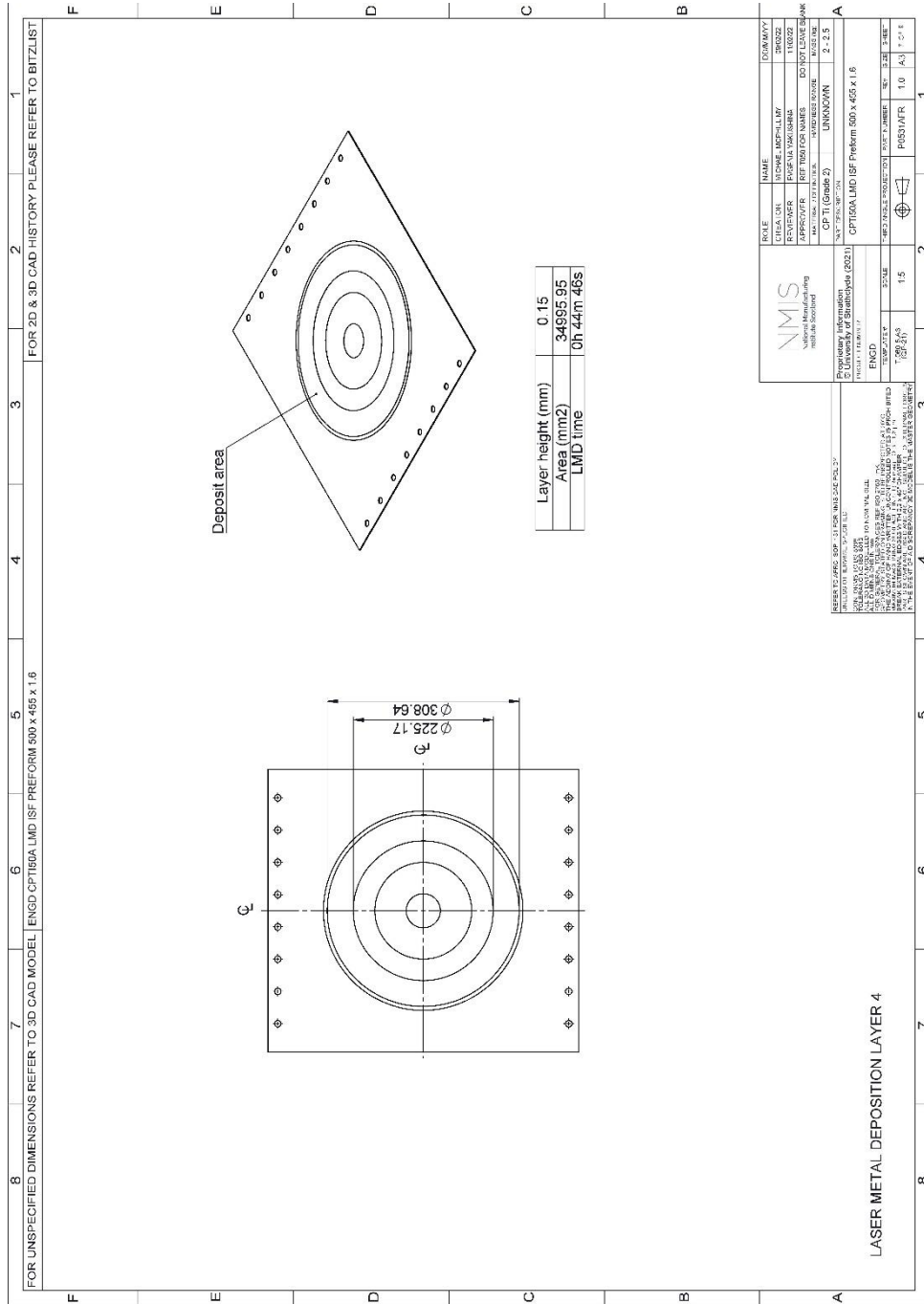
10.5 Engineering Drawings, LMD/ISF preform

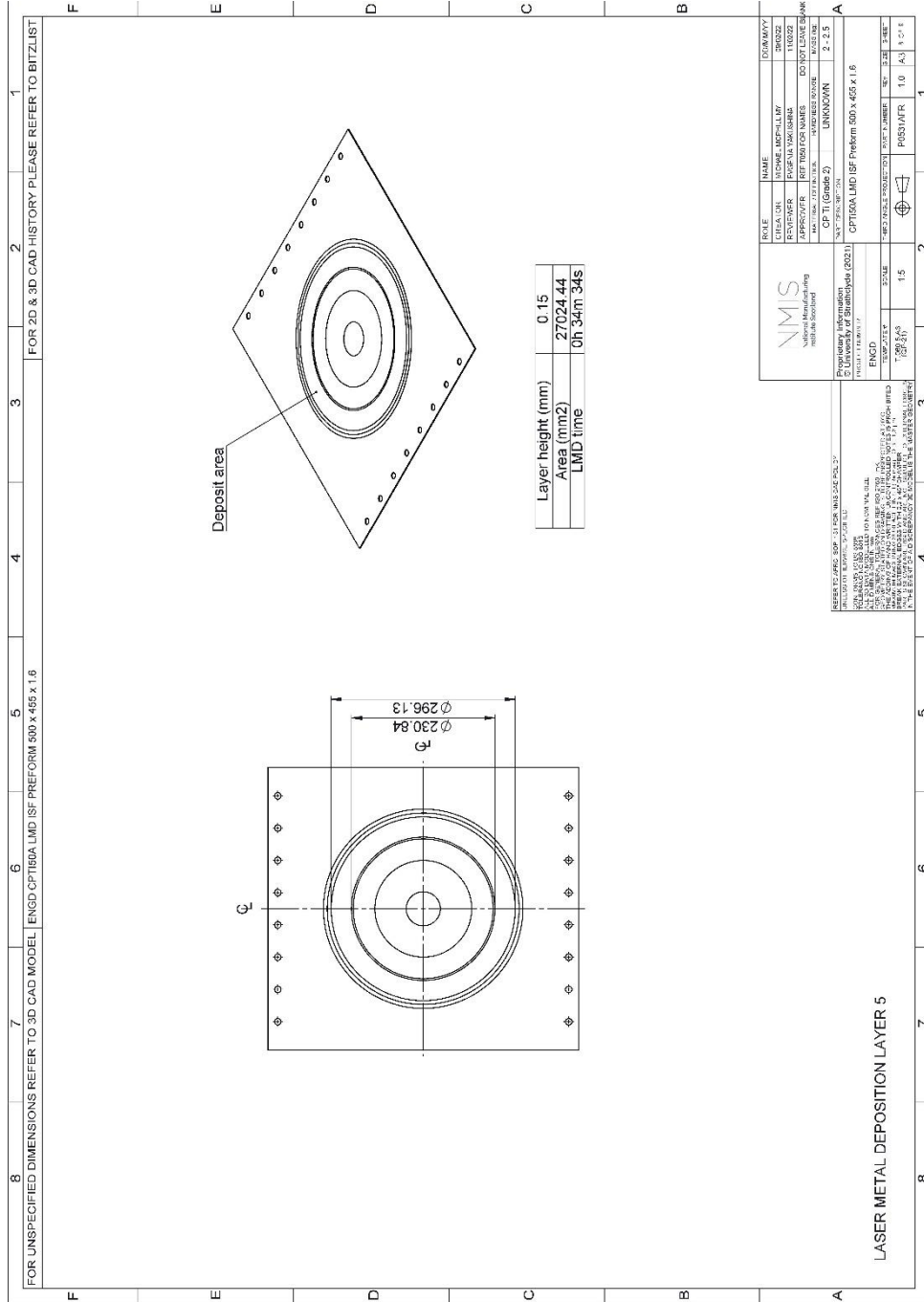


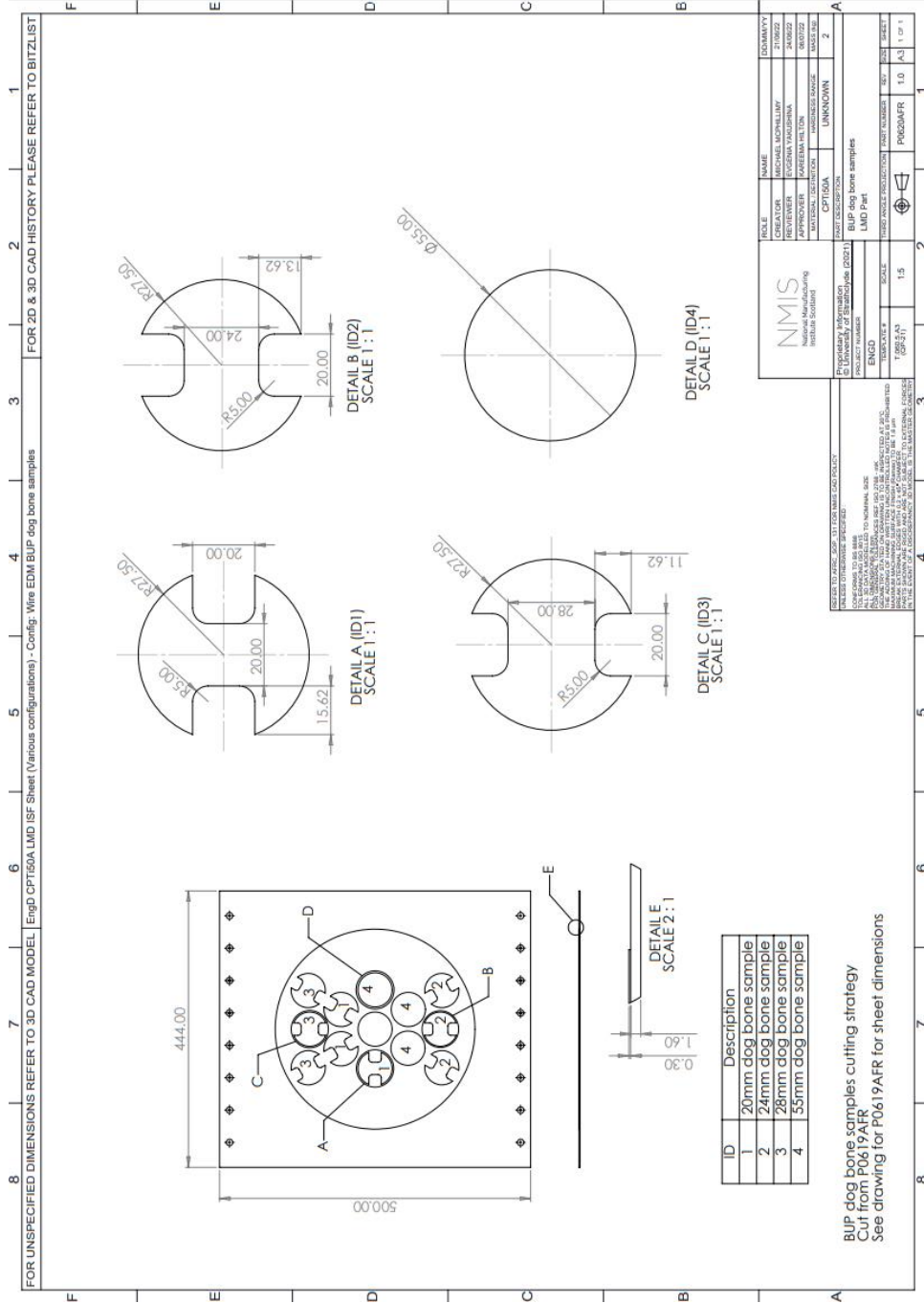












10.8 LMD sub-contractor logbook

30/09/2020. J311 - Log Book No 708 - 20200930
Page 1.
J311. AFRC.

(LMD OF CP TITANIUM SHEET.)

Powder - AP + C / SPHERICAL APA CP Ti Powder.
CP Ti GRADE 2. LOT: 201-C0050
45-106µm 2.5 Kg.

5.0/0.6 Disc, SPREADER + EXHAUSTOR.

VACUUM PORT - PLUGGED.

Continued... THURS 1st October.

- ACTIONS TO FOLLOW - BP:

- MARKETING PICS OF WAS KIT.

- IMPORT DUTIES BILL:

TASK 1
Step 1/2: LMD trials onto US Ti Piece...
the twopatt..

TASK 1

Part 2

D101

TP8 TOOLPATH =
"J311-TASK1-PAD2"

Gases:

Carrier (Plugged) = 1.5 bar, 4 l/min

Nozzle = 2.0 bar, 10 l/min + 2 Revs.

• Speed = 15 mm/sec, Separation = ~~2.0~~ 2.0 mm

Dial = 8.0, Power = ~~650W~~ 375W, Powder = 6%

D102:

→ Power increased to 675W.

↳ Looked OK.. Good power level..

But deep valleys so Next Step is to

reduce width

D103:

• Separation reduced to 1.4 mm → Was 2.0 mm.

TP8 = "J311-TASK1-PAD2"

Build Height seems to be IRO 0.25mm.

Page 3

D104.

EXACTLY SAME AS D103 BUT 3.5%
POWDER POW RAZO. = BUILD HEIGHT IS NOMINAL!
0.15 mm POW LAYER.

↳ Good. Next Step is to:

- Continue using LAS Ti substrate

TASK 2

↑ exact material
alloy is
unknown.

- Build a larger pad. This time do with
2x layers → ~~total~~ Layer 1 = Y Travel
Layer 2 = X Travel.

- Dimensions = 60mm long
x 30mm wide

TP8 program: "S311_TASK 1_PAD3"

D105: Worked well.

Summary of Parameters:

- Laser = 675W
- Powder = 3.5%
- Separation = 1.4mm.

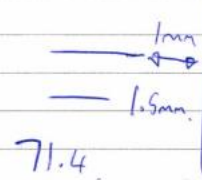
Fri 02/10/2020.

~~PPB~~ Cont.

- 15mm/sec
- Dial = 8.0
-
-
-

Pad 4

CHAMFER 15125...



PPB Metallurgically Sectioned D105.

→ Result: • Looks OK....

→ Moving on... Now do final PADS onto fullsize

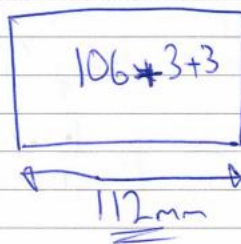
TASK 3

Ti Sheet on AFRC fixture..

D106

• Pad size requested by Michael = 106 x 65

but due to edges not building great - LAS to build oversized..



$$\begin{array}{c} \updownarrow \\ 65 + 3 + 3 = \underline{71\text{mm}} \end{array}$$

→ TOOLPATH = "S311-TASK3-PAD4"

Paces

$L1 = Ln60.$

$L2 = Ln2922.$

$A7 = -1.0540^\circ$

$A8 = \text{DEG} = -70.1450^\circ$

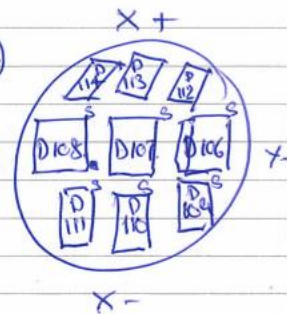
$Z = -543.00 \text{ m}$

Line 2919.

STARTED @ 13:58 Hrs. (2 LAYERS) VIDEO RECORDED.
 ENDED @ 14: Hrs.

D107 (4 LAYERS)

STARTED @ 14:41 Hrs.
 ENDED @ 15:22 Hrs.



D108 (6 LAYERS)

STARTED @ 15:54 Hrs. GOING OUT OF PACES SO
 ENDED @ 16:55 Hrs. BELIEVE IT TO BE UNDER
 BUILDING HEIGHTWISE.

PAGE 6

05/10/2020. J311 CONT.

MORE Ti GRADE 2 POWDER ADDED TO THE HOPPER
ON TO THE ~~45°~~^{90°} DEPOSITS.

D109. (2 LAYERS) SPR. J311-T3-PAD5-L1-L2

STARTED DEPOSITING @ 11:59 Hrs.
ENDED @ 12:10 Hrs.

* EXTENDED LUNCH, - TO GO AND BUY FLOOR BUMPER.

D110. (4 LAYERS) STARTED @ 13:37 Hrs.
ENDED @ 14:18 Hrs.

* THINK FIXTURE MAY HAVE MOVED DURING CLAMPING, TIGHTEN
IN

D111. (6 LAYERS) STARTED @ 14:34 Hrs.
ENDED @ 15:36 Hrs.

LINE 9930 APPROX.

CHECKED CARRIER GAS FLOW. (WAS SLIGHTLY LOW, SO
INCREASED TO MAINTAIN 4 lpm)

ON TO THE 45° DEPOSITS.

D112. (2 LAYERS) SPR. J311-T3-PAD6-L1-L2

NO CLAMPING POSSIBLE TOWARDS CORNER OF TIC

DUE TO LIMITED ACCESS AND PROCESS HOOD.

Phase 7

J 311 - D112 CONT. (2 LAYERS)

STARTED @ 16:49 Hrs.

ENDED @ 17:09 Hrs.

D113 (4 LAYERS)

SPR. J311-T3-PAD6-L1-L4

STARTED @ 17:39 Hrs.

ENDED @ 18:20 Hrs.

D114. (6 LAYERS.)

SPR. J311-T3-PAD6-L1-L6

STARTED @ 18:36 Hrs.

ENDED @ 19:36 Hrs.

06/10/2020.

EMPTY POWDER FEED HOPPER

J331 LB PLASTICS. 2 X EXT 1474 -
1 OFF KI T3, 1 OFF KI T7.

POWDER FEEDER COMMAND OUT READY PEN

S/STEEL DEBRISON METCO DIAMALLOY 1013
(LOT NO 481687.)

T, SLOT TABLE FIXED TO MANIPULATOR.

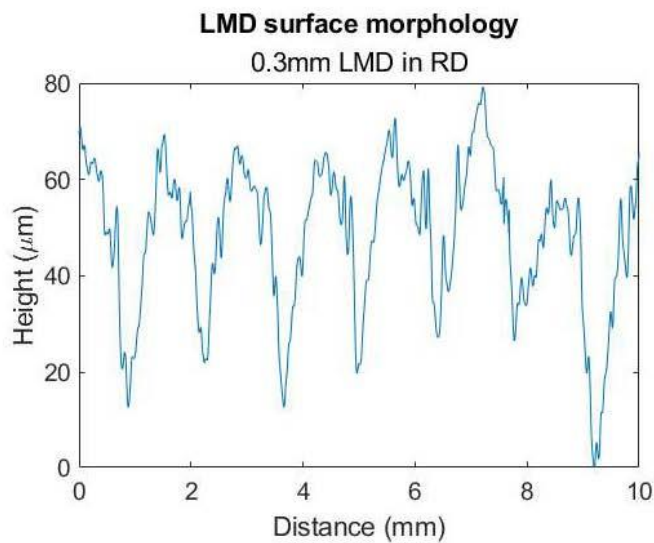
FORMER J 327 SUB PROGRAM ADOPTED

10.9 MATLAB code, Tensile testing data

```
clear all;close all;fclose all;clc;
a = 9.5733; % insert cross-section area of tensile specimen
g = 20; % insert gauge length
%
% load tensile specimen experimental f x d data
data=load('TS1f_d.txt');
fexp_1=data(:,1);
dexp_1=data(:,2);
fexp_2=data(:,3);
dexp_2=data(:,4);
fexp_3=data(:,5);
dexp_3=data(:,6);
%
% calculate mean
mf = (fexp_1 + fexp_2 + fexp_3)/3;
md = (dexp_1 + dexp_2 + dexp_3)/3;
%
% calculate eng s and e
es = mf/a;
ee = md/g;
%
% plot engineering curve
plot(ee,es,'LineWidth',1.0);
xlim([0 0.5]);
ylim([0 600]);
grid on;
datacursormode on;
%
% find uts and % elongation
uts = max(es);
elon = (max(md)/20)*100;
%
% calculate and plot young's modulus
f1=fit(ee(1:50),es(1:50),'poly1');
p1=coeffvalues(f1); % coefficient of fit
Ex=p1(1); % young's modulus
%
% plot 0.2% line for ys
x = 0.02:0.000001:0.1;
y = Ex*(x-0.02);
hold on;plot(x, y, 'r');hold off; % extract ys with point selection, y value = ys
% to improve find intersection of curves instead of selecting point manually
%
% label engineering plot
xlabel('strain');
ylabel('stress (MPa)');
title('Engineering sve TS1');
legend('eng sve curve','0.2% yield stress proof','Location','southeast');
%
% find true values
ts=es.*(1+ee);
te=log(1+ee);
[val, smax] = max(ts);
te(smax+1:end) = [] ;
ts(smax+1:end) = [] ;
%
% plot true curve
figure;plot(te,ts,'LineWidth',1.0);
xlim([0 0.5]);
```

10.10 MATLAB code, Alicona profile

```
clear all;close all;fclose all;clc;
data=load('ts21_z.txt');
x = data(:,1)*1000;
y = data(:,2)*1000000;
%
% High and low values
high = islocalmax(y);
low = islocalmin(y);
z_high = y(high);
z_low = y(low);
datapoints = high | low;
z_datapoints = y(datapoints);
max_datapoint = max(z_datapoints);
min_datapoint = min(z_datapoints);
z_datapoints = y(datapoints)+(-min_datapoint);
%
% plot
plot(x,y+(-min_datapoint), 'linewidth', 1);
xlabel('Length [mm]');
ylabel('Height [\u00b5m]');
title('LMD surface morphology');
subtitle('0.3mm LMD in RD');
xlabel('Distance (mm)');
ylabel('Height (\u00b5m)');
xlim([0 10]);
```



Published with MATLAB\u2122 R2020b

10.11 MATLAB code, Alicona roughness

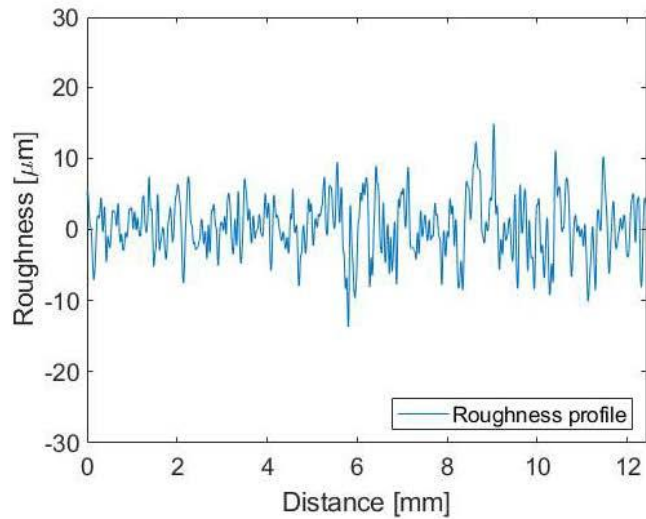
Contents

- [Plot roughness profile](#)
- [Add gaussian bell data](#)

Plot roughness profile

```
clear all;close all;fclose all;clc;
data=readmatrix('LMDSPIF_0deg_profiletable.txt');
data2=readmatrix('LMDSPIF_0deg_profiletable2.txt');
data3=readmatrix('LMDSPIF_0deg_profiletable3.txt');
l=data(:,4); %length (mm)
p=data(:,5); %roughness (um)
l2=data2(:,4);
z2=data2(:,5);
l3=data3(:,4);
z3=data3(:,5);
%
l=(l+l2+l3)/3; %mean of length
p=(p+z2+z3)/3; %mean of roughness
lo=l(1);l=l-lo;clear lo
%
plot(l,p); hold on
xlim([0 l(end)]);
ylim([-30 30]);
ylabel('Roughness [\num]');
xlabel('Distance [mm]');
legend('Roughness profile','Ra','Location','SouthEast');
```

Warning: Ignoring extra legend entries.

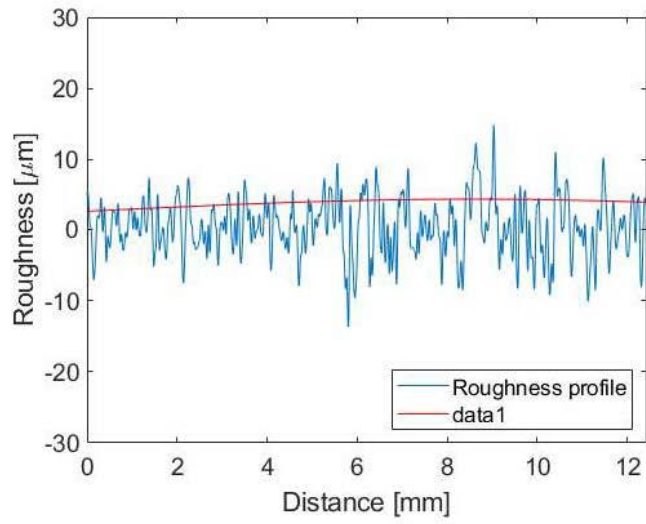


Add gaussian bell data

```

g = @(A,X) A(1)*exp(-(X-A(2)).^2/(2*A(3)^2));
f = @(A,X) A(1)*exp(A(2)*X);
pmax=max(p); lnew=[]; pnew=[];
for n=1:length(l)
    if p(n)>0.1*pmax;
        lnew=[lnew,l(n)];
        pnew=[pnew,p(n)];
    end
end
and
%fitting
plog=log(pnew);
llog=lnew;
f=polyfit(llog,plog,2);
% compute parameters
sigma=sqrt(-1/(2*f(1))); mu=f(2)*sigma^2; a=exp(f(3)+mu^2/(2*sigma^2));
% plot fitting curve
h=4; pfit=-48:l/h:48; A=[a,mu,sigma]; plot(pfit,g(A,pfit),'-r');

```



Published with MATLAB® R2020b

10.12 MATLAB code, Generating mesh .txt file

```
clear all;close all;fclose all;clc;
%
file='modelv1_4.inp';
%
nodes=[];
elements=[];
sample=[];
top=[];
bottom=[];
nodetop=[];
nodebottom=[];
basematerial=[];
AMmaterial=[];
%
line=[];
file=fopen(file,'r');
while ~feof(file)
    if strcmp(line,'*Node')==1
        line=fgetl(file);
        while line(1)~='*'
            nodes=[nodes;str2num(line)];
            line=fgetl(file);
        end
    elseif strcmp(line,'*Element, type=C3D8R')==1
        line=fgetl(file);
        while line(1)~='*'
            elements=[elements;str2num(line)];
            line=fgetl(file);
        end
    elseif strcmp(line,'*Nset, nset=top')==1
        line=fgetl(file);
        while line(1)~='*'
            top=[top,str2num(line)];
            line=fgetl(file);
        end
    elseif strcmp(line,'*Nset, nset=bottom')==1
        line=fgetl(file);
        while line(1)~='*'
            bottom=[bottom,str2num(line)];
            line=fgetl(file);
        end
    elseif strcmp(line,'*Nset, nset=nodetop')==1
        line=fgetl(file);
        while line(1)~='*'
            nodetop=[nodetop,str2num(line)];
            line=fgetl(file);
        end
    elseif strcmp(line,'*Nset, nset=nodebottom')==1
        line=fgetl(file);
        while line(1)~='*'
            nodebottom=[nodebottom,str2num(line)];
            line=fgetl(file);
        end
    elseif strcmp(line,'*Elset, elset=basematerial')==1
        line=fgetl(file);
```

```

while line(1)~='*'
    basematerial=[basematerial,str2num(line)];
    line=fgetl(file);
end
elseif strcmp(line,'*Elset, elset=AMmaterial')==1
    line=fgetl(file);
    while line(1)~='*'
        AMmaterial=[AMmaterial,str2num(line)];
        line=fgetl(file);
    end
else
    line=fgetl(file);
end
end
fclose(file);
%
nodes2=nodes;
nodes2(:,5)=-.373290e+31;
%
elements2=elements;
elements2(:,10)=-.373290E+31;
%
file=fopen('mesh_pamstamp.asc','w');
%
fprintf(file,'%10.f\n',length(nodes(:,1)));
fprintf(file,'%10.f, %10.5f, %10.5f, %10.5f, %10.5e\n',nodes2');
%
fprintf(file,'%10.f\n',0);
fprintf(file,'%10.f\n',0);
fprintf(file,'%10.f\n',0);
%
fprintf(file,'%10.f\n',length(elements(:,1)));
fprintf(file,'%10.f, %10.f, %10.f, %10.f, %10.f, %10.f\n%10.f, %10.f, %10.f, %10.5e\n',elements2');
%
fprintf(file,'%10.f\n',0);
%
fprintf(file,'%10.f\n',4);
%
fprintf(file,'top\n');
fprintf(file,'%10.f\n',length(top));
fprintf(file,'%10.f\n',top);
%
fprintf(file,'bottom\n');
fprintf(file,'%10.f\n',length(bottom));
fprintf(file,'%10.f\n',bottom);
%
fprintf(file,'nodetop\n');
fprintf(file,'%10.f\n',length(nodetop));
fprintf(file,'%10.f\n',nodetop);
%
fprintf(file,'nodebottom\n');
fprintf(file,'%10.f\n',length(nodebottom));
fprintf(file,'%10.f\n',nodebottom);
%
fprintf(file,'%10.f\n',3);
%

```

```
fprintf(file, 'sample\n');
fprintf(file, '%10.f\n', length(elements(:,1)));
fprintf(file, '%10.f\n', elements(:,1));
%
fprintf(file, 'basematerial\n');
fprintf(file, '%10.f\n', length(basematerial));
fprintf(file, '%10.f\n', basematerial);
%
fprintf(file, 'AMmaterial\n');
fprintf(file, '%10.f\n', length(AMmaterial));
fprintf(file, '%10.f\n', AMmaterial);
%
fprintf(file, '%10.f\n', 0);
%
fclose(file);
```

Published with MATLAB® R2018b

10.13 MATLAB code, Generating IPF map

Import Script for EBSD Data

This script was automatically created by the import wizard. You should run the whole script or parts of it in order to import your data. There is no problem in making any changes to this script.

Contents

- Specify Crystal and Specimen Symmetries
- Specify File Names
- Import the Data
- Plot IPF map

Specify Crystal and Specimen Symmetries

```
% crystal symmetry
CS = {...
    'notIndexed',...
    crystalSymmetry('m-3m', [3.6 3.6 3.6], 'mineral', 'Ni-superalloy', 'color', [0.53 0.81 0.98]),...
    crystalSymmetry('6/mmm', [3 3 4.7], 'X|[a]', 'Y|[b]', 'Z|[c]', 'mineral', 'Ti-Hex', 'color', [0.56 0.74 0.56]),...
    crystalSymmetry('m-3m', [3.2 3.2 3.2], 'mineral', 'Titanium cubic', 'color', [0.85 0.65 0.13]);

% plotting convention
setMTExpref('xAxisDirection', 'east');
setMTExpref('zAxisDirection', 'intoPlane');
```

Specify File Names

```
% path to files
pname = 'C:\Users\Michael\OneDrive - University of Strathclyde\Michael McPhillimy EngD Files\LMD project\Analysis\SEM\EBSD\MS\MS x 2000';

% which files to be imported
fname = [pname '\MS x2000.ctf'];
```

Import the Data

```
% create an EBSD variable containing the data
ebds = EBSD.load(fname, CS, 'interface', 'ctf', ...
    'convertEuler2SpatialReferenceFrame');
```

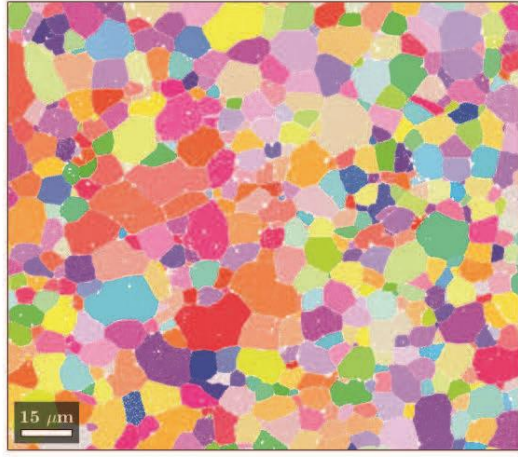
Plot IPF map

```
% colour map of ipf orientations
oM = ipfHSVkey(ebds('Ti-Hex'));

% direction of ipf
oM.inversePoleFigureDirection = xvector;

% convert ebsd map orientations to color based on the ipf
color = oM.orientation2color(ebds('Ti-Hex').orientations);

% plot ipf map
figure; plot(ebds('Ti-Hex'), color);
```



Published with ANTLABS REPOSITORY

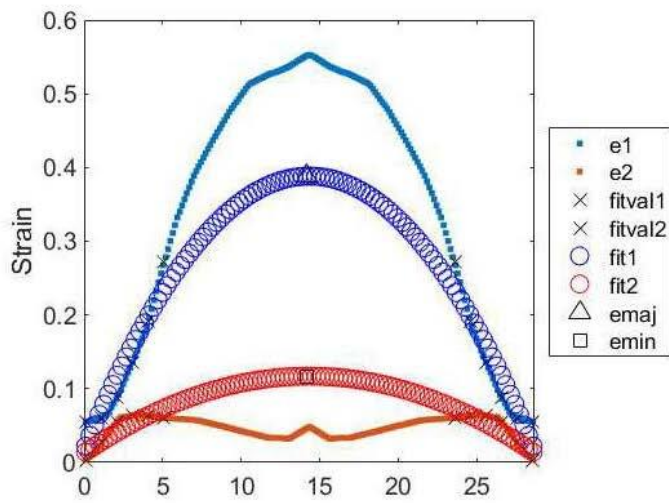
10.14 MATLAB code, Multiple curve fitting

```
clear all;close all;fclose all;clc;
%
% load in
data0=load('CPTI50A_2_S3_Section0_FLC.txt');
l=data0(:,1);
emaj=data0(:,2);
emin=data0(:,3);
plot(l,emaj, '.');hold on;plot(l,emin, '.');hold off
xlim([0 max(l)]);
legend('emaj','emin','Location','NorthEast');
xlabel('Section line');
ylabel('Strain');
%
% interpolate
step=0.1;
start=find(l, 1, 'first');start=l(start);
last=find(l, 1, 'last');last=l(last);
peak=(find(emaj==max(emaj)));peak=l(peak);
l0=peak:step:last;
emajj=interp1(l,emaj,l0);
emin=interp1(l,emin,l0);
plot(l0,emajj, '.');hold on;plot(l0,emin, '.');hold off
xlabel('Section line');
ylabel('Strain');
%
% mirror and shift plot
move=(last-peak)*1.5;
l0=((l0-peak)*1.5)+move;
l00=flip(-l0+(move*2));
x=[l00,l0];
emajjj=flip(emajj);
emin=flip(emin);
ymaj=[emajjj,emajj];
ymin=[emin,emin];
plot(x,ymaj, '.');hold on;plot(x,ymin, '.');
xlim([0 move*2]);
ylabel('Strain');
%
% write to txt file
curve_2_S3_0=[x;ymaj;ymin];
file=fopen('curve_2_S3_0.txt','w');
fprintf(file,'%f %f %f\n',curve_2_S3_0);
fclose(file);
%
% curve fitting
step=1;
xf1=x(1):step:x(1)+5;xf2=x(length(x))-5:step:x(length(x));
xf=[xf1,xf2]; %<----- data set for interpolated x data
yf1=interp1(l00,emajjj,xf1);yf2=interp1(l0,emajj,xf2);
yf3=interp1(l00,emin,xf1);yf4=interp1(l0,emin,xf2);
yfmax=[yf1,yf2]; %<----- data set for interpolated emax y data
yfmin=[yf3,yf4]; %<----- data set for interpolated emin y data
plot(xf,yfmax,'xk');plot(xf,yfmin,'xk');
pmax=polyfit(xf,yfmax,2); %<----- coefficients for polynomial p(xf)
pmin=polyfit(xf,yfmin,2); %<----- degree of 2
x=linspace(x(1),x(length(x))); %<----- x data for fit
ymax=polyval(pmax,x); %<----- evaluates polynomial p
ymin=polyval(pmin,x);
plot(x,ymax,'ob');plot(x,ymin,'or'); %<----- plot fitted curves
```

```

%
% strain values
e1=[(x(find(ymax==max(ymax),1))),max(ymax)]; % find() for double values
e2=[(x(find(ymin==max(ymin),1))),max(ymin)];
plot(e1(:,1),e1(:,2),'sk');
plot(e2(:,1),e2(:,2),'sk');
legend('e1','e2','fitval1','fitval2','fit1','fit2','emaj','emin','Location','EastOutside');
ylabel('Strain');

```



Published with MATLAB® R2020b

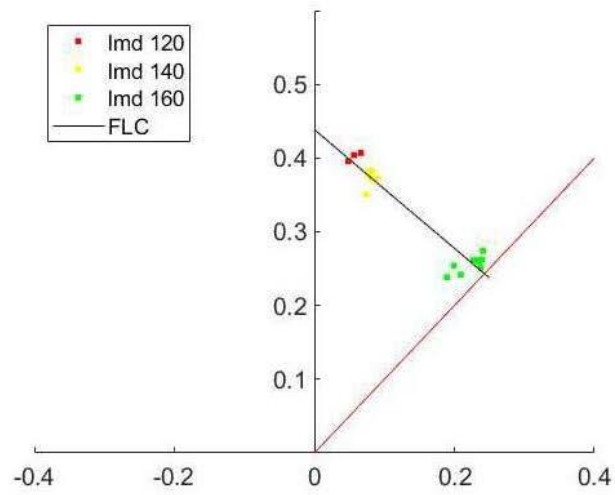
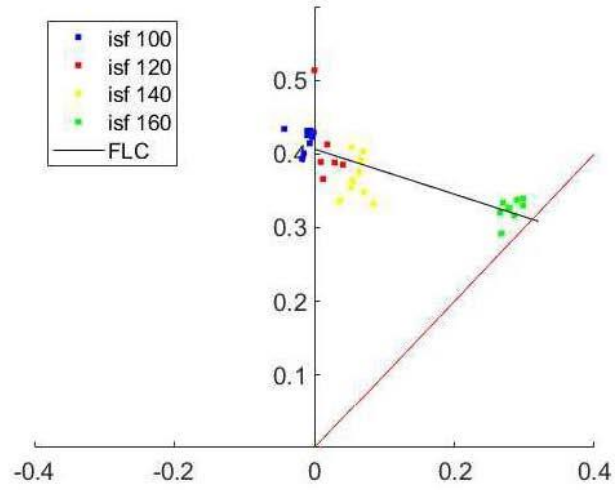
10.15 MATLAB code, Nakajima FLD

```

clear all;clc;fclose all;
%
% read data
isfemax = xlsread("Analysis.xlsx","isf","A:A");
isfemin = xlsread("Analysis.xlsx","isf","B:B");
lmdemax = xlsread("Analysis.xlsx","lmd","A:A");
lmdemin = xlsread("Analysis.xlsx","lmd","B:B");
%
% create variables for modes
isf100 = [isfemax(1:9,1) isfemin(1:9,1)];
isf120 = [isfemax(10:15,1) isfemin(10:15,1)];
isf140 = [isfemax(16:24,1) isfemin(16:24,1)];
isf160 = [isfemax(25:33,1) isfemin(25:33,1)];
lmd120 = [lmdemax(1:3,1) lmdemin(1:3,1)];
lmd140 = [lmdemax(4:9,1) lmdemin(4:9,1)];
lmd160 = [lmdemax(10:18,1) lmdemin(10:18,1)];
%
% plot flc isf
plot(isf100(:,2),isf100(:,1),"b.");
hold on
plot(isf120(:,2),isf120(:,1),"r.");plot(isf140(:,2),isf140(:,1),"y.");plot(isf160(:,2),isf160(:,1),"g.");
ylim([0 0.6]);
xlim([-0.4 0.4]);
ax = gca;
ax.YAxisLocation = "origin";
box off;
%
% Biaxial tension line
xbi = [0 0.4];
ybi = xbi;
%
% 1st degree polynomial line isf
pisf = polyfit(isfemin,isfemax,1);
x = linspace(0, 0.32);
y = polyval(pisf,x);
plot(x,y,'k');
hold on; plot(xbi, ybi, '-r'); % Biaxial tension line
legend("isf 100","isf 120","isf 140","isf 160","FLC","Location","NorthWest");
%
% plot flc lmd
figure;
plot(lmd120(:,2),lmd120(:,1),"r.");
hold on
plot(lmd140(:,2),lmd140(:,1),"y.");plot(lmd160(:,2),lmd160(:,1),"g.");
ylim([0 0.6]);
xlim([-0.4 0.4]);
ax = gca;
ax.YAxisLocation = "origin";
box off;
legend("lmd 120","lmd 140","lmd 160","FLC","Location","NorthWest");
%
% 1st degree polynomial curve lmd
pisf = polyfit(lmdemin,lmdemax,1);
x = linspace(0, 0.25);
y = polyval(pisf,x);
plot(x,y,'k');%hold on;plot(x,y+(y*0.075),'b');plot(x,y-(y*0.075),'b');
plot(xbi, ybi, '-r'); % Biaxial tension line
legend("lmd 120","lmd 140","lmd 160","FLC", "Location","NorthWest");

```

Warning: Ignoring extra legend entries.



10.16 MATLAB code, Material hardening curve

```
clear all;close all;fclose all;clc;
%-----
l0=20;
A0=1.588*6.017;
E=185.e3;
%
s0=261;
%
step=0.005;
ep2=0.0001:step:0.34;
inc_ep2=0.26:step:1.5;
%
a=0.23;b=0.25;c=0.27;
%-----
f=xlsread('MT0294 TS_1(1).xls',4,'B4:B1000');
u=xlsread('MT0294 TS_1(1).xls',4,'C4:C1000');
%
e=log(1+u/l0);
s=f/A0.*exp(e);
e=e*s(1)/E;
%
figure(1);hold on;xlabel('true strain');ylabel('true stress (MPa)');axis([0 0.4 0 600]);
plot(e,s,'.b');
%-----
pos1=find(s>s0,1,'first');
ep=e(pos1:1:end)-s(pos1:1:end)/E;
ep=ep-ep(1);
ss=s(pos1:1:end);
%
figure(2);hold on;xlabel('true plastic strain');ylabel('true stress (MPa)');axis([0 0.4 0 600]);
plot(ep,ss,'.b');
%
ss2=interp1(ep,ss,ep2);
plot(ep2,ss2,'ob');
%-----
p=polyfit([a,b],[ss2(find(ep2>a,1,'first')),ss2(find(ep2>b,1,'first'))],1);
%
ss3=[ss2(1:1:find(ep2>inc_ep2(1)-step,1,'first')),polyval(p,inc_ep2)];
ep3=[ep2(1:1:find(ep2>inc_ep2(1)-step,1,'first')),inc_ep2];
ep3(1)=0;
%
plot(ep3,ss3,'o-r');
%-----
% write to txt file
temp1=[ss3;ep3];
file=fopen('plastic_mod2.txt','w');
fprintf(file,'%12.8f, %12.8f\n',temp1);
fclose(file);
%-----
```

10.17 Material anisotropic function parameters

EXPERIMENTAL DATA:BARLAT 91	
R0	0.84
R45	2.44
R90	2.77
SIG0	1
SIG45	1.0989
SIG90	1.2344
SIGB	1.254809

FUNCTION PARAMETERS	
A	0.649696
B	0.971982
C	0.907155
F	1
G	1
H	1.039114
m	6

Accuracy(%) 85.8705

